Investigations of Structure-Property Relationships in Some A_2BX_4-type Organic-Inorganic Halide Hybrids

A Thesis
Submitted for the Degree of

DOCTOR OF PHILOSOPHY

by

Abhijit Sen

Chemistry and Physics of Materials Unit
Jawaharlal Nehru Centre for Advanced
Scientific Research
(A Deemed University)
Bangalore, India.

July 2019

Dedicated to my family

DECLARATION

I hereby declare that the matter embodied in this Ph.D. thesis entitled **"Investigations of Structure-Property Relationships in Some A_2BX_4-type Organic-Inorganic Halide Hybrids"** is the outcome of the investigations carried out by me under the supervision of Prof. A. Sundaresan at the Chemistry and Physics of Materials Unit, Jawaharlal Nehru Centre for Advanced Scientific Research, Bangalore, India. I would like to state that this work is unique, being submitted nowhere else for the award of any degree or diploma.

Thus going with the pre-existing practice of reporting scientific observations, due acknowledgement has been made whenever a work mentioned is based on the findings of other investigators.

23/07/2019

Abhijit Sen

Abhijit Sen

CERTIFICATE

I hereby certify that the matter embodied in this Ph.D. thesis entitled **"Investigations of Structure-Property Relationships in Some A_2BX_4-type Organic-Inorganic Halide Hybrids"** has been carried out by Mr. Abhijit Sen at the Chemistry and Physics of Materials Unit, Jawaharlal Nehru Centre for Advanced Scientific Research, Bangalore, India under my supervision and it has not been submitted elsewhere for the award of any degree or diploma.

23/07/2019

Prof. A. Sundaresan
(Research Supervisor)

Acknowledgements

At first, I would like to express my sincere gratitude to my research supervisor Prof. A. Sundaresan for introducing me to the class of organic-inorganic halide hybrid materials, their chemical diversity and captivating physical properties. I will always be thankful to him for allowing me huge freedom and giving me opportunity to work under his constant guidance and encouragement. I am highly grateful for his patience, positive attitude towards my research work and his support during my difficult times.

I would like to sincerely thank Prof. C. N. R. Rao, FRS for providing me various experimental facilities and for being a constant source of inspiration.

I convey my sincere thanks to past and present CPMU chairmen, Prof. G. U. Kulkarani, Prof. Balasubramanian and Prof. Chandrabhas Narayana for allowing me to utilize all the experimental facilities.

I would like to thank Sheikh Saqr Laboratory at JNCASR for providing experimental facilities.

I specially thank Dr. Diptikanta Swain and Prof. T. N. Guru Row from Indian Institute of Science for their rigorous help in solving single crystal structures and numerous effective discussions; Dr. Soumyabrata Roy and Dr. Sebastian C. Peter from JNCASR for their help in crystal structure solving; Dr. Arptia pal, Prof. U. V. Waghmare, Mr. Gurshid Ali, Dr. N. S. Vidhyadhiraja from JNCASR for providing theoretical insights; Prof. K.S. Narayan from JNCASR for providing low temperature photoluminescence facilities; Ms. Mahima, Dr. Murthy Grandhi and Dr. Ranjani Viswanatha from JNCASR for providing lifetime measurement facility.

I would like to thank Prof. A. Sundaresan, Prof. S. Narasimhan, Dr. N. S. Vidhyadhiraja and Prof. T. N. Guru Row (IISc) for offering their valuable courses.

I would like to thank technical staffs Mr. Srinath, Mr. Anil, Mr. Srinivasa, Mr. Sunil Mr. Mahesh and Mr. Shiva for their help during various measurements.

I convey my heartfelt thanks to all my past and present lab mates, Dr. Rambabu, Dr. Nitesh, Dr. Rana, Dr. Somnath, Dr. Chandan, Mr. Amit, Mr. Premakumar, Mr. Ravishankar, Ms. Pavitra, Ms. Swarnamayee, Mr. Debendra and Dr. Chandraiah for various helps during research and also for maintaining a very friendly atmosphere in the lab.

I would like to thank Complab, Library, Hostel, Dhanvantari, Academics and Administration staffs for providing and maintaining various facilities.

I would like to thank my batch mates Uttam, Rajib, Raaghesh, Sonu, Suchtra, and Komal for their cheerful company and good memories throughout the period.

I would also like to thank my past school and college teachers who were unparalleled in their teaching and guidance.

I would like to thank all my friends at JNCASR, specially Somnath da, Arpan da, Jia da, Saikat da, Sisir da, Shantanu, Mahima, Priyanka, Syamantak da, Soumyabrata, Sohini, Ananya, Ritesh da, Suman da, Raagya and Pragya who have been source of positive energy in all situation.

I would like to specially thank JNCASR football community, especially Sunil, Shanshank, Piyush, CD, Manan, Paaji, Dheeraj Bhai, Alam Sir and others.

Above all, I would like to thank my parents and my sister for all the love, affection and support to my research work.

Preface

The aim of the thesis was to design and synthesize new multifunctional organic-inorganic halide hybrids having A_2BX_4 chemical formula with different crystalline phases and study their structure-property relationships. The thesis, with its six chapters, highlights the component dependent structural diversities and supramolecular interactions in hybrid halides, and structure dependent interesting thermal, optical, magnetic and dielectric properties of the materials. A total of three different types of organic ammonium cations have been chosen as ***A*** cations e.g. Ethylammonium cation, $C_2H_5NH_3^+$ (monopositive alkylammonium cation); Guanidinium cation, $CH_6N_3^+$ (monopositive planar cation); Benzylammonium cation, $C_6H_5CH_2NH_3^+$ (monopositive arylammonium cation). As ***B*** cations, three different bivalent metal ions, Mn^{2+}, Co^{2+}, Cu^{2+} have been chosen. As halide anions ***X***, chloride (Cl^-) and bromide (Br^-) have been chosen. Depending on the structure and the components of each material, crystal structures, thermally stimulated phase transitions, surface roughness, electronic absorption spectra, photoluminescence, magnetic, magnetocaloric and dielectric properties have been studied in these materials.

Chapter 1 provides a brief introduction to crystalline hybrid halides composed of organic ammonium halide and inorganic bivalent metal halides. The component dependent structural diversities, various types of supramolecular interactions and their principle role in obtaining varied range of attractive physical properties i.e. phase transitions, thermo/piezo-chromism, photoluminescence, classical and quantum magnetism, dielectric switching and ferro/piezo-electricity have been discussed thoroughly.

Chapter 2 describes the different experimental techniques that have been used in the present work. Detailed discussions on the theories and methodologies behind single and poly crystal diffraction data analysis, thermogravimetry, differential scanning calorimetry, electronic absorption, photoluminescence, surface characterization, magnetic and dielectric measurements have been included here.

Chapter 3 discusses detailed experimental and theoretical investigations of structural, optical, magnetic and magnetocaloric properties of a new organic-inorganic halide hybrid $(C_2H_5NH_3)_2CoCl_4$. The single-crystalline compound exhibits zero dimensional orthorhombic structure (centrosymmetric *Pnma*) at room temperature and undergoes reversible phase transition at 235/241K (cooling/heating) to noncentrosymmetric $P2_12_12_1$ space group. Transition is associated with combination of order-disorder transformation of enthylammonium ions and cooperative molecular rearrangement. Electronic absorption spectra indicate presence of weak spin-orbit coupling in distorted $(CoCl_4)^{2-}$ units. Magnetic studies reveal paramagnetic behaviour down to 2 K. At low temperature region, magnetic field induced spin orientation is observed. First principles density functional calculations reveal weak magnetic interactions among cobalt spins with ferromagnetic state as ground state. The entropy change associated with the spin orientation has a maximum value of 16 J Kg^{-1} K^{-1} at 2.5 K under 7 T magnetic field (magnetocaloric effect).

Chapter 4 presents detailed structural, dielectric, magnetic and optical properties of a new A_2BX_4 type luminescent halide hybrid $(CH_6N_3)_2MnCl_4$ (CH_6N_3: Guanidinium cation or GC), The compound exhibits unique $(Mn_3Cl_{12})^{6-}$ units and possible ion-pair interactions among GCs in its zero dimensional crystal structure (space group $P2_1/c$ at 295 K). Thermally stimulated, reversible, first-order structural transition at 166/195 K to orthorhombic structure (space group $P2_12_12_1$) has been observed. The transition is rendered by order-disorder behaviour of GCs and also subtle changes in crystal packing. Large thermal hysteresis across the transition is conjured by modulation of extensive supramolecular interactions. Remarkably, the transition is seen to be decorated with switchable dielectric anomaly constructing beautiful 30 K wide hysteresis loop-like feature. The high and low dielectric states can be described by taking disordered (dipolar + quadrupolar) and frozen (quadrupolar) phases of GCs respectively. Moreover, the transition and hysteresis have also been uniquely visualized *via* reversible, weak magnetic switching. Presence of octahedral Mn^{2+} ion in $(Mn_3Cl_{12})^{6-}$ units causes fascinating bright orange-red emission at 645 nm under ultraviolet excitation. The luminescence has been well characterized which yields a long lifetime of 1.72 ms and 39.5% quantum yield at room temperature. The material also tends to exhibit optical switching across structural phase transition, as has been observed during cooling.

Chapter 5 presents detailed crystal structure analysis, low dimensional antiferromagnetic behavior and the correlation between the structure and magnetism in a new halide hybrid $(CH_6N_3)_2CuBr_4$ (CH_6N_3: Guanidinium cation or GC). The compound exhibits triclinic crystal structure (P-1 space group) at 295 K which features isolated $(CuBr_4)^{2-}$ units separated by planar, thermally ordered guanidinium cations. The guanidinium cations are closely placed and take part in ion-pair interactions in both “head-on” and “eclipsed” geometries. Such interactions and also hydrogen bonding between guanidinium cations and

$(CuBr_4)^{2-}$ units stabilize the structure as a result of which the compound maintains same crystal structure (P-1 space group) even at 95 K. DC magnetization measurements reveal a broad anomaly centered at 10 K which indicates low dimensional antiferromagnetic behavior (supported by negative Weiss constant – 24 K). Isothermal measurement at 2 K exhibits very small magnetization (0.18 μ_B/f.u. under 7 T). From crystal structure analysis, we find two halide exchange pathway (Cu-Br$\cdots$Br-Cu pathway) to be the mechanism behind the aforementioned magnetic behavior. Careful comparisons of Br$\cdots$Br distances, Cu-Br$\cdots$Br angles, Br$\cdots$Br-Cu angles and the Cu-Br$\cdots$Br-Cu dihedral angles along different crystallographic axes reveal that the antiferromagnetic interaction constructs a coupled ladder topology. Based on such analogy we have fitted the temperature dependent susceptibility data with spin Hamiltonian equations for spin chain, spin ladder, square lattice and rectangular lattice antiferromagnetic models. Among these, the spin ladder and rectangular lattice model fits really well with the later having the best fitting parameter.

Chapter 6 presents crystal structure and physical properties of a layered perovskite-like halide hybrid $(C_6H_5CH_2NH_3)_2CuBr_4$. The compound forms as plate shaped dark-brown opaque crystals. The single crystal structure solution reveal strong thermal disorder in benzylammonium cations. On introducing restraint on benzylammonium cations we could get a structure solution which is centrosymmetric monoclinic structure (*C*2/*c* space group symmetry). Space group symmetry was further confirmed using P vs E loop and PFM studies. The crystal structure contains corner shared $CuBr_6$ octahedral layers separated by two layers of benzylammonium cations with their nitrogen heads pointed towards metal halide layer. Structural analyses reveal that the $CuBr_6$ octahedra are Jahn-Teller distorted with adjacent octahedra having orthogonal J-T distortion. Such distortion favors antisymmetric wave function of orbitals and one can expect in layer ferromagnetic order via a 180° Cu−Br−Cu super-exchange mechanism. Temperature dependent dc magnetization measurements reveal magnetic transition at 13 K. Strong magnetocrystalline anisotropy has been observed where magnetization behavior indicates that the easy axis is perpendicular to the *c*-axis. The compound although having a layered structure behaves almost as a 3D magnet below transition temperature. Most interestingly, field induced step-like magnetization has been observed with magnetic field perpendicular to *c*-axis. Moreover, the crystals have mirror-like highly smooth surface which was confirmed using AFM studies which reveal that the surface roughness is well comparable with that of commercial sapphire surface.

Publications

[1] Order-disorder structural phase transition and magnetocaloric effect in novel organic-inorganic halide hybrid $(C_2H_5NH_3)_2CoCl_4$, **A. Sen**, S. Roy, S.C. Peter, A. Paul, U. V Waghmare, and A. Sundaresan, **J. Solid State Chem., 258, 431 (2018).**

[2] Highly Photoluminescent Hybrid $(CH_6N_3)_2MnCl_4$ Featuring 30 K Hysteresis in a Structural Phase Transition Marked by Switchable Dielectric and Magnetic Anomalies, **A. Sen**, D. Swain, T. N Guru Row, and A. Sundaresan, **J. Mater. Chem. C, 7 (16), 4838 (2019).**

[3] Structural and magnetic properties of a new low dimensional spin-1/2 antiferromagnet compound $(CH_6N_3)_2CuBr_4$, **A. Sen,** D. Swain, T. N Guru Row, and A. Sundaresan, (Manuscript under preparation).

[4] A perovskite-like hybrid $(C_6H_5CH_2NH_3)_2CuBr_4$ with mirror-like surface and field induced metamagnetic transitions, **A. Sen**, D. Swain, T. N Guru Row, and A. Sundaresan, (Manuscript under preparation).

Table of Contents

1. Introduction to Organic-Inorganic Halide Hybrids

2. Experimental Techniques

3. Structural Phase Transition, Optical Properties and Magnetocaloric Effect in Organic-Inorganic Hybrid $(C_2H_5NH_3)_2CoCl_4$

4. Highly Photoluminescent Hybrid $(CH_6N_3)_2MnCl_4$ Featuring 30 K Hysteresis in a Structural Phase Transition Marked by Switchable Dielectric and Magnetic Anomalies

5. Crystal Structure and Magnetic Properties of Low-dimensional Spin-1/2 Antiferromagnetic Compound $(CH_6N_3)_2CuBr_4$

6. A Perovskite-like Hybrid $(C_6H_5CH_2NH_3)_2CuBr_4$ with Mirror-like Surface and Field Induced Metamagnetic Transitions

Chapter 1

Introduction to Organic-Inorganic Halide Hybrids

Summary

This chapter presents a brief introduction to the transition-metal containing organic-inorganic hybrid halide materials, their structural diversities, various interesting physical properties and possible applications. At first, we briefly discuss the chemical bonding and the different crystal structural dimentionality that has been observed in this class of materials. Followed by this, we have focused on the interesting physical properties that these materials exhibit. A detailed discussion on the structural phase transition, different dielectric properties, magnetic properties and optical properties has been included. The effects of crystal structure dimension and the different components on these properties have been discussed in detail.

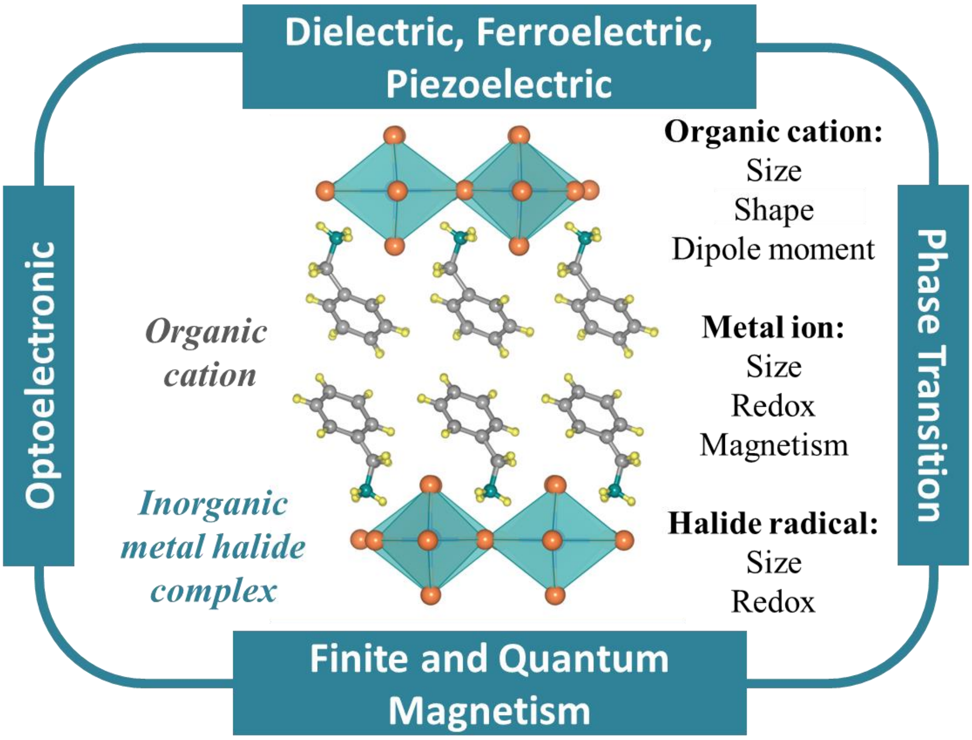

1.1 Organic-Inorganic Halide Hybrids:

The "organic-inorganic halide hybrids", as the name suggests, are the class of materials which incorporates both organic ammonium and inorganic metal halides in single phase and exhibits different component-dependent interesting physical properties. Originally known since the start of 20th century, the organic-inorganic halide hybrid materials have emerged over last two decades with ample promises by featuring pronounced structural diversity coupled with exciting range of remarkable dielectric, ferroelectric, magnetic and optoelectronic properties.[1–8] To mention, recent years have seen unparalleled progress being achieved in photovoltaic properties of the perovskite based materials $CH_3NH_3MX_3$ (M = Pb, Sn; X = Br, I).[7–11] With modern day materials-based research continuously focused on design and fabrication of multifunctional materials, the hybrid halides with their broad range of exciting properties and application can be claimed as truly multifunctional and are worthy to be focused on. Such diversity in physical properties arises from the different components that these materials contain. To describe, the organic ammonium cation with its own shape, size and dipole moment influence the structural symmetry largely, often giving rise to ferroelectric or piezoelectric states. The inorganic ions are seen to form various types of metal-halide complexes and influence the optoelectronic and magnetic properties of the material. Interestingly, as there are vast numbers of different ammonium ions, metal ions and halides which can play role of possible components, permuting them can lead to innumerable number of hybrids which can be studied. To mention, Cheetham *et al.* have modified the traditional tolerance factor equation and predicted that over 400 hybrid halides can have perovskite structures.[12,13] For this they have selected 13 different ammonium cations, 21 different bivalent metal ions and four halide ions (radii of selected cations and halide anions have been incorporated in **Table 1.1** and **1.2**).[13] In this chapter, we will briefly discuss the chemical bonding, structural diversity, physical properties of few transition metal based (Mn^{2+}, Fe^{2+}, Co^{2+}, Ni^{2+}, Cu^{2+}) organic-inorganic halide hybrids.

1.2 Chemical Bonding:

The chemical bonding present in the hybrid halides is at the heart of structure and properties and can be categorized into three components: the metal-halide architecture, intermolecular interaction and organic-organic interaction. Various types of metal-halide coordination complexes have been observed in hybrid halides where the metal halide bonds within the metal halide architecture are purely hetero-polar, where both ionic and covalent interactions can be observed.[14] Electrostatic interactions are seen to play dominant role as both metal and halogen atoms are charged species. The intermolecular interactions between organic molecules and metal halide architecture are mainly electrostatic in nature. Both hydrogen-bonding interaction and van der Waals interaction are seen to play important role in stabilizing the crystal structure. Since the organic cations have certain dipole moment associated with them, thus the interactions between them are seen to be of dipolar nature. Significant van der Waals interactions are observed among the organic ions. Such assortment of the various bonding interactions often gives rise to complex crystal structures featuring interesting physical properties.

1.3 Crystal Structures:

The crystal structures of the halide hybrids play pivotal role in governing the various physical properties of them. The structural diversity in hybrid halides comes mainly from the versatile metal-halide bonds and weakly on the template effect of the ammonium cations. It has been observed that the bivalent transition metal ions can form various types of coordination complexes with the halides and such variety of coordination complexes largely affects the crystal structure dimensionality of transition metal based halide hybrids. On the other hand, the size of the ammonium cations imprints its effect on the macroscopic symmetry and structural dimensionality. Over the years, continuous research efforts have resulted in realization of spectrum of hybrid halides with diverse structures, starting from zero-dimensional (0D) clusters, one-dimensional (1D) chains, two-dimensional (2D) layers to three dimensional (3D) frameworks. The diversity in structures is so vast that it is quite tedious to construct a comprehensive review on all the observed structures and their properties. With the increased research focus on perovskite halides due to superlative photovoltaic properties, a handful of reviews on this class of materials can be found whereas reviews on the other types of structures are scarse.[2,3,7,8,12] In order to prepare an inorganic solid state perovskite (formula ABX_3), the Goldschmidt's Tolerance Factor (t) is considered where the radii of the spherical inorganic cations (r_A and r_B) and anions (r_X) are considered using the following equation:[15]

$$t = \frac{(r_A + r_X)}{\sqrt{(r_B + r_X)}}, 0.8 \leq t \leq 1.0$$

For hybrid halides, where the ammonium cations are three dimensional molecules with effective size and shape, the tolerance factor expression was extended by Cheetham *et al.* who considered the rotational freedom around centre of mass of the different ammonium cations to determine the effective radii (r_{Aeff}).[12,13]

$$t = \frac{(r_{A_{eff}} + r_X)}{\sqrt{(r_B + r_X)}}$$

The following table includes the effective and ionic radii of a number of ammonium cations, metal ions and halide ions which have been calculated till date.[3,16]

Table 1.1 Effective radii of the different ammonium cations:[3,16]

Ammonium ion	Effective radius (pm)	Ammonium ion	Effective radius (pm)
Ammonium, $(NH_4)^+$	146	Dimethylammonium, $[(CH_3)_2NH_2]^+$	272
Hydrozylammonium, $(H_3NOH)^+$	216	3-Pyrollinium, $(NC_4H_8)^+$	272
Methylammonium, $(CH_3NH_3)^+$	217	Ethylammonium, $(C_2H_5NH_3)^+$	274
Hydrazinium, $[(H_3N\text{-}NH_2]^+$	217	Guanidinium, $[C(NH_2)_3]^+$	278
Azetidinium, $[(CH_2)_3NH_2]^+$	250	Tetramethylammonium, $[(CH_3)_4N]^+$	292
Formamidinium, $[CH(NH_2)_2]^+$	253	Piperazinium, $(C_4H_{12}N_2)^{2+}$	322
Imidazolium, $(C_3N_2H_5)^+$	258	Dabconium, $(C_6H_{14}N_2)^{2+}$	339

Table 1.2 Ionic Radii of different metal cations and halide anions:[3,16]

Metal ion	Ionic radius (pm)	Halide ion	Ionic radius (pm)
Mn^{2+}	67 (low spin) 83 (high spin)	Fluoride, F^-	129
Fe^{2+}	61 (low spin) 78 (high spin)	Chloride, Cl^-	181
Co^{2+}	65 (low spin) 74 (high spin)	Bromide, Br^-	195
Ni^{2+}	69	Iodide, I^-	220
Cu^{2+}	73		

This table gives a glimpse of the large variety of components which are available for the preparation of halide hybrids. For a selected set of components, if the tolerance factor deviates from the 0.8-1.0 range, then the resultant compound deviates from regular perovskite structure. Deviation from perovskite structure also hugely depends on the metal-halide complex formation. We now discuss about a few hybrid halides that contains the following transition metal ions Mn^{2+}, Fe^{2+}, Co^{2+}, Cu^{2+} and exhibits different dimensionalities in their crystal structures. The halide hybrids with above mentioned metal ions are seen to form structures of various dimensionalities starting from zero-dimensional discrete structures to two-dimensional layered structures. Till date no three-dimensional hybrid halides have been reported which contain transition metal ions.

1.3.1 Zero-dimensional (*0-D*) Halide Hybrids:

In the zero-dimensional hybrids, discrete metal-halide complexes are observed where the ammonium cations occupy the intermediate spaces. The general chemical formulae for the transition metal containing zero-dimensional hybrids are RMX_4 and R_2MX_4 (where *R*: organic ammonium ion, *M*: metal ion and *X*: halide ion). In general, it is observed that the bulkier ammonium cations with less number of hydrogen bonding centres hinder the growth of metal–halide complexes along different directions and force the structure to become discrete in nature. Thus, big-sized cations like tetramethylammonium cation $(CH_3)_4N^+$ or tetrapropylammonium cation $(C_3H_7)_4N^+$ are seen to form zero-dimensional structures with transition metals.[17,18] Both tetrahedral and octahedral metal-halide complexes have been observed in zero-dimensional hybrids (see **Scheme 1.1**). It is observed that among the different transition metals, the Co^{2+} ions always form tetrahedral $(CoX_4)^{2-}$ complexes due to crystal field effect and thus most of the structures are seen to be discrete.[18–22] Tetrahedral metal-halide complexes have also been observed in iron, copper and manganese containing hybrids where multiple phase transitions among different zero-dimensional structures have been observed.[17,23,24] Apart from the regular tetrahedral or octahedral complexes, tetragonal bipyramidal metal-halide complex has been uniquely seen in zero-dimensional structure of Cu-based ferroelectric $[H_2dbco]_2\cdot[Cl_3]\cdot[CuCl_3(H_2O)_2]\cdot H_2O$ Also.[25]

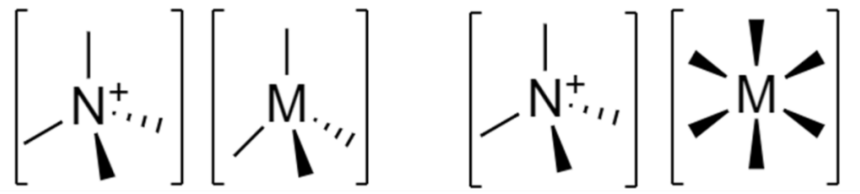

I **II**

Scheme 1.1 Schematic structures of zero-dimensional hybrid halides containing bulky ammonium ions and metal-halide tetrahedral (I) or octahedral (II) units.

1.3.2 One-dimensional (*1-D*) Halide Hybrids:

In the crystal structures of one-dimensional hybrids, metal-halide complexes are seen to extend along one direction *via* face-sharing (see **Scheme 1.2**). The general formula of these hybrids is RMX_3. To mention, well-known luminescent ferroelectric hybrid materials (Pyrrolidinium)$MnCl_3$ and (3-Pyrrolinium)MnX_3 (X: Cl, Br) feature one-dimensional metal-halide chains formed via face-shared octahedral $MnCl_6$ units.[26–28] The ammonium ions are seen to occupy spaces in between adjacent chains and take part in hydrogen bonding with metal-halide chains through nitrogen ends. Face-shared *1-D* chains have been observed in Mn-based halide hybrids but have not been observed for other transitional metal ions.[29–31] Among organic ions, heterocyclic ammonium ions with mono-nitrogen centres and very few alkylammonium ions e.g. pyridinium ion $(C_5H_5N)^+$, pyrrolidinium ion $(C_4H_{10}N)^+$, 3-pyrrolinium ion $(C_4H_8N)^+$, dimethylammonium ion $(CH_3)_2NH_2^+$ are seen to give rise to one-dimensional crystal structures with bivalent manganese ions.

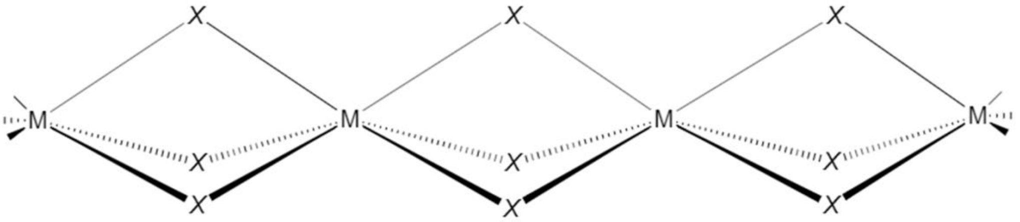

Scheme 1.2 Schematic structures of one-dimensional metal-halide (M-X) chain formed via face-sharing of octahedral MX_6 units.

1.3.3 Two-dimensional (*2-D*) Halide Hybrids:

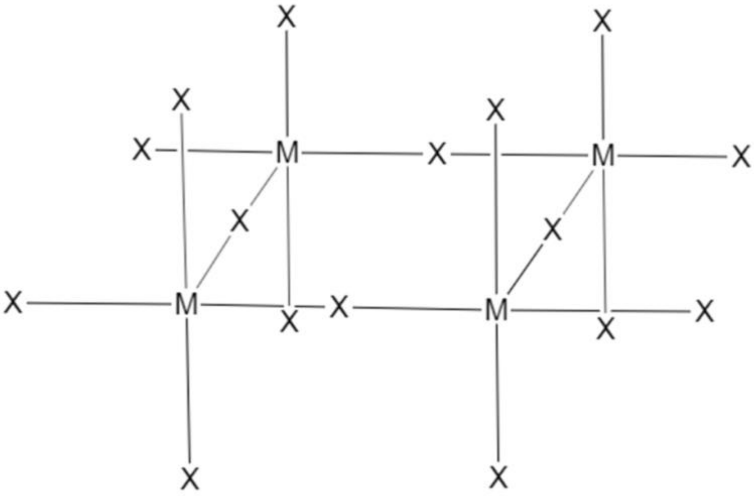

Scheme 1.3 Schematic structures of two-dimensional metal-halide MX_4 layer formed via corner-sharing of octahedral MX_6 units.

A two-dimensional hybrid structure is observed when the metal halide complex extends along two different directions forming layers and the ammonium cations occupy the inter-layer spaces. General formula of this category of hybrids is R_2MX_4. Most of the alkyl ammonium or aryl-alkyl ammonium cations form two-dimensional layered hybrids with bipositive ions of manganese, copper and iron metals. Well-known materials in this category are layered structures of materials with general formula $(C_nH_{2n+1}NH_3)_2MX_4$ where M: Mn^{2+}, Fe^{2+} and Cu^{2+} which exhibit *2-D* magnetism and ferroic properties.[32–36] In the two-dimensional metal-halide layer, it has been observed that the Mn^{2+} or Fe^{2+} ions exhibit tilted octahedra while the Cu^{2+} ions, due to Jahn-Teller distortions in them, exhibit distorted octahedra where the J-T elongation directions are seen to be orthogonal to each other in neighboring Cu centres.[32,36–38]

1.4 Physical Properties:

Over the years, a plethora of exciting physical properties has been observed in various organic-inorganic halide hybrid materials. Such properties include temperature and pressure dependent structural phase transition, optical absorption and luminescence, thermochromism, semiconducting and photovoltaic properties, dielectric transition and switching, ferroelectric and piezoelectric switching, quantum and classical magnetism.[5,7,26,28,38–49] Here, we will briefly discuss on thermally driven structural phase transition, photoluminescence, dielectric and magnetic properties observed in some of these materials.

1.4.1 Thermal Stability and Phase Transition:

Most of the hybrid halide materials struggle to withstand even moderately high temperature, as presence of the organic components in crystal structure often makes these materials behave softly. Typically, the melting and decomposition of hybrid materials start at around 473 K and gets completed by 873 K. Thus, focus has been given on studying material properties from room temperature to lowest possible temperature. As can be seen, a broad range of ammonium cations can be chosen to prepare the hybrid halides where each of the cations has its own shape, size and asymmetry associated with it.[4,12] These ammonium ions, being light-weight and connected to metal-halide architecture via weak intermolecular interactions, are often seen to have sizeable thermal parameters which influence them to have rotational or vibrational degrees of freedom. By changing the temperature of the material, one can alter the thermal parameters accordingly. As a result, under heating and/or cooling, the shape and the asymmetry of the ammonium cations distinctly change at certain temperature which is macroscopically realised in the form of structural phase transition.[2,50–52] The structural phase transitions in hybrid halides are seen to be first or second order type and are mostly reversible in nature.[5,23,53–55] In first order transition, sizable thermal hysteresis is observed where the first derivative i.e. entropy and volume are discontinuous across transition while in second order transitions are mostly diffused in nature and are seen to feature discontinuity in second order derivative (specific heat).[56,57] From crystallographic viewpoint, hybrid halides are seen to undergo mainly two types of transitions, (1) order-disorder type where ammonium cations reorient in between disordered and ordered state across transition and (2) displace type where the ammonium ions (and also at times the metal halide complex) get displaced relatively.[2,58] Among these, the order-disorder type phase transition are most common, as have been realized in numerous hybrids.[2,5] To mention, (Pyrrolidinium)MnX_3 (X = Cl and Br) compounds are well-known ferroelectric materials to exhibit orientational disorder in the organic pyrrolidinium cations in their one-dimensional crystal structures where the ferroelectric properties are governed by the symmetry changes associated with order-disorder type structural transition.[27,28] Another material is $((CH_3)_4N)_2ZnI_4$ where the order-disorder nature of the $(CH_3)_4N^+$ ions give rise to ferroelectric phase transition.[17] Displacive type phase transitions in hybrid halides are comparatively less seen, which have been observed in zero-dimensional $((CH_3)_4P)FeCl_4$ compound and one-dimensional $(C_6H_{11}NH_3)_2CdCl_4$.[23,54] Overall, it has been observed that the temperature dependent structural phase transition in hybrid halides is very common event. Interestingly, such phase transitions are often seen to be coupled with distinct changes in one or more bulk physical properties which can have potential applications. The properties will be discussed under individual sections.

1.4.2 Dielectric Properties:

The dielectric properties of hybrid halides depend significantly on the components and the dimensionality of the structure. Since the hybrid halides are prone to undergo one or more phase transition features, one can expect interesting dielectric properties in these materials. The structural phase transitions in hybrids imprint its signatures in form of distinct dielectric anomalies at phase transition temperatures. In some hybrids it is observed that one component of crystal structure features dynamic nature due to thermal disorder while the rest of the structure behaves rigidly. The order-disorder phase transition associated with such dynamic nature mostly leads to a step-like dielectric anomaly (known as dielectric switching). To mention, *0-D* hybrids $(C_6H_{15}ClNO)_2MnCl_4$, $(C_6H_{14}N)FeBr_4$ feature dynamic disorders in crystal structures and exhibit switching dielectric properties across reversible phase transition temperatures at 382/406 K and 336/340 K respectively.[59,60] Among *1-D* hybrids, switchable dielectric properties have been observed in otherwise luminescent material $(C_4H_7N_2)MnCl_3(H_2O)$.[41] Dielectric switching has also been observed in *2-D* hybrids, among which the compound $NH_3(CH_2)_5NH_3MnCl_4$ need notable mention as it exhibits dielectric switching near room temperature with remarkable anisotropy.[61]

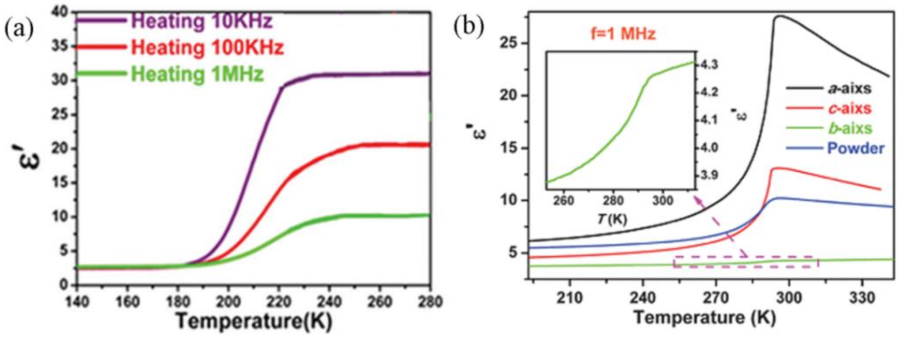

Figure 1.1 Switchable dielectric transitions observed in (a) *0-D* hybrid $(C_4H_7N_2)MnCl_3(H_2O)$ (a) *2-D* hybrid $NH_3(CH_2)_5NH_3MnCl_4$. Adapted after acquiring copyright permissions from © The Royal Society of Chemistry.[41,61]

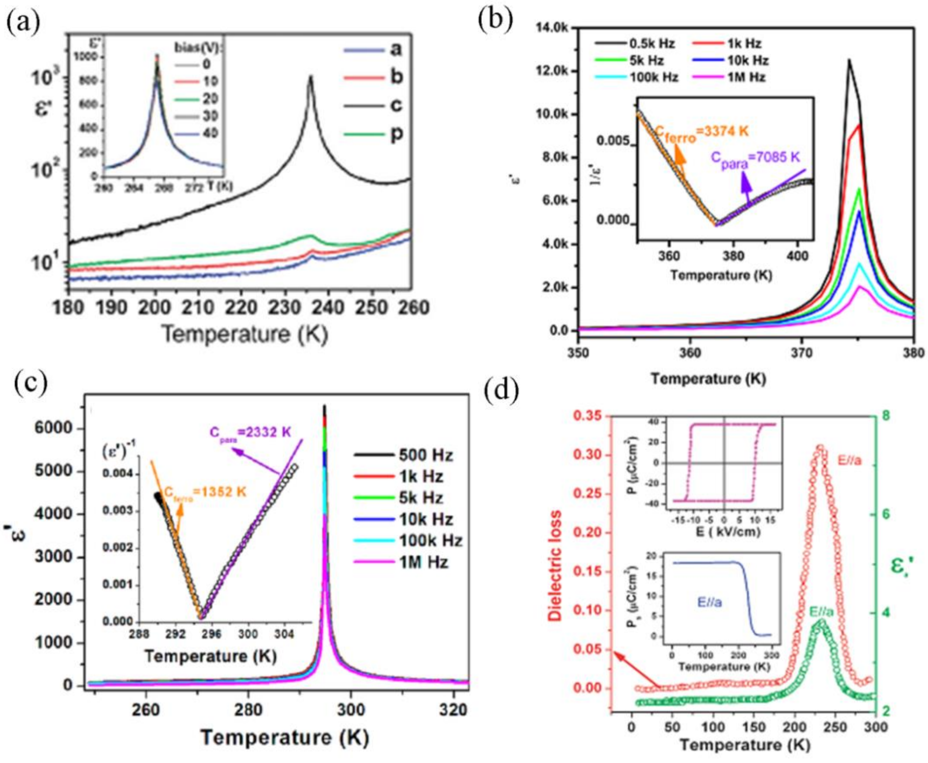

Figure 1.2 λ-shaped dielectric transitions in (a) *0-D* hybrid $[H_2dbco]_2\cdot[Cl_3]\cdot[CuCl_3(H_2O)_2]\cdot H_2O$, (b) *1-D* $C_4H_{10}NMnCl_3$, (c) *1-D* hybrid $C_4H_8NMnCl_3$ and (d) *2-D* hybrid $(C_2H_5NH_3)_2CuCl_4$. Adapted after taking copyright permissions from © The Royal Society of Chemistry and © American Chemical Society.[26,27,62]

When a phase transition is associated with inter-conversion between centrosymmetric and noncentrosymmetric structures, the dielectric behavior across transition is seen to be strongly coupled with it, featuring λ-shaped transition anomalies. Thus it has been observed that hybrid halides undergoing paraelectric-ferroelectric or paraelectric-piezoelectric phase transitions exhibit sharp dielectric transitions at the phase transition temperatures.[2] *0-D* hybrid compounds $[(CH_3)_4N]_2MCl_4$ (Mn^{2+}, Fe^{2+}, Co^{2+}, Cu^{2+}) exhibit weak ferroelectric nature coupled with dielectric transitions at ambient and under high pressure.[17] Another notable *0-D* hybrid is $[Cu(HDABCO)(H_2O)Cl_3]$ which undergoes a ferroelectric transition fashioned by a λ-shaped dielectric anomaly at 235 K where the ferroelectricity originates from symmetry breaking due to twisting motion of rotator molecules.[63] Ferroelectric transitions have also been observed in *1-D* hybrid materials e.g. $C_4H_{10}NMnCl_3$, $C_4H_8NMnCl_3$ which are also well-known to exhibit brilliant luminescence properties.[26–28] The *2-D* $(C_nH_{2n+1}NH_3)_2MX_4$ group of hybrids are well-known group of ferroics materials which exhibit dielectric transition at symmetry breaking phase transition temperatures.

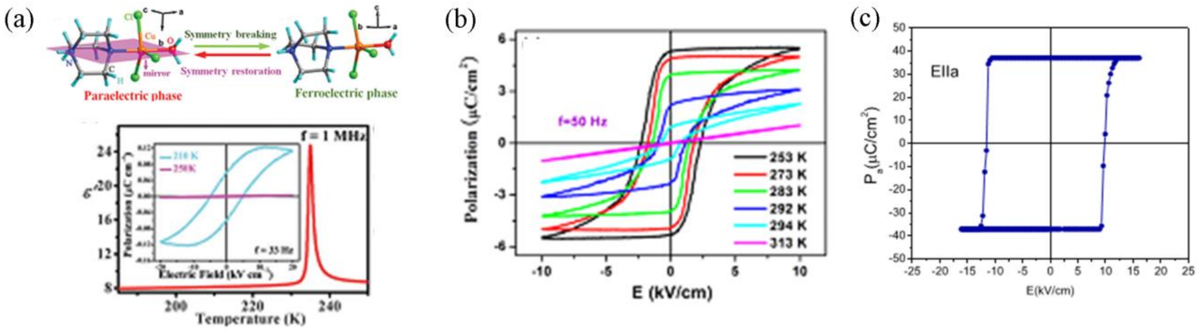

Figure 1.3 Ferroelectric properties of (a) *0-D* hybrid [Cu(HDABCO)(H_2O)Cl_3] where the ferroelectric property is influenced from the twisting motion of molecular rotator, (b) *1-D* (Pyrrolidinium)$MnCl_3$, (c) *2-D* $(C_2H_5NH_3)_2CuCl_4$ where the ferroelectric phase appears below 235 K and features a very large polarization, 37 μC cm^{-2} Reprinted after copyright permissions from © The Royal Society of Chemistry and © American Chemical Society and © American Physical Society.[2,27,38]

1.4.3 Magnetic Properties:

The transition metal based hybrid halides are well-known to exhibit broad range of magnetic properties which are dependent on the metal ion and also the crystal structural dimensionality. The zero-dimensional hybrids with discrete metal-halide complexes are seen to exhibit paramagnetic susceptibilities where no magnetic transitions are observed down to 2 K.[19,21–24] The magnetic properties in these materials often mimic single ion magnet behaviour as the discrete halide complexes are associated with deviation from regular geometry giving rise to zero field splitting.[19,21] The magnetic properties of *1-D* chains are largely different, as the copper and manganese based chains are seen to exhibit antiferromagnetic properties fashioned with broad anomalies in susceptibility data.[6,43,64–66] The magnetic behavior in these materials is largely governed by the Heisenberg exchange interactions propagating within one-dimension which often gives rise to quantum phases.[6,67,68] Such *1-D* antiferromagnetism has drawn huge interest from fundamental understanding point of view. Specifically, the antiferromagnetic spin-1/2 ladders and chains have been extensively studied where multiple exotic phases of matter have been experimentally realized.[69–72] Also, long range magnetic order have been observed in the *2-D* hybrids where the ferromagnetic ordering is governed by Jahn-Teller distorted Cu^{2+} ions in CuX_4 layers while the antiferromagnetic transitions are observed in compounds featuring MnX_4 and FeX_4 layers.[36,38,73] To mention further, the Cu (II)-based *2-D* hybrids are well-known to exhibit fast switching behavior under external magnetic field.[36,38,74]

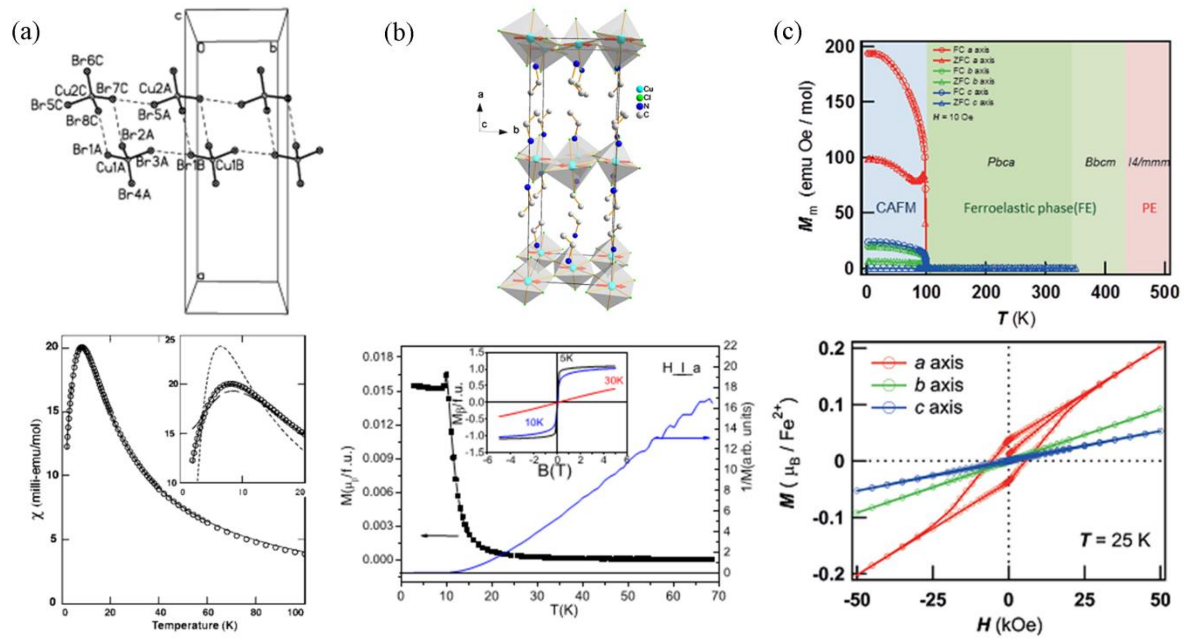

Figure 1.4 Magnetic transitions in (a) *1-D* ladder antiferromagnet $(C_5H_9NH_3)_2CuBr_4$ where the magnetic exchange interaction propagates through two-halide exchange pathway as depicted in the top picture, (b) *2-D* layered $(C_2H_5NH_3)_2CuCl_4$ where the ferromagnetic interactions are seen to propagate within one layer while the interlayer interactions are seen to be antiferromagnetic type, (c) *2-D* antiferromagnet $(C_6H_5CH_2NH_3)_2FeCl_4$. Adapted with copyright permissions from © The Royal Society of Chemistry and © American Chemical Society and © John Wiley & Sons, Inc.[38,66,73]

1.4.4 Optical Properties:

The single crystals of transition metal based halide hybrids have different colors and they exhibit various interesting optical properties e.g. photoluminescence, thermochromism and piezochromism. The crystal color and optical properties of these materials mainly depend on the transition metal ion, halide ion and the coordination geometry of metal-halide complex. It has been observed that the cobalt based hybrids form as blue colored crystals due to presence of the tetrahedral CoX_4 complexes. These materials show extensive absorption over a broad wavelength region where the absorption are weakly affected by spin-orbit coupling effect.[19,75,76] The hybrids containing manganese ions are seen to feature brilliant luminescence properties under ultraviolet spectra absorption. The color associated with luminescence depends on the manganese-halide complex geometry, as green emission has been observed in tetrahedral manganese complex while the octahedral complexes have exhibited efficient red emission.[24,27,77] To mention, Jiang *et al.* reported the zero-dimensional hybrid compound $(C_6H_{16}N)_2MnBr_4$ to exhibit efficient green emission at room temperature with large quantum yield of 62.2%.[24]

In the one-dimensional hybrids, bright red luminescence have been well observed in $C_4H_{10}NMnCl_3$, $C_4H_8NMnCl_3$ at room temperature fashioned by significant quantum yield and sizeable lifetime.[26–28] Luminescence has also been observed in *2-D* hybrids, with perovskite-type hybrids $NH_3(CH_2)_5NH_3MnCl_4$ and $(C_2H_5NH_3)_2MnCl_4$ exhibiting orange-red and pink luminescence properties respectively.[61,78] Among the copper based hybrids, since the *2-D* perovskite like materials feature antiferrodistortive arrangements of the square-planar CuX_6 complex in CuX_4 metal halide layer, the absorption resemble that of a molecular system where all the absorpion bands can be assigned based on crystal field splitting of a square-planar complex. The unique optical properties of Cu^{2+} hybrids are thermochromism and piezochromism. Mostafa *et al* have reported *2-D* material (*p*-toluidinium)$_2$CuCl$_4$ to exhibit temperature dependent reversible color change from orange high temperature phase to yellow intermediate phase at 294 K and from yellow phase to green low temperature phase at 214 K.[79] In another compound $(EDBE)_2CuCl_4$ (EDBE = 2,2′-(ethylenedioxy)bis(ethylammonium)), pressure dependent blackening has been observed by Karunadasa group.[48]

1.5 Applications:

The coexistence of several interesting yet independent properties in halide hybrids holds strong promise towards facile applications. The Cu-based hybrids have been considered as an alternative of Pb^{2+} and Sn^{2+} based light absorbers. For example, $(p-F-C_6H_5C_2H_4NH_3)_2CuBr_4$ and $(C_6H_5CH_2NH_3)_2CuBr_4$ are reported to have optical band gaps of 1.74 and 1.81 eV.[80,81] In fact, Zhou *et al.* have fabricated devices in FTO/TiO_2/Cu-halide perovskites/spiroOMeTAD/Ag structures which showed open-circuit voltages (V_{oc}) 0.87−0.88 V, short-circuit photocurrent densities (J_{sc}) of 1.46−1.78 mA cm^{-2}, and a fill factor (FF) of ∼0.40, giving power conversion efficiencies of 0.51−0.63%.[80] The major problem in achieving higher efficiency is the higher effective mass of charge carriers due to local *d*-orbitals of copper atoms.[3] The Cu-based layered hybrids are also seen to allow facile intercalation of ions and be used as battery cathodes as demonstrated by Karunadasa group. The have shown that perovskite based hybrid, $(EDBE)CuCl_4$ can be cycled over 200 times at a rate of 28 mA g^{-1} as a lithium battery cathode with an open-circuit voltage of 3.2 V.[82] The effect of temperature fluctuations on battery performance, the cell was kept under the sun for over a 24 hours period and the average capacities were over 225 cycles which gave impressive value of 38 (6) mA g^{-1} at 40 ° C and 26 (4) mA g^{-1} at 22 ° C.[82] The ferroelectric hybrid halides

1.6 Scope of The Thesis:

The fundamental and application oriented research on hybrid halides has been ever-evolving for decades, with numerous materials being designed which exhibit diverse structures and excellent physical properties. In this fast growing field of research, large scopes of improving in fundamental understanding on various physical properties and also achieving multifunctional materials are evident. To mention, there is always a strong demand of new ferroic hybrids or switchable hybrids due to their huge application potential. Increasing the thermal hysteresis across dielectric switching has not been explored thoroughly although it is very important in controlling the data loss in memory devices. Understanding the dependence of hysteresis on the cumulative supramolecular interactions is very important in this line. Also, although the magnetic properties of *2-D* R_2CuCl_4 have been thoroughly explored, the bromide counterparts have not been studied thoroughly.

In this thesis, we have prepared four new hybrid halides with the general formula R_2MX_4 by varying the compositions and have studied the structure-property relationships in them. We have focused on the general formula R_2MX_4 as they exhibit wide range of structural dimensions. We have chosen three different ammonium ions, ethylammonium ion ($C_2H_5NH_3^+$), guanidinium ion ($CN_3H_6^+$) and benzylammonium ion ($C_6H_5CH_2NH_3^+$) as the *R* cation. Among these, the ethylammonium and benzylammonium cations are mono nitrogen ammonium ions with finite dipole moments which along with the hydrogen bonding with metal halide architecture can potentially give rise to macroscopic polarization. On the other hand, the guanidinium cation with three nitrogen centres is a planar cation at its resonance hybrid state which: [1] makes this cation feature nearly zero dipole moment and [2] influences more number of hydrogen bonding and also possible ion-pair interactions within guanidinium cations. As bipositive metal ions, we have chosen cobalt, manganese and copper as they can be magnetically and optically active. We have chosen chloride and bromide ions as halide ion components. In the first work chapter, we present our studies on bis ethylammonium cobalt chloride $(C_2H_5NH_3)_2CoCl_4$ compound. The $(C_2H_5NH_3)_2MCl_4$ (M = Cu, Fe) are reported to be layered compounds with long range ferroic and magnetic orders. Our detailed studies show that the compound is paramagnetic down to 2 K with its low temperature crystal structure being noncentrosymmetric yet nonpolar (possible piezoelectric material at low temperature). In next two chapters, we have discussed our studies on two guanidinium ion containing hybrids: $(CN_3H_6)_2MnCl_4$ and $(CN_3H_6)_2CuBr_4$. Both of the materials exhibit zero-dimensional crystal structures where extensive hydrogen bonding and ion-pair interactions are observed. The bright luminescent $(CN_3H_6)_2MnCl_4$ compound features unique $(Mn_3Cl_{12})^{6-}$ units in crystal structure and exhibits large hysteresis across structural phase transition coupled with dielectric and weak magnetic switching. The large hysteresis across phase transition is governed by the extensive nature of the supramolecular interactions present among the components. The compound $(CN_3H_6)_2CuBr_4$, on the other hand behaves as low dimensional coupled spin ladder antiferromagnet where the magnetic interaction propagates in two halide magnetic exchange pathways. Further, we have prepared benzylammonium cations containing layered perovskite-like hybrid $(C_6H_5CH_2NH_6)_2CuBr_4$ and studied its crystal structure, surface, electrical and magnetic properties. The structure of this compound could not be solved completely before due to the crystal quality and twinning issues. However, our studies reveal that the crystals form as stacked single crystal plates with ultra-smooth surfaces where the crystals have centrosymmetric monoclinic structure ($C2/c$) which exhibit strong magnetocrystalline anisotropy with unique “in-plane” field induced metamagnetic transitions.

1.7 Bibliography:

(1) Wyckoff, R. W. G. The Crystal Structures of Monomethyl Ammonium Chlorostannate and Chloroplatinate. *Am. J. Sci.* **1928**, *16* (series 5), 349–359.

(2) Shi, P.-P.; Tang, Y.-Y.; Li, P.-F.; Liao, W.-Q.; Wang, Z.-X.; Ye, Q.; Xiong, R.-G. Symmetry Breaking in Molecular Ferroelectrics. *Chem. Soc. Rev.* **2016**, *45* (14), 3811–3827.

(3) Saparov, B.; Mitzi, D. B. Organic–Inorganic Perovskites: Structural Versatility for Functional Materials Design. *Chem. Rev.* **2016**, *116* (7), 4558–4596.

(4) Thirumurugan, C. N. R. R. and A. K. C. and A. Hybrid Inorganic–Organic

Materials: A New Family in Condensed Matter Physics. *J. Phys. Condens. Matter* **2008**, *20* (8), 83202.

(5) Shi, C.; Han, X.-B.; Zhang, W. Structural Phase Transition-Associated Dielectric Transition and Ferroelectricity in Coordination Compounds. *Coord. Chem. Rev.* **2017**.

(6) Landee, C. P.; Turnbull, M. M. Review: A Gentle Introduction to Magnetism: Units, Fields, Theory, and Experiment. *J. Coord. Chem.* **2014**, *67* (3), 375–439.

(7) Green, M. A.; Ho-Baillie, A.; Snaith, H. J. The Emergence of Perovskite Solar Cells. *Nat. Photonics* **2014**, *8*, 506.

(8) Boix, P. P.; Nonomura, K.; Mathews, N.; Mhaisalkar, S. G. Current Progress and Future Perspectives for Organic/Inorganic Perovskite Solar Cells. *Mater. Today* **2014**, *17* (1), 16–23.

(9) Park, N.-G. Organometal Perovskite Light Absorbers Toward a 20% Efficiency Low-Cost Solid-State Mesoscopic Solar Cell. *J. Phys. Chem. Lett.* **2013**, *4* (15), 2423–2429.

(10) Arora, N.; Dar, M. I.; Hinderhofer, A.; Pellet, N.; Schreiber, F.; Zakeeruddin, S. M.; Grätzel, M. Perovskite Solar Cells with CuSCN Hole Extraction Layers Yield Stabilized Efficiencies Greater than 20%. *Science (80-.).* **2017**, *358* (6364), 768 LP – 771.

(11) Grätzel, M. The Light and Shade of Perovskite Solar Cells. *Nat. Mater.* **2014**, *13*, 838.

(12) Kieslich, G.; Sun, S.; Cheetham, T. Solid-State Principles Applied to Organic-Inorganic Perovskites: New Tricks for an Old Dog. *Chem. Sci.* **2014**, *5*, 4712–4715.

(13) Kieslich, G.; Sun, S.; Cheetham, A. K. An Extended Tolerance Factor Approach for Organic–Inorganic Perovskites. *Chem. Sci.* **2015**, *6* (6), 3430–3433.

(14) Walsh, A. Principles of Chemical Bonding and Band Gap Engineering in Hybrid Organic–Inorganic Halide Perovskites. *J. Phys. Chem. C* **2015**, *119* (11), 5755–5760.

(15) Goldschmidt, V. M. Die Gesetze Der Krystallochemie. *Naturwissenschaften* **1926**, *14* (21), 477–485.

(16) Shannon, R. D. Revised Effective Ionic Radii and Systematic Studies of Interatomic Distances in Halides and Chalcogenides. *Acta Crystallogr. Sect. A* **1976**, *A32*, 751–767.

(17) Gesi, K. Phase Transitions and Ferroelectricity in $\{N(CH_3)_4\}_2XBr_4$ (X: Zn, Co, Cu). *J. Phys. Soc. Japan* **1982**, *51* (1), 203–207.

(18) Moutia, N.; Ben Gzaiel, M.; Oueslati, A.; Khirouni, K. Electrical Characterization and Vibrational Spectroscopic Investigations of Order-Disorder Phase Transitions in $[N(C_3H_7)_4]_2CoCl_4$ Compound. *J. Mol. Struct.* **2017**, *1134*, 697–705.

(19) Piecha-Bisiorek, A.; Bieńko, A.; Jakubas, R.; Boča, R.; Weselski, M.; Kinzhybalo, V.; Pietraszko, A.; Wojciechowska, M.; Medycki, W.; Kruk, D. Physical and Structural Characterization of Imidazolium-Based Organic-Inorganic Hybrid: $(C_3N_2H_5)_2[CoCl_4]$. *J. Phys. Chem. A* **2016**, *120* (12).

(20) Sawada, S.; Shiroishi, Y.; Yamamoto, A.; Takashige, M.; Matsuo, M. Ferroelectricity in $\{N(CH_3)_4\}_2CoCl_4$. *Phys. Lett. A* **1978**, *67* (1), 56–58.

(21) Decaroli, C.; Arevalo-Lopez, A. M.; Woodall, C. H.; Rodriguez, E. E.; Attfield, J. P.; Parker, S. F.; Stock, C. $(C_4H_{12}N_2)[CoCl_4]$: Tetrahedrally Coordinated Co^{2+} without the Orbital Degeneracy. *Acta Crystallogr. B. Struct. Sci. Cryst. Eng. Mater.* **2015**, *71* (Pt 1), 20–24.

(22) Hua, X.-N.; Huang, C.-R.; Gao, J.-X.; Lu, Y.; Chen, X.-G.; Liao, W.-Q. High-Temperature Reversible Phase Transitions and Exceptional Dielectric Anomalies in Cobalt(II) Based Ionic Crystals: $[Me_3NCH_2X]_2[CoX_4]$ (X = Cl and Br). *Dalt. Trans.* **2018**, *47* (17), 6218–6224.

(23) Shi, P.-P.; Ye, Q.; Li, Q.; Wang, H.-T.; Fu, D.-W.; Zhang, Y.; Xiong, R.-G. Novel Phase-Transition Materials Coupled with Switchable Dielectric, Magnetic, and Optical Properties: $[(CH_3)_4P][FeCl_4]$ and $[(CH_3)_4P][FeBr_4]$. *Chem. Mater.* **2014**, *26* (20), 6042–6049.

(24) Jiang, C.; Zhong, N.; Luo, C.; Lin, H.; Zhang, Y.; Peng, H.; Duan, C.-G.

(Diisopropylammonium)$_2$MnBr$_4$: A Multifunctional Ferroelectric with Efficient Green-Emission and Excellent Gas Sensing Properties. *Chem. Commun.* **2017**, *53* (44), 5954–5957.

(25) Zhang, W.; Ye, H.-Y.; Cai, H.-L.; Ge, J.-Z.; Xiong, R.-G.; Huang, S. D. Discovery of New Ferroelectrics: [H$_2$dbco]$_2$ x [Cl$_3$] x [CuCl$_3$(H$_2$O)$_2$] x H$_2$O (Dbco = 1,4-Diaza-Bicyclo[2.2.2]Octane). *J. Am. Chem. Soc.* **2010**, *132* (21), 7300–7302.

(26) Ye, H.-Y.; Zhou, Q.; Niu, X.; Liao, W.-Q.; Fu, D.-W.; Zhang, Y.; You, Y.-M.; Wang, J.; Chen, Z.-N.; Xiong, R.-G. High-Temperature Ferroelectricity and Photoluminescence in a Hybrid Organic–Inorganic Compound: (3-Pyrrolinium)MnCl$_3$. *J. Am. Chem. Soc.* **2015**, *137* (40), 13148–13154.

(27) Zhang, Y.; Liao, W.-Q.; Fu, D.-W.; Ye, H.-Y.; Chen, Z.-N.; Xiong, R.-G. Highly Efficient Red-Light Emission in An Organic–Inorganic Hybrid Ferroelectric: (Pyrrolidinium)MnCl$_3$. *J. Am. Chem. Soc.* **2015**, *137* (15), 4928–4931.

(28) Zhang, Y.; Liao, W.-Q.; Fu, D.-W.; Ye, H.-Y.; Liu, C.-M.; Chen, Z.-N.; Xiong, R.-G. The First Organic–Inorganic Hybrid Luminescent Multiferroic: (Pyrrolidinium)MnBr$_3$. *Adv. Mater.* **2015**, *27* (26), 3942–3946.

(29) Dingle, R.; Lines, M. E.; Holt, S. L. Linear-Chain Antiferromagnetism in [(CH$_3$)$_4$N][MnCl$_3$]. *Phys. Rev.* **1969**, *187* (2), 643–648.

(30) Birgeneau, R. J.; Dingle, R.; Hutchings, M. T.; Shirane, G.; Holt, S. L. Spin Correlations in a One-Dimensional Heisenberg Antiferromagnet. *Phys. Rev. Lett.* **1971**, *26* (12), 718–721.

(31) Takeda, K.; Schouten, J. C.; Kopinga, K.; de Jonge, W. J. M. Quasi-One-Dimensional Behavior of (CH$_3$)$_2$NH$_2$MnCl$_3$ (DMMC). *Phys. Rev. B* **1978**, *17* (3), 1285–1288.

(32) Han, J.; Nishihara, S.; Inoue, K.; Kurmoo, M. On the Nature of the Structural and Magnetic Phase Transitions in the Layered Perovskite-Like (CH$_3$NH$_3$)$_2$[Fe^{II}Cl$_4$]. *Inorg. Chem.* **2014**, *53* (4), 2068–2075.

(33) Suzuki, T.; Yoshizawa, M.; Goto, T.; Yamakami, T.; Takahashi, M.; Fujimura, T. Structural Phase Transition of Layer Compound (C$_2$H$_5$NH$_3$)$_2$FeCl$_4$. *J. Phys. Soc.*

Japan **1983**, *52* (5), 1669–1675.

(34) Steadman, J. P.; Willett, R. D. The Crystal Structure of $(C_2H_5NH_3)_2CuCl_4$. *Inorganica Chim. Acta* **1970**, *4*, 367–371.

(35) Barendregt, F.; Schenk, H. The Crystal Structure of $CuCl_4(NH_3C_3H_7)_2$. *Physica* **1970**, *49* (3), 465–468.

(36) Polyakov, A. O.; Arkenbout, A. H.; Baas, J.; Blake, G. R.; Meetsma, A.; Caretta, A.; van Loosdrecht, P. H. M.; Palstra, T. T. M. Coexisting Ferromagnetic and Ferroelectric Order in a $CuCl_4$-Based Organic–Inorganic Hybrid. *Chem. Mater.* **2012**, *24* (1), 133–139.

(37) Kamminga, M. E.; Hidayat, R.; Baas, J.; Blake, G. R.; Palstra, T. T. M. Out-of-Plane Polarization in a Layered Manganese Chloride Hybrid. *APL Mater.* **2018**, *6* (6), 66106.

(38) Kundys, B.; Lappas, a.; Viret, M.; Kapustianyk, V.; Rudyk, V.; Semak, S.; Simon, C.; Bakaimi, I. Multiferroicity and Hydrogen-Bond Ordering in $(C_2H_5NH_3)_2CuCl_4$ Featuring Dominant Ferromagnetic Interactions. *Phys. Rev. B - Condens. Matter Mater. Phys.* **2010**, *81* (22), 1–6.

(39) Wang, Y.; Runnerstrom, E. L.; Milliron, D. J. Switchable Materials for Smart Windows. *Annu. Rev. Chem. Biomol. Eng.* **2016**, *7* (1), 283–304.

(40) Liao, W.-Q.; Zhang, Y.; Hu, C.-L.; Mao, J.-G.; Ye, H.-Y.; Li, P.-F.; Huang, S. D.; Xiong, R.-G. A Lead-Halide Perovskite Molecular Ferroelectric Semiconductor. *Nat. Commun.* **2015**, *6*, 7338.

(41) Guo, Q.; Zhang, W.-Y.; Chen, C.; Ye, Q.; Fu, D.-W. Red-Light Emission and Dielectric Reversible Duple Opto-Electronic Switches in a Hybrid Multifunctional Material: (2-Methylimidazolium)$MnCl_3(H_2O)$. *J. Mater. Chem. C* **2017**, *5* (22), 5458–5464.

(42) Tylczyński, Z.; Wiesner, M.; Trzaskowska, A. Spontaneous Piezoelectric Effect as Order Parameter in $(NH_4)_2CuBr_4{\cdot}2H_2O$ Crystal. *Phys. B Condens. Matter* **2016**, *500*, 85–88.

(43) Shapiro, A.; Landee, C. P.; Turnbull, M. M.; Jornet, J.; Deumal, M.; Novoa, J. J.;

Robb, M. A.; Lewis, W. Synthesis, Structure, and Magnetic Properties of an Antiferromagnetic Spin-Ladder Complex: Bis(2,3-Dimethylpyridinium) Tetrabromocuprate. *J. Am. Chem. Soc.* **2007**, *129* (4), 952–959.

(44) Turnbull, M. M.; Landee, C. P.; Wells, B. M. Magnetic Exchange Interactions in Tetrabromocuprate Compounds. *Coord. Chem. Rev.* **2005**, *249* (23), 2567–2576.

(45) Shi, C.; Yu, C.-H.; Zhang, W. Predicting and Screening Dielectric Transitions in a Series of Hybrid Organic–Inorganic Double Perovskites via an Extended Tolerance Factor Approach. *Angew. Chemie Int. Ed.* **2016**, *55* (19), 5798–5802.

(46) Pitula, S.; Mudring, A.-V. Synthesis, Structure, and Physico-Optical Properties of Manganate(II)-Based Ionic Liquids. *Chem. – A Eur. J.* **2010**, *16* (11), 3355–3365.

(47) Lee, Y.; Mitzi, D. B.; Barnes, P. W.; Vogt, T. Pressure-Induced Phase Transitions and Templating Effect in Three-Dimensional Organic-Inorganic Hybrid Perovskites. *Phys. Rev. B* **2003**, *68* (2), 20103.

(48) Jaffe, A.; Lin, Y.; Mao, W. L.; Karunadasa, H. I. Pressure-Induced Conductivity and Yellow-to-Black Piezochromism in a Layered Cu–Cl Hybrid Perovskite. *J. Am. Chem. Soc.* **2015**, *137* (4), 1673–1678.

(49) Julià-López, A.; Hernando, J.; Ruiz-Molina, D.; González-Monje, P.; Sedó, J.; Roscini, C. Temperature-Controlled Switchable Photochromism in Solid Materials. *Angew. Chemie* **2016**, *128* (48), 15268–15272.

(50) Zhang, H.-Y.; Mei, G.-Q.; Liao, W.-Q. Symmetry Breaking Phase Transition, Second-Order Nonlinear Optical and Dielectric Properties of a One-Dimensional Organic–Inorganic Hybrid Zigzag Chain Compound $[NH_3(CH_2)_5NH_3]SbBr_5$. *Cryst. Growth Des.* **2016**, *16* (10), 6105–6110.

(51) Gomez-Cuevas, M. J. T. and A. L.-E. and J. Z. and I. R.-L. and F. J. Z. and G. M. and A. A New $(C_2H_5NH_3)_2ZnCl_4$ Crystal with a Pure $Pnma$-$P2_12_12_1$ Ferroelastic Phase Transition. *J. Phys. Condens. Matter* **1994**, *6* (34), 6751.

(52) Han, J.; Nishihara, S.; Inoue, K.; Kurmoo, M. High Magnetic Hardness for the Canted Antiferromagnetic, Ferroelectric, and Ferroelastic Layered Perovskite-like $(C_2H_5NH_3)_2[Fe^{II}Cl_4]$. *Inorg. Chem.* **2015**, *54* (6), 2866–2874.

(53) Sen, A.; Roy, S.; Peter, S. C.; Paul, A.; Waghmare, U. V; Sundaresan, A. Order-Disorder Structural Phase Transition and Magnetocaloric Effect in Organic-Inorganic Halide Hybrid $(C_2H_5NH_3)_2CoCl_4$. *J. Solid State Chem.* **2018**, *258*, 431–440.

(54) Liao, W.-Q.; Ye, H.-Y.; Fu, D.-W.; Li, P.-F.; Chen, L.-Z.; Zhang, Y. Temperature-Triggered Reversible Dielectric and Nonlinear Optical Switch Based on the One-Dimensional Organic–Inorganic Hybrid Phase Transition Compound $[C_6H_{11}NH_3]_2CdCl_4$. *Inorg. Chem.* **2014**, *53* (20), 11146–11151.

(55) Mao, C.-Y.; Liao, W.-Q.; Wang, Z.-X.; Zafar, Z.; Li, P.-F.; Lv, X.-H.; Fu, D.-W. Temperature-Triggered Dielectric-Optical Duple Switch Based on an Organic–Inorganic Hybrid Phase Transition Crystal: $[C_5N_2H_{16}]_2SbBr_5$. *Inorg. Chem.* **2016**, *55* (15), 7661–7666.

(56) Fujimoto, M. *The Physics of Structural Phase Transitions*; 2005.

(57) Izyumov, Yurii Aleksandrovich, Syromyatnikov, V. . *Phase Transitions and Crystal Symmetry*.

(58) Tolédano, P.; Dmitriev, V. *Reconstructive Phase Transitions*; WORLD SCIENTIFIC, 1996.

(59) Xu, C.; Zhang, W.-Y.; Chen, C.; Ye, Q.; Fu, D.-W. Fast and Slow Integrated Single-Molecule Dual Dielectric Switch Based on a Crystal/Flexible Thin Film. *J. Mater. Chem. C* **2017**, *5* (28), 6945–6953.

(60) Han, S.; Zhang, J.; Teng, B.; Ji, C.; Zhang, W.; Sun, Z.; Luo, J. Inorganic–Organic Hybrid Switchable Dielectric Materials with the Coexistence of Magnetic Anomalies Induced by Reversible High-Temperature Phase Transition. *J. Mater. Chem. C* **2017**, *5* (33), 8509–8515.

(61) Lv, X.-H.; Liao, W.-Q.; Li, P.-F.; Wang, Z.-X.; Mao, C.-Y.; Zhang, Y. Dielectric and Photoluminescence Properties of a Layered Perovskite-Type Organic–Inorganic Hybrid Phase Transition Compound: $NH_3(CH_2)_5NH_3MnCl_4$. *J. Mater. Chem. C* **2016**, *4* (9), 1881–1885.

(62) Hang, T.; Zhang, W.; Ye, H.-Y.; Xiong, R.-G. Metal–Organic Complex

Ferroelectrics. *Chem. Soc. Rev.* **2011**, *40* (7), 3577–3598.

(63) Zhang, Y.; Zhang, W.; Li, S.-H.; Ye, Q.; Cai, H.-L.; Deng, F.; Xiong, R.-G.; Huang, S. D. Ferroelectricity Induced by Ordering of Twisting Motion in a Molecular Rotor. *J. Am. Chem. Soc.* **2012**, *134* (26), 11044–11049.

(64) Phaff, A. C.; Swuste, C. H. W.; Kopinga, K.; Jonge, W. J. M. de. Anomalous AFMR in Some Quasi-One-Dimensional Mn2+compounds. *J. Phys. C Solid State Phys.* **1983**, *16* (34), 6635–6649.

(65) Schouten, J. C.; Hadders, H.; Kopinga, K.; de Jonge, W. J. M. Quasi One-Dimensional Magnetic Behavior of (C5H5NH)MnCl3 (PMCA) and (C5H5NH)NiCl3 (PNCA). *Solid State Commun.* **1980**, *34* (8), 667–670.

(66) Willett, R. D.; Galeriu, C.; Landee, C. P.; Turnbull, M. M.; Twamley, B. Structure and Magnetism of a Spin Ladder System: $(C_5H_9NH_3)_2CuBr_4$. *Inorg. Chem.* **2004**, *43* (13), 3804–3811.

(67) R.D. Willett, D. Gatteschi, O. K. (Eds. . Magneto-Structural Correlations in Exchange Coupled Systems. *Rei-del, Boston,* **1989**, 389.

(68) Woodward, F. M.; Landee, C. P.; Giantsidis, J.; Turnbull, M. M.; Richardson, C. Structure and Magnetic Properties of $(5BAP)_2CuBr_4$: Magneto-Structural Correlations of Layered S = 1/2 Heisenberg Antiferromagnets. *Inorganica Chim. Acta* **2001**, *324* (1), 324–330.

(69) Jeong, M.; Mayaffre, H.; Berthier, C.; Schmidiger, D.; Zheludev, A.; Horvatić, M. Magnetic-Order Crossover in Coupled Spin Ladders. *Phys. Rev. Lett.* **2017**, *118* (16), 1–5.

(70) Hong, T.; Kim, Y. H.; Hotta, C.; Takano, Y.; Tremelling, G.; Turnbull, M. M.; Landee, C. P.; Kang, H.-J.; Christensen, N. B.; Lefmann, K.; et al. Field-Induced Tomonaga-Luttinger Liquid Phase of a Two-Leg Spin-1/2 Ladder with Strong Leg Interactions. *Phys. Rev. Lett.* **2010**, *105* (13), 137207.

(71) Schmidiger, D.; Bouillot, P.; Mühlbauer, S.; Gvasaliya, S.; Kollath, C.; Giamarchi, T.; Zheludev, A. Spectral and Thermodynamic Properties of a Strong-Leg Quantum Spin Ladder. *Phys. Rev. Lett.* **2012**, *108* (16), 18–22.

(72) Hong, T.; Zheludev, A.; Manaka, H.; Regnault, L.-P. Evidence of a Magnetic Bose Glass in $(CH_3)_2CHNH_3Cu(Cl_{0.95}Br_{0.05})_3$ from Neutron Diffraction. *Phys. Rev. B* **2010**, *81* (6), 60410.

(73) Nakayama, Y.; Nishihara, S.; Inoue, K.; Suzuki, T.; Kurmoo, M. Coupling of Magnetic and Elastic Domains in the Organic–Inorganic Layered Perovskite-Like $(C_6H_5C_2H_4NH_3)_2FeIICl_4$ Crystal. *Angew. Chemie* **2017**, *129* (32), 9495–9498.

(74) De Jongh, L. J.; Van Amstel, W. D.; Miedema, A. R. Magnetic Measurements on $(C_2H_5NH_3)_2CuCl_4$: Ferromagnetic Layers Coupled by a Very Weak Antiferromagnetic Interaction. *Physica* **1972**, *58* (2), 277–304.

(75) Ferguson, J. Crystal-Field Spectra of D3,7 Ions. I. Electronic Absorption Spectrum of CoCl4= in Three Crystalline Environments. *J. Chem. Phys.* **1963**, *39* (1), 116–128.

(76) Kapustianyk, V. B.; Yonak, P. K.; Rudyk, V. P. Temperature Evolution of the Intra-Ion Absorption Spectra of Cobalt in $(NH_2(CH_3)_2)_2CoCl_4$ Crystals. *J. Appl. Spectrosc.* **2015**, *82* (4), 591–597.

(77) Orgel, L. E. Phosphorescence of Solids Containing the Manganous or Ferric Ions. *J. Chem. Phys.* **1955**, *23* (10), 1958.

(78) Garanderie, P. de la H. Complexes Luminescents Du Chlorure de Manganese Avuc Les Amines. *C. R. Hebd. Seances Acad. Sci.* **1962**, *254*, 2739.

(79) Mostafa, M. F.; Abdel-Kader, M. M.; Arafat, S. S.; Kandeel, E. M. Thermochromic Phase Transitions in Two Aromatic Tetrachlorocuprates. *Phys. Scr.* **1991**, *43* (6), 627–629.

(80) Cui, X.-P.; Jiang, K.-J.; Huang, J.-H.; Zhang, Q.-Q.; Su, M.-J.; Yang, L.-M.; Song, Y.-L.; Zhou, X.-Q. Cupric Bromide Hybrid Perovskite Heterojunction Solar Cells. *Synth. Met.* **2015**, *209*, 247–250.

(81) Li, X.; Li, B.; Chang, J.; Ding, B.; Zheng, S.; Wu, Y.; Yang, J.; Yang, G.; Zhong, X.; Wang, J. $(C_6H_5CH_2NH_3)_2CuBr_4$: A Lead-Free, Highly Stable Two-Dimensional Perovskite for Solar Cell Applications. *ACS Appl. Energy Mater.* **2018**, *1* (6), 2709–2716.

(82) Jaffe, A.; Karunadasa, H. I. Lithium Cycling in a Self-Assembled Copper Chloride–Polyether Hybrid Electrode. *Inorg. Chem.* **2014**, *53* (13), 6494–6496.

Chapter 2

Experimental Techniques

Summery

This chapter gives a detailed discussion about the various preparation techniques used to synthesize the hybrid halide compounds and study the properties of the same.

2.1 Synthetic Strategies:

All the compounds investigated in this thesis are single crystalline materials. As the inorganic components, we chose bromides and chlorides of cobalt, manganese and copper. Solvent evaporation technique has been followed in order to grow the single or polycrystalline materials. The starting reactants are halide salts of organic amines, the metal halide salts, corresponding haloacids (HCl or HBr) and suitable solvents (H_2O or EtOH).

2.1.1 Slow Evaporation Method:

The slow evaporation method is the oldest and simplest process of crystal growth. In this method, an excess of a given solute is established with time by utilizing the difference between the rate of evaporation of the solvent and solute.[1] During slow evaporation, the vapour pressure of the solvent above the solution is higher than the vapour pressure of the solute and, therefore the solvent evaporates more rapidly and the solution becomes supersaturated. The two important factors associated with crystal growth from solution are the supersaturation and the nucleation process. Once the solution reaches supersaturation stage, the solute molecules start gathering together in clusters in a defined way and the stable clusters reach the “critical cluster size”. This process is known as “nucleation”. Afterwards, nuclei that have successfully realised the “critical cluster size” begin to grow in size (see **Figure 2.1**). Typically, the rate of nucleation and crystal growth rate follow an inverse relationship while the nucleation precedes crystal growth. For suitable crystal growth after nucleation, the rate of mass deposition is very important which can be expressed using power law which is:[2,3]

$$R = \frac{1}{A}\frac{dW}{dt} = k_G\,(c - c^*)^g$$

Where, W = mass of crystal per volume of solvent,

A = Surface area of crystal per volume of solvent,

k_G = Overall mass transfer coefficient (depends on T, crystal size, hydrodynamic conditions),

c = Instantaneous solute concentration

c^* = Solute concentration during saturation

g = Exponent (usually between 0-2.5; near unity is most common)

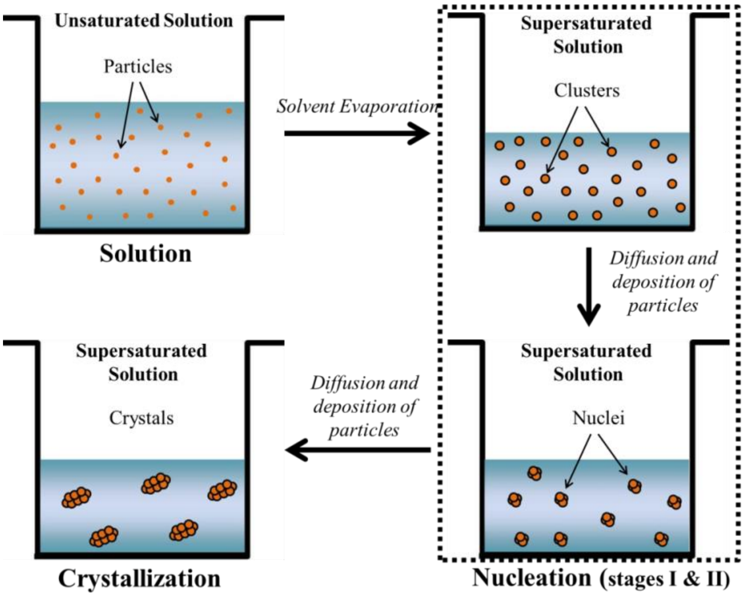

Figure 2.1 Scheme of different stages of crystallization process via slow evaporation of solvent.

The organic ammine and inorganic metal halide compounds mostly form as single crystals via the self-assembly process from the precursor solutions. Over many years, various amines with different structures, asymmetry and conjugation have been selected as the organic precursor. For my work, stoichiometric amount of respective precursor salts of organic ammonium halide RX (R = $C_2H_5NH_3^+$, $CH_6N_3^+$ or $C_6H_5CH_2NH_3^+$ and X = Br^- and Cl^-) and inorganic metal halide $MX_2.nH_2O$ (M = Co^{2+}, Mn^{2+} or Cu^{2+} and X = Br^- and Cl^-) are dissolved in suitable solvent (water or ethanol) in a borosil container which is further covered with porous lid. With time, the solvent slowly evaporates, leading to a supersaturated solution. The suitable crystals grow from the supersaturated solution after a respective amount of time period. In such process we have prepared crystals of different shapes e.g. rod, block and plate.

2.2 X-ray Diffraction Analysis:

The X-Ray diffraction technique is the most simple and extensively used method for crystal structure analysis.[4] For our studies, we collected and analyzed X-ray diffraction data for both single and polycrystalline (crushed single crystals) forms of a compound. With X-Ray wavelength comparable to the crystal interplanar spacings, When X-ray is incident on a powder sample, some of it get scattered by the atoms of the first layer or plane, and the rest of the X-ray passes through the first layer and gets scattered by succeeding layers. Constructive interference happens when these scattered rays coming from two different planes are in same phase resulting a peak in the X-ray diffraction pattern. If these two scattered X-rays are out phase, no such peak will appear. X-Ray diffraction in powder samples follow Bragg's law (see **Figure 2.2**), in which the constructive interference will occur if and only if the following condition is satisfied:[4,5]

$$2d\,\sin\theta = \lambda$$

Where d is the spacing between consecutive crystallographic planes, λ is the wavelength of incident X-Rays, θ is the angle of incident X-Rays. When Bragg's law is satisfied by a few sets of crystallographic planes, a number of peaks will appear at different 2θ positions and we will observe a diffraction pattern. This diffraction pattern is unique for each material, since the peak positions and intensity highly depend on interplanar spacings and crystal symmetry.

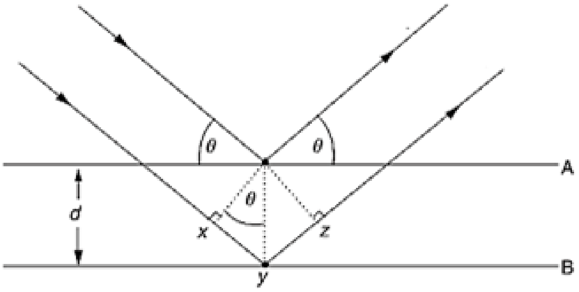

Figure 2.2 Schematic of X-ray diffraction - Bragg's law (Adapted with permission from Ref. [1], © (2014) by John Wiley and Sons).

2.2.1 Single-crystal Measurements:

The single-crystal diffractometer uses either 3- or 4-circle goniometers for data collection (**Figure 2.3**). These circles refer to the four angles (2θ, χ, φ, and Ω) which define the relationship between the crystal lattice, the incident ray and detector.[4,6]

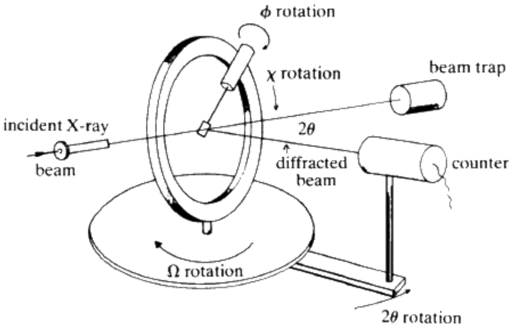

Figure 2.3 Schematic of a 4-circle diffractometer (adapted from the https://serc.carleton.edu/download/images/8400).

For data collection, a suitable single crystal piece is selected under a polarizing microscope which is then attached to a very thin glass fiber using commercial adhesive. This fibre piece is then connected to the goniometer head and the head is further mounted on the diffraction machine platform. For hygroscopic crystals, a suitable crystal piece was put inside a Lindemann capillary and oil was put in to avoid exposure to air. The capillary was further mounted on the top of goniometer head. Adjustment of the goniometer along X, Y and Z orthogonal directions was performed for accurate centering of the crystal within the X-ray beam. Variable temperature X-ray data were collected on Bruker D8 Venture diffractometer (Photon CMOS detector) and on an Oxford Xcalibur (Mova) diffractometer equipped with an EOS CCD detector. Micro-focus, graphite monochromatic Mo-K_α radiation (λ = 0.7107 Å, 50 kV and 1 mA) X-ray source was used. SADABS program was used for doing empirical correction on absorption based on symmetry equivalent reflections while SAINT program was used to integrate the diffraction profile.[7,8] The structure solution was obtained by direct methods followed by successive Fourier and difference Fourier syntheses. The relevant details of the structure determination of different compounds have been included in respective chapters. On determining the atomic positions, anisotropic refinement was carried out for all the non-hydrogen atoms while for hydrogen, isotropic thermal parameters were used. We have used CrysalisPro, SHELXTL, PLATON, WinGX system, version 2014.1 and Olex2 programs for structure solution.[9–13] Supplementary tables have been included at the end of each chapter which presents the atom coordinates, bond lengths and bond angles, anisotropic displacement parameters.

2.2.2 Poly-crystal Measurements:

We have performed polycrystalline X-ray diffraction experiments on a laboratory BrukerD8AdvanceX-ray diffractometer & PANalytical Empyrean alpha1 diffractometer (monochromatic Cu-$K_{\alpha 1}$ radiation). As compared to single crystals, powder samples are composed of multiple grains arranged randomly along different directions.

From powder diffraction data, the lattice parameters can be determined by doing indexing. The phase purity or impurity of a compound can be checked by comparing its X-ray diffraction pattern with the pattern available in online databases such as Inorganic Crystal Structure Database (ICSD). The complete crystal structure can be determined using powder X-ray diffraction data via Reitveld refinement method.[14] In Reitveld method, a diffraction pattern is compared with a calculated model pattern by adjusting certain number of parameters. For some materials, it is observed that the laboratory X-ray diffraction pattern consists of overlapped peaks which make the indexing process difficult or even erroneous. Such issue can be resolved using synchrotron X-ray diffraction experiments, where the wavelength can be tuned. Synchrotron X-ray provides better data statistics i.e. increased peak intensity due to the higher intensity of the synchrotron X-ray beams and better resolution of the peaks giving rise to better signal to noise ratio. Therefore, refinement using synchrotron data draws more authenticity with better refinement parameters and can provide more accurate structural parameters. We have recorded synchrotron X-ray diffraction data at the Materials Science Powder Diffraction (BL04-MSPD) beamline of the ALBA synchrotron facility at Barcelona (Spain).[15,16]

2.3 Physical Properties Measurements:

As a part of this thesis work, we have investigated physical properties such as surface properties, thermal stability and temperature dependent phase transition, magnetization, dielectric and optical properties of some halide hybrid materials.

2.3.1 Atomic Force Microscopy (AFM):

The Atomic Force Microscopy (AFM) is a very high resolution scanning probe microscopy (resolution < 1 nm).[17] The technique is used to study various types of properties of materials i.e. friction, electrical forces, capacitance, magnetic forces, conductivity, viscoelasticity, surface potential, and resistance. A typical AFM measurement setup consists of a tip (connected to a cantilever end), scanner, laser and position sensitive photodiode (see **Figure 2.4**). The AFM working principle is based on the cantilever/tip assembly (referred to as probe) that interacts with the sample. The probe interacts with the sample through a raster scanning motion (up/down and side to side motion). Such motion of AFM tip, while it scans along the surface, is monitored through a laser beam reflected off the cantilever. This reflected laser beam is further tracked by a position sensitive photo-detector (PSPD) that monitors the vertical and lateral motion of the probe.

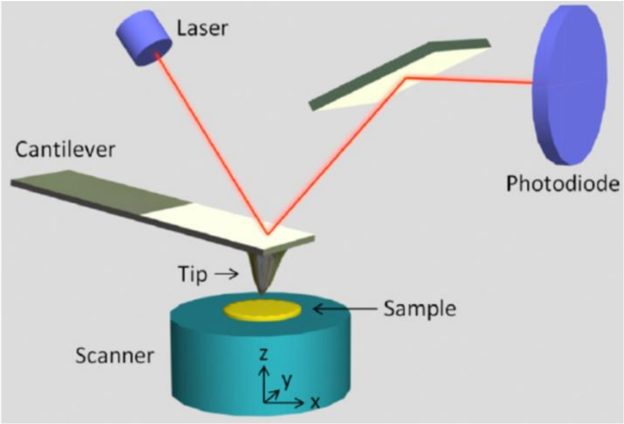

Figure 2.4 Schematic diagram of AFM working principle.[18]

2.3.2 Thermal Studies:

We have studied the thermal stabilities and phase transitions of different hybrid halides via using three techniques viz. Thermogravimetric Analysis (TGA), Differential Scanning Calorimetry (DSC) and Heat Capacity (HC). The principles and instrumentations of these two techniques have been described below.

2.3.2.1 Thermogravimetric Analyses:

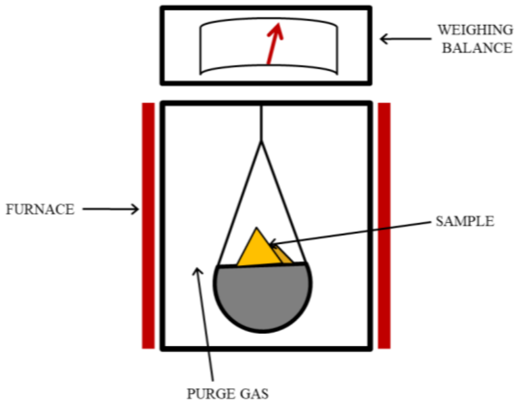

Figure 2.5 Schematic diagram of the TGA measurement setup.

The thermogravimetric analysis (TGA) is a well-known thermal analysis technique in which the thermal stability and composition of a material are interpreted by estimation of change in mass of the material as a function of temperature.[19] A TGA instrument consists of a sample container that is connected to a high precision balance (see **Figure 2.5**). That container is heated or cooled in a controlled manner during the experiment while the mass of the sample is continuously monitored. During the measurement, a specific gas is purged into the chamber to modulate the environment. The gas may act as inert (N_2 or Ar) or may react (O_2) while it flows over the sample and exits through an exhaust.

2.3.2.2 Differential Scanning Calorimetry:

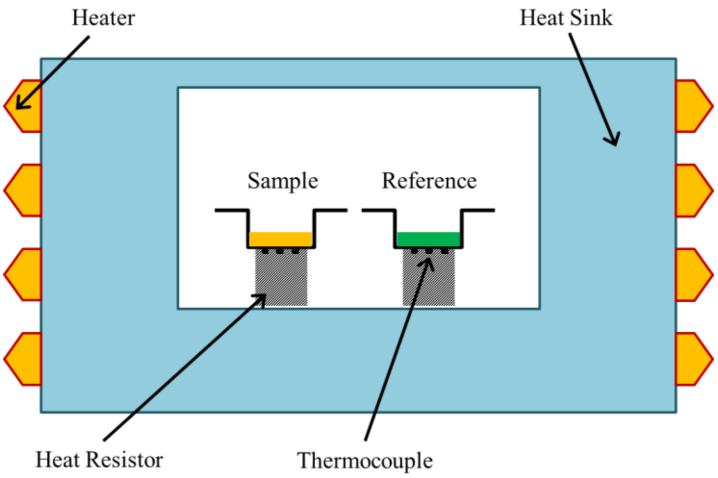

Figure 2.6 Schematic diagram of the DSC measurement setup.[20]

Differential scanning calorimetry (DSC) is a well-known thermal analysis technique in which the phase stability of sample is measured via monitoring the difference in the amount of heat required to increase the temperature of the sample and the reference as a function of temperature.[19] A typical DSC instrument consists of a sample and reference platform both connected to heat resistors, thermocouples (see **Figure 2.6**).[20] This whole setup along-with heat sink is connected to a heat source. To conduct an experiment, measured weight of sample and reference material is loaded onto sample platform. The setup was further heated in controlled fashion where, most importantly, the temperature of sample and reference was maintained as same. The difference in negative or positive heat flow from the sample and surrounding is computed continuously. In the vicinity of possible phase transition, there is always an exchange of latent heat with the surroundings (heat sink). Thus one can observe anomalies representing bulk heat flow difference at the phase transition temperature. DSC is very much accurate and efficient tool for measuring the temperature of phase transition and thermodynamic parameters associated with it.

2.3.2.3 Heat Capacity Measurements:

The heat capacity of single crystal samples as a function of temperature was recorded to observe structural transition feature as well as to calculate the magnetic spin dependent entropy. Quantum Design PPMS has been used to measure the heat capacity, a schematic of the setup has been included in **Figure 2.7**.[21] The setup includes sample platform connected to a heater (for heating), thermometer (for measuring temperature), thermal bath connected using wires. For measurement, the sample has to be put on top of the platform suing Apeizon grease as shown in the schematic. During measurement, firstly the heat capacity of addenda that includes sample holder thermometer, Apeizon grease and leads, is recorded. Once addenda measurement is over, a small pellet sized sample is placed on the same grease and the heat capacity of the whole setup measured again. The sample heat capacity is obtained by subtracting the addenda heat capacity from total heat capacity. The overall measurements are carried out using the relaxation technique. A high vacuum is maintained in the sample chamber throughout the measurement to nullify the heat dissipation. A cycle of consecutive heating and cooling of the sample is performed during measurements. A known amount of heat is supplied to the sample for a constant time after which, the sample is allowed to cool for the exactly same time. For each cycle, the temperature response is recorded and the heat capacity is extracted by fitting the temperature response using a program available in MultiVu software.[21]

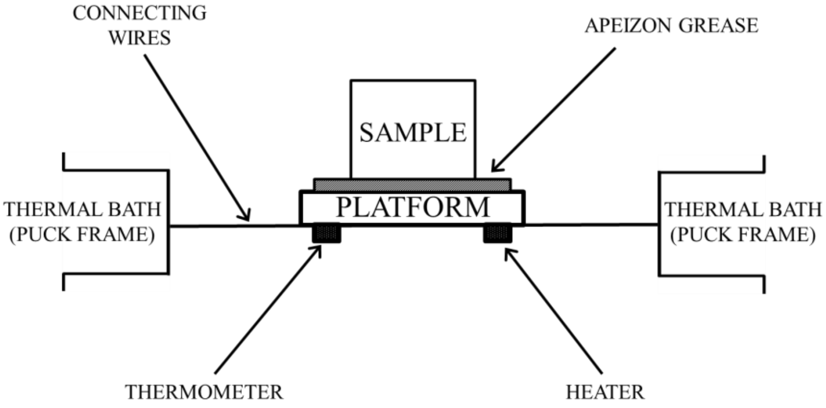

Figure 2.7 Schematic diagram of the Heat Capacity measurement setup.[21]

2.3.3 Optical Characterizations:

In principle, careful choice of appropriate metal cation and halide anion can give rise to fascinating optical properties in a hybrid halide. As part of thesis, we have explored UV-Visible absorption and also photoluminescence properties of few materials.

2.3.3.1 UV-Vis Absorption:

UV-Vis technique is a spectroscopic technique that is used to explore materials absorption using light energy in the ultraviolet to visible region ($\lambda \sim 10^{-9} - 10^{-6}$ m). This energy spectrum is associated with excitation of electrons, in both atoms and molecules, from lower to higher energy levels. The method is quantitative and can be applied for solid, liquid and even for gases also. Since the chosen different transition metals exhibited diverse complexes in different compounds, we have observed different types of optical activity exhibited by the synthesized compounds. We have recorded UV-Vis spectra of crushed crystals in reflectance mode. Further, the reflectance data was converted into absorbance equivalent unit known as the Kubelka-Munk unit (K.M unit). Conversion to K.M. unit is based on certain assumptions which are:

- Particles are randomly distributed,
- Particle average diameter is less than wavelength of incident light,
- Incident light diffuses and thus no regular reflections occur.

The expression of Kubelka Munk function is:

$$f(R) = \frac{(1-R)^2}{2R} = \frac{k}{s}$$

Where R is the reflectance of the solid, and k and s are absorption and scattering coefficient respectively.

2.3.3.2 Photoluminescence:

Photoluminescence (PL) is a process of light emission from a material after it absorbs photons. It is one of the many forms of luminescence and is triggered by photoexcitation.[22] Thus, photoluminescence is associated with photoexcitation, emission and the decay time, all of which are characteristic of the sample. The decay time is basically the time required for electronic deactivation process to get completed (emission to diminish). Photoluminescence can be of different types, viz. fluorescence and phosphorescence. In phosphorescence, the time between emission and absorption is much longer as compared to fluorescence. In general, lifetime for fluorescence has value in nanoseconds while for phosphorescence it is in microseconds. In photoluminescence, the spectrum of the wavelengths emitted can be used to identify atoms and molecules, as well as to determine chemical structures. The intensity of the photons emitted can be used to determine the concentration of chemical species. For a given PL spectra, one can perceive corresponding absorption contribution by measuring the photoluminescence excitation spectra (PLE). While the PL spectroscopy is based on a fixed excitation wavelength and a varied detection wavelength, the PLE is somewhat the inverse case. In PLE, one selects the detection energy and varies the excitation. In PLE, one can see all the energy states contribution to the luminescence of the selected level. Another important factor associated with photoluminescence is Quantum Yield (QY). The Photoluminescence Quantum Yield or PLQY of a material is defined as the ratio of number of photons emitted and number of photons absorbed. This characteristic property of a luminescent material is important for understanding the behavior and interactions for many key materials. Quantum Yield is expressed as:

$$Q = \frac{number\ of\ photons\ emitted}{number\ of\ photons\ absorbed}$$

We have collected the PL and PLE spectra using a 450 W xenon lamp source on an FLSP920 spectrometer (Edinburgh Instruments). Lifetime measurements were carried out on an EPL-405 ps pulsed diode laser used as the excitation source. The absolute PL QY was determined using an integrating sphere.

2.3.4 Magnetic Measurements:

When a material is placed under an external magnetic field, the magnetic forces of the material will get affected. Under applied external magnetic field, materials can interact quite differently and this interaction depends on a number of factors, such as the crystal structure of the material, and the net applied magnetic field. Accordingly, different principle classes of magnetic materials have been surfaced e.g. Diamagnetic, Paramagnetic, Ferromagnetic, Antiferromagnetic, Ferrimagnetic materials. Diamagnetic materials have a weak, negative susceptibility to magnetic field while the paramagnetic materials have a small, positive susceptibility to magnetic field. Ferromagnetic materials have a large, positive susceptibility to an external magnetic field and have a finite transition temperature above which it go into paramagnetic phase (Curie temperature T_C). Antiferromagnetic materials have non zero magnetization to an external field and also have a finite transition temperature (Neel temperature T_N). Ferrimagnetic materials also have alternating spin structure (like antiferromagnets) but the opposite spins are of different moments. The field of magnetism is really vast and encompasses plethora of theories and subclasses of magnetic materials as with the discovery of new varieties of crystal structures, many new exotic phases of magnetic materials have been realized i.e. spin glass, spin ice, spin liquids etc.

Proper magnetic measurements lead to characterization and understanding on the different magnetic materials and thus choice of measurement technique is very important. Characteristically there are two types of magnetic measurements that are widely used to characterize magnetic materials i.e. DC and AC magnetization.

2.3.4.1 DC Magnetization:

Magnetic measurements are based on the principle of Faraday's law of induction, which states that induced voltage in a closed circuit is proportional to the rate of magnetic flux change through the circuit. For a coil with n turns and area A, the magnetic flux φ becomes $\varphi = AB$ where B is the applied magnetic field. The associated induced voltage V in the coil is represented as:

$$V = -n\frac{d\varphi}{dt} = -nA\frac{dB}{dt}$$

All the DC measurements have been carried out using a Magnetic Property Measurement System (MPMS3-SQUID), Quantum Design, USA (see the schematic diagram of different parts of MPMS3 in **Figure 2.8 (a)**).[23] The principle unit of the MPMS3 is a Superconducting Quantum Interference Device (SQUID), which is an instrument built with a superconducting magnet and connected with a helium cryostat (see **Figure 2.8 (b)**).[23] The SQUID has a superconducting coil connected through superconducting wires forming a closed loop at its core which acts as a highly sensitive current to voltage converter and can detect even miniscule magnetic field. During magnetization measurement, the sample (single crystal or powder) is made to move through the superconducting detection coil which induces a change in the flux passing through it. The vertical movement is made through a pick-up coil system which is an arrangement of an induction coil where the upper and lower single turns are counter wound with respect to the two-turn center coil. Such a change in magnetic flux produces a change in the persistent current in the detection coil. It is to be noted that the SQUID acts as an extremely sensitive linear current to voltage converter. So the change in current in detection coil results in a corresponding change in the output voltage, which is proportional to the magnetic moment of the sample. In such way, the magnetization of a sample is measured. In MPMS3, the magnetization can be measured by two different modes i.e. dc scan mode and Vibrating sample magnetometer (VSM) mode. In dc scan mode, the sample is moved up and down uniformly while in VSM mode, the sample vibrates sinusoidally up and down with very high frequency. As a result, dc scan mode always gives more reliable data. The helium cryostat is used to control the sample temperature. The samples are mounted on a quartz sample holder with the help of a stand, provided with a mirror for centering the sample position. The quartz holder is attached in the sample probe, which is inserted into the sample chamber of the SQUID.

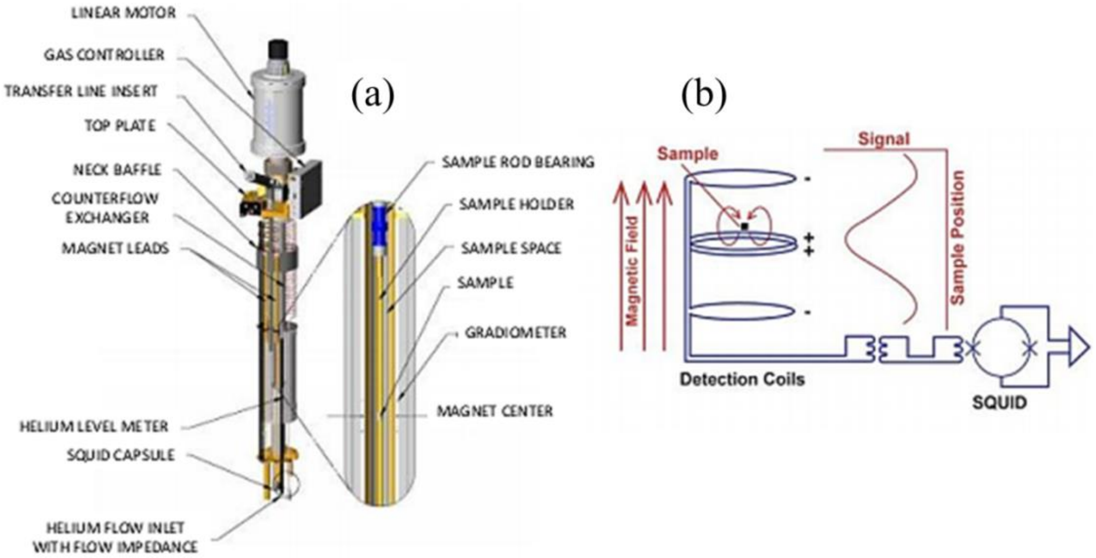

Figure 2.8 (a) The different parts of MPMS3 system, (b) Schematic of superconducting detection coil and SQUID in MPMS3.[23]

The magnetic measurements of a material are done mainly in two ways i.e. fixed field temperature dependent measurement and fixed temperature field sweep measurements. There are two types of temperature dependent measurements e,g, Field Cooled (FC) and Zero Field Cooled (ZFC). In Field Cooled (FC) measurement, a constant magnetic field is applied before cooling and the magnetization data is recorded in the presence of the constant field applied during warming. For Zero Field Cooled (ZFC) measurement, field is applied after cooling and data is recorded in presence of a constant field during warming. In fixed temperature field sweep measurement, at a fixed temperature, magnetic moment of the sample is recorded with an oscillating external magnetic field. For thesis work, all the magnetic susceptibility measurements have been carried out within temperature range: 2 K - 390 K with application of appropriate magnetic field.

2.3.4.2 AC Susceptibility:

Investigation of magnetization dynamics carries huge importance, particularly in analysing the dynamics of spin glass or molecular magnet materials, where the magnetization decays with time below spin glass transition temperature. The AC susceptibility measurement is a highly appropriate and sought after technique to study the magnetization dynamics in a material. Since dc magnetization remains constant during measurement, it thus fails to provide information regarding the magnetization dynamics.

In ac susceptibility measurement, sample's position remains static, without oscillation. During measurement, a small ac magnetic field ($H = H_{ac}\sin(\omega t)$) is applied in the presence (or absence) of dc magnetic field, where H_{ac} and ω are the amplitude and frequency of applied ac field, respectively. A time-dependent magnetization in the sample is induced by this ac magnetic field, which causes a change in the current in the detection coil. The magnetization under a small ac field is given by:[24]

$$M_{ac} = \frac{dM}{dH} H_{ac} \sin(\omega t)$$

Where $\chi = \frac{dM}{dH}$ is the slope of the magnetization (M) vs. magnetic field (H) data. Since the ac magnetization depends on the slope, it is highly sensitive compared to the dc magnetization and it can probe even very small changes in magnetization.

In case of higher frequency of the applied ac magnetic field, the magnetization of the sample cannot follow the driving frequency and thus lags behind the applied ac field [11]. This lag can be detected by the ac magnetometer. Thus, the ac magnetic susceptibility has two components,

$$\chi' = \chi \cos\varphi$$

$$\chi'' = \chi \sin\varphi$$

$$\chi'^2 + \chi''^2 = \chi^2$$

$$\varphi = \tan^{-1}\frac{\chi''}{\chi'}$$

where χ' and χ'' are the real and imaginary parts of the ac susceptibility, φ is the phase

shift.

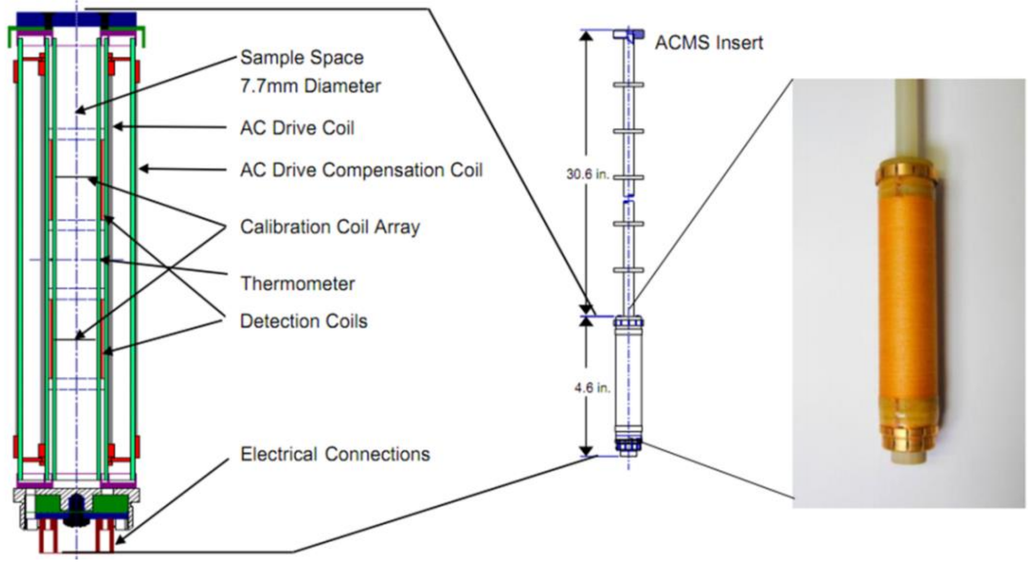

Figure 2.9 Schematic diagrams of the different parts of ACMS coil.[25]

We have measured the AC susceptibility using the Physical Property Measurement System (PPMS). In PPMS, the sample is placed in an ACMS coil (see **Figure 2.9**).[25] The measurements are performed by five-point BTBCC (bottom-top-bottom-centre-centre) measurement process.[25] First three readings are recorded by placing the sample at centre of the bottom detection coil, at centre of the top detection coil and again at centre of the bottom detection coil. Then the sample is placed at the centre of the top and bottom detection coil and two further readings are recorded with opposing polarities of the calibration coil switched into the detection circuit. The signals from the detection coil in first three readings are amplified and digitized by an analog to digital converter to be saved as response waveform. The real and imaginary components of each response waveform are obtained by fitting the data and comparing with the driving signal. Finally, the calibration readings are utilized in order to get the real and imaginary parts of the ac susceptibility of the sample.[25]

2.3.5 Dielectric Measurements:

The dielectric constant of a material is the measure of the macroscopic polarization behavior of localized dipoles (bound ionic or molecular components) in the material. Dielectric constant can be derived from capacitance measurement and the corresponding energy dissipation, known as dielectric loss can be obtained from loss data. The complex dielectric constant is expressed as:

$$\varepsilon_r = \varepsilon_r' - i\varepsilon_r''$$

$$\text{Loss} = \tan(\delta) = \frac{\varepsilon_r''}{\varepsilon_r'}$$

Where ε_r' and ε_r'' are the real and imaginary parts of complex dielectric constant. The real part is directly proportional to capacitance. Considering a parallel plate capacitor geometry of measurement, where material area is A and thickness is t, the real part of dielectric constant is expressed as:

$$\varepsilon_r' = \frac{t}{\varepsilon_0 A} C$$

Where is ε_0 the permittivity of free space (value: 8.85 x 10^{-12} farad per meter).

The capacitance value is derived from the impedance (Z) of a material under certain electric field ($E_0 \sin \omega t$).

$$C = \frac{1}{i\omega Z}$$

To measure the dielectric constant, we have used the Agilent 4294A Impedance analyzer which uses the autobalancing bridge method for accurate measurement of material impedance. In autobalancing bridge method, with maintaining the low terminal at zero volt, the voltage across the high terminal and ground (V_x) and the voltage across the range resistor R_r and the ground (V_r) are measured (see **Figure 2.10**).[26] The impedance of the material is measured by:

$$\frac{V_x}{Z_x} = I_x = I_r = \frac{V_r}{R_r}$$

$$Z_x = \frac{V_x}{I_x} = R_r \frac{V_r}{R_r}$$

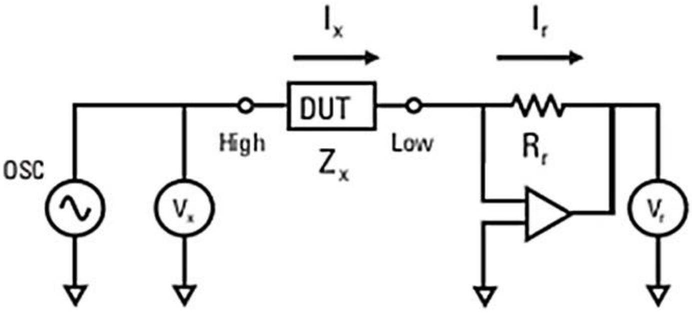

Figure 2.10 An auto-balancing bridge method used for impedance measurements.[26]

2.4 Bibliography:

(1) Govindhan Dhanaraj, Kullaiah Byrappa, Vishwanath Prasad, M. D. *Springer Handbook of Crystal Growth*; Govindhan Dhanaraj, Kullaiah Byrappa, Vishwanath Prasad, M. D., Ed.; Springer, Berlin, Heidelberg: Heidelberg, 2010.

(2) Theories and Methods of Crystal Growth: A General Review.

(3) Vekilov, P. G. What Determines the Rate of Growth of Crystals from Solution? *Cryst. Growth Des.* **2007**, *7* (12), 2796–2810.

(4) Carmelo Giacovazzo, Hugo Luis Monaco, Gilberto Artioli, Davide Viterbo, Marco Milanesio, Gastone Gilli, Paola Gilli, Giuseppe Zanotti, Giovanni Ferraris, and M. C. *Fundamentals of Crystallography,* Third.; Giacovazzo, C., Ed.; Oxford Scholarship Online: December 2013.

(5) A. R. West. Solid State Chemistry and Its Applications. John Wiley and Sons, 1985 Paper Back, Price £ 14.95, US $ 19.95. *Cryst. Res. Technol.* **1986**, *21* (1), 166.

(6) Bennett, D. W. *Understanding Single-Crystal X-Ray Crystallography*; Weinheim : Wiley-VCH, c2010, 2010.

(7) G. M. Sheldrick, Go¨ttingen, G. SADABS,. **1997**.

(8) Bruker AXS Inc., Madison, Wisconsin, USA. SAINT ,. **2000**.

(9) Sheldrick, G. M. , SHELXTL, program for crystal structure refine-ment. , SHELXTL, Program for Crystal Structure Refine-Ment,. **1997**.

(10) Sheldrick, G. M. No Title. *Acta Crystallogr., Sect. A Found. Adv.* **2015**, *71*, 3–8.

(11) A. L. Spek. PLATON. *J. Appl. Crystallogr.* **2003**, *36*, 7–13.

(12) O. V. Dolomanov, L. J. Bourhis, R. J. Gildea, J. A. K. H.; Puschmann, and H. Olexys2. *J. Appl. Crystallogr.* **2009**, *42*, 339–341.

(13) Farrugia, L. WinGX. *J. Appl. Crystallogr.* **1999**, *32*, 837–838.

(14) Rodriguez-Carvajal, J. FULLPROF 2000: A Rietveld Refinement and Pattern Matching Analysis Program. In *"FULLPROF: A program for Rietveld refinement and pattern matching analysis,"Abstracts of the Satellite Meeting on Powder Diffraction of the XV Congress of the IUCr.*; Toulouse, France, 1990; p 127.

(15) Fauth, F.; Peral, I.; Popescu, C.; Knapp, M. The New Material Science Powder Diffraction Beamline at ALBA Synchrotron. *Powder Diffr.* **2013**, *28* (S2), S360–S370.

(16) Fauth, F.; Boer, R.; Gil-Ortiz, F.; Popescu, C.; Vallcorba, O.; Peral, I.; Fullà, D.;

Benach, J.; Juanhuix, J. The Crystallography Stations at the Alba Synchrotron. *Eur. Phys. J. Plus* **2015**, *130* (8), 160.

(17) Reifenberger, R. *Fundamentals of Atomic Force Microscopy*; WORLD SCIENTIFIC, 2014; Vol. Volume 4.

(18) Guanghong Zeng, Yusheng Duan, F. B. and M. D. Nanomechanics of Amyloid Materials Studied by Atomic Force Microscopy. **2012**.

(19) Sorai, T. J. S. of C. and T. A. and M. *Comprehensive Handbook of Calorimetry and Thermal Analysis*; Sorai, M., Ed.; West Sussex John Wiley 2006, 2004.

(20) Https://Www.Hitachi-Hightech.Com/Global/Products/Science/Tech/Ana/Thermal/Descriptions/Dsc.Html .

(21) Physical Property Measurement System - Heat Capacity Option - User's Manual (Quantum Design).

(22) Lakowicz, J. R. *Principles of Fluorescence Spectroscopy*, 3rd ed.; Springer US, 2006.

(23) Magnetic Property Measurement System - MPMS 3 User's Manual (Quantum Design).

(24) D. Martien, Introduction to AC Susceptibility (Quantum Design) (2002).

(25) Physical Property Measurement System - AC Measurement System (ACMS) Option - User's Manual (Quantum Design).

(26) Agilent Impedance Measurement Handbook - A Guide to Measurement Technology and Techniques (Agilent Technologies).

Chapter 3

Structural Phase Transition, Optical Properties and Magnetocaloric Effect in Organic-Inorganic Hybrid $(C_2H_5NH_3)_2CoCl_4$

Summary

$(C_2H_5NH_3)_2MCl_4$ (M = Cu, Fe) hybrids are well-known materials to exhibit multiple ferroic properties. In this chapter, we focus on studying the cobalt analog of this series i.e. $(C_2H_5NH_3)_2CoCl_4$ and present detailed experimental and theoretical investigations of structural, optical and magnetic properties of the hybrid compound. The blue single crystalline compound exhibits centrosymmetric orthorhombic structure (space group *Pnma*) at room temperature. The material undergoes a reversible structural phase transition at 235/241 K (cooling/heating) to noncentrosymmetric yet nonpolar orthorhombic structure (space group $P2_12_12_1$). Transition is associated with combination of order-disorder transformation of the enthylammonium ions and cooperative molecular rearrangements. Electronic absorption spectra exhibits features of weak spin-orbit coupling effect in distorted $(CoCl_4)^{2-}$ units. Magnetic studies reveal paramagnetic behavior down to 2 K while near 2 K, magnetic field induced spin reorientation is observed. Weak magnetic interactions among cobalt spins having ferromagnetic ground state have been obtained via First principles density functional calculations. The corresponding magnetocaloric effect has been experimentally estimated by magnetic and heat capacity measurements which has a maximum value of 16 J Kg^{-1} K^{-1} at 2.5 K under 7 T magnetic field.

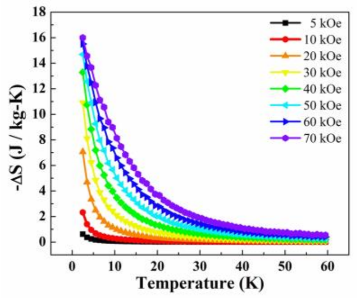

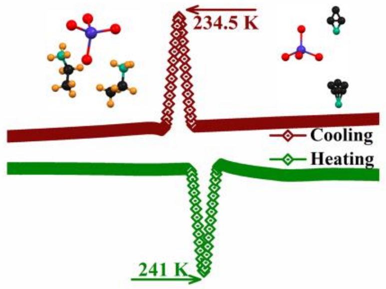

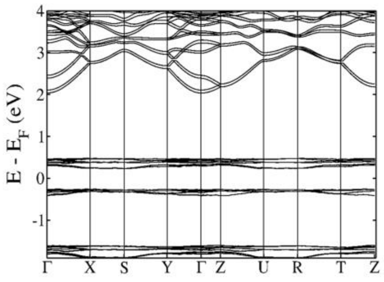

3.1 Introduction

The contemporary material science research is mainly thriving on design and preparation of multifunctional materials which can have potential applications. In reality, the target-driven preparation of a material in which various interesting physical properties can be simultaneously observed is a fairly challenging task. However, such materials can fundamentally be realized by consciously assembling two (or more) different components in a crystalline solid phase. In such phase, facile integration of distinct properties furnished by each component can be observed. In this aspect, the hybrid organic-inorganic halides comprising organic ammonium halides and metal halides deserve a strong mention as these materials can efficiently integrate multiple desirable properties in single phase. In fact over past few years, the hybrid halides have escalated materials research with interesting properties e.g. symmetry breaking phase transitions, ferro-/antiferro-/quantum-magnetism, thermochromism,photoluminescence, dielectric, ferroelectric and piezoelectric properties.[1–10]

Among these hybrids, the materials featuring general molecular formula R_2MX_4 (where R = alkyl or aryl alkyl ammonium ion, M = divalent metal ion and X = halide anion) are the most interesting group of compounds which have been studied thoroughly and often found to exhibit excellent ferroic properties.[8,11–14] These materials are well-known to form as single crystals featuring layered crystal structures. Each layer in crystal structure is seen to be composed of the metal-halide octahedral complexes connected with each other *via* corner sharing. The alkyl ammonium or aryl-alkyl ammonium cations are seen to occupy the inter-layer spaces as two consecutive layers in which they project their nitrogen heads towards the adjacent metal-halide layer. Thus the nitrogen heads of the ammonium cations form hydrogen bonds with adjacent metal-halide layer while van der Waals interactions are observed among the adjacent ammonium ion layers. Such two-dimensional extension of metal-halide layer influences long range magnetic order below certain temperatures. To mention, the Cu (II) containing hybrids are well-known to exhibit two-dimensional ferromagnetism whereas the Mn (II) and Fe (II) based hybrids are well-known antiferromagnets.[11,14–17] The ammonium cations, on the other hand, are often seen to undergo order-disorder transitions resulting in a symmetry breaking of the crystal structure. Polar crystal structure with ferroelectric properties has also been observed through hydrogen-bond ordering in these materials.[8] Thus, these materials often tend to uniquely exhibit symmetry breaking structural transitions, interesting ferroelastic or ferroelectric properties and also long range magnetic ordering.

The cobaltous ions (Co^{2+}) in presence of halide ligand field are well-known to form tetrahedral coordination complexes. Thus, considering the cobalt based R_2MX_4 compounds, the Co^{2+} ions are seen to form $(CoX_4)^{2-}$ tetrahedra which remain discrete in nature.[18–21] The protonated ammonium cations stay in the void spaces and form hydrogen bonds with the halide ions thereby stabilizing the crystal structure. Due to the presence of the unequal interactions among the individual halide ions with ammonium ions, the tetrahderal CoX_4 complexes exhibit weak geometric distortion. As a result, the electronic absorption spectra of cobalt-based hybrids contain features of geometrically distorted $(CoX_4)^{2-}$ tetrahedra having weak spin-orbit coupling (SOC).[22,23]. As the symmetry of $(CoX_4)^{2-}$ become lower than the regular tetrahedral geometry, a weak magnetic anisotropy arises and weak zero field splitting comes into play.[20,24–26] These materials, thus behave as paramagnets down to low temperature while at very low temperature region, the magnetic properties are determined by the magnetic ground and excited states.[20] This behavior is prototypical of single-ion magnets in which the magnetic bistable nature, superparamagnetic behavior and characteristic magnetic relaxation pathways are seen.[24–28]

Conventional research on magnetic properties of halide hybrids has largely concentrated on studying the classical and quantum features by looking at the microscopic spin ordering or studying the nature of magnetic frustration.[11,12,29–32] Over the years, wide range of magnetic properties starting from paramagnetism to low dimensional antiferromagnets to two-dimensional long range magnetic ordering have been observed in different materials.[13,21,33] The research efforts on studying the magnetocaloric effect and designing related materials have focused on incorporating rare earth elements in oxides or in alloys.[34–36] Recently the huge potential of the paramagnetic transition metal (TM),[37–39] rare earth (RE) and TM-RE combined molecular clusters have shown large potential in this magnetic cooling materials.[36,40–42] In this context, the cobalt based halide hybrids featuring discrete cobalt-halide tetrahedra and parmagnetic properties can have sizable change in magnetic entropy at low temperature region.

With this motivation, we have prepared and thoroughly studied the structural, optical, magnetic and dielectric properties of single crystalline hybrid compound

$(C_2H_5NH_3)_2CoCl_4$ (hereafter referred as **1**). The compound features discrete $CoCl_4$ tetrahedra and ethylammonium cations in its zero-dimensional crystal structure. A reversible first order structural phase transition has been observed at 235/241 K (cooling/heating) which involves interconversion between centrosymmetric and noncentrosymmetric (yet nonpolar) structures. Crystal structure analyses indicate that the phase transition is influenced by the collective effect of the order-disorder nature of the ethylammonium cations and also the cooperative rearrangement of the components. We have also observed a dielectric anomaly at the structural transition temperature. Through the optical and magnetic studies, we have confirmed the presence and effect of geometric distortion and spin-orbit coupling in $CoCl_4$ tetrahedra. In the low temperature region, field induced spin reorientation has been observed in isothermal magnetization measurements. The magnetocaloric effect studies confirm that the entropy change of this material stands in the same line with well-known transition metal cluster magnetic coolers.

3.2 Experimental Section:

3.2.1 Chemicals:

Anhydrous cobalt chloride ($CoCl_2$) (AR 99.7%) and ethylamine hydrochloride ($C_2H_5NH_3Cl$) (AR 98%) were bought from Alfa Aesar. Ethanol (AR 99%) was bought from SDFCL. All of the chemicals were used without further purification.

3.2.2 Synthesis:

Single crystalline compound **1** was prepared *via* solution growth method. For this, 0.6502 g (7.9735 mmol) of ethylammonium chloride $C_2H_5NH_3Cl$ and 0.5176 g (3.9867 mmol) of anhydrous $CoCl_2$ (maintaining the 2:1 molar ratio) were dissolved in ethanol. The whole solution was kept in crystallization beaker and kept at room temperature where blue plate-shaped crystals formed by slow evaporation of the solvent after about two weeks. The formation process can be represented using simple addition reaction:

$$2\ C_2H_5NH_3Cl + CoCl_2 = (C_2H_5NH_3)_2CoCl_4$$

3.2.3 Characterization:

The elemental percentage analyses have been carried out using the Thermo Scientific Flash 2000 CHN analyzer. Using Mettler Toledo TGA 850 instrument, the Thermogravimetric analysis (TGA) data was recorded under nitrogen atmosphere from 298 K to 1073 K with a ramp rate of 5 K min^{-1}. The structural transition features were visualized via modulated DSC experiment which was carried out in TA Q2000 instrument in the temperature range of 150 K – 310 K under nitrogen atmosphere. Heating and cooling rate was kept at 2 K min^{-1}. The single crystals were pre-dried under vacuum for 12 hours for these experiments.

The crystals of compound **1** were found to be hygroscopic in nature. Thus suitable crystal piece was pre-dried and inserted into Lindemann capillary. Oil was then put into the capillary to avoid any air contact. Further, the capillary was mounted on top of a goniometer head. X-ray diffraction data were collected in ω scan mode using micro focus, graphite monochromatic Mo-K_α radiation (λ = 0.7107 Å, 50 kV and 1 mA) X-ray source on Bruker D8 Venture diffractometer. The diffraction profile was integrated using the SAINT program while the SADABS program was used to do absorption correction.[43,44] Direct methods followed by successive Fourier and difference Fourier syntheses were carried out to solve the structure. Anisotropic refinement was executed for all the non-hydrogen atoms. SHELXT, SHELXL-2014, SHELXS 97, PLATON, WinGX system, version 2014.1 and Olex2 programs were considered for the structure solution.[45–48] To confirm the space groups, we have recorded synchrotron X-ray diffraction data of polycrystalline compound at the Materials Science Powder Diffraction (BL04-MSPD) beamline of the ALBA synchrotron facility (Barcelona, Spain, wavelength λ = 0.3171 Å). We have carried out pattern matching using the FULLPROF software on 300 K data to confirm the crystal symmetry in powder form.

Using crushed crystals, we have recorded the diffused reflectance data using Perkin-Elmer Lambda 750 spectrometer. The background correction was done by subtracting pre-recorded reflectance spectra of $BaSO_4$ disc from the compound spectra. Further, we have converted the background subtracted data into absorbance equivalent data by using Kubelka-Munk function.

Temperature dependent heat capacity (HC) was recorded to study the structural phase transition and also the magnetocaloric effect. Data was collected in the temperature range of 2- 50 K for magnetocaloric effect studies and in the range of 210 K – 260 K for structural transition studies using Quantum Design PPMS. For this experiment, firstly the HC of addenda (which includes Apeizon grease and sample platform and define the thermodynamic surrounding) was recorded, following which a suitable crystal was mounted on the same grease and heat capacity of the whole setup (system + surrounding) was recorded. HC was measured via relaxation technique where HC of addenda was auto subtracted to derive the HC of the compound.

Structural transition feature was visualized via studying temperature dependent capacitance measurements. Electrical contacts were put on both end surfaces of plate-shaped single crystal in also in perpendicular geometry of that using silver paste. Sample was inserted inside Quantum Design PPMS chamber. Capacitance and loss were measured using Agilent (E4980A) Precision LCR meter in the temperature range of 10 K – 300 K with 2 K min^{-1} heating/cooling rate under 50 kHz frequency with an applied peak voltage of 0.5 V.

DC magnetic susceptibility and magnetization measurements on single crystals were carried out using Quantum Design SQUID-based MPMSXL-3-type magnetometer. Zero field cooled and field cooled data were recorded in the temperature range of 1.8 K – 350 K with applied magnetic field of 100 Oe. Isothermal magnetizations were measured at 2 K and at 300 K with field sweep range of ±70 kOe. For magnetocaloric effect studies, first quadrant isothermal magnetization data were recorded from 2 K to 60 K.

With the density functional theory as implemented in QUANTUM ESPRESSO package we determined electronic structure by using fully relativistic ultrasoft pseudopotentials that include the effects of SOC.[49,50] We have used an energy cut-off of 30 Ry in order to truncate the plane wave basis in expansion of wave functions and 240 Ry in the representation of charge density. The complex dielectric function was obtained within a random phase approximation (RPA) method.[49] For this, we have used the normconserving pseudopotentials and an energy cut-off value of 80 Ry to truncate the plane wave basis used for representing the wave functions and a cut-off of 320 Ry to represent the charge density. For all the calculations, we have treated spin dependent exchange-correlation energy within a local density approximation of Perdew-Zunger parameterized functional.[51] We sampled the Brillouin Zone integrations on a 5× 3 × 2 uniform mesh of *k*-points. Ferromagnetic and G-type antiferromagnetic ordering were considered and the experimental lattice parameters (*a* = 7.621 Å, *b* = 9.673 Å and *c* =16.831 Å) were used and the electronic structure and complex dielectric function were determined.

3.3 Results and Discussion:

3.3.1 Crystal Structures:

The chemical composition and phase purity of the as-grown crystals were confirmed by elemental analysis which yielded the following mass percentage outputs:

Table 3.1 Elemental Purity Analysis:

Elements	Experimental Mass (%)	Calculated Mass (%)
H	5.57	5.50
C	16.43	16.40
N	9.52	9.56

Single crystal structure solution reveal that at 300 K, the compound **1** has orthorhombic structure (centrosymmetric space group *Pnma*) with lattice parameters *a* = 10.0256 (16) Å, *b* = 7.4030 (7) Å and *c* = 17.6039 (3) Å and Z = 4 (refinement parameters and atomic coordinates are included in **Table 3.2**, **Table 3.6**, **3.7** and **3.8**). The molecular unit at 300 K consists of a $(CoCl_4)^{2-}$ tetrahedral anion and two ethylammonium cations (see **Figure 3.1** (a)). Both of the ammonium ions are seen to be thermally disordered where one (N2 cation) has its secondary carbon atom in doubly disordered state while the other ammonium cation (N1 cation) features triply disordered sites in its primary and secondary carbon atoms. The disorder in N1 cation is higher than the N2 cation due to the larger degrees of freedom and greater molecular flexibility. The $(CoCl_4)^{2-}$ tetrahedral anions are seen to be weakly distorted and far from each other (nearest and next-nearest Co-Co distances are 6.06 Å and 8.902 Å). The organic molecules being in highly disordered state, H atom positions could not be assigned.

In order to see the effect of cooling on thermal disorder, we have gradually cooled the crystal to 100 K and recorded single crystal diffraction data at 200 K and at 100 K. Interestingly, the compound at 200 K exhibits noncentrosymmetric, nonpolar, orthorhombic structure (space group $P2_12_12_1$) structure with lattice parameters *a* = 7.6215 (11) Å, *b* = 9.7364 (15) Å and *c* = 16.983 (3) Å (see **Table 3.2**). In the molecular unit at 200 K, cooperative rearrangement of the tetrahedral anion and the ammonium cations are observed. Notably, all the ammonium cations are seen to be in thermally ordered state **(Figure 3.1** (b)). On further cooling to 100 K, the crystal was seen to retain the space group symmetry with weak changes in lattice parameters being observed ($P2_12_12_1$ with *a* = 7.6216 (11) Å, *b* = 9.6734 (15) Å and *c* = 16.831 (3) Å). At this temperature, further rearrangement among components is noticed **(Figure 3.1** (c)).

The symmetry change from *Pnma* to $P2_12_12_1$ clearly indicates that the compound undergoes a structural phase transition in between 300 and 200K. Based on the symmetry analyses, the phase transition is seen to be associated with a decrease in symmetry elements by half in number, from 8 (E, C_2, C_2', C_2'', i, σ_h, σ_V and σ'_V) at 300 K for *Pnma* space group to 4 (E, C_2, C_2' and C_2'') at 200 K for $P2_12_12_1$ space group. Moreover, the $P2_12_12_1$ space group is a subgroup of *Pnma* space group which confirms the conservation of the Curie symmetry principle.

The molecular rearrangement across temperature can be clearly visualized in the unit cell diagrams (see **Figure 3.2** (a), (b) and (c)). The rearrangements across temperature become facile owing to the availability of sufficient spaces in between the components. Such type of behavior is generally observed in case of plastic crystals. To mention, the plastic crystals are a category of materials which exhibit large disorder in their crystal structure and in the crystal structure the lighter organic components are seen to be oriented randomly. On gradual cooling, the disordered molecules take preferred orientations resulting in a disorder-to-order transition associated with lattice symmetry breaking.[52]

As we could not assign the hydrogen atoms on disordered ammonium cations at 300 K, the extent of hydrogen bonding within a molecular unit could be visualized at 300 K. On cooling down to 200 K and 100 K, all four Cl atoms in $(CoCl_4)^{2-}$ are seen to take part in hydrogen bonding with surrounding ethylammonium cations (see **Figure 3.3** (a) and (b)). At 200 K, each tetrahedron is seen to take part in total six hydrogen bond interactions. Two of these interactions are seen to be present involving Cl1 and Cl4 atoms of $(CoCl_4)^{2-}$ tetrahedron and N2 atom of ammonium cation within the same molecular unit (see **Figure 3.3** (a)). The other four hydrogen bonds are two Cl3-N1 interactions, two Cl2-N2 interactions within different molecular units (**Figure 3.3** (a)). At 100 K, each tetrahedron is seen to take part in four hydrogen bonds. Among these, three (Cl2-N2, Cl3-

N2 and Cl1-N1) are seen to be present within the same molecular unit (see **Figure 3.3** (b)). The fourth interaction (Cl4-N2) can be visualized by considering the enthylammonium cation from neighboring molecular unit (**Figure 3.3** (b)). The $CoCl_4$ tetrahedra at different temperatures are seen to have distortion and as a result the regular tetrahedral geometry gets lowered (see **Table 3.3**).

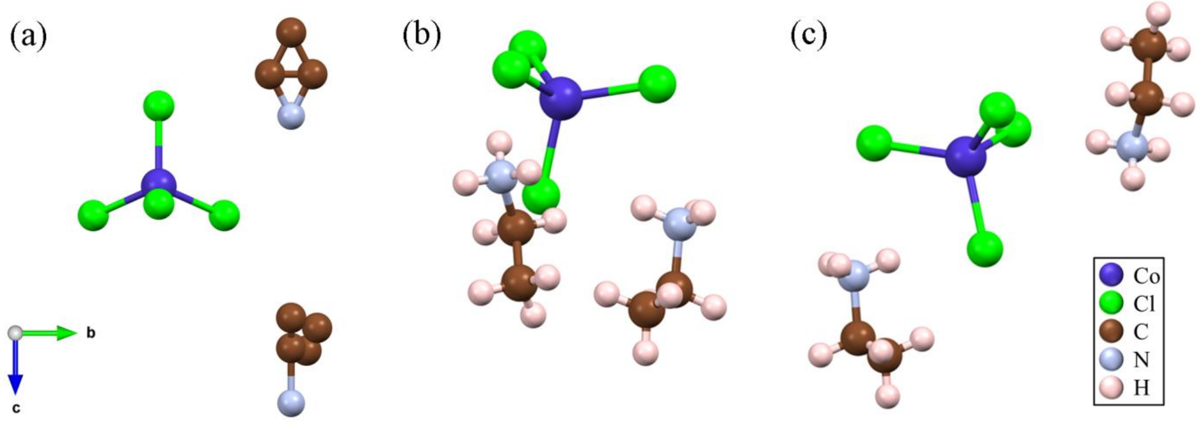

Figure 3.1 Molecular Units of compound **1** at (a) 300 K, (b) 200 K and (c) at 100K. Thermal disorder in ethylammonium cations can be observed at 300 K. At low temperatures, all the organic ions are seen to be in thermally ordered state.

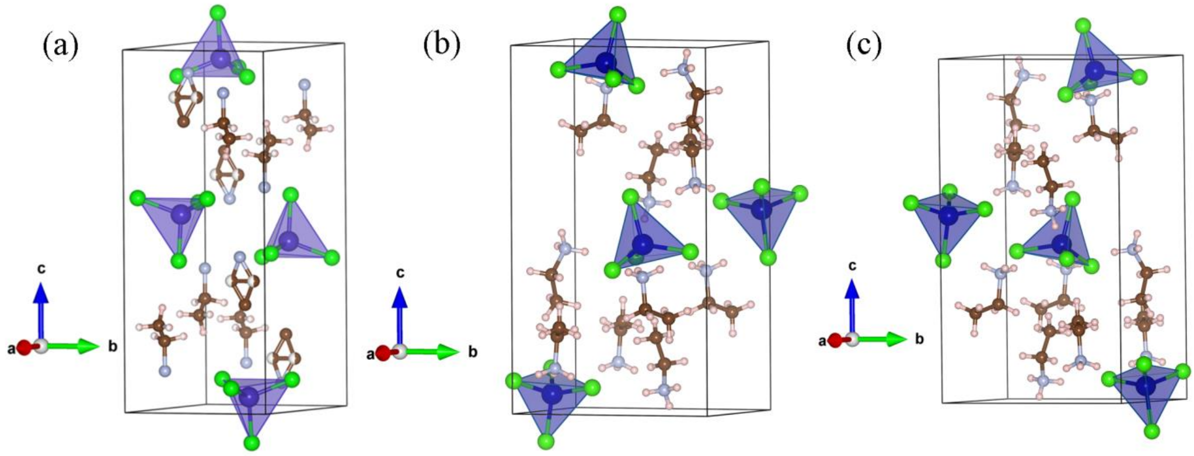

Figure 3.2 Unit cell representations for data recorded at (a) 300 K, (b) 200 K and (c) at 100K. With gradual change in temperature, cooperative rearrangements among different components can be seen.

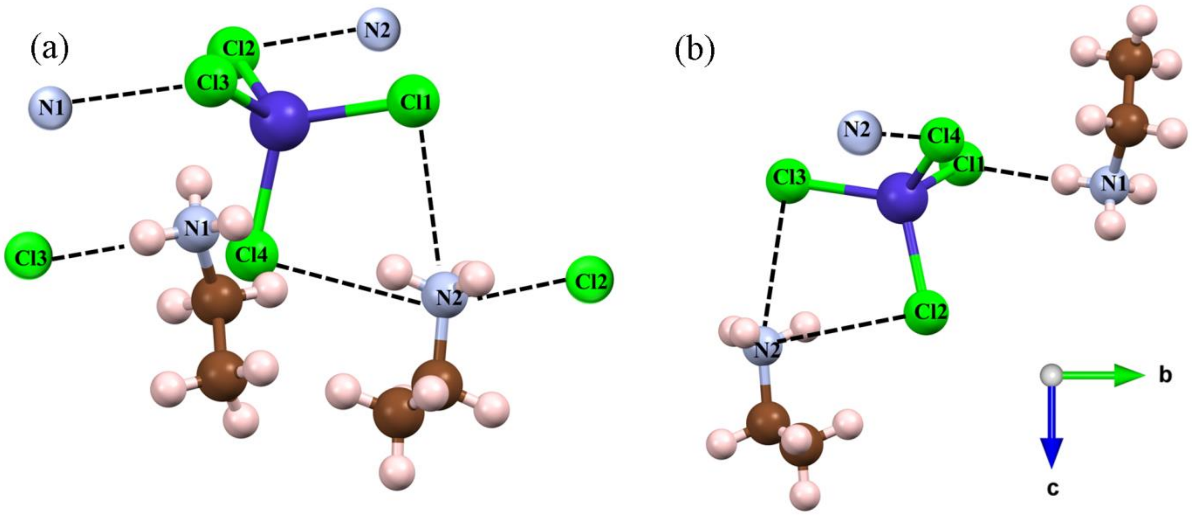

Figure 3.3 Hydrogen bonding interactions within a molecular unit at (a) 200 K and at (b) 100 K.

Table 3.2 Crystal data and Structural Refinement Details:

Parameters	**300 K**	**200 K**	**100 K**
Empirical formula	$C_4Cl_4CoN_2$	$C_4H_{16}Cl_4CoN_2$	$C_4H_{16}Cl_4CoN_2$
Formula weight (g/mol)	276.79	292.92	292.92
Temperature (K)	300	200	100
Wavelength (Å)	0.71073	0.71073	0.71073
Crystal system	Orthorhombic	Orthorhombic	Orthorhombic
Space group	*Pnma*	$P2_12_12_1$	$P2_12_12_1$
Unit cell dimensions (Å)	a = 10.0256 (6), b= 7.4030 (4), c = 17.6039 (13)	a = 7.6215 (11), b = 9.7364 (15), c = 16.983 (3)	a = 7.6216 (12), b = 9.6734 (15), c = 16.831 (3)
Volume (Å^3)	1306.55 (14)	1260.3 (3)	1240.9 (3)
Z	4	4	4
Calculated density (g/cm^3)	1.407	1.544	1.568
Absorption coefficient (mm^{-1})	2.084	2.164	2.198
F(000)	532	596	596
Crystal dimension (mm^3)	0.2 x 0.16 x 0.06	0.2 x 0.16 x 0.06	0.2 x 0.16 x 0.06
Reflections collected	4095	18004	9301
Independent reflections	1283 (R_{int} = 0.0701)	3135 (R_{int} = 0.022)	3042 (R_{int} = 0.0491)
Completeness	99.6% to θ = 25.24°	99.9%	99.4%
Number of parameters	86	104	102
Goodness-of-fit	1.075	1.051	1.141
Final R indices [I > 2σ(I)]	R_{obs} = 0.0751, wR_{obs} = 0.2055	R_{obs} = 0.0391, wR_{obs} = 0.0787	R_{obs} = 0.0415, wR_{obs} = 0.0894
R indices (all data)	R_{all} = 0.1080, wR_{all} = 0.2263	R_{all} = 0.0519, wR_{all} = 0.0840	R_{all} = 0.0494, wR_{all} = 0.0922

Table 3.3 Co-Cl bond distances and Cl-Co-Cl bond angles in $CoCl_4$ tetrahedron at three temperatures:

Type	Label	300 K	200 K	100 K
Bond Distances (Å)	**Co-Cl1**	2.258 (4)	2.2592 (14)	2.2916 (14)
	Co-Cl2	2.233 (3)	2.2628 (14)	2.2772 (14)
	Co-Cl3	2.254 (2)	2.2895 (13)	2.2660 (15)
	Co-Cl4	2.254 (2)	2.2754 (13)	2.2651 (14)
Bond Angles (°)	**Cl1-Co-Cl2**	110.66 (14)	114.47 (6)	107.50 (5)
	Cl1-Co-Cl3	107.44 (10)	106.04 (5)	105.60 (5)
	Cl1-Co-Cl4	107.44 (10)	111.48 (5)	110.14 (6)
	Cl2-Co-Cl3	111.23 (9)	110.11 (5)	111.51 (6)
	Cl2-Co-Cl4	111.23 (9)	107.07 (5)	107.07 (6)
	Cl3-Co-Cl4	108.70 (13)	107.50 (5)	114.82 (6)

We have also recorded powder diffraction data of crushed crystals using synchrotron radiation source and carried out pattern matching to confirm the phase purity.

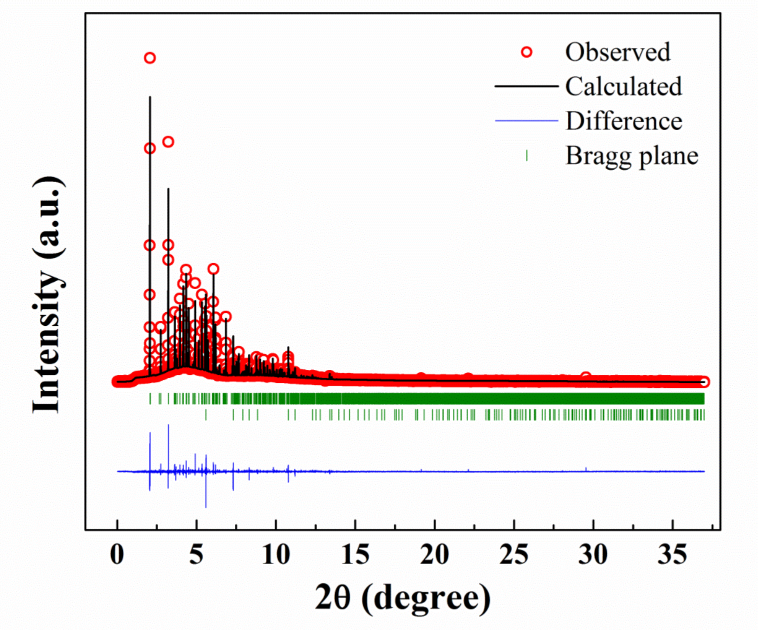

Figure 3.4 Pattern matched synchrotron data collected at 300 K confirming the phase purity.

3.3.2 Thermal Stability and Structural Phase Transition:

We have carried out thermogravimetric analyses which indicate that compound **1** starts decomposing above 440 K (see **Figure 3.5**).

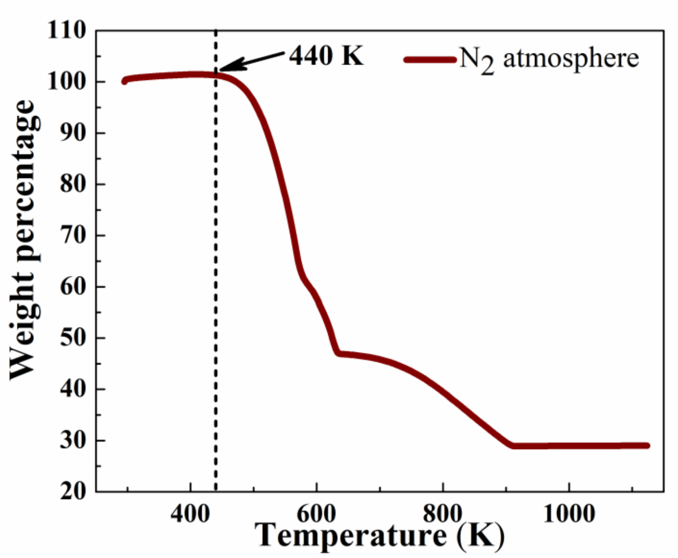

Figure 3.5 Thermogravimetric analyses data showing decomposition of compound 1 above 440 K.

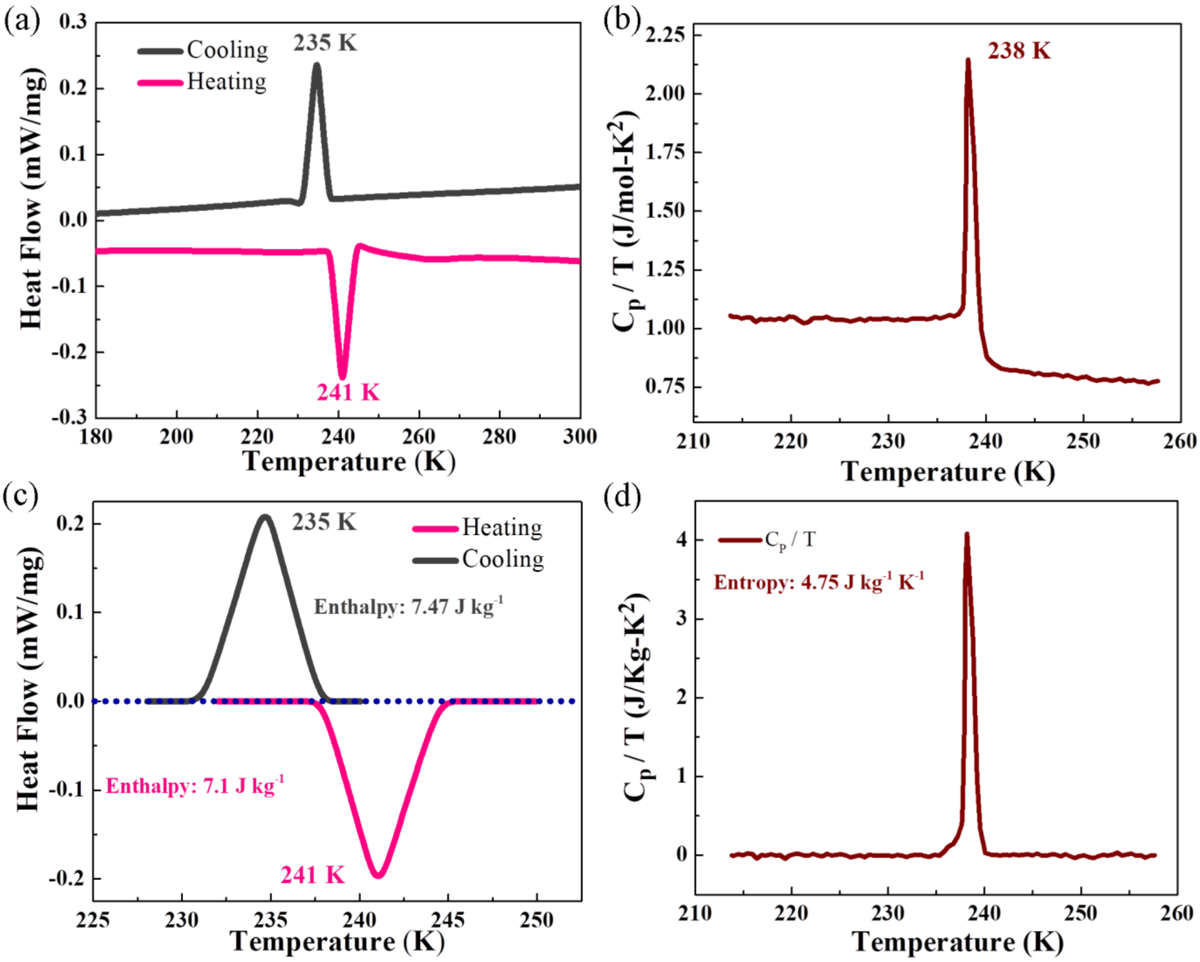

Figure 3.6 Structural transition features of compound **1**: (a) Reversible DSC anomalies, (b) Heat capacity data obtained during heating procedure, (c) Background subtracted DSC anomalies for enthalpy calculations, (d) background subtracted heat capacity anomaly for entropy calculations.

Further, the possibility of thermally stimulated phase transition has been assessed via the very reliable techniques: differential scanning calorimetry (DSC) and heat capacity measurements. The DSC data exhibit that compound **1** undergoes a reversible phase transition at 235 K/241 K (cooling/heating) (**Figure 3.6** (a)). Sharp nature of anomalies along with sizeable thermal hysteresis (6 K) indicates that the transition is a first order type. The phase transition has also been confirmed through the heat capacity measurements which showed an anomaly at 238 K as recorded during warming (see **Figure 3.6** (b)). We expect the phase transition to be related to structure.

Corresponding enthalpy and entropy changes have been calculated by integrating the area under the curve in DSC data (for enthalpies) and also C_p/T vs T data (for entropy) (see **Figure 3.6** (c), (d)). For a pure order-disorder type of transition, the entropy change (ΔS) can be calculated using the Boltzmann equation:

$$\Delta S = R \ln N$$

where R is gas constant and N is ratio of distinguishable configurations.

We have attempted to extract the enthalpy from entropy and vice versa and tabulated the values in **Table 3.4**. The experimental values have been put in bold numbers. which is $\Delta S = 4.53$ J mol^{-1}K^{-1}.

Table 3.4 Thermodynamic parameters associated with the structural transition process across transition temperature:

Experiment	Enthalpy (J kg^{-1})	Entropy ΔS (J kg^{-1} K^{-1})	N from R*ln*N
DSC (Heating)	**7.1**	0.029	1.01
DSC (Cooling)	**7.47**	0.031	1.00
Specific Heat	66.3	**4.75**	1.04

From X-Ray data analysis, it is seen that at 300 K, total number of disordered sites per molecular unit (N) at 300 K is 8 (2 + 6). As the phase transition is order-disorder type, the entropy change ΔS of phase transition can be defined using the Boltzmann equation as $\Delta S = R \ln N$ (where ΔS = entropy change, R = universal gas constant and N = number of disordered sites). For $N = 8$, the associated entropy change ΔS is 17 J mol^{-1} K^{-1}, which is almost four times to that obtained from C_p/T vs T data. Again from heat capacity anomaly, plugging the ΔS and R value in the Boltzmann equation gives N as 1.7 which does not match with the number of disordered sites observed in crystallographic data. This inconsistency in value of N and the entropy change indicates that the transition is complicated beyond a straightforward order-disorder transition. Possible reason behind this complexity can be the slow process of ordering on lowering the temperature below T_c because of which partial ordering happens just below T_c and complete ordering happens over a broad temperature region.[53] Temperature dependent phenomena e.g. freezing of degrees of freedom of the organic molecules and breaking/formation of H-bonding and the interrelationship between these two are the governing factors behind the ordering process. To mention further, DSC data was recorded using “crushed crystals” under nitrogen atmosphere while the heat capacity data was recorded using a “single crystal piece” under high vacuum. Thus, the thermal response of the sample on temperature sweep can be different due to the morphology. Further, DSC is a kinetic process owing to the fast rate of the temperature sweep. The heat capacity measurement, on the other hand is very slow process (thermodynamic process). Moreover, one cannot completely ignore a possible contribution from adsorbed or absorbed moisture as the compound was highly hygroscopic and also the gas used was nitrogen.

3.3.3 Capacitance Properties:

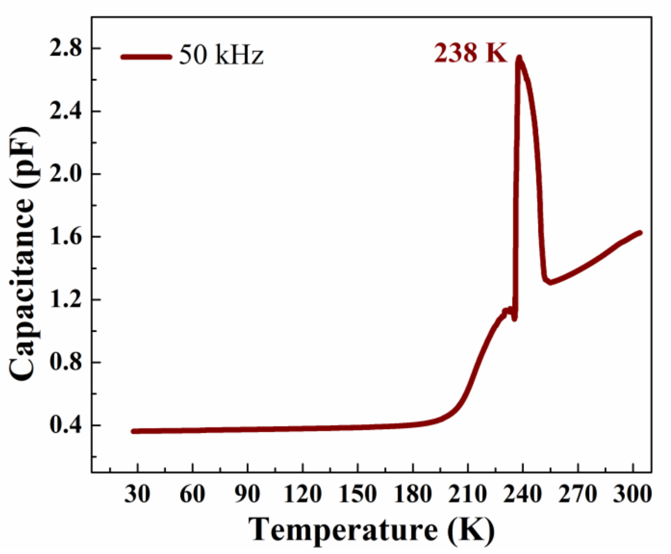

Figure 3.7 Capacitance anomaly at 238 K representing the structural transition feature of compound **1**.

Generally, the dielectric properties of a solid material tend to undergo distinct change across a structural transition owing to the change in dipolar rearrangement. We have recorded macroscopic dielectric properties of single crystals of compound **1** across the phase transition temperature during cooling. Interestingly, a sharp anomaly centred at 238 K was observed which can be considered to be associated with the phase transition process (see **Figure 3.7**). The broad anomaly in the temperature range of 220-300 K in **Figure 3.7** is possibly due to interference of water dipoles. This is possible, as the hygroscopic nature of the crystals can give rise to incorporation of polar water molecules in the sample capacitor which can undergo abrupt changes in the above mentioned temperature range due to freezing (the phase transition temperature being very close to the water crystallization temperature).

3.3.4 Optical Properties:

3.3.4.1 Experimental Optical Spectra:

From the crystal structure discussion, weak distortion in $(CoCl_4)^{2-}$ tetrahedra at 300 K is observed (symmetry below T_d). Considering a Co^{2+} ion in a regular $(CoCl_4)^{2-}$ tetrahedron, the electronic energy states can be categorized into two quartet states ^4F and ^4P and six doublet states as ^2G, ^2H, ^2P, ^2D, ^2F and ^2D. The energy of these states are seen to be considerably dependent on geometric distortion in the tetrahedra and/or spin orbit coupling (SOC) in Co^{2+} ions. The effect of SOC and distoriton in optical properties of metal halide complexes are not studied much. In 1963, the electronic absorption spectra of tetrahderal R_2CoCl_4 hybrids (R = Cs, $N(CH_3)_4$ or quinolinium ion) were analyzed by Ferguson where by considering strong ligand field, SOC and two interelectronic repulsion parameters he calculated the respective energy levels of the electronic states.[23] It was observed that forbidden transitions gain intensity as the SOC mixes the higher energy states. Attempt of quantitative estimation of the transitions reveal that the $^4A_2 \rightarrow {}^4T_1$ (^4F) and $^4A_2 \rightarrow {}^4T_1$ (^4P) transitions appear at around 6,000 cm^{-1} and 13,000 cm^{-1} – 16,000 cm^{-1} respectively.[23] Among the transitions to doublet states, transitions to ^2F and ^2D to were estimated with considerable accuracy. Recently, Kapustianyk *et al.* have reported their attempt to estimate the higher energy states in hybrid halide $(NH_2(CH_3))_2CoCl_4$ from the electronic absorption spectra.[22] Together, both of these studies shows that as the symmetry gets lowered and the higher energy terms $^4T_1$ (^4P) and ^2G mix due to SOC, the higher energy electronic term $^4T_1(^4P)$ splits. We have recorded the electronic absorption spectra of compound **1** on exposure to the visible spectrum (300-800 nm, 12,500–28,000 cm^{-1}) at 300 K. The absorption spectra is seen to be very much comparable to that of $(NH_2(CH_3))_2CoCl_4$. The intra electronic transition band in tetrahderal Co (II) (d^7) ion gives rise to a broad maximum centred at around 15,000 cm^{-1} and many other absorption maxima of different intensity and wavenumbers. We have deconvoluted the maxima at different energies into multiple elementary absorbances which are individually defined by Gaussian contours. The complete region of deconvoluted spectra has been sectioned into three regions: Region-I (12,500 cm^{-1} to 17,500 cm^{-1}), Region-II (17,500 cm^{-1} to 21,600 cm^{-1}) and Region-III (21,600 cm^{-1} to 28,000 cm^{-1}).

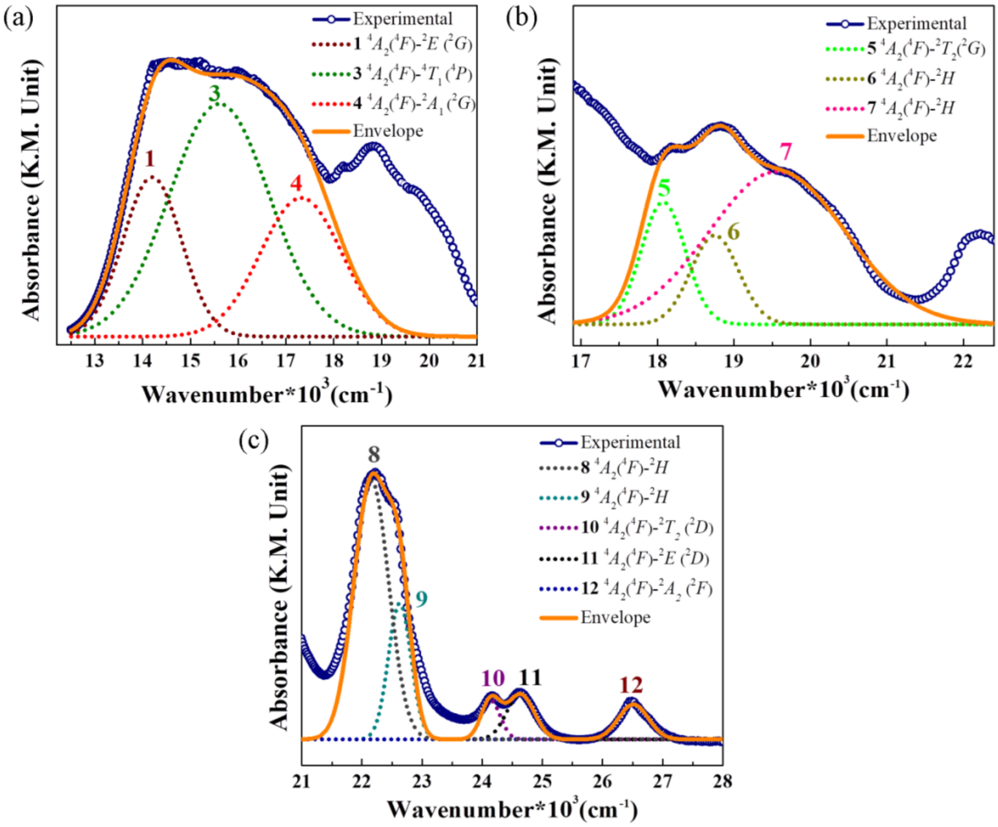

Figure 3.8 (a), (b) and (c) Electronic absorption spectra of compound **1** recorded at 300 K.

In the Region-I (see **Figure 3.8** (a))**,** the maximum intensity peak is **3** which is near 15,625 cm^{-1} and can be assigned to the transition from ground state $^4A_2$ to $^4T_1$ (^4P).[22,23] This absorption can be seen to be associated with two more absorptions named here as **1** and **4** which feature their maxima at 14,204 cm^{-1} and 17,286 cm^{-1} respectively. These associated absorptions appear due to the spin-orbit coupling between $^4T_1$ (^4P) and ^2G energy states.[23] This coupling is complicated in nature as the ^2G state itself contains electronic configurations $e^3t_2^4$ and $e^2t_2^5$ under strong ligand field and thus features some mixed character. On comparing with the estimations made by Kapustianyk *et al*, the peaks **1** and **4** can be ascribed to transitions to $^2A_1$ (^2G) and $^2T_1$ (^2G) respectively.[22,23] The ^2E (^2G) term features an energy which is comparable to that of $^2A_1$ (^2G) and thus it has been possibly suppressed by peak **1** (absence of peak **2**). The experimental and/or theoretical studies on calculations of the higher energy states are very scarce. The ^{2}H in tetrahedral field is seen to be split into 4 sublevels $^{2}T_{1}$, ^{2}E, $^{2}T_{1}$ and $^{2}T_{2}$.[22,54] Now focusing on the Region-II (see **Figure 3.8** (b)), absorption maxima **5** (18,067 cm^{-1}), **6** (18,744 cm^{-1}) can be seen which can be ascribed to the transitions to $^{2}T_{2}(^{2}G)$. The maximum **7** at 19,588 cm^{-1} is possibly spurring from transition to energy state ^{2}H.[22,54] In the Region-III (**Figure 3.8** (c)), we have obtained 5 component maxima on deconvolution (labeled as **8**, **9**, **10**, **11** and **12**). Since the higher energy ^{2}D term splits into ^{2}E and $^{2}T_{2}$ states in tetrahedral symmetry, we have considered the splitting of ^{2}H and ^{2}D and qualitatively compared the absorption maxima with the results obtained by Kapustianyk *et al*.[22]

3.3.4.2 Band Structure and Theoretical Optical Spectra:

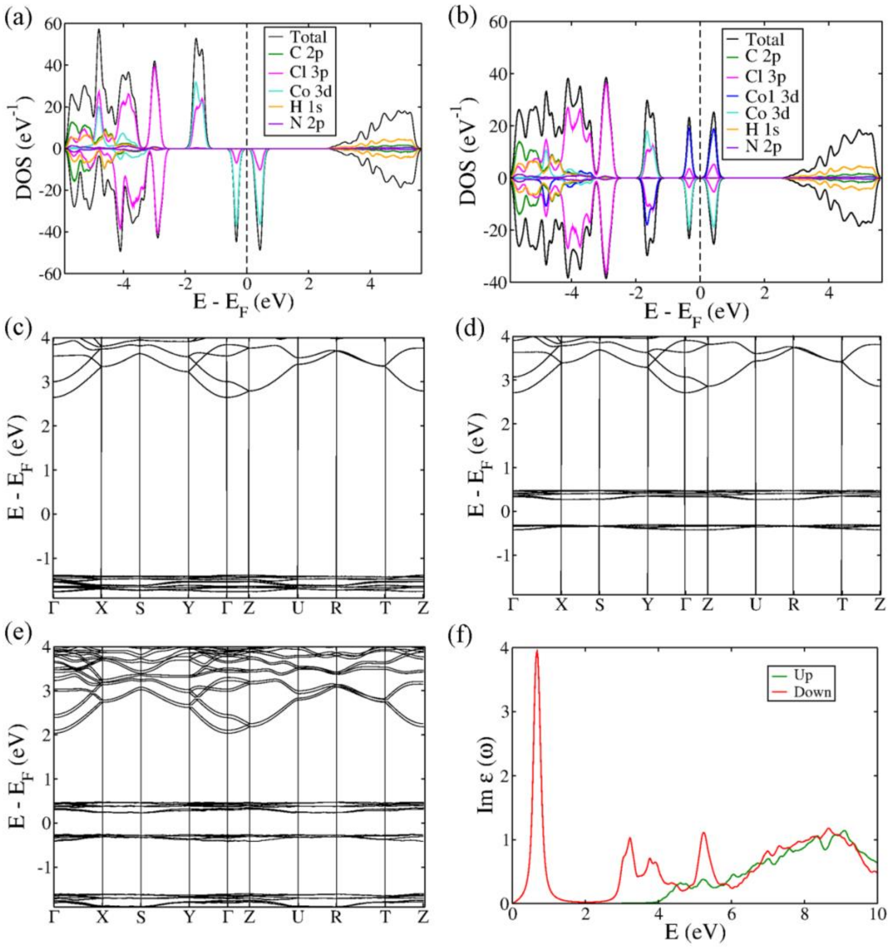

Figure 3.9 Spin-resolved electronic density of states of **1** considering (a) ferromagnetic and (b) G-type antiferromagnetic orderings. Band structure of **1** with ferromagnetic ordering, (c) spin up channel and (d) spin down channel, (e) Band structure of the ECC obtained with calculations that include spin-orbit coupling. (f) spin-resolved optical transition spectra with ferromagnetic ordering.

We have calculated the electronic structure of compound 1 using Local-Density approximation. It was seen that the electronic states near Fermi energy of both the spin channels (for both FM and AFM) are significantly contributed by the cobalt *d* orbitals (see **Figure 3.9**) (theoretical studies on magnetic properties have been discussed in the next section). The electronic states in the energy range between -5.8 eV and -2.5 eV were seen to be composed of Cl 3*p* and C 2*p* orbitals. The conduction band was seen to have significant contribution from H 1*s*, C 2*p* and N 2*p* orbitals (>2.5 eV). Compound 1 was seen to be half-semiconducting in nature with an estimated band gap of 3.97 eV and 0.62 eV in the up-spin and down spin channels respectively. To compare with experimentally observed optical spectra, we have calculated optical absorbance spectra and observed a distinct peak at 0.62 eV (**Figure 3.9** (f)) in the down spin channel, which corresponds to the experimentally observed spin-allowed *d*-*d* transition (0.49 eV and 0.71 eV). However, the SOC influences relaxation in the optical selection rule by mixing up- and down-spin levels as can be seen in **Figure 3.9** (e). Thus the *d*-electrons can potentially get excited from the top of the valence band in the up-spin channel to the conduction band (*d* levels) in the down spin channel. This gives rise to optical transition across an energy gap of 1.85 eV (experimentally observed gap 1.93 eV).

3.3.5 Magnetic Properties:

As the $(CoCl_4)^{2-}$ tetrahedra are far from each other in the crystal, one can expect very weak magnetic interaction among the cobalt spins. We have recorded the temperature dependent dc magnetic susceptibility which exhibit typical paramagnetic behavior down to 2 K (**Figure 3.10** (a)). Interestingly, a subtle magnetic anomaly has been observed at 238 K. This is possibly due to the distinct changes in crystal across structural transition. Curie-Weiss fitting have been carried out in the temperature range of 50 K - 230 K which gives Curie constant value C = 2.81 emu mol^{-1} Oe^{-1} and a temperature intercept θ of -4.2 K. Such small intercept clearly indicates that the spins at cobalt sites have weak antiferromagnetic interactions between them. The effective magnetic moment obtained from Curie constant is μ_{eff} = 4.73 μ_B which is higher than the spin-only moment 3.8 μ_B. This confirms the presence of orbital contribution. Interestingly, isothermally magnetization data recorded at 2 K exhibits a sigmoidal reorientation behavior of magnetic spinf under induction of magnetic field (see **Figure 3.10** (b)). The maximum moment was found to be 2.69 μ_B/f.u. at 7 T [for the saturation to complete, the moment value should be 3 μ_B/f.u. {Co^{2+}, d^7 (t_d) $e^4 t_2^3$}]. On increasing the temperature, the reorientation feature was seen to decrease (see **Figure 3.10** (c)).

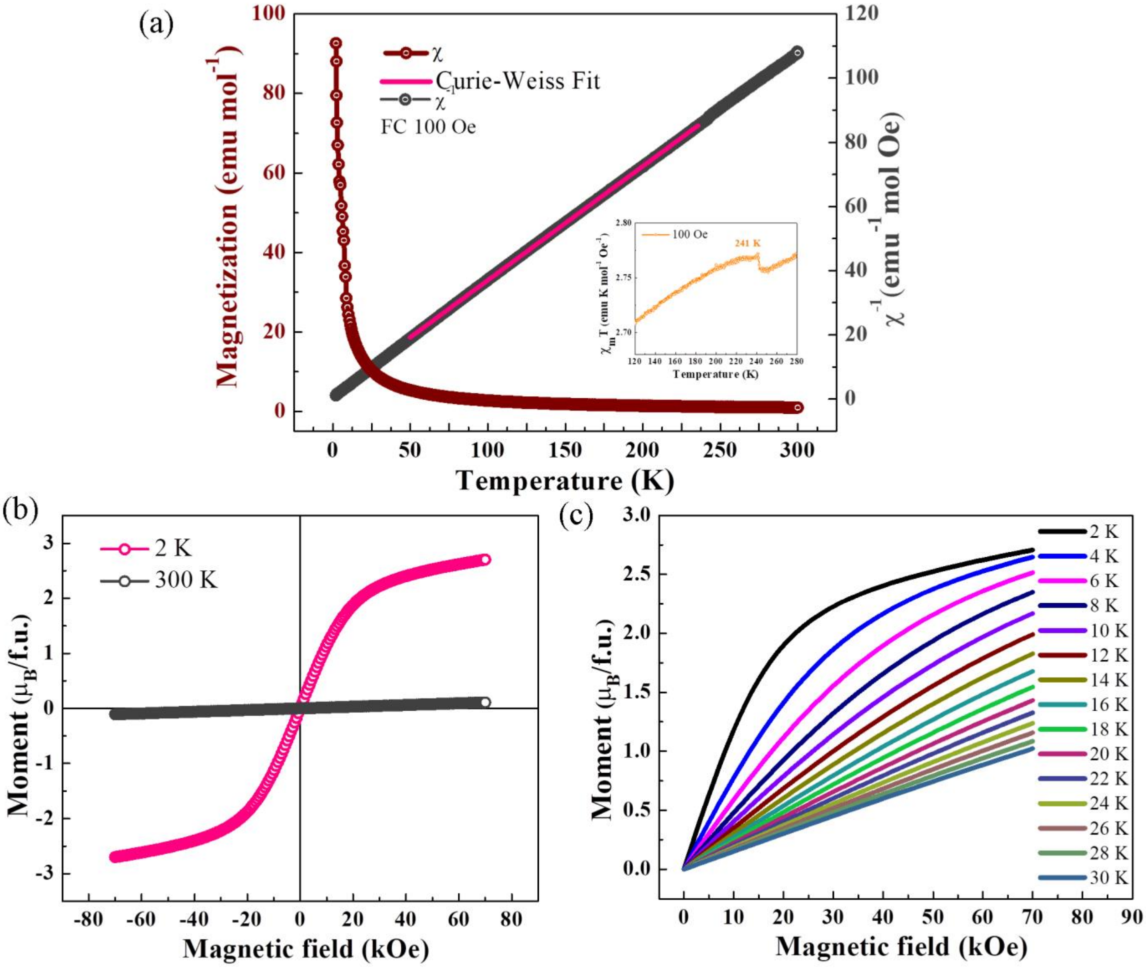

Figure 3.10 (a) Temperature dependence of magnetic susceptibility and inverse magnetic susceptibility under 100 Oe applied dc field. Curie-Weiss fitting has been carried out in the temperature range of 50-250 K. **Inset** shows signature of structural phase transition in χ_mT vs T graph. (b) Isothermal magnetization vs magnetic field measured at 2 K and at 300 K. (c) Dependence of the M vs H isotherm on temperature variation as recorded with a field sweep from 0 to +70 k Oe (first quadrant).

To understand the nature of interaction at low temperature, we calculated and compared the energies of ferromagnetic and G-type antiferromagnetic states from DFT calculations with LDA and LDA+SOC. LDA calculations predicted that the ferromagnetic state is the lowest energy state while the G-type antiferromagnetic state is marginally higher in energy (by 1 meV/f.u.). From LDA magnetic exchange coupling value was calculated which was − 0.45 meV. Such small energy difference, and weak exchange coupling constant is fairly consistent with the large nearest and next nearest neighbor distances berween cobalt atoms (5.93 Å, 6.97 Å). This certainly indicates that the spins at Co atoms are weakly coupled. Overall, the magnetizations studies indicate that because of the isolated nature of $(CoCl_4)^{2-}$ tetrahedra, the compound behaves as a paramagnet while the macroscopic magnetization behavior becomes almost comparable to that of single $(CoCl_4)^{2-}$ tetrahedron.

3.3.6 Magnetothermal Properties:

From the changes in field induced magnetization behavior on increasing the temperature (**Figure 3.10** (c)) one can expect interesting changes in magnetic spin induced entropy. Thus, we have further focused on the magneto-thermal properties (magnetocaloric effect) of compound **1** in the low temperature region. The magnetocaloric effect (MCE) is known as the entropy change associated with change in magnetic spins on application of external magnetic field. Magnetocaloric effect is technologically very important, as it can further influence in lowering of material temperature under adiabatic conditions. From the first quadrant isothermal magnetization data recorded at different temperatures, we have calculated the respective entropy changes and constructed the MCE against temperature plot. For this, we have recorded the first quadrant M vs H data with field range of 0 T – 7 T from 2 K to 60 K.

Making use of the Maxwell's equation:

$$\left(\frac{\partial S}{\partial H}\right)_T = \left(\frac{\partial M}{\partial T}\right)_H \qquad 1.1$$

we obtain

$$\Delta S\,(T,H) = \int_0^H \left(\frac{\partial M}{\partial T}\right)_H dH \qquad 1.2$$

As we have recorded isotherm data at different steps of temperature and field, the above equation takes the following form:[55]

$$\sum_i \frac{1}{T_{i+1}-T_i}(M_i - M_{i+1})_H\, \Delta H_i \qquad 1.3$$

where M_i and M_{i+1} are the experimentally recorded magnetization values under constant applied field H at temperatures T_i and T_{i+1} respectively.

We have also extracted the entropy change from heat capacity measurements for which, firstly we first calculated the total entropy as a function of temperature at different fields using the following equation,

$$\Delta S = \int_0^T \frac{C(T)_H}{T}\, dT \qquad 1.4$$

Here, it needs to be mentioned that although the equation considers integration till 0 K, we could integrate down to lowest achievable temperature 2 K only. Due to the absence of any magnetic transition in the measurement window, we failed to extrapolate the heat capacity data and effectively make any correction to it. After extracting the entropy values, we then calculated the entropy change (-Δ*S (H)*) by subtracting the *S (H)* from *S* (0 T). The ΔT_{ad} was obtained from entropy against temperature plot (0 T and 7 T).

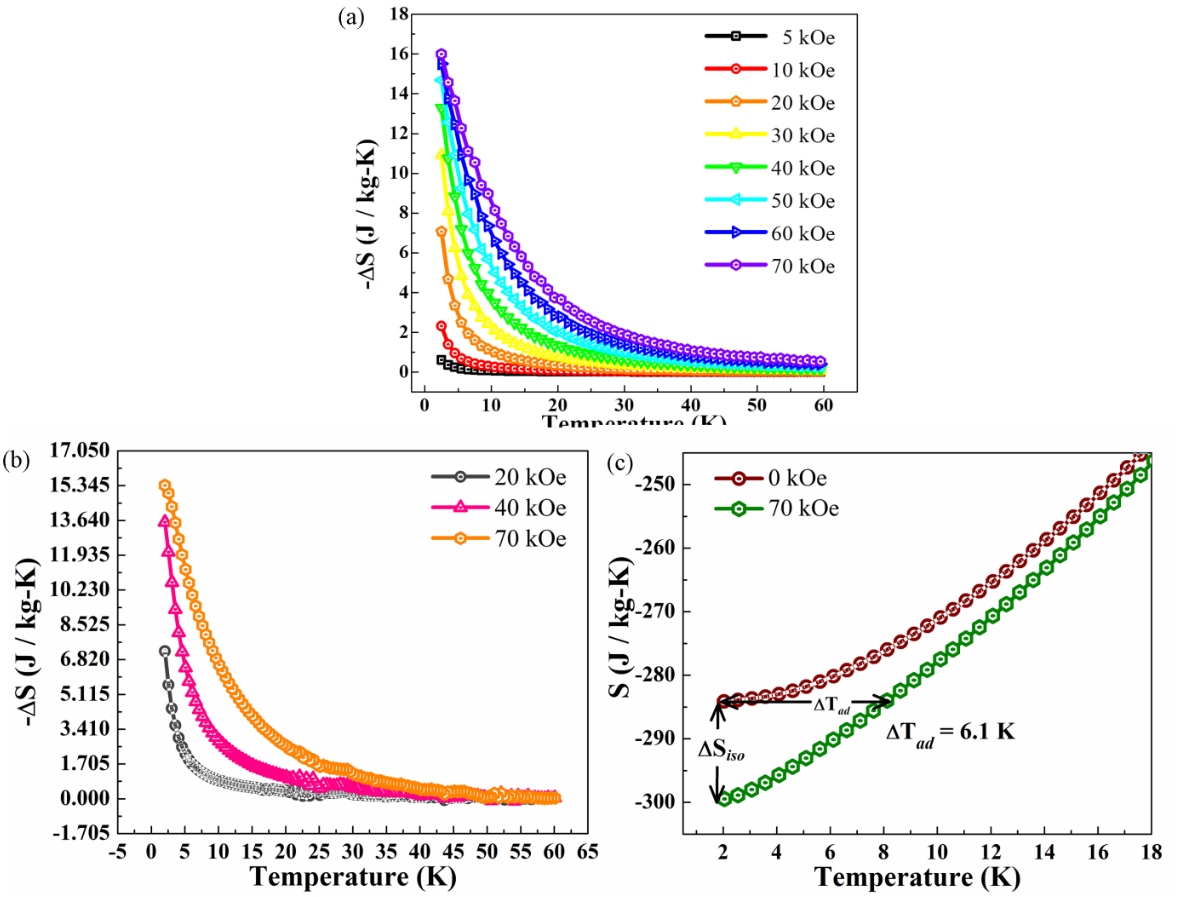

Figure 3.11 Entropy change as extracted from (a) magnetization measurements and (b) heat capacity measurements. (c) S vs T data showing adiabatic change of temperature ΔT_{ad} calculated from the isotherm and the isentrope.

We have observed that the magnetic entropy gradually increases with lowering of temperature till 25 K after which it rapidly increases till 2.5 K. This is because the magnetic interaction between cobalt spins becomes prominent on lowering the temperature. The maximum value of estimated entropy change is ΔS = 16 J kg^{-1} K^{-1} (4.7 J mol^{-1} K^{-1}) at 2.5 K under 70 k Oe applied field (**Figure 3.11** (a)). Entropy extracted from the heat capacity measurements also exhibits similar temperature dependent behavior as it reaches the maximum value of 15.4 J kg^{-1} K^{-1} at 2 K under 70 k Oe applied field (see **Figure 3.11** (b)). The corresponding adiabatic change in temperature ΔT_{ad} was obtained to be 6.1 K (see **Figure 3.11** (c)). It can be seen that the entropy change estimated from heat capacity data agrees very well with the entropy obtained from the magnetic measurements. The maximum extractable entropy for complete magnetization (3 μ_B) which is 38.4 J kg^{-1} K^{-1}. We have compared the experimental entropy change with literature where we have found that the entropy change is higher than a number of transition metal based molecular cluster magnets Mn_{12} or Fe_8 and is comparable to Fe_{14} all of which are cluster magnets.[37–39]

Table 3.5 Literature comparison of magnetocaloric effect:

Compound	Entropy Change (J kg^{-1} K^{-1})	Reference
Mn_{12}	12.5	[37]
Fe_8	11	[38]
Fe_{12}	17.6	[39]
$(C_2H_5NH_3)_2CoCl_4$	**16**	**Our Work**

3.4 Conclusion:

In conclusion, we present detailed experimental and theoretical studies of the physical properties of a new cobalt containing R_2MX_4 hybrid halide. The single crystalline compound features centrosymmetric orthorhombic structure (space group *Pnma*) at room temperature. A reversible, first order structural phase transition has been observed at 235/241 K (cooling/heating) below which the compound exhibits noncentrosymmetric yet nonpolar orthorhombic structure (space group $P2_12_12_1$). In the electronic absorption spectra, effect of symmetry lowering and SOC effect in $CoCl_4$ tetrahedra have been observed. Magnetic measurements reveal paramagnet behavior down to low temperature, with field induced spin reorientation is observed near 2 K. First-principles density functional calculations demonstrate that both (i) ferromagnetic and G-type antiferromagnetic states are comparable in energy and a very weak magnetic interaction is present between spins at Co sites and (ii) the SOC is very important in understanding optical absorption spectra. The field induced spin reorientation behavior at low temperature region has been studied to extract the associated magnetic entropy. The obtained entropy value was found to be sizable and comparable with transition metal based cluster magnets.

Atomic Position List:

Table 3.6 Atomic coordinates (x10^{4}) and equivalent isotropic displacement parameters (Å^{2}x10^{3}) for compound **1** at 300 K with estimated standard deviations in parentheses

Label	x	y	z	Occupancy	U_{eq}^{*}
N(1)	10622(10)	7500	8857(5)	1	97(3)
C(2A)	10400(200)	7500	7980(150)	0.21(8)	180(90)
C(3A)	9810(50)	7500	7500(20)	0.21(8)	50(20)
C(1)	10700(40)	8080(50)	8020(20)	0.39(4)	109(12)
C(2)	9920(30)	8480(80)	7660(20)	0.39(4)	127(12)
Co(1)	7282(2)	2500	5410(1)	1	73(1)
Cl(1)	7584(3)	2500	4139(2)	1	149(2)
Cl(2)	5112(3)	2500	5695(2)	1	120(2)
Cl(3)	8306(2)	4974(3)	5876(2)	1	110(1)
N(2)	8714(13)	7500	4294(6)	1	123(4)
C(3)	8380(30)	8300(30)	3632(17)	0.5	153(9)
C(4)	8100(30)	7500	2971(11)	1	185(10)

Table 3.7 Atomic coordinates (x10^{4}) and equivalent isotropic displacement parameters (Å^{2}x10^{3}) for compound **1** at 200 K with estimated standard deviations in parentheses

Label	x	y	z	Occupancy	U_{eq}^{*}
N(1)	66(5)	3851(5)	5599(3)	1	39(1)
H(1A)	-455	3023	5682	1	47
H(1B)	733	3811	5155	1	47
H1C()	-773	4508	5541	1	47
C(1)	156(9)	4287(8)	7019(4)	1	62(2)
H(1D)	-813	4936	6946	1	93
H(1E)	911	4604	7449	1	93
H(1F)	-317	3378	7149	1	93
C(2)	1197(7)	4198(6)	6283(3)	1	40(2)
H(2A)	2115	3486	6343	1	48
H(2B)	1787	5088	6185	1	48
N(2)	5725(6)	8041(4)	6237(2)	1	38(1)
H2C()	5616	7193	6017	1	46
H(2D)	6752	8429	6079	1	46
H(2E)	4812	8579	6082	1	46
C(3)	4054(10)	7266(7)	7379(4)	1	61(2)

H(3A)	3976	6329	7170	1	91
H(3B)	3054	7805	7189	1	91
H3C()	4037	7237	7955	1	91
C(4)	5716(9)	7913(6)	7107(3)	1	47(2)
H(4A)	5838	8834	7348	1	56
H(4B)	6726	7346	7277	1	56
Co(1)	5476(1)	5261(1)	4552(1)	1	28(1)
Cl(1)	4892(2)	7510(2)	4357(1)	1	44(1)
Cl(2)	7851(2)	4472(2)	3892(1)	1	41(1)
Cl(3)	3016(2)	4096(2)	4162(1)	1	34(1)
Cl(4)	5914(2)	4789(2)	5849(1)	1	34(1)

Table 3.8 Atomic coordinates (x10^4) and equivalent isotropic displacement parameters (Å^{2}x10^3) for compound **1** at 100 K with estimated standard deviations in parentheses**:**

Label	**x**	**y**	**z**	**Occupancy**	**U_{eq}^***
Co(1)	4470(1)	4738(1)	4551(1)	1	15(1)
Cl(2)	4031(2)	5214(2)	5861(1)	1	18(1)
Cl(1)	6927(2)	5916(2)	4155(1)	1	18(1)
Cl(3)	5089(2)	2472(2)	4356(1)	1	22(1)
Cl(4)	2088(2)	5523(2)	3885(1)	1	21(1)
N(1)	4881(6)	8866(5)	4408(3)	1	20(1)
H(1A)	5354	8011	4339	1	25
H(1B)	4228	8876	4861	1	25
H1C()	5756	9502	4447	1	25
N(2)	4206(6)	1953(5)	6245(2)	1	19(1)
H2C()	4351	2805	6026	1	23
H(2D)	3149	1601	6096	1	23
H(2E)	5079	1383	6075	1	23
C(2)	3740(7)	9209(6)	3715(3)	1	20(2)
H(2A)	3156	10109	3808	1	23
H(2B)	2820	8494	3657	1	23
C(4)	4273(9)	2068(6)	7128(3)	1	24(2)
H(4A)	4175	1137	7369	1	29
H(4B)	3275	2633	7319	1	29
C(3)	5970(9)	2727(7)	7376(3)	1	30(2)
H(3A)	6008	2800	7956	1	46

H(3B)	6954	2159	7192	1	46
H3C()	6055	3652	7142	1	46
C(1)	4811(8)	9284(8)	2965(3)	1	33(2)
H(1D)	4042	9510	2517	1	50
H(1E)	5710	10001	3020	1	50
H(1F)	5375	8389	2870	1	50

3.5 Bibliography:

(1) Shi, P.-P.; Tang, Y.-Y.; Li, P.-F.; Liao, W.-Q.; Wang, Z.-X.; Ye, Q.; Xiong, R.-G. Symmetry Breaking in Molecular Ferroelectrics. *Chem. Soc. Rev.* **2016**, *45* (14), 3811–3827.

(2) Hang, T.; Zhang, W.; Ye, H.-Y.; Xiong, R.-G. Metal–Organic Complex Ferroelectrics. *Chem. Soc. Rev.* **2011**, *40* (7), 3577–3598.

(3) Walsh, A. Principles of Chemical Bonding and Band Gap Engineering in Hybrid Organic–Inorganic Halide Perovskites. *J. Phys. Chem. C* **2015**, *119* (11), 5755–5760.

(4) Wang, Y.; Runnerstrom, E. L.; Milliron, D. J. Switchable Materials for Smart Windows. *Annu. Rev. Chem. Biomol. Eng.* **2016**, *7* (1), 283–304.

(5) Mostafa, M. F.; Abdel-Kader, M. M.; Arafat, S. S.; Kandeel, E. M. Thermochromic Phase Transitions in Two Aromatic Tetrachlorocuprates. *Phys. Scr.* **1991**, *43* (6), 627–629.

(6) Jaffe, A.; Lin, Y.; Mao, W. L.; Karunadasa, H. I. Pressure-Induced Conductivity and Yellow-to-Black Piezochromism in a Layered Cu–Cl Hybrid Perovskite. *J. Am. Chem. Soc.* **2015**, *137* (4), 1673–1678.

(7) Zhang, Y.; Liao, W.-Q.; Fu, D.-W.; Ye, H.-Y.; Liu, C.-M.; Chen, Z.-N.; Xiong, R.-G. The First Organic–Inorganic Hybrid Luminescent Multiferroic: (Pyrrolidinium)$MnBr_3$. *Adv. Mater.* **2015**, *27* (26), 3942–3946.

(8) Kundys, B.; Lappas, a.; Viret, M.; Kapustianyk, V.; Rudyk, V.; Semak, S.; Simon, C.; Bakaimi, I. Multiferroicity and Hydrogen-Bond Ordering in $(C_2H_5NH_3)_2CuCl_4$ Featuring Dominant Ferromagnetic Interactions. *Phys. Rev. B - Condens. Matter Mater. Phys.* **2010**, *81* (22), 1–6.

(9) Liao, W.-Q.; Tang, Y.-Y.; Li, P.-F.; You, Y.-M.; Xiong, R.-G. Large Piezoelectric Effect in a Lead-Free Molecular Ferroelectric Thin Film. *J. Am. Chem. Soc.* **2017**, *139* (49), 18071–18077.

(10) Saparov, B.; Mitzi, D. B. Organic–Inorganic Perovskites: Structural Versatility for Functional Materials Design. *Chem. Rev.* **2016**, *116* (7), 4558–4596.

(11) De Jongh, L. J.; Van Amstel, W. D.; Miedema, A. R. Magnetic Measurements on (C2H5NH3)2 CuCl4: Ferromagnetic Layers Coupled by a Very Weak Antiferromagnetic Interaction. *Physica* **1972**, *58* (2), 277–304.

(12) van Amstel, W. D.; de Jongh, L. J. Magnetic Measurements on (CH3NH3)2MnCl4, a Quasi Two-Dimensional Heisenberg Antiferromagnet. *Solid State Commun.* **1972**, *11* (10), 1423–1429.

(13) Polyakov, A. O.; Arkenbout, A. H.; Baas, J.; Blake, G. R.; Meetsma, A.; Caretta, A.; Van Loosdrecht, P. H. M.; Palstra, T. T. M. Coexisting Ferromagnetic and Ferroelectric Order in a $CuCl_4$-Based Organic-Inorganic Hybrid. *Chem. Mater.* **2012**, *24* (1), 133–139.

(14) Nakayama, Y.; Nishihara, S.; Inoue, K.; Suzuki, T.; Kurmoo, M. Coupling of Magnetic and Elastic Domains in the Organic–Inorganic Layered Perovskite-Like $(C_6H_5C_2H_4NH_3)_2Fe^{II}Cl_4$ Crystal. *Angew. Chemie* **2017**, *129* (32), 9495–9498.

(15) Suzuki, T.; Yoshizawa, M.; Goto, T.; Yamakami, T.; Takahashi, M.; Fujimura, T. Structural Phase Transition of Layer Compound $(C_2H_5NH_3)_2FeCl_4$. *J. Phys. Soc. Japan* **1983**, *52* (5), 1669–1675.

(16) Nakajima, T.; Yamauchi, H.; Goto, T.; Yoshizawa, M.; Suzuki, T.; Fujimura, T. Magnetic and Elastic Properties of $(CH_3NH_3)_2FeCl_4$ and $(C_2H_5NH_3)_2FeCl_4$. *J. Magn. Magn. Mater.* **1983**, *31–34*, 1189–1190.

(17) Han, J.; Nishihara, S.; Inoue, K.; Kurmoo, M. High Magnetic Hardness for the Canted Antiferromagnetic, Ferroelectric, and Ferroelastic Layered Perovskite-like $(C_2H_5NH_3)_2[Fe^{II}Cl_4]$. *Inorg. Chem.* **2015**, *54* (6), 2866–2874.

(18) Sawada, S.; Shiroishi, Y.; Yamamoto, A.; Takashige, M.; Matsuo, M. Ferroelectricity in $\{N(CH_3)_4\}_2CoCl_4$. *Phys. Lett. A* **1978**, *67* (1), 56–58.

(19) Decaroli, C.; Arevalo-Lopez, A. M.; Woodall, C. H.; Rodriguez, E. E.; Attfield, J. P.; Parker, S. F.; Stock, C. $(C_4H_{12}N_2)[CoCl_4]$: Tetrahedrally Coordinated Co^{2+} without the Orbital Degeneracy. *Acta Crystallogr. B. Struct. Sci. Cryst. Eng. Mater.* **2015**, *71* (Pt 1), 20–24.

(20) Piecha-Bisiorek, A.; Bieńko, A.; Jakubas, R.; Boča, R.; Weselski, M.; Kinzhybalo,

V.; Pietraszko, A.; Wojciechowska, M.; Medycki, W.; Kruk, D. Physical and Structural Characterization of Imidazolium-Based Organic–Inorganic Hybrid: $(C_3N_2H_5)_2[CoCl_4]$. *J. Phys. Chem. A* **2016**, *120* (12), 2014–2021.

(21) Kapustianyk, V.; Rudyk, V.; Yonak, P.; Kundys, B. Magnetic and Dielectric Properties of $[N(C_2H_5)_4]_2CoClBr_3$ Solid Solution: A New Potential Multiferroic. *Phys. Status Solidi* **2015**, *5*.

(22) Kapustianyk, V. B.; Yonak, P. K.; Rudyk, V. P. Temperature Evolution of the Intra-Ion Absorption Spectra of Cobalt in $(NH_2(CH_3)_2)_2CoCl_4$ Crystals. *J. Appl. Spectrosc.* **2015**, *82* (4), 591–597.

(23) Ferguson, J. Crystal-Field Spectra of D3,7 Ions. I. Electronic Absorption Spectrum of $CoCl_4^{=}$ in Three Crystalline Environments. *J. Chem. Phys.* **1963**, *39* (1), 116–128.

(24) Murrie, M. Cobalt(II) Single-Molecule Magnets. *Chem. Soc. Rev.* **2010**, *39* (6), 1986–1995.

(25) Craig, G. A.; Murrie, M. 3d Single-Ion Magnets. *Chem. Soc. Rev.* **2015**, *44* (8), 2135–2147.

(26) Idešicová, M.; Titiš, J.; Krzystek, J.; Boča, R. Zero-Field Splitting in Pseudotetrahedral Co(II) Complexes: A Magnetic, High-Frequency and -Field EPR, and Computational Study. *Inorg. Chem.* **2013**, *52* (16), 9409–9417.

(27) Zadrozny, J. M.; Atanasov, M.; Bryan, A. M.; Lin, C.-Y.; Rekken, B. D.; Power, P. P.; Neese, F.; Long, J. R. Slow Magnetization Dynamics in a Series of Two-Coordinate Iron(II) Complexes. *Chem. Sci.* **2013**, *4* (1), 125–138.

(28) Herchel, R.; Váhovská, L.; Potočňák, I.; Trávníček, Z. Slow Magnetic Relaxation in Octahedral Cobalt(II) Field-Induced Single-Ion Magnet with Positive Axial and Large Rhombic Anisotropy. *Inorg. Chem.* **2014**, *53* (12), 5896–5898.

(29) de Jongh, L. J.; Miedema, A. R. Experiments on Simple Magnetic Model Systems. *Adv. Phys.* **1974**, *23* (1), 1–260.

(30) Willett R.D., Gaura R.M., L. C. P. Ferromagnetism in Linear Chains. In: Miller J.S. (Eds) Extended Linear Chain Compounds. *Springer, Boston, MA* **1983**, 143–

191.

(31) Snively, L. O.; Haines, D. N.; Emerson, K.; Drumheller, J. E. Two-Halide Superexchange in $[NH_3(CH_2)_nNH_3]CuBr_4$ for n = 3 and 4. *Phys. Rev. B* **1982**, *26* (9), 5245–5247.

(32) Turnbull, M. M.; Landee, C. P.; Wells, B. M. Magnetic Exchange Interactions in Tetrabromocuprate Compounds. *Coord. Chem. Rev.* **2005**, *249* (23), 2567–2576.

(33) Willett, R. D.; Galeriu, C.; Landee, C. P.; Turnbull, M. M.; Twamley, B. Structure and Magnetism of a Spin Ladder System: $(C_5H_9NH_3)_2CuBr_4$. *Inorg. Chem.* **2004**, *43* (13), 3804–3811.

(34) Zheng, Y.-Z.; Zhou, G.-J.; Zheng, Z.; Winpenny, R. E. P. Molecule-Based Magnetic Coolers. *Chem. Soc. Rev.* **2014**, *43* (5), 1462–1475.

(35) Pecharsky, V. K.; Gschneidner K. A., J. Giant Magnetocaloric Effect in Gd5Si2Ge2. *Phys. Rev. Lett.* **1997**, *78* (23), 4494–4497.

(36) Lorusso, G.; Sharples, J. W.; Palacios, E.; Roubeau, O.; Brechin, E. K.; Sessoli, R.; Rossin, A.; Tuna, F.; McInnes, E. J. L.; Collison, D.; et al. A Dense Metal–Organic Framework for Enhanced Magnetic Refrigeration. *Adv. Mater.* **2013**, *25* (33), 4653–4656.

(37) Torres, F.; Hernández, J. M.; Bohigas, X.; Tejada, J. Giant and Time-Dependent Magnetocaloric Effect in High-Spin Molecular Magnets. *Appl. Phys. Lett.* **2000**, *77* (20), 3248–3250.

(38) Zhang, X. X.; Wei, H. L.; Zhang, Z. Q.; Zhang, L. Anisotropic Magnetocaloric Effect in Nanostructured Magnetic Clusters. *Phys. Rev. Lett.* **2001**, *87* (15), 157203.

(39) Low, D. M.; Jones, L. F.; Bell, A.; Brechin, E. K.; Mallah, T.; Rivière, E.; Teat, S. J.; McInnes, E. J. L. Solvothermal Synthesis of a Tetradecametallic FeIII Cluster. *Angew. Chemie Int. Ed.* **2003**, *42* (32), 3781–3784.

(40) Chang, L.-X.; Xiong, G.; Wang, L.; Cheng, P.; Zhao, B. A 24-Gd Nanocapsule with a Large Magnetocaloric Effect. *Chem. Commun.* **2013**, *49* (11), 1055–1057.

(41) Peng, J.-B.; Zhang, Q.-C.; Kong, X.-J.; Ren, Y.-P.; Long, L.-S.; Huang, R.-B.; Zheng, L.-S.; Zheng, Z. A 48-Metal Cluster Exhibiting a Large Magnetocaloric Effect. *Angew. Chemie Int. Ed.* **2011**, *50* (45), 10649–10652.

(42) Peng, J.-B.; Zhang, Q.-C.; Kong, X.-J.; Zheng, Y.-Z.; Ren, Y.-P.; Long, L.-S.; Huang, R.-B.; Zheng, L.-S.; Zheng, Z. High-Nuclearity 3d–4f Clusters as Enhanced Magnetic Coolers and Molecular Magnets. *J. Am. Chem. Soc.* **2012**, *134* (7), 3314–3317.

(43) Bruker AXS Inc., Madison, Wisconsin, USA. SAINT ,. **2000**.

(44) G. M. Sheldrick, Go¨ttingen, G. SADABS,. **1997**.

(45) Sheldrick, G. M. , SHELXTL, program for crystal structure refine-ment. , SHELXTL, Program for Crystal Structure Refine-Ment,. **1997**.

(46) A. L. Spek. PLATON. *J. Appl. Crystallogr.* **2003**, *36*, 7–13.

(47) Farrugia, L. WinGX. *J. Appl. Crystallogr.* **1999**, *32*, 837–838.

(48) O. V. Dolomanov, L. J. Bourhis, R. J. Gildea, J. A. K. H.; Puschmann, and H. Olexys2. *J. Appl. Crystallogr.* **2009**, *42*, 339–341.

(49) Wentzcovitch, P. G. and S. B. and N. B. and M. C. and R. C. and C. C. and D. C. and G. L. C. and M. C. and I. D. and A. D. C. and S. de G. and S. F. QUANTUM ESPRESSO: A Modular and Open-Source Software Project for Quantum Simulations of Materials. *J. Phys. Condens. Matter* **2009**, *21* (39), 395502.

(50) Hamann, D. R.; Schlüter, M.; Chiang, C. Norm-Conserving Pseudopotentials. *Phys. Rev. Lett.* **1979**, *43* (20), 1494–1497.

(51) Perdew, J. P.; Zunger, A. Self-Interaction Correction to Density-Functional Approximations for Many-Electron Systems. *Phys. Rev. B* **1981**, *23* (10), 5048–5079.

(52) Cahn, R. W. Disorder in Crystals. *Nature* **1979**, *280* (5720), 343–344.

(53) Jain, P.; Dalal, N. S.; Toby, B. H.; Kroto, H. W.; Cheetham, A. K. Order−Disorder Antiferroelectric Phase Transition in a Hybrid Inorganic−Organic Framework with the Perovskite Architecture. *J. Am. Chem. Soc.* **2008**, *130* (32), 10450–10451.

(54) Kapustianik, V. B. Manifestations of Incommensurate Modulation in the Spectral Properties of A_2MeCl_4 Type Crystals. *Phys. status solidi* **1998**, *207* (2), 509–520.

(55) Mandal, P.; Serrao, C. R.; Suard, E.; Caignaert, V.; Raveau, B.; Sundaresan, A.; Rao, C. N. R. Spin Reorientation and Magnetization Reversal in the Perovskite Oxides, $YFe_{1-x}Mn_xO_3$ ($0\leq x\leq 0.45$): A Neutron Diffraction Study. *J. Solid State Chem.* **2013**, *197*, 408–413.

Chapter 4

Highly Photoluminescent Hybrid $(CH_6N_3)_2MnCl_4$ Featuring 30 K Hysteresis in a Structural Phase Transition Marked by Switchable Dielectric and Magnetic Anomalies

Summary

We have designed and investigated detailed structural, dielectric, magnetic and optical properties of a new luminescent hybrid halide $(CH_6N_3)_2MnCl_4$ (CH_6N_3: Guanidinium cation or GC). The compound features unique $(Mn_3Cl_{12})^{6-}$ units and possible ion-pair interactions among GCs in its zero dimensional crystal structure (space group $P2_1/c$ at 295 K) that endures reversible, first-order structural transition at 166/195 K to orthorhombic structure (space group $P2_12_12_1$) on thermal treatment. The transition is rendered by reorientation and ordering of GCs and also subtle changes in crystal packing, resulting in modulation of extensive supramolecular interactions. Remarkably, the transition is seen to be coupled with switchable dielectric anomaly fashioned by 30 K hysteresis loop-like feature where the disordered (dipolar+quadrupolar) and frozen (quadrupolar) phases of GCs portray the high and low dielectric states respectively. Moreover, the transition and hysteresis have also been uniquely visualized *via* subtle magnetic anomalies. Presence of octahedral Mn^{2+} ion causes fascinating bright orange-red emission at 645 nm under ultraviolet excitation with sizeable lifetime and quantum yield.

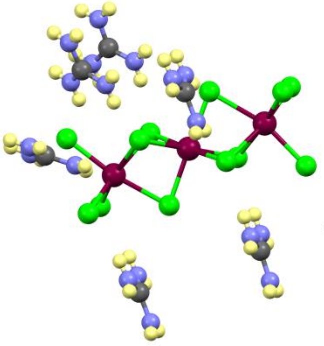

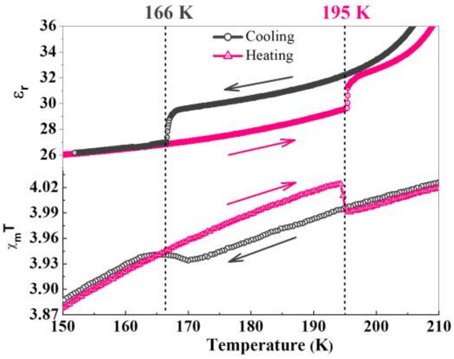

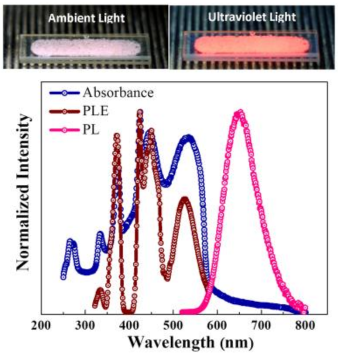

4.1 Introduction

Structural phase transitions (SPT) are fundamental driving factors behind emergence of a number of physical properties in materials, well-known examples include ferroelectricity, piezoelectricity, spin crossover, dielectric or optical switching behavior.[1–8] Among these, switchable physical properties, where SPTs influence distinct changes in physical properties and evolution of switching states (i.e. the high and low states, see **Scheme 4.1**) across transition are unique, having wide range of technological applications in sensors, displays, storage and memory devices.[7,9,10] The switchable physical/chemical properties of a material between the distinct states across phase transition can be controlled by a number of external stimuli e.g. temperature, pressure, light, magnetic or electric field as have been reported in various materials.[8–13] In this aspect, the molecular materials hold strong promises, as they can easily undergo structural phase transitions and exhibit various switching properties coupled with the same. In fact in recent years, a series of molecular materials exhibiting one or multiple switchable properties under different stimuli at phase transition has been reported.[12,14–20] Among the various stimuli mentioned above, temperature can be controlled very efficiently with very high precision and thus is most frequently used to study the switching properties. Among all the switchable properties, magnetic and dielectric switching properties are most important in terms of technological application. In magnetic switching, the spin-rearrangement among the magnetically active ions affects the cumulative magnetization, which results in realization of high and low spin states (known as "spin crossover"). The switchable dielectrics, rearrangement of polar components under application of stimulus governs the high and low dielectric states (HDS and LDS respectively).[6,21–23]

In principle, the cumulative response of polarizable bound charges in a material give rise to the dielectric behavior with the degree of polarizability representing the real part ε_r (complex dielectric constant $\varepsilon = \varepsilon_r - i\varepsilon_i$). In the thermally driven switchable dielectric materials, the HDS and LDS across transition temperature (T_c) can be expressed using an ultra-simplified expression of ε_r derived from Langevin-Debye formula which is: $\varepsilon_r = C_0 + C_1/T$ (C_0 and C_1 correspond to LDS and HDS respectively).[24] In the switchable dielectrics, the switching behavior are seen to appear as across the transition, the polar components (ions or molecules) in the crystal undergo dynamic (or motional) changes between "ordered" (or frozen) and "disordered" (or liquid) states (see **Scheme 4.1**).[11,22] In such materials, one component of the crystal remains rigid throughout the transition while the other component exhibits dynamic behavior (known as amphidynamic crystal). In molecular crystals, the dielectric switching behavior is often associated with symmetry breaking phase transition due to reorientation and/or ordering of the dynamic molecules across transition temperature.

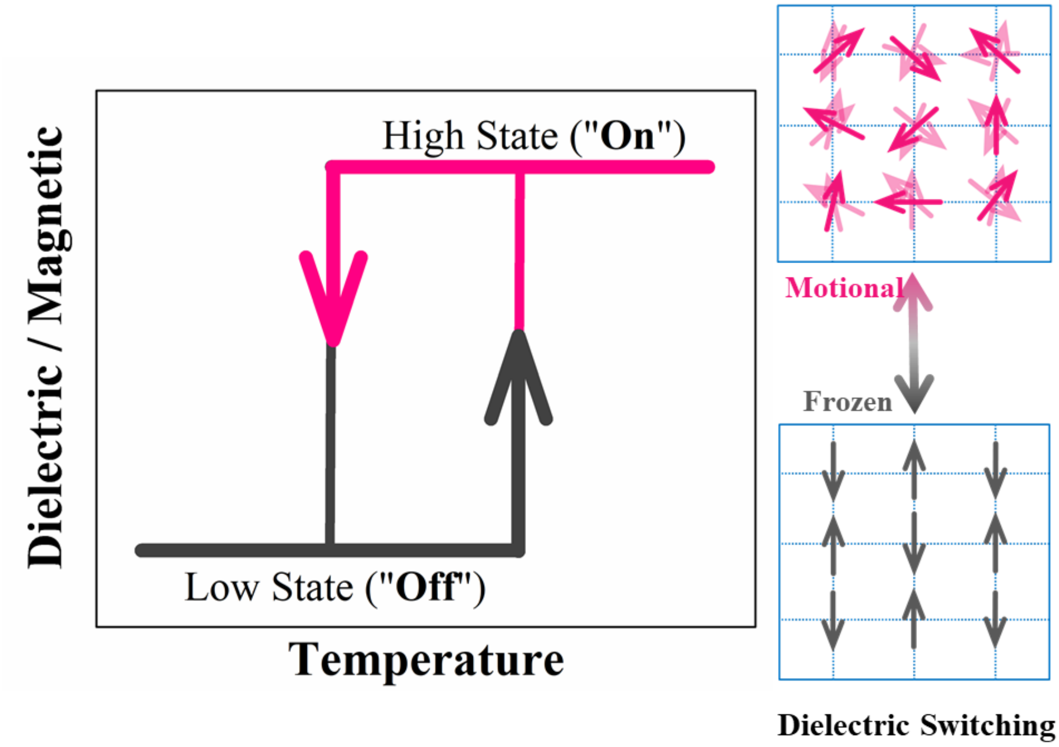

Scheme 4.1. Left Schematic illustration of temperature driven switchable dielectric and magnetic properties. **Right** the dynamic nature of electrical dipoles across dielectric switching has been illustrated.

The metal organic frameworks (MOFs) and the inclusion compounds are well-known materials which exhibit switching physical properties owing to their structural diversities, presence of various supramolecular interactions and a tendency of undergoing a phase transition.[13,22,25,26] To mention, a dielectric switching has been observed near 240 K in compound $(HPy)_2[Na(H_2O)Co(CN)_6]$ influenced by structural phase transition.[13] Also, the azido-bridged perovskite-type compounds $[(CH_3)_nNH_{4-n}][Mn(N_3)_3]$ ($n = 1-4$) is observed to exhibit both dielectric and magnetic switching behavior at SPT, as reported by Wang *et al.*[23] To mention further, Zhang *et al.* have reported a series of metal-cyanide-based perovskite-type metal−organic framework materials, which exhibit distinct dielectric switching triggered by guest molecules.[13,27] Very recently, the inclusion compound $(C_2H_6N_5)^+(H_2PO_4)^-$ has been reported which features 40 K wide thermal hysteresis across dielectric switching near room temperature triggered by the rotation in cation and modulation in crystal packing.[28] In this context, the organic-inorganic halides (OIHs) can be considered as promising candidates. OIHs are a class of materials which are well-known to exhibit diverse crystal structures attained by efficient combination various metal halide architectures and dynamic ammonium cations in numerous fashion in crystal packing.[4,29] Along with such diversity, OIHs often undergo thermally induced SPTs at different temperatures and efficiently combine one or more component dependent physical properties in a single phase.[1,30–34] To focus further, the OIHs with low dimensional crystal structure offer sufficient space for the dynamic nature of the light ammonium ions to flourish. As a result, low dimensional OIHs with appropriate components can form unique and technologically important class of materials that can integrate multiple switchable properties across SPT. To refer, zero dimensional compound $C_6H_{14}NFeBr_4$ has been reported to combine both dielectric and magnetic anomalies at structural phase transition.[12] Another OIH, the one-dimensional red photoluminescent hybrid (2-methylimidazolium)$MnCl_3(H_2O)$ material has been reported to exhibit both dielectric and optical switching properties across order-disorder SPT.[8] Ren-Gen Xiong *et al.* have recently reported that molecular hybrid compounds $(Me_3NCH_2Br)MnBr_3$ and $(Me_3NCH_2Cl)MnCl_3$ exhibit dielectric switching coupled with structural phase transitions at high temperature.[35,36]

The switching properties in a material are qualitatively characterized based on two parameters viz. the transition temperature (T_c) and thermal hysteresis (ΔT). The effective size of the rotating component(s) and the crystalline packing largely affect the transition temperature while the thermal hysteresis is primarily affected by the cooperative nature of the different microscopic interactions across the transition process.[28,37] In reality, the design and synthesis of a switchable molecular OIH that assemble static and dynamic components in single crystalline phase and also give rise to high T_c and sizeable ΔT values are fairly challenging. This is because the insufficient understanding on the complicated mechanism of changes in dynamic components and their interactions across T_c fails to delineate the microscopic process across SPT. As a result, the number of reports on thermally switchable OIHs where the control of ΔT and T_c has been achieved via modulation of supramolecular interactions among the components are almost zero. We believe that increasing number of supramolecular interactions, or strengthening these can fundamentally stabilize the structure to greater extent and increase the ΔT of SPT by effectively obstructing the SPT process.

Here in this chapter, we present synthesis and studies of the physical properties of a novel zero-dimensional halide hybrid $(CH_6N_3)_2MnCl_4$ (hereafter referred as **2**). The crystal structure of compound **2** uniquely exhibits face-shared $(Mn_3Cl_{12})^{6-}$ trimers and guanidinium cations featuring extensive supramolecular interactions among themselves (H-bonding and ion-pair interactions). DSC studies revealed reversible phase transition anomalies at 166/195 K (cooling/heating) fashioned by exceptional ~30 K wide hysteresis. Systematic SC-XRD analyses confirm that the phase transition is associated with structural inter-conversion between $P2_1/c$ (HTP) to $P2_12_12_1$ (LTP). Notably, the SPT has been observed to be coupled with switchable dielectric and magnetic anomalies portraying beautiful hysteresis loop-like feature. Presence of octahedral Mn^{2+} in crystal field gives rise to bright-red photoluminescence at room temperature with long lifetime and sizable quantum yield.

4.2 Experimental Section:

4.2.1 Chemicals:

Guanidinium hydrochloride (CH_6N_3Cl) and manganese chloride tetrahydrate ($MnCl_2.4H_2O$) have been acquired from Alfa Aesar. Ethanol (C_2H_5OH) was bought from SDFCL. All chemicals were of analytical grade and were used without further purification.

4.2.2 Synthesis:

In 100 mL of deionized water, 0.4359 g (2.202 mmol) of $MnCl_2.4H_2O$ was added and was dissolved thoroughly. Under constant stirring, 0.4207 g (4.404 mmol) of CH_6N_3Cl was added into the solution and stirring was continued till complete dissolution. The whole solution was kept at room temperature inside crystallization beaker for slow evaporation of the solvent. Rod shaped semi-transparent pale pink single crystals were obtained after about two weeks. As-grown crystals were washed with hexane and taken for further studies. The formation process can be represented using simple addition reaction:

$$2\ CH_6N_3Cl + MnCl_2 = (CH_6N_3)_2MnCl_4$$

4.2.3 Characterization:

The elemental percentage analyses were conducted using the Thermo Scientific Flash 2000 CHN analyzer. The thermogravimetric analysis (TGA) experiment was recorded in the Mettler Toledo TGA 850 under nitrogen atmosphere in the temperature range of 298 K – 1073 K with heating rate of 5 K min^{-1}. Modulated DSC data was collected in the TA Q2000 instrument in the temperature range of 93 K – 463 K under nitrogen atmosphere. Heating and cooling rate was kept at 2 K min^{-1} for this. The single crystals were pre-dried under vacuum for 12 hours for these experiments.

As the crystals were hygroscopic, a suitable crystal piece was cut and mounted inside Lindemann capillary which was filled with oil to avoid air contact. The capillary was then mounted on top of the goniometer head in order to record single crystal diffraction data. X-ray diffraction data were collected at different temperatures on an Oxford Xcalibur (Mova) diffractometer equipped with an EOS CCD detector using Mo K_α radiation ($\lambda = 0.7107$ Å). For data collection at low temperature, Oxford Cobra open stream nonliquid nitrogen cooling device was used. Further, lattice parameter refinement, data integration were executed using the program CrysalisPro.[38] The structure solution was obtained using SHELXS.[39,40,41]

Temperature dependent heat capacity (HC) was recorded in the temperature range of 130 K – 220 K using Quantum Design PPMS. For this experiment, firstly the HC of addenda (which includes Apeizon grease and sample platform and define the thermodynamic surrounding) was recorded, following which a suitable crystal was mounted on the same grease and heat capacity of the whole setup (system + surrounding) was recorded. HC was measured via relaxation technique where HC of addenda was auto subtracted to derive the HC of the compound.

Structural transition feature was visualized via studying temperature and frequency dependence of dielectric constant. Electrical contacts were put on both end surfaces of rod-shaped single crystal (along crystallographic *b*-direction) using silver paste. Sample was inserted inside Quantum Design PPMS chamber. Capacitance and dielectric loss were measured using Agilent (E4980A) Precision LCR meter in the temperature range of 150 K – 220 K with 2 K min^{-1} heating/cooling rate in the frequency range of 5 kHz – 300 kHz under applied peak voltage of 0.5 V.

The dc magnetic susceptibility and magnetization measurements on single crystals were carried out using Quantum Design SQUID-based MPMSXL-3-type magnetometer. Zero field cooled and field cooled data were recorded in the temperature range of 1.8 K – 350 K with applied magnetic field of 100 Oe and 1000 Oe. Isothermal magnetization have been measured at 1.8 K and at 300 K with field sweep range of ±7 T.

Diffused reflectance spectral data were recorded using the Perkin-Elmer Lambda 750 spectrometer. For this, the reflectance spectra of $BaSO_4$ disc and the compound were recorded consecutively. Then the background correction was done by subtracting the $BaSO_4$ data from the compound spectra. Further, the background corrected data was converted into absorbance equivalent by using Kubelka-Munk function.

4.3 Results and Discussion:

4.3.1 Crystal Structure:

The chemical composition and purity of the as-grown crystals of compound **2** were confirmed by elemental analysis which yielded the following mass percentage outputs:

Table 4.1 Elemental Purity Analysis

Elements	Experimental Mass (%)	Calculated Mass (%)
H	3.76	3.81
C	7.54	7.57
N	26.55	26.51

The single crystal structure determination reveal that the compound **2** at 295 K has centrosymmetric monoclinic structure with space group $P2_1/c$ featuring lattice parameters a = 8.6611 (4) Å, b = 27.0793 (14) Å, c = 15.6284 (7) Å, β = 93.237 (4)° and Z=12 (refinement parameters and atomic coordinates are included in **Table 4.2**, **Table 4.8**, **Table 4.9**).

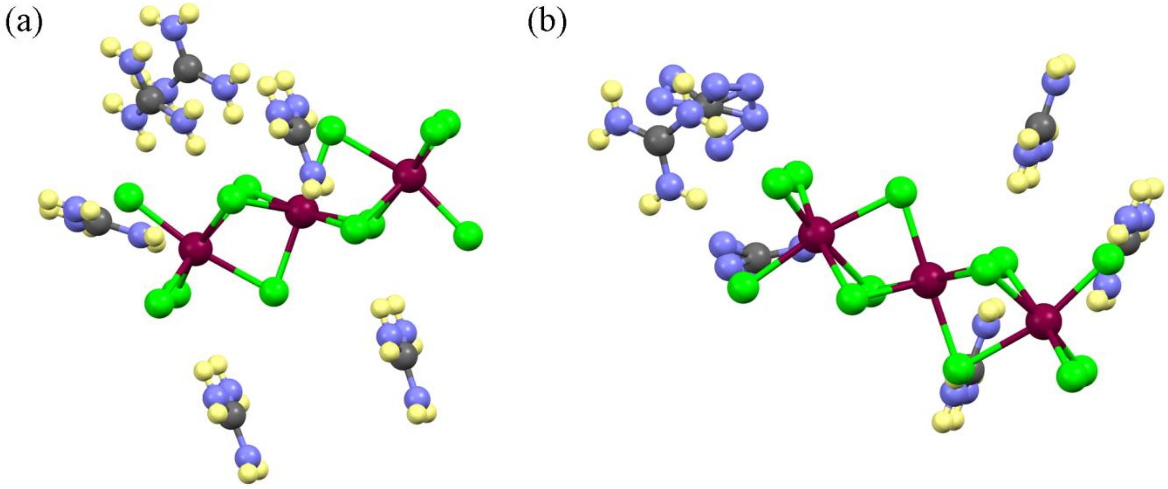

Figure 4.1 Molecular Structures of compound **2**: (a) Asymmetric unit at 150 K, All the guanidinium ions are seen to be in thermally ordered state, (b) Asymmetric unit at 295 K, two guanidinium cations are in thermally disordered state and four are in ordered state.

The asymmetric unit at 295 K contains three formula units of $(CH_6N_3)_2MnCl_4$ where all atoms occupy general crystallographic positions (Wyckoff: 4*e*) (**Figure 4.1** (b)). Interestingly, each of three crystallographically independent Mn atoms in asymmetric unit are seen to be coordinated with six Cl atoms in octahedral geometry. Further, these three $MnCl_6$ units are seen to share faces with each other forming a trimeric $(Mn_3Cl_{12})^{6-}$ unit (Mn-Mn distances 3.3168(12) and 3.3380(12) Å) as can be seen in **Figure 4.2** (b). Such trimeric unit is unprecedented in OIH crystals and can be considered as an intermediate between well-known infinite one dimensional chain of $MnCl_6$ octahedra and single $MnCl_6$ unit. The $MnCl_6$ octahedra are seen to be distorted with Mn-Cl bond distances and Cl-Mn-Cl angles in the range of 2.4605 (16)-2.6990 (16) Å and 165.27 (5)-179.74 (6)° respectively (see **Table 4.3**). Notably, the two end $MnCl_6$ members in each $(Mn_3Cl_{12})^{6-}$ unit are more distorted as compared to the central $MnCl_6$ octahedron. The distortions can be qualitatively viewed by analyzing Cl-Mn-Cl angles of each $MnCl_6$ octahedron. The two end $MnCl_6$ octahedra are seen to have Cl-Mn-Cl angles 165.27 (5)°, 168.21 (7)°, 172.84 (7)° and 170.34 (6)°, 170.81 (5)°, 170.86 (7)° however the angles for the central octahedral unit are 177.90 (6)°, 178.29 (6)°, 179.74 (6)°. Similarly, the Mn-Cl bond distances for the two end octahedra are more varied (2.4605 (16)-2.6725 (15) Å and 2.4614 (17)-2.6990 (16) Å) compared to the central one (2.5059 (13)-2.5663 (16) Å) (**Figure 4.2** (b)). Further the inter-octahedral angles Mn-Cl-Mn which indicate the octahedral rotation are in the range 78.11 (4)-80.79 (4)°. Importantly, two out of six crystallographically independent GCs are significantly disordered at room temperature

(**Figure 4.1** (b)). Among the six GCs, two, namely **C5** and **C6** GCs occupy relatively larger spaces and are thermally disordered, with **C6** having all three and the **C5** having two nitrogen atoms in doubly disordered states. Each trimer participates in seven hydrogen bonds (Cl---N distances 3.219-3.297 Å) with seven nearby GCs, four of which are from different molecular units (**Figure 4.3** (a)). Additional H-bond interactions can be seen between **C5** and **C6** GCs along *c*-direction. Here it is worth mentioning that the planar GCs are exclusively known to form H-bonds restricted within their molecular planes.[42,43]

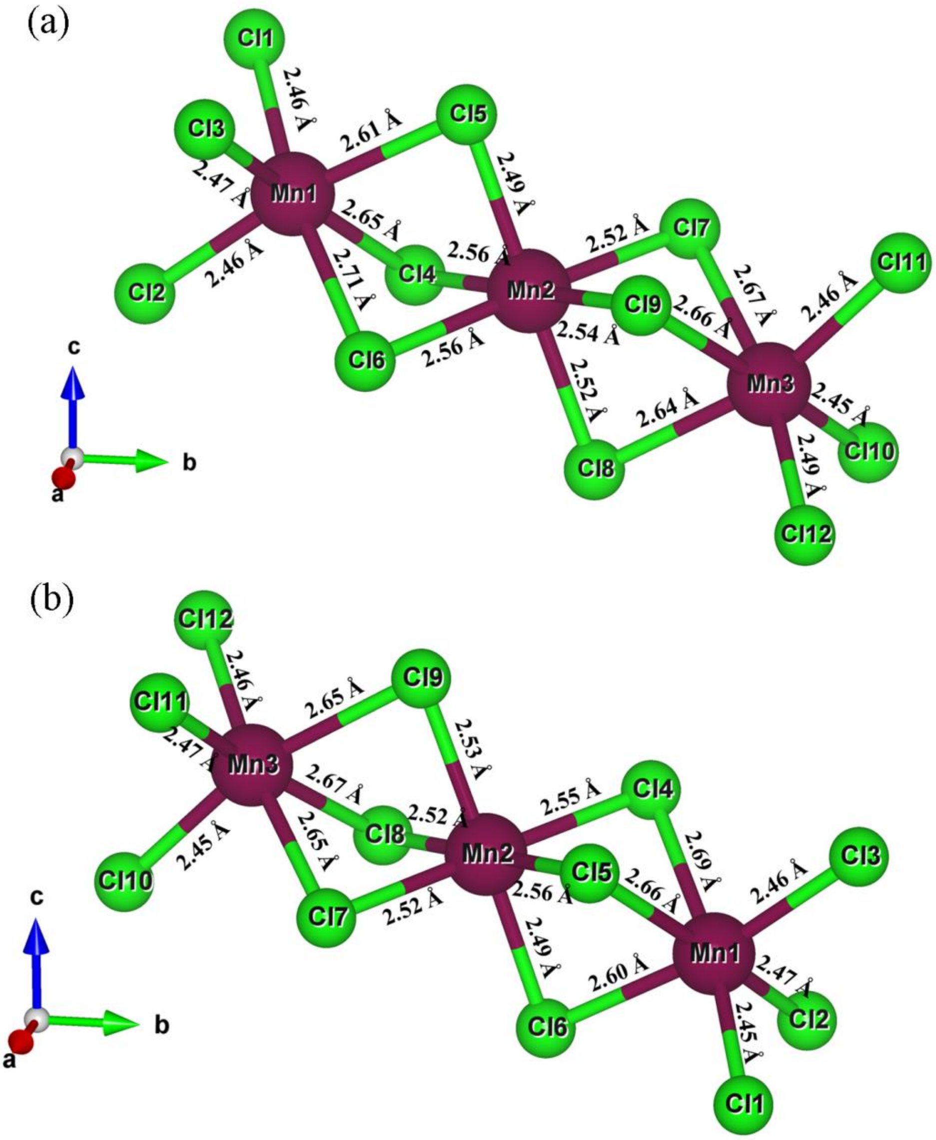

Figure 4.2 The trimeric $(Mn_3Cl_{12})^{6-}$ units at (a) 295 K and at (b) 150 K, the Mn-Cl bond distances have been included.

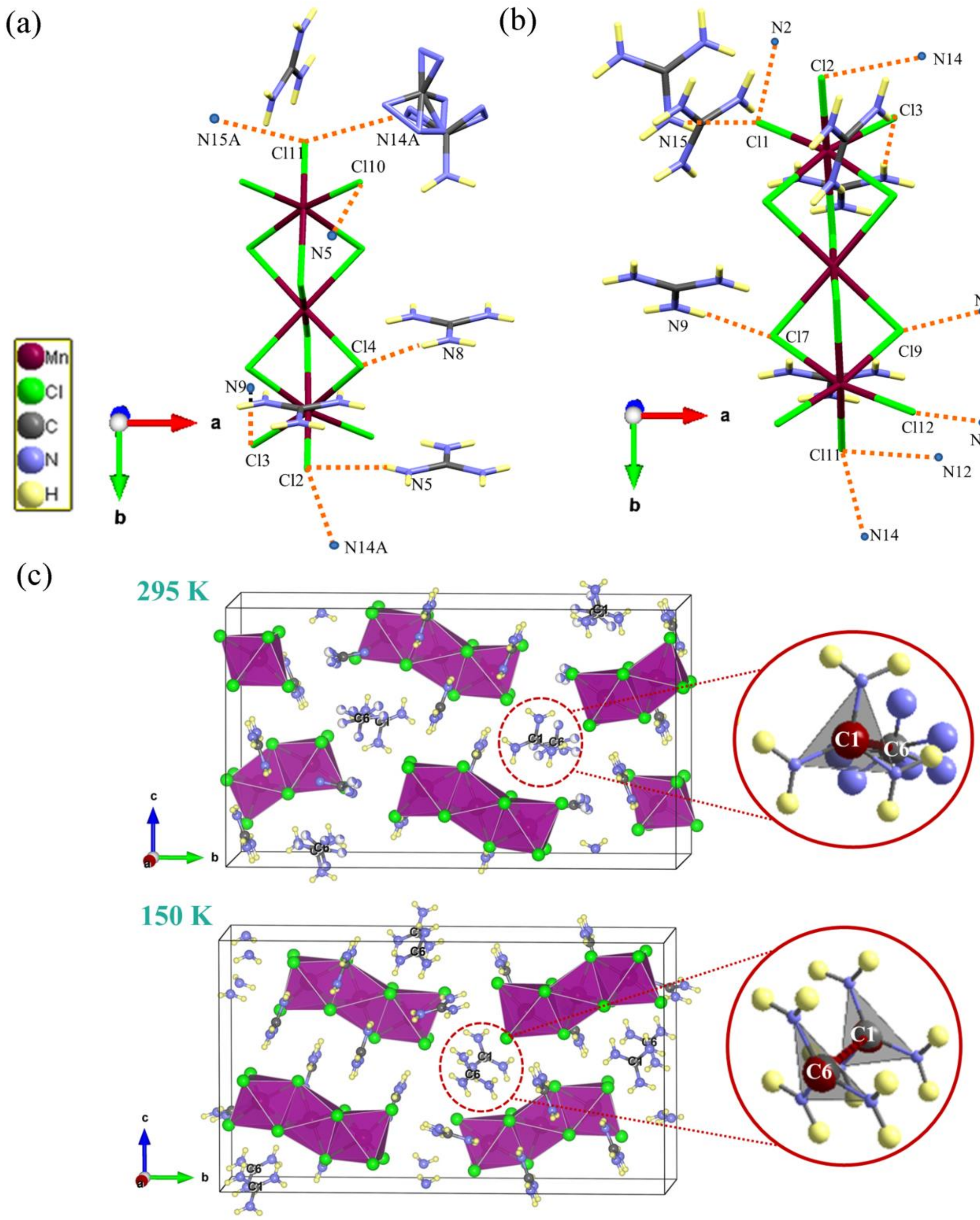

Figure 4.3 Views of various supramolecular interactions present among different components in crystal. Molecular units at (a) 295 K and (b) 150 K showing hydrogen bonding interactions present between each $(Mn_3Cl_{12})^{6-}$ units and GCs. (c) Unit cell diagrams of 1 at 295 K and 150 K. Zoomed fractions showing modulation of one of many ion-pair interactions among GCs across SPT.

To see the effect of temperature on disorder of GCs, we gradually cooled the material to 150 K recorded single crystal X-Ray data at this temperature (change in crystal volume has been recorded during gradual cooling and incorporated in **Figure 4.4**, volumetric expansion coefficients have been calculated and included). We observed that the crystal symmetry changes into noncentrosymmetric yet nonpolar orthorhombic crystal system with a space group $P2_12_12_1$ having a = 8.6227(5) Å, b = 27.0625(12) Å, c = 15.4503(7) Å and Z = 12 lattice parameters. Although the lattice parameters do not change substantially as compared to 295 K structure, completely ordered GCs are observed at this temperature (**Figure 4.1** (a)). In asymmetric unit, each of three formula units of $(CH_6N_3)_2MnCl_4$ occupy general crystallographic position (Wyckoff: 4*a*). In the $(Mn_3Cl_{12})^{6-}$ unit, more distortions in $MnCl_6$ octahedra compared to room temperature structure is observed. The Cl-Mn-Cl angles for $MnCl_6$ octahedra are in the range of 168.99(13)-171.27(13)°, 177.28(14)-179.64(14)° and 164.27(12)-172.24(13)° while the Mn-Cl bond distances are in the range of 2.464(3)-2.711(4) Å, 2.494(4)-2.567(4) Å and 2.452(4)-2.674(4) Å (**Figure 4.2** (a) and **Table 4.3**). Similarly, the inter-octahedral angles are in the range 77.85(11)-80.88(9)° and 80.07(10)-80.50(9)°. At 150 K, nine H-bonding interactions has been observed between each $(Mn_3Cl_{12})^{6-}$ unit and GCs (**Figure 4.3** (b)).

Considering the non-spherical charge distribution around each planar GC (D_{3h} symmetry in planar form), one can expect substantial quadrupole moment. Such moment, along with the van der Waals interactions and cavitation effects often influence supramolecular ion-pair interactions between the adjacent GCs having "eclipsed" or "head-on" orientations among themselves, as have been theoretically and experimentally well-observed in aqueous solution of guanidinium cations and in biomolecules.[42–44] Interestingly, we have observed that the C-C distances between nearest and next nearest neighbor GCs in both phases of **2** are withing the cut-off distance for facile ion-pair interaction (3.948-5.475 (8) Å at 295 K and 3.947 (19) - 5.452 (12) Å at 150 K, for eclipsed arrangements). Thus, considerable ion-pair interactions among thermally ordered GCs are expected to be present, further stabilizing the structure in both phases of **2** (**Figure 4.3** (c)). Such extensive supramolecular interactions among the GCs along different directions possibly obstruct linear extension of Mn-Cl architecture thereby resulting in overall zero dimensional structure.

Table 4.2 Crystal Structures Refinement Details:

Parameters	**HTP**	**LTP**
Empirical formula	$C_2H_{12}Cl_4MnN_6$	$C_2H_{12}Cl_4MnN_6$
Formula weight (g/mol)	316.92	316.92
Temperature (K)	295	150
Wavelength (Å)	0.71073	0.71073
Crystal system	Monoclinic	Orthorhombic
Space group	$P2_1/c$	$P2_12_12_1$
Unit cell dimensions (Å)	a = 8.6611 (4), α = 90.00° b=27.0793 (14), β = 93.237 (4)° c = 15.6284 (7), γ = 90.00°	a = 8.6227 (5), α = 90.00° b = 27.0625 (12), β = 90.00° c = 15.4303 (7), γ = 90.00°
Volume (Å^3)	3659.6 (3)	3600.7 (3)
Z	12	12
Calculated density (g/cm^3)	1.726	1.754
Absorption coefficient (mm^{-1})	1.928	1.960
F (000)	1908	1908
Crystal dimension (mm^3)	0.17 x 0.15 x 0.32	0.17 x 0.15 x 0.32
Reflections collected	14809	9405
Independent reflections	7417 (R_{int} = 0.0687)	4129 (R_{int} = 0.0830)
Completeness to θ = 26.44°	99%	99.7%
Number of parameters	374	353
Goodness-of-fit	1.029	1.029
Final R indices [I > 2σ(I)]	R_{obs} = 0.0597, wR_{obs} = 0.1207	R_{obs} = 0.0664, wR_{obs} = 0.1466
R indices (all data)	R_{all} = 0.0965, wR_{all} = 0.1454	R_{all} = 0.0851, wR_{all} = 0.1618

Table 4.3 Mn-Cl Bond distances at both phases

295 K		150 K	
Bond Label	**Bond distance (Å)**	**Bond Label**	**Bond distance (Å)**
Mn1-Cl1	2.4689(16)	Mn1-Cl1	2.4633(3)
Mn1-Cl2	2.4598(18)	Mn1-Cl2	2.4643(3)
Mn1-Cl3	2.4730(17)	Mn1-Cl3	2.4713(3)
Mn1-Cl4	2.6654(15)	Mn1-Cl4	2.6563(3)
Mn1-Cl5	2.6962(15)	Mn1-Cl5	2.6113(3)
Mn1-Cl6	2.6079(15)	Mn1-Cl6	2.7143(3)
Mn2-Cl4	2.5659(16)	Mn2-Cl4	2.5653(3)
Mn2-Cl5	2.5617(15)	Mn2-Cl5	2.4953(3)
Mn2-Cl6	2.5021(13)	Mn2-Cl6	2.5623(3)
Mn2-Cl7	2.5286(15)	Mn2-Cl7	2.5183(3)
Mn2-Cl8	2.5253(15)	Mn2-Cl8	2.5243(3)
Mn2-Cl9	2.5375(13)	Mn2-Cl9	2.5373(3)
Mn3-Cl7	2.6717(15)	Mn3-Cl7	2.6733(3)
Mn3-Cl8	2.6523(15)	Mn3-Cl8	2.6463(3)
Mn3-Cl9	2.6568(15)	Mn3-Cl9	2.6583(3)
Mn3-Cl10	2.4750(17)	Mn3-Cl10	2.4503(3)
Mn3-Cl11	2.4647(17)	Mn3-Cl11	2.4593(3)
Mn3-Cl12	2.4560(15)	Mn3-Cl12	2.4963(3)

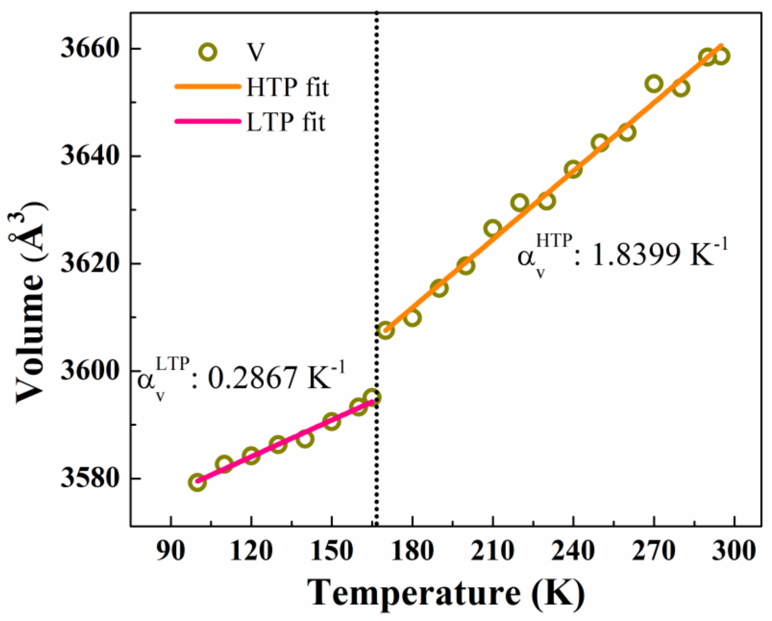

Figure 4.4 Volumetric expansion coefficients calculated at both side of T_c from SCXRD.

4.3.2 Thermal Stability and Structural Phase Transition:

The thermal stability of compound **2** has been studied via thermogravimetric analysis (TGA) technique. TGA data recorded under N_2 atmosphere indicates that the compound starts decomposing above 520 K (**Figure 4.5**).

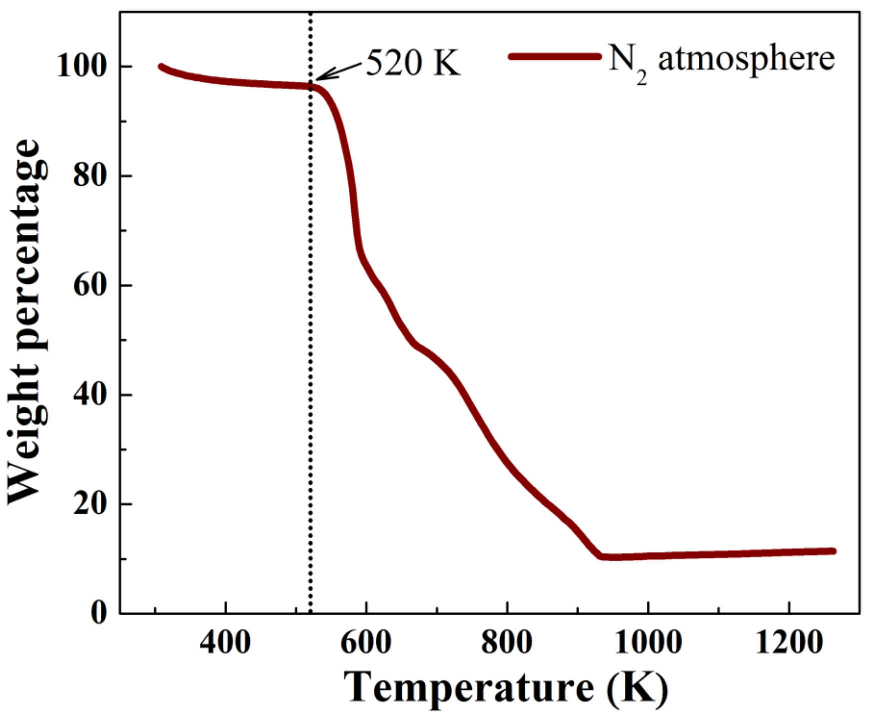

Figure 4.5 Thermogravimetric analysis graph showing compound decomposition

DSC and specific heat measurements are highly reliable methods to detect a structural phase transition and study thermodynamic properties associated with it. In view of the transformation from one space group symmetry to another across temperature, we have carried out DSC and heat capacity measurements. In DSC experiment, reversible exothermic/endothermic anomalies at 166K/195K (cooling/heating) were observed which is indicative of structural transition (**Figure 4.6** (a)). Sharp nature of anomalies and also very large thermal hysteresis of 30 K indicate that the transition is a 1st order type. The corresponding enthalpy changes for cooling and heating have been calculated from background subtracted DSC data which are 11.09 and 17.57 J mol^{-1} respectively (**Figure 4.6** (c)). The difference along with the comparatively broader nature of cooling anomaly indicates that the ordering and orientational changes during cooling are comparatively sluggish. We have also recorded the specific heat data during warming the materials and observed a sharp anomaly at 195 K (**Figure 4.6** (b)). For a pure order-disorder type of transition, the entropy change (ΔS) can be calculated using the Boltzmann equation:

$$\Delta S = R \ln N$$

where R is gas constant and N is ratio of distinguishable configurations.

We have calculated the entropy change from background subtracted specific heat anomaly which is 0.34 J mol^{-1} K^{-1}(**Figure 4.6** (d)). On plugging this value into above equation we obtained N as 1.04 which indicates that the transition is order-disorder type (see **Table 4.4**). Again, from DSC enthalpies we have calculated corresponding entropies which are 0.089 and 0.069 J mol^{-1} K^{-1} for heating and cooling respectively (**Figure 4.6** (c), **Table 4.4**). These discrepancies indicate that the transition is complicated, beyond a simple order-disorder transition model. The crystal symmetry analysis indicates absence of any group-subgroup relation among the two crystal phases ($P2_1/c$ and $P2_12_12_1$) which suggests that the transition must be a complicated process in which both reorientation and ordering of different components take place concurrently.

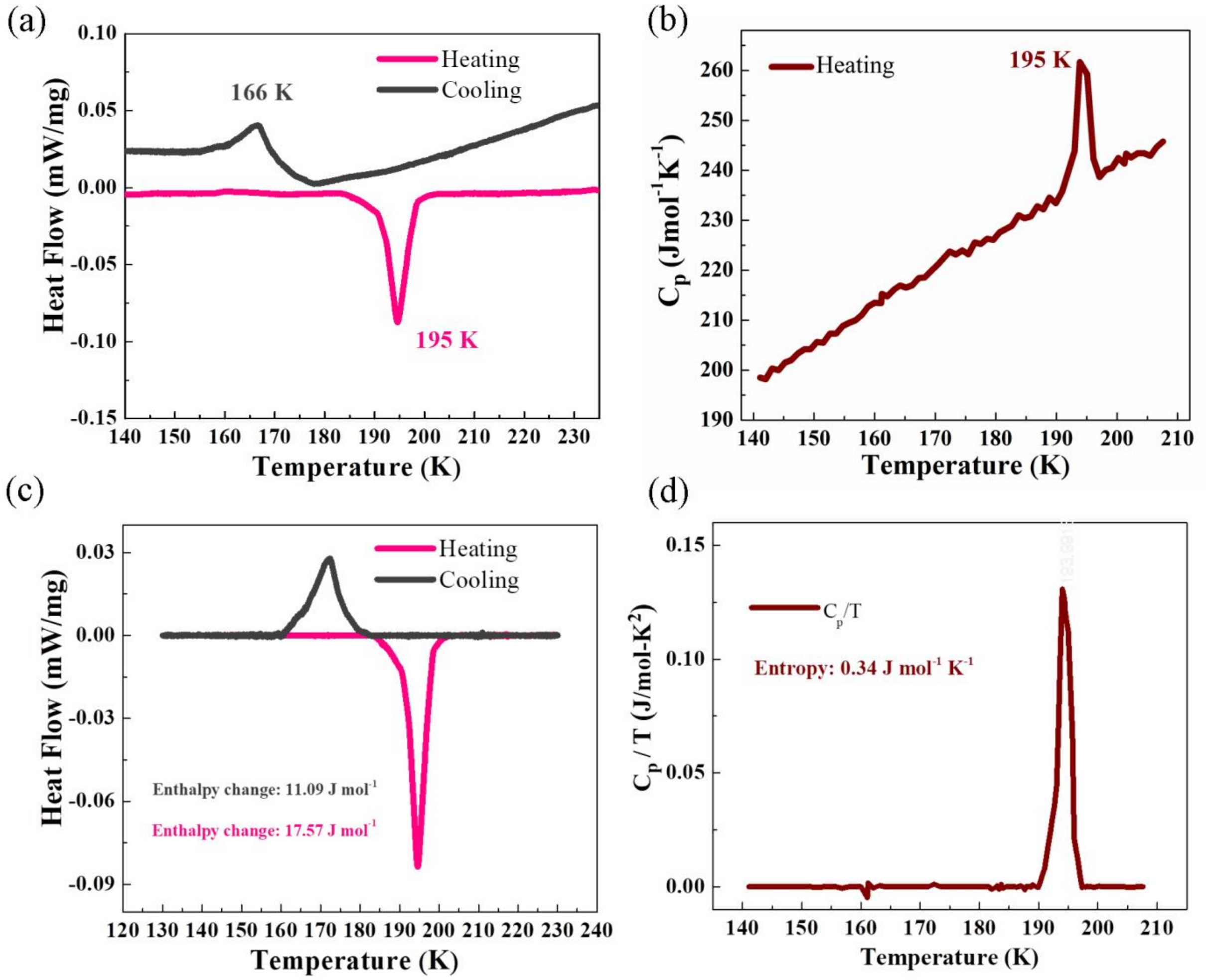

Figure 4.6 Structural transition features: (a) Reversible DSC anomalies, (b) Heat capacity data obtained during heating procedure, (c) Background subtracted DSC anomalies, (d) Background subtracted Heat capacity anomalies for enthalpy and entropy calculations.

Table 4.4 Thermodynamic parameters associated with structural phase transition. Bold numerical values have been directly calculated from the respective experimental data.

Experiment	Enthalpy (J mol^{-1})	Entropy ΔS (J mol^{-1} K^{-1})	N from R*ln*N
DSC (Heating)	**17.57**	0.089	1.01
DSC (Cooling)	**11**	0.066	1.00
Specific Heat	66.3	**0.34**	1.04

Table 4.5 Molecular materials with number of supramolecular interactions, thermal hysteresis, transition temperature and crystal structural dimensionality.

Material	Supramolecular Interactions in Asymmetric Unit	Thermal Hysteresis	Tc Cooling/Heating	Dimension
$(C_7H_{16}N)_2CdCl_4$	3 H-Bonds	7 K	335 K/342 K	2 D [45]
$C_5H_6NCdCl_3$	1 H-Bond	8 K	150 K/158 K	1 D [46]
$[C_2H_6N_5]^+[H_2PO_4]^-$	14 H-Bonds (293 K)	40 K	233 K/293 K	3 D [28]
$(C_6H_5NH_3)_2CdCl_4$	Multiple H-Bonds	25 K	344 K/369 K	3 D [47]
$C_4H_7N_2MnCl_3(H_2O)$	9 H-Bonds (293 K)	16.2 K	223.2 K/239.4 K	1 D [8]
$(CH_6N_3)_2MnCl_4$	**16 H-bonds (150 K), 13 H-bonds (293 K) + Ion-Pair interactions**	**30 K**	**166 K/195 K**	**0 D (This Work)**

The most striking feature of the SPT of $(CH_6N_3)_2MnCl_4$ is clearly the large thermal hysteresis of 30 K. We believe that the presence of extensive supramolecular interactions in the crystal plays governing role in it. To elaborate, let us consider a molecular material in which multiple numbers of supramolecular interactions are present among different molecular components. The process of structural phase transition in such a material will always be associated with breaking and formation of such interactions, sometimes coupled with additional order-disorder behaviour of component (s). In principle, breaking of any interaction requires energy and thus, the more the number of interactions breaking means that more energy will be required across transition which can hinder the process. Effectively, during transition, many numbers of supramolecular bonds get broken and formed simultaneously and this degree of cooperativity plays tremendous role, influencing the thermal hysteresis as well as the transition temperature. **Table 4.5** portrays a comparative picture of thermal hysteresis, transition temperature across SPTs with supramolecular interactions and dimensionalities of a number of molecular hybrids. As can be seen, $(C_5H_6N)CdCl_3$ is a *1-D* compound that exhibits only 1 H-bond in its asymmetric unit at room temperature and shows only 8 K hysteresis across SPT at 150 K/ 158 K.[46] On the other hand, the inclusion compound $(C_2H_6N_5)^+(H_2PO_4)^-$ exhibits 14 H-Bonds at 293 K, features 40 K hysteresis across phase transition.[28] The *1-D* compound $C_4H_7N_2MnCl_3(H_2O)$ exhibits 9 H-bonds at 293 K and exhibits hysteresis of around 16 K across SPT.[8] In our compound $(CH_6N_3)_2MnCl_4$, we have observed multiple number of H-Bonds (16 H-bonds 150 K and 13 H-bonds at 293 K within single molecular unit) and also possible Ion-Pair interactions among GCs. We believe that these altogether hinder the transition process from one crystalline phase to another, thereby resulting large hysteresis.

4.3.3 Dielectric Properties:

Typically, the dielectric properties of a material undergo distinct change across structural phase transition due to modulation in dipolar orientation. We have recorded the temperature dependent response of complex dielectric permittivity during both cooling and heating in the temperature range of 220 − 120 K at different frequencies in between 5 – 300 kHz. Considering the rod shape of the single crystals, we have carried out the dielectric measurements along crystallographic *b*-axis (along the rod). Remarkably, reversible switching dielectric anomalies have been observed at SPT under 50 kHz frequency. The real part of dielectric constant, ε_r was seen to gradually decrease during cooling till it reached a value of 29.5 at 166 K (HDS). At 166 K, it follows a distinct step-like decrease to a value of 27 (LDS) (see **Figure 4.7** (a)) after which it decreases very slowly. During heating, the ε_r is seen to increase distinctly in a step-like fashion from 29.6 to 32.1 at 195 K. Thus the dielectric data recorded during heating and cooling together portrays a hysteresis loop like behavior and confirming the reversible nature (see **Figure 4.7** (a)). Such behavior indicates that the dielectric transition is the direct manifestation of the structural phase transition discussed above. The switching behavior is typical of a crystal having disordered rotator phase at HTP which orders into frozen state at LTP. From crystal structure analysis, thermally disordered and ordered phases of GCs has been observed at above and below SPT respectively. The GCs are also seen to reorient themselves across SPT. Additionally, subtle displacements in $(Mn_3Cl_{12})^{6-}$ trimers across transition are also seen. These altogether induce a net change in overall polarity and give rise to high and low dielectric states across SPT. Here it is worthy of a mention that the guanidinium cations in thermally ordered state (LDS) are planar molecules with D_{3h} symmetry which results in having almost zero dipole moment but with some quadrupole moment spurring from the nonspherical (Y-shaped) charge distribution.[48,49] The step-like switching is distinct but small in magnitude (difference between LDS and HDS is 2 only), as the change in overall polarity is very small. Almost no frequency dispersion of dielectric constant has been observed in dielectric data recorded with a frequency sweep between 5000 Hz – 3 MHz, which implies that the dipolar motion is fast across transition temperature (**Figure 4.7** (b)). With increase in frequency, ε_r gradually decreases as the loss in response increases proportionately with frequency. Overall, such distinct switchable transition along with such large hysteresis suggests that the supramolecular interactions can have large effect on thermal hysteresis across dielectric switching in molecular materials.

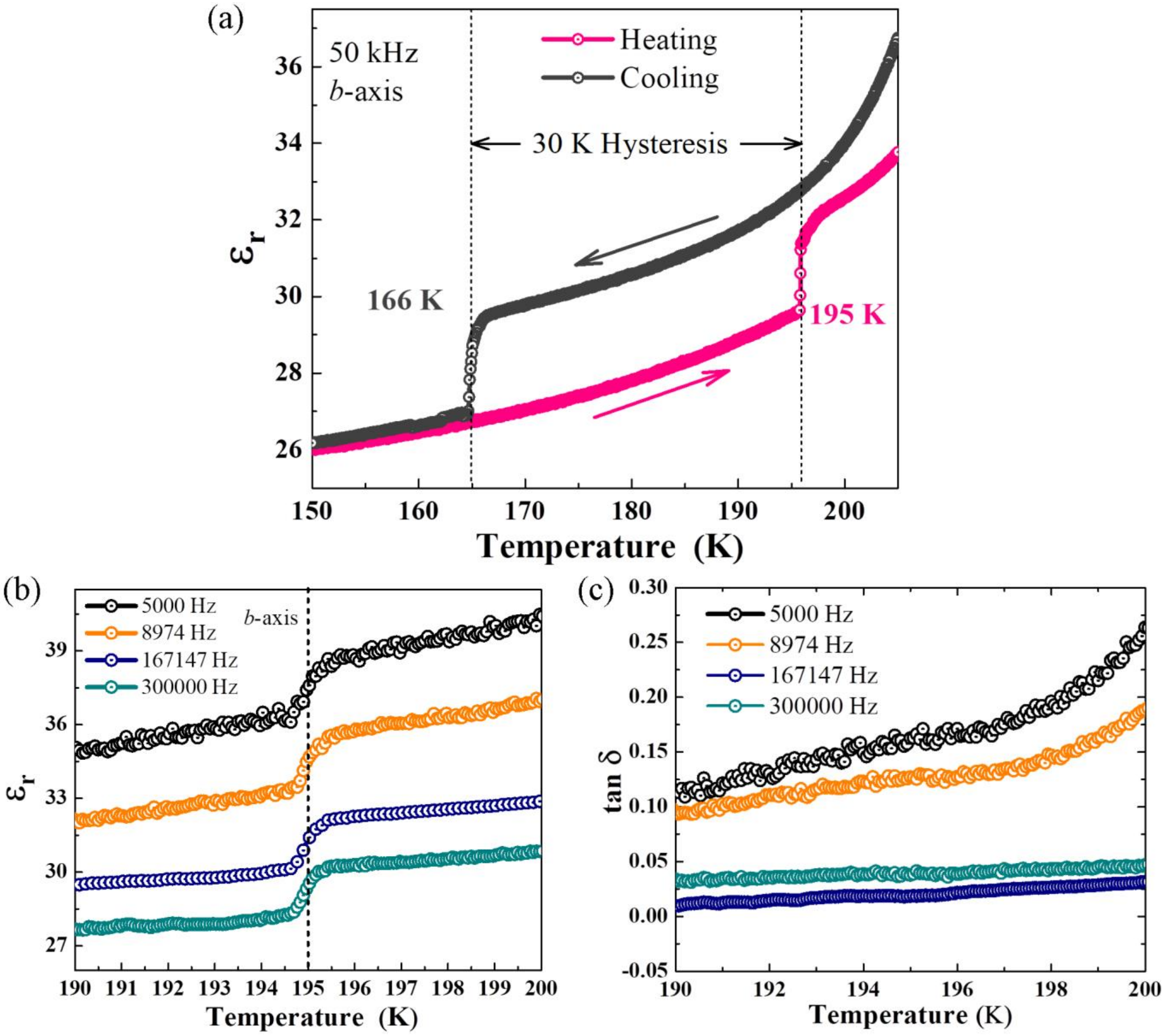

Figure 4.7 Thermally switchable dielectric properties (a) Temperature dependent reversible switching of real part of complex dielectric constant, (b) Dielectric constant under different frequencies showing intrinsic nature of the transition, (c) Dielectric loss vs temperature at different frequencies.

4.3.4 Magnetic Properties:

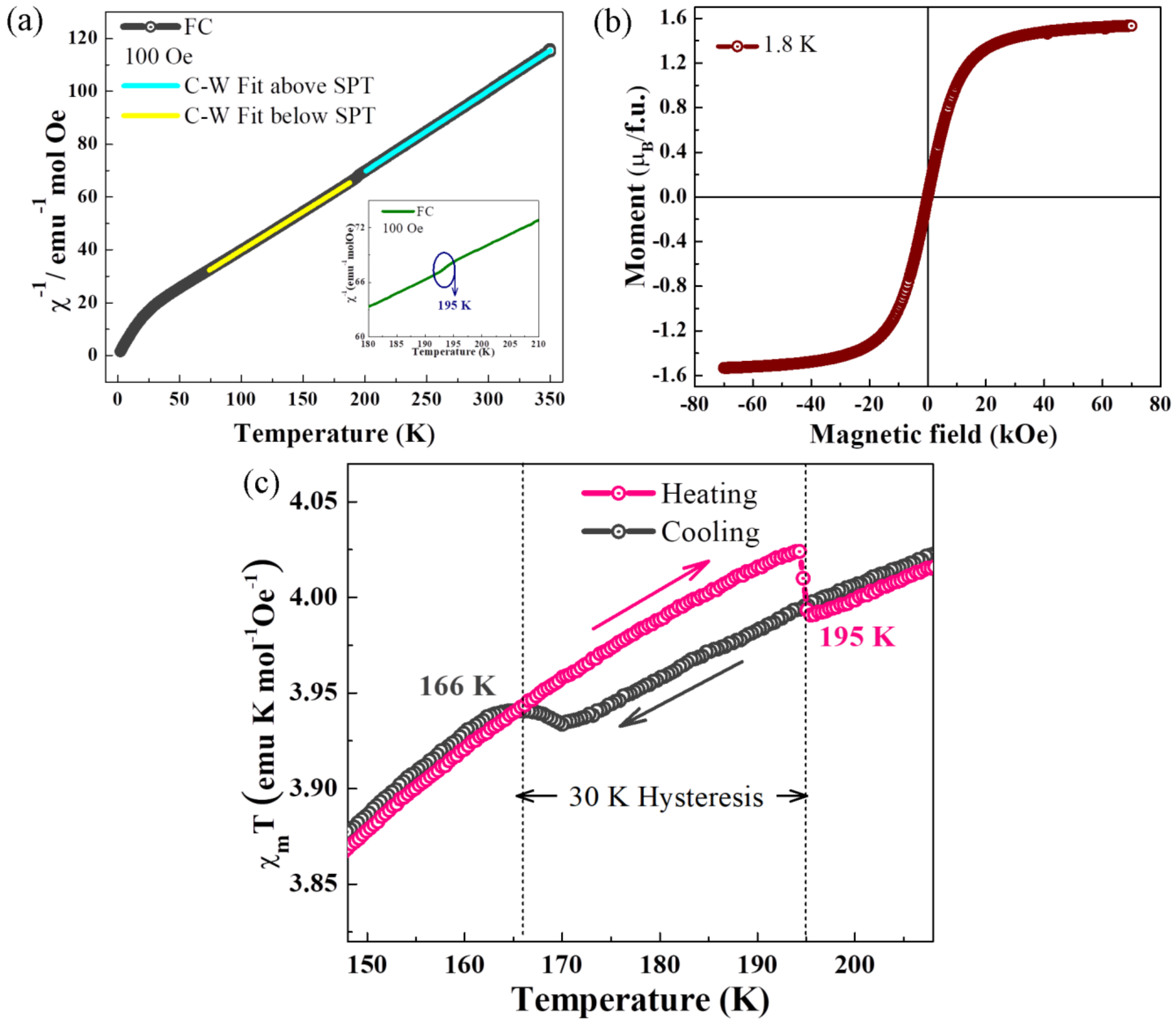

Figure 4.8 (a) Temperature dependent inverse magnetic susceptibility of **2** as recorded under 100 Oe dc field. (b) Moment vs dc Magnetic field measured at 1.8 K, (c) Reversible, weak magnetic switching at SPT observed when recorded during cooling and heating under 1000 Oe field.

Table 4.6 Curie-Weiss fitting parameters:

Region	*C* (emu mol^{-1} Oe^{-1})	θ (K)	R-square
High T Region	3.28	-28.4	0.99994
Low T Region	66.3	-37	0.99993

The presence of the trimeric $(Mn_3Cl_{12})^{6-}$ units in the crystal indicates that the magnetic properties of **2** can be interesting. We have recorded the temperature dependent dc magnetic susceptibility under 100 Oe applied field which shows typical paramagnetic behaviour (linear inverse susceptibility) with no magnetic transition observed down to 1.8 K (**Figure 4.8** (a)). The Curie-Weiss fit above phase transition region gave Curie constant C = 3.28 emu mol^{-1} Oe^{-1} with temperature intercept $\theta = -28.4$ K (see **Table 4.6**). The negative value of θ indicates presence of weak antiferromagnetic interactions between spins at manganese sites. Below SPT, the Curie constant increases while the temperature intercept (θ) decreases further to more negative value of -37 K (**Table 4.6**). This indicates that the antiferromagnetic interaction becomes stronger below the SPT. In inverse susceptibility vs temperature (χ^{-1} vs T) graph, it is observed that the χ^{-1} drops rapidly from ~25 K till 2 K as can be seen in **Figure 4.8** (a) which is possibly due to approach towards onset of long range magnetic ordering (ordering temperature below 1.8 K). Isothermal magnetization measurement at 1.8 K exhibits sigmoidal dependence of magnetization on magnetic field (**Figure 4.8** (b)) which supports presence of antiferromagnetic nature of interactions.

In χ^{-1} vs T behavior (measured during heating), a weak anomaly can be seen at 195 K (**Figure 4.8** (a) inset, marked with blue circle) which agrees nicely with DSC heating anomaly. This indicates that the anomaly can be associated with structural transition. To confirm the analogy, dc susceptibility vs temperature data was recorded during both heating and cooling under 100 Oe field. Remarkably, temperature dependent χ_mT exhibits switchable magnetic bistability with a thermal hysteresis of about 30 K (**Figure 4.8** (c)). On cooling, χ_mT is seen to gradually decrease till a value of 3.9356 $emu{\cdot}K{\cdot}mol^{-1}{\cdot}Oe^{-1}$ at 168 K below which it distinctly increases to 3.9382 $emu{\cdot}K{\cdot}mol^{-1}{\cdot}Oe^{-1}$ in step-like fashion. Similar step-like anomaly was seen to appear while heating at 194 K, where χ_mT decreased from 4.02 to 3.99 $emu{\cdot}K{\cdot}mol^{-1}{\cdot}Oe^{-1}$. Such excellent agreement of switching temperatures with phase transition anomalies indicates that the switching process is well coupled with the structural transition. Very small magnitude of switching and also the higher magnetic state being at lower temperature across switching rule out any possibility of spin state transition. From crystal structure analyses, we have observed minute changes in Mn-Mn distances and Cl-Mn-Cl angles within a $(Mn_3Cl_{12})^{6-}$ trimer across SPT. The relative distances among trimers also vary across SPT. Such structural changes across SPT weakly affect the magnetic coupling strength. As a result of this, subtle magnetic anomalies of reversible nature have been observed at SPT.

4.3.5 Optical Properties:

Manganese based hybrid halides are well-known to exhibit brilliant photoluminescence properties.[1,3,8,50] We have observed that the as-grown pale pink single crystals of compound **2** are semi-transparent under ambient light while under UV light these show bright reddish luminescence (**Figure 4.9**).

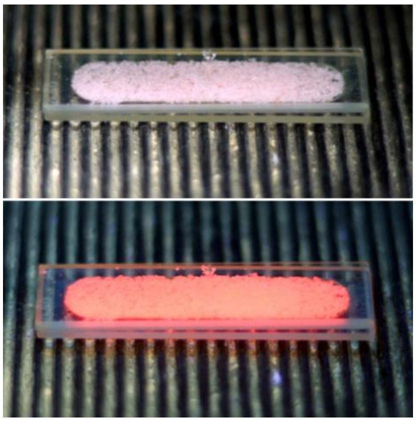

Figure 4.9 Crushed crystals of compound **2** under visible light (top) and UV light (bottom).

This indicates that the fascinating luminescence is originating from the bulk material, not from the surface defects. We have first recorded the room temperature UV-Vis absorbance spectra of crushed crystals under reflectance mode which show evolution of multiple absorption maxima at different wavelengths (**Figure 4.10** (a), blue). The multiple absorptions can be ascribed to electronic transitions between ground and different excited states of octahedral Mn^{2+} ion in ligand field.[50–53] Among these, prominent absorption of broad nature at 533 nm can be ascribed to the electronic transition between t_{2g} and e_g orbitals of octahedral Mn^{2+} ions.[3,51] The emission spectrum was then collected with keeping excitation wavelength at 450 nm. A strong maximum centred at 645 nm (*fwhm* = ~90 nm) is observed (**Figure 4.10** (a) pink) indicating bright luminescence. To find the contribution of absorption maxima to the luminescence, we have recorded the photoluminescence excitation (PLE) spectrum. The PLE spectra (**Figure 4.10** (a), wine) agrees reasonably well with multiple absorption maxima, which indicates that the observed emission has contributions from almost all the absorption maxima.[8] The emission wavelength is close to red phosphor Pr^{3+}-doped $CaTiO_3$ while the *fwhm* is much larger.[54] Interestingly, the photoluminescence is seen to be associated with a single decay process having a long lifetime of 1.71 ms (**Figure 4.10** (b)) combined with a quantum yield (QY) value of 39.5 %.

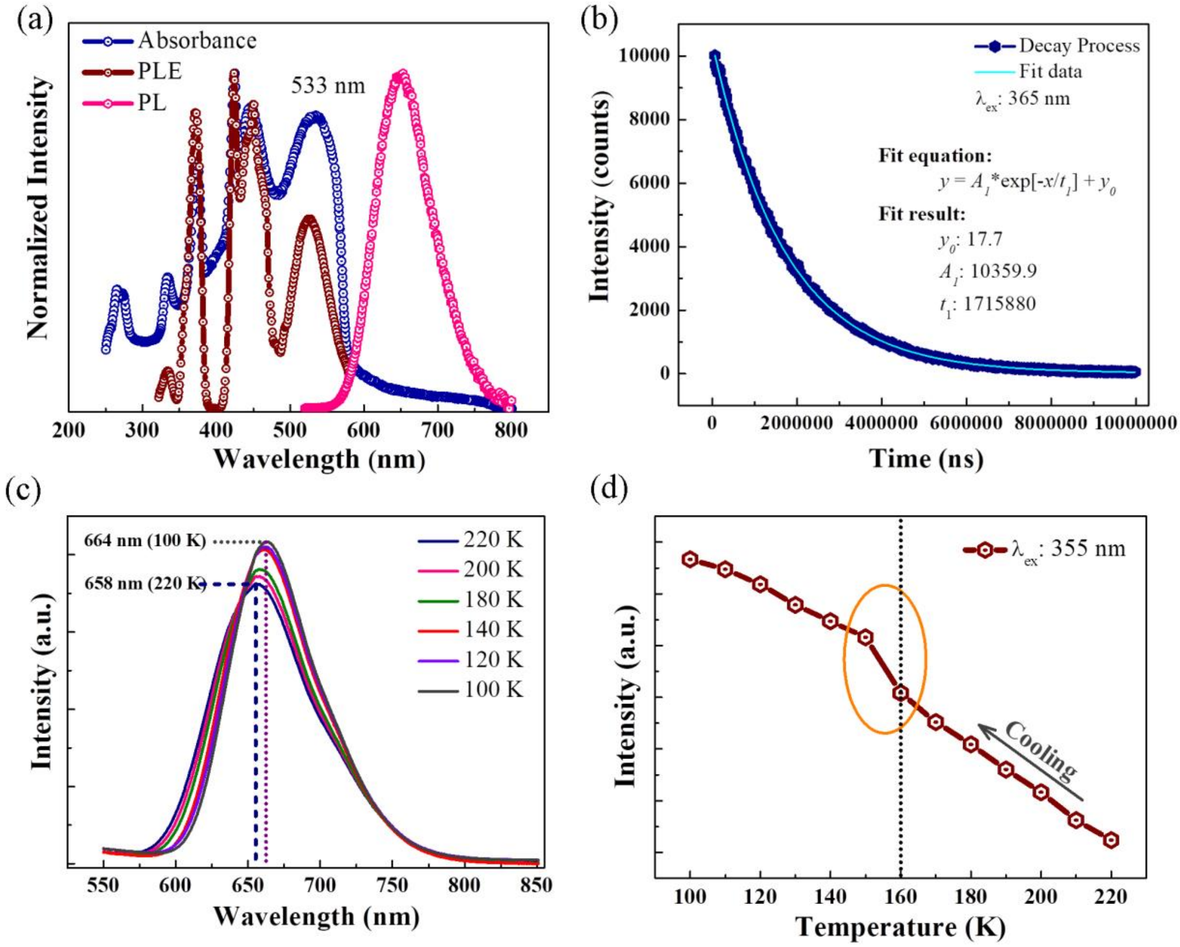

Figure 4.10 Photoluminescence properties of **2**: (a) UV-Vis absorbance (blue), PLE (wine) and PL (pink) spectra recorded at room temperature (b) Room temperature photoluminescence decay lifetime analysis showing single exponential decay process. (c) Temperature dependent photoluminescence spectra (d) PL intensity switching across temperature.

The experimental QY value is comparable with two well-known luminescent hybrids $(C_4H_8N)MnCl_3$ (QY = 56%) and $(C_4H_{10}N)MnCl_3$ (QY = 28.2%), both of which contain linear metal-halide chains composed of face sharing $MnCl_6$ octahedra in contrast to trimeric $(Mn_3Cl_{12})^{6-}$ units containing face shared Mn-Cl octahedra in **4** (see **Table 4.7**).[3,50] Further, to see the effect of phase transition on luminescence, we have also recorded the photoluminescence spectra across the phase transition temperature during cooling with keeping the cooling rate at 10 K min^{-1}. We have observed that with decrease in temperature, the emission maxima shifts to longer wavelengths and also the emission intensity gets enhanced gradually (**Figure 4.10** (c)). Most interestingly, a step-like increase in intensity has been observed at 160 K (**Figure 4.10** (d)). The intensity maximum at 100 K is 1.15 times higher than the maximum at 220 K. Such distinct change in luminescence originates from abrupt changes in Mn-Cl units and also the crystal structure across phase transition. In a nutshell, compound **2** features brilliant emission characteristics and holds strong application potential in the optical coatings industry and semiconductor devices.

Table 4.7 Literature comparison of room temperature photoluminescence

Compound	Lifetime	Quantum Yield (%)	Reference
$(C_4H_8N)MnCl_3$	515 μs	56	[3]
$(C_4H_{10}N)MnCl_3$	333.6 μs	28.2	[50]
$(CH_6N_3)_2MnCl_4$	**1.71 ms**	**39.5**	**Our Work**

4.4 Conclusion:

In conclusion, we have designed and studied a new single-crystalline luminescent hybrid $(CH_6N_3)_2MnCl_4$, that exhibits intriguing ~30 K wide hysteresis in thermally induced dielectric and magnetic switching accompanying a first order structural phase transition. The compound exhibits zero dimensional (0D) structure containing unique $(Mn_3Cl_{12})^{6-}$ trimeric units and guanidinium cations. The transition is rendered by reorientation and ordering of GCs and cooperative displacements of $(Mn_3Cl_{12})^{6-}$ units, resulting in modulation of H-bonding and short contact interactions. The large hysteresis mainly spurs from the complicated mechanism of modulation in extensive supramolecular interactions across transition. Remarkably, a reversible switchable dielectric anomaly is observed at phase transition temperatures where the disordered and frozen phases of GCs along with subtle changes in crystal packing portray the high and low dielectric states respectively. Volume change, change in crystal packing and subtle change in $(Mn_3Cl_{12})^{6-}$ geometry across phase transition collectively give rise to reversible, weak magnetic anomalies. Presence of octahedral Mn^{2+} ion causes fascinating bright orange-red emission at 645 nm under ultraviolet excitation with sizeable lifetime and quantum yield.

Atomic positions list:

Table 4.8. Atomic coordinates (x10^4) and equivalent isotropic displacement parameters (Å^{2}x10^3) for compound **2** at 150 K with estimated standard deviations in parentheses.

Label	x	y	z	Occupancy	U_{eq}^*
Mn(1)	17497(2)	10858(1)	-6528(1)	1	20(1)
Mn(2)	17705(2)	12009(1)	-7255(1)	1	18(1)
Mn(3)	17920(2)	13178(1)	-7946(1)	1	20(1)
Cl(1)	15391(3)	10578(1)	-5569(2)	1	26(1)
Cl(2)	17333(3)	10137(1)	-7497(2)	1	21(1)
Cl(3)	19596(4)	10529(1)	-5603(2)	1	28(1)
Cl(4)	15595(3)	11363(1)	-7553(2)	1	20(1)
Cl(5)	17682(3)	11706(1)	-5727(2)	1	18(1)
Cl(6)	19588(3)	11302(1)	-7588(2)	1	21(1)
Cl(7)	15802(3)	12700(1)	-6999(2)	1	19(1)
Cl(8)	17794(3)	12328(1)	-8791(2)	1	18(1)
Cl(9)	19798(3)	12645(1)	-6950(2)	1	19(1)
Cl(10)	15967(3)	13567(1)	-8874(2)	1	27(1)
Cl(11)	17968(3)	13817(1)	-6815(2)	1	25(1)
Cl(12)	20167(4)	13452(2)	-8846(2)	1	31(1)
C(1)	16939(15)	9257(4)	-4924(7)	1	29(3)
N(1)	17344(12)	8831(3)	-4588(6)	1	31(2)
H(1A)	17910	8630	-4881	1	37
H(1B)	17044	8753	-4074	1	37
N(2)	15942(15)	9562(4)	-4459(7)	1	50(3)
H(2A)	15602	9469	-3961	1	59
H(2B)	15664	9842	-4670	1	59
N(3)	17386(12)	9384(3)	-5708(6)	1	30(2)
H(3A)	17952	9186	-6008	1	36
H(3B)	17113	9664	-5920	1	36
C(2)	22649(14)	11876(3)	-5459(6)	1	22(2)
N(4)	22584(13)	11720(3)	-6278(5)	1	29(2)
H(4A)	23426	11664	-6560	1	35
H(4B)	21700	11674	-6523	1	35
N(5)	21326(11)	11953(3)	-5045(7)	1	28(2)
H(5A)	21334	12050	-4514	1	34
H(5B)	20458	11905	-5306	1	34

N(6)	23999(11)	11946(4)	-5078(6)	1	28(2)
H(6A)	24035	12044	-4548	1	33
H(6B)	24844	11894	-5360	1	33
C(3)	22784(14)	12224(3)	-8964(6)	1	19(2)
N(7)	21469(11)	12105(3)	-9350(7)	1	23(2)
H(7A)	21482	11977	-9860	1	28
H(7B)	20600	12156	-9091	1	28
N(8)	24132(10)	12148(4)	-9356(7)	1	30(3)
H(8A)	24154	12020	-9866	1	36
H(8B)	24983	12227	-9101	1	36
N(9)	22757(13)	12404(3)	-8160(6)	1	33(2)
H(9A)	21886	12442	-7896	1	40
H(9B)	23609	12483	-7905	1	40
C(4)	22949(14)	13774(4)	-6632(7)	1	24(3)
N(10)	22949(12)	13595(3)	-7438(6)	1	29(2)
H(10A)	22086	13544	-7703	1	35
H(10B)	23812	13529	-7693	1	35
N(11)	24279(11)	13873(3)	-6241(7)	1	30(2)
H(11A)	24279	14003	-5732	1	36
H(11B)	25142	13807	-6495	1	36
N(12)	21610(12)	13872(3)	-6257(7)	1	31(2)
H(12A)	21590	14002	-5749	1	37
H(12B)	20757	13805	-6521	1	37
C(5)	17559(14)	15068(4)	-7772(7)	1	24(2)
N(13)	16341(11)	14776(3)	-7780(7)	1	32(2)
H(13A)	16422	14476	-7604	1	38
H(13B)	15463	14885	-7962	1	38
N(14)	18920(12)	14910(4)	-7496(8)	1	42(3)
H(14A)	19023	14610	-7318	1	51
H(14B)	19704	15106	-7495	1	51
N(15)	17439(12)	15535(3)	-8030(6)	1	32(2)
H(15A)	16561	15648	-8204	1	38
H(15B)	18240	15724	-8023	1	38
C(6)	16422(16)	15581(4)	-5508(7)	1	30(3)
N(16)	15236(13)	15342(4)	-5881(7)	1	41(3)
H(16A)	14860	15448	-6363	1	50
H(16B)	14851	15084	-5639	1	50

N(17)	17033(14)	15981(3)	-5872(7)	1	46(3)
H(17A)	16667	16090	-6354	1	55
H(17B)	17794	16131	-5626	1	55
N(18)	17063(14)	15419(4)	-4759(7)	1	44(3)
H(18A)	17837	15574	-4536	1	53
H(18B)	16697	15161	-4506	1	53

Table 4.9. Atomic coordinates (x10^4) and equivalent isotropic displacement parameters (Å^{2}x10^3) for compound **2** at 295 K with estimated standard deviations in parentheses.

Label	**x**	**Y**	**z**	**Occupancy**	**U_{eq}^***
Mn(2)	2354(1)	503(1)	2766(1)	1	31(1)
Mn(3)	2218(1)	-660(1)	2057(1)	1	35(1)
Mn(1)	2388(1)	1641(1)	3548(1)	1	36(1)
Cl(9)	2250(2)	198(1)	1226(1)	1	34(1)
Cl(5)	317(2)	1182(1)	2501(1)	1	38(1)
Cl(7)	344(2)	-151(1)	3015(1)	1	33(1)
Cl(6)	2495(2)	780(1)	4298(1)	1	34(1)
Cl(4)	4311(2)	1187(1)	2498(1)	1	36(1)
Cl(8)	4350(2)	-170(1)	3023(1)	1	34(1)
Cl(10)	2256(2)	-1315(1)	3149(1)	1	43(1)
Cl(3)	2336(2)	2383(1)	2621(1)	1	45(1)
Cl(11)	-6(2)	-946(1)	1125(1)	1	55(1)
Cl(12)	4163(2)	-1040(1)	1170(1)	1	53(1)
Cl(2)	4558(2)	1936(1)	4508(1)	1	50(1)
Cl(1)	395(2)	1933(1)	4490(1)	1	55(1)
N(7)	-1136(5)	555(2)	4957(3)	1	50(2)
H(7A)	-306	607	4692	1	60
H(7B)	-1079	454	5481	1	60
N(8)	-3767(5)	557(2)	4960(3)	1	47(2)
H(8A)	-3721	459	5486	1	56
H(8B)	-4649	608	4694	1	56
N(4)	2711(6)	1076(2)	7473(3)	1	49(2)
H(4A)	1863	1015	7714	1	59
H(4B)	3584	1017	7743	1	59
N(9)	-2563(6)	785(2)	3761(2)	1	51(2)
H(9A)	-1728	836	3500	1	61
H(9B)	-3447	836	3498	1	61

N(6)	3970(5)	1355(2)	6334(3)	1	48(2)
H(6A)	3962	1479	5825	1	58
H(6B)	4834	1294	6611	1	58
N(5)	1351(6)	1347(2)	6283(3)	1	52(2)
H(5A)	1316	1471	5774	1	62
H(5B)	508	1281	6527	1	62
N(12)	1491(6)	-417(2)	-688(3)	1	55(2)
H(12A)	629	-361	-972	1	66
H(12B)	1492	-531	-172	1	66
N(10)	4138(6)	-427(2)	-642(3)	1	61(2)
H(10A)	4984	-379	-893	1	73
H(10B)	4164	-540	-125	1	73
N(3)	2501(6)	3127(2)	4374(3)	1	61(2)
H(3A)	2066	3347	4044	1	73
H(3B)	2735	2842	4169	1	73
N(11)	2767(6)	-154(2)	-1826(3)	1	56(2)
H(11A)	3612	-106	-2079	1	67
H(11B)	1893	-88	-2089	1	67
N(2)	2455(7)	3648(2)	5494(3)	1	76(2)
H(2A)	2020	3870	5166	1	92
H(2B)	2658	3710	6030	1	92
C(3)	-2487(6)	631(2)	4561(3)	1	34(2)
C(1)	2802(7)	3223(2)	5182(3)	1	49(2)
C(2)	2674(7)	1260(2)	6684(3)	1	37(2)
N(13)	2673(6)	-2995(2)	1845(4)	1	62(2)
N(14A)	4030(16)	-2322(6)	2367(11)	0.55(2)	53(3)
N(14B)	3940(20)	-2224(7)	1997(13)	0.45(2)	53(3)
N(15A)	1297(17)	-2301(8)	2141(19)	0.65(4)	66(5)
N(15B)	1410(40)	-2247(15)	1770(20)	0.35(4)	66(5)
C(4)	2812(6)	-326(2)	-1044(3)	1	39(2)
C(5)	2675(7)	-2521(3)	2024(4)	1	63(2)
N(1)	3480(8)	2881(3)	5670(3)	1	100(3)
H(1A)	3698	2939	6206	1	120
H(1B)	3706	2598	5454	1	120
C(6)	1788(12)	-2947(5)	4366(6)	1	106(4)
N(16A)	466(13)	-2816(5)	3994(7)	0.778(15)	113(4)
N(16B)	1430(50)	-2516(11)	4000(20)	0.222(15)	113(4)

N(17A)	2460(40)	-3309(10)	3908(16)	0.46(2)	143(7)
N(17B)	1900(40)	-3440(7)	4257(16)	0.54(2)	143(7)
N(18A)	2500(30)	-2507(9)	4578(14)	0.377(12)	115(5)
N(18B)	2613(16)	-2863(6)	5105(8)	0.623(12)	115(5)

4.5 Bibliography:

(1) Zhang, Y.; Liao, W.-Q.; Fu, D.-W.; Ye, H.-Y.; Liu, C.-M.; Chen, Z.-N.; Xiong, R.-G. The First Organic–Inorganic Hybrid Luminescent Multiferroic: (Pyrrolidinium)$MnBr_3$. *Adv. Mater.* **2015**, *27* (26), 3942–3946.

(2) Polyakov, A. O.; Arkenbout, A. H.; Baas, J.; Blake, G. R.; Meetsma, A.; Caretta, A.; Van Loosdrecht, P. H. M.; Palstra, T. T. M. Coexisting Ferromagnetic and Ferroelectric Order in a $CuCl_4$-Based Organic-Inorganic Hybrid. *Chem. Mater.* **2012**, *24* (1), 133–139.

(3) Zhang, Y.; Liao, W.-Q.; Fu, D.-W.; Ye, H.-Y.; Chen, Z.-N.; Xiong, R.-G. Highly Efficient Red-Light Emission in An Organic–Inorganic Hybrid Ferroelectric: (Pyrrolidinium)$MnCl_3$. *J. Am. Chem. Soc.* **2015**, *137* (15), 4928–4931.

(4) Shi, P.-P.; Tang, Y.-Y.; Li, P.-F.; Liao, W.-Q.; Wang, Z.-X.; Ye, Q.; Xiong, R.-G. Symmetry Breaking in Molecular Ferroelectrics. *Chem. Soc. Rev.* **2016**, *45* (14), 3811–3827.

(5) Gomez-Cuevas, M. J. T. and A. L.-E. and J. Z. and I. R.-L. and F. J. Z. and G. M. and A. A New $(C_2H_5NH3)_2ZnCl_4$ Crystal with a Pure $Pnma$-$P2_12_12_1$ Ferroelastic Phase Transition. *J. Phys. Condens. Matter* **1994**, *6* (34), 6751.

(6) Bousseksou, A.; Molnár, G.; Salmon, L.; Nicolazzi, W. Molecular Spin Crossover Phenomenon: Recent Achievements and Prospects. *Chem. Soc. Rev.* **2011**, *40* (6), 3313–3335.

(7) Sato, O.; Tao, J.; Zhang, Y.-Z. Control of Magnetic Properties through External Stimuli. *Angew. Chemie Int. Ed.* **2007**, *46* (13), 2152–2187.

(8) Guo, Q.; Zhang, W.-Y.; Chen, C.; Ye, Q.; Fu, D.-W. Red-Light Emission and Dielectric Reversible Duple Opto-Electronic Switches in a Hybrid Multifunctional Material: (2-Methylimidazolium)$MnCl_3(H_2O)$. *J. Mater. Chem. C* **2017**, *5* (22), 5458–5464.

(9) Real, J. A.; Gaspar, A. B.; Muñoz, M. C. Thermal, Pressure and Light Switchable Spin-Crossover Materials. *Dalt. Trans.* **2005**, No. 12, 2062–2079.

(10) Dou, C.; Han, L.; Zhao, S.; Zhang, H.; Wang, Y. Multi-Stimuli-Responsive

Fluorescence Switching of a Donor−Acceptor π-Conjugated Compound. *J. Phys. Chem. Lett.* **2011**, *2* (6), 666–670.

(11) Shi, C.; Han, X.-B.; Zhang, W. Structural Phase Transition-Associated Dielectric Transition and Ferroelectricity in Coordination Compounds. *Coord. Chem. Rev.* **2017**.

(12) Han, S.; Zhang, J.; Teng, B.; Ji, C.; Zhang, W.; Sun, Z.; Luo, J. Inorganic–Organic Hybrid Switchable Dielectric Materials with the Coexistence of Magnetic Anomalies Induced by Reversible High-Temperature Phase Transition. *J. Mater. Chem. C* **2017**, *5* (33), 8509–8515.

(13) Shi, C.; Zhang, X.; Cai, Y.; Yao, Y.-F.; Zhang, W. A Chemically Triggered and Thermally Switched Dielectric Constant Transition in a Metal Cyanide Based Crystal. *Angew. Chemie Int. Ed.* **2015**, *54* (21), 6206–6210.

(14) Theato, P.; Sumerlin, B. S.; O’Reilly, R. K.; Epps Thomas H., I. I. I. Stimuli Responsive Materials. *Chem. Soc. Rev.* **2013**, *42* (17), 7055–7056.

(15) Shi, P.-P.; Ye, Q.; Li, Q.; Wang, H.-T.; Fu, D.-W.; Zhang, Y.; Xiong, R.-G. Novel Phase-Transition Materials Coupled with Switchable Dielectric, Magnetic, and Optical Properties: $[(CH_3)_4P][FeCl_4]$ and $[(CH_3)_4P][FeBr_4]$. *Chem. Mater.* **2014**, *26* (20), 6042–6049.

(16) Stuart, M. A. C.; Huck, W. T. S.; Genzer, J.; Müller, M.; Ober, C.; Stamm, M.; Sukhorukov, G. B.; Szleifer, I.; Tsukruk, V. V; Urban, M.; et al. Emerging Applications of Stimuli-Responsive Polymer Materials. *Nat. Mater.* **2010**, *9*, 101.

(17) Sato, O. Dynamic Molecular Crystals with Switchable Physical Properties. *Nat. Chem.* **2016**, *8*, 644.

(18) Julià-López, A.; Hernando, J.; Ruiz-Molina, D.; González-Monje, P.; Sedó, J.; Roscini, C. Temperature-Controlled Switchable Photochromism in Solid Materials. *Angew. Chemie* **2016**, *128* (48), 15268–15272.

(19) Wang, Y.; Runnerstrom, E. L.; Milliron, D. J. Switchable Materials for Smart Windows. *Annu. Rev. Chem. Biomol. Eng.* **2016**, *7* (1), 283–304.

(20) Hu, Y.; Zhang, H.; Chong, W. K.; Li, Y.; Ke, Y.; Ganguly, R.; Morris, S. A.; You,

L.; Yu, T.; Sum, T. C.; et al. Molecular Engineering toward Coexistence of Dielectric and Optical Switch Behavior in Hybrid Perovskite Phase Transition Material. *J. Phys. Chem. A* **2018**, *122* (31), 6416–6423.

(21) Gütlich, P.; Goodwin, H. A. *Spin Crossover in Transition Metal Compounds II*.

(22) Zhang, W.; Ye, H.-Y.; Graf, R.; Spiess, H. W.; Yao, Y.-F.; Zhu, R.-Q.; Xiong, R.-G. Tunable and Switchable Dielectric Constant in an Amphidynamic Crystal. *J. Am. Chem. Soc.* **2013**, *135* (14), 5230–5233.

(23) Zhao, X.-H.; Huang, X.-C.; Zhang, S.-L.; Shao, D.; Wei, H.-Y.; Wang, X.-Y. Cation-Dependent Magnetic Ordering and Room-Temperature Bistability in Azido-Bridged Perovskite-Type Compounds. *J. Am. Chem. Soc.* **2013**, *135* (43), 16006–16009.

(24) Van Vleck, J. H. On Dielectric Constants and Magnetic Susceptibilities in the New Quantum Mechanics Part I. A General Proof of the Langevin-Debye Formula. *Phys. Rev.* **1927**, *29* (5), 727–744.

(25) Zheng, X.; Shi, P.-P.; Lu, Y.; Zhou, L.; Gao, J.-X.; Geng, F.-J.; Wu, D.-H.; Fu, D.-W.; Ye, Q. Dielectric and Nonlinear Optical Dual Switching in an Organic–Inorganic Hybrid Relaxor $[(CH_3)_3PCH_2OH][Cd(SCN)_3]$. *Inorg. Chem. Front.* **2017**, *4* (9), 1445–1450.

(26) Shao, X.-D.; Zhang, X.; Shi, C.; Yao, Y.-F.; Zhang, W. Switching Dielectric Constant Near Room Temperature in a Molecular Crystal. *Adv. Sci.* **2015**, *2* (5), 1500029.

(27) Shi, C.; Yu, C.-H.; Zhang, W. Predicting and Screening Dielectric Transitions in a Series of Hybrid Organic–Inorganic Double Perovskites via an Extended Tolerance Factor Approach. *Angew. Chemie Int. Ed.* **2016**, *55* (19), 5798–5802.

(28) Luo, Y.-H.; Chen, C.; Hong, D.-L.; He, X.-T.; Wang, J.-W.; Sun, B.-W. Thermal-Induced Dielectric Switching with 40K Wide Hysteresis Loop Near Room Temperature. *J. Phys. Chem. Lett.* **2018**, *9* (9), 2158–2163.

(29) Saparov, B.; Mitzi, D. B. Organic–Inorganic Perovskites: Structural Versatility for Functional Materials Design. *Chem. Rev.* **2016**, *116* (7), 4558–4596.

(30) Kundys, B.; Lappas, a.; Viret, M.; Kapustianyk, V.; Rudyk, V.; Semak, S.; Simon, C.; Bakaimi, I. Multiferroicity and Hydrogen-Bond Ordering in $(C_2H_5NH_3)_2CuCl_4$ Featuring Dominant Ferromagnetic Interactions. *Phys. Rev. B - Condens. Matter Mater. Phys.* **2010**, *81* (22), 1–6.

(31) Zhang, H.-Y.; Mei, G.-Q.; Liao, W.-Q. Symmetry Breaking Phase Transition, Second-Order Nonlinear Optical and Dielectric Properties of a One-Dimensional Organic–Inorganic Hybrid Zigzag Chain Compound $[NH_3(CH_2)_5NH_3]SbBr_5$. *Cryst. Growth Des.* **2016**, *16* (10), 6105–6110.

(32) Asghar, M. A.; Zhang, S.; Khan, T.; Sun, Z.; Zeb, A.; Ji, C.; Li, L.; Zhao, S.; Luo, J. Reversible Phase Transition Driven by Order-Disorder Transformations of Metal-Halide Moieties in $[(C_6H_{14})NH_2]_2CuBr_4$. *J. Mater. Chem. C* **2016**, *4* (32), 7537–7540.

(33) Zhang, W.; Ye, H.-Y.; Cai, H.-L.; Ge, J.-Z.; Xiong, R.-G.; Huang, S. D. Discovery of New Ferroelectrics: $[H_2dbco]_2 \cdot [Cl_3] \cdot [CuCl_3(H_2O)_2] \cdot H_2O$ (Dbco = 1,4-Diaza-Bicyclo[2.2.2]Octane). *J. Am. Chem. Soc.* **2010**, *132* (21), 7300–7302.

(34) Sen, A.; Roy, S.; Peter, S. C.; Paul, A.; Waghmare, U. V; Sundaresan, A. Order-Disorder Structural Phase Transition and Magnetocaloric Effect in Organic-Inorganic Halide Hybrid (C2H5NH3)2CoCl4. *J. Solid State Chem.* **2018**, *258*, 431–440.

(35) Liao, W.-Q.; Tang, Y.-Y.; Li, P.-F.; You, Y.-M.; Xiong, R.-G. Large Piezoelectric Effect in a Lead-Free Molecular Ferroelectric Thin Film. *J. Am. Chem. Soc.* **2017**, *139* (49), 18071–18077.

(36) You, Y.-M.; Liao, W.-Q.; Zhao, D.; Ye, H.-Y.; Zhang, Y.; Zhou, Q.; Niu, X.; Wang, J.; Li, P.-F.; Fu, D.-W.; et al. An Organic-Inorganic Perovskite Ferroelectric with Large Piezoelectric Response. *Science (80-.).* **2017**, *357* (6348), 306 LP – 309.

(37) Vogelsberg, C. S.; Garcia-Garibay, M. A. Crystalline Molecular Machines: Function, Phase Order, Dimensionality, and Composition. *Chem. Soc. Rev.* **2012**, *41* (5), 1892–1910.

(38) G. M. Sheldrick, Go¨ttingen, G. SADABS,. **1997**.

(39) Sheldrick, G. M. No Title. *Acta Crystallogr., Sect. A Found. Adv.* **2015**, *71*, 3–8.

(40) Sheldrick, G. M. , SHELXTL, program for crystal structure refine-ment. , SHELXTL, Program for Crystal Structure Refine-Ment,. **1997**.

(41) Farrugia, L. No Title. *J. Appl. Crystallogr.* **1999**, *32*, 837–838.

(42) Mason, P. E.; Neilson, G. W.; Enderby, J. E.; Saboungi, M.-L.; Dempsey, C. E.; MacKerell Alexander D.; Brady, J. W. The Structure of Aqueous Guanidinium Chloride Solutions. *J. Am. Chem. Soc.* **2004**, *126* (37), 11462–11470.

(43) Vazdar, M.; Uhlig, F.; Jungwirth, P. Like-Charge Ion Pairing in Water: An Ab Initio Molecular Dynamics Study of Aqueous Guanidinium Cations. *J. Phys. Chem. Lett.* **2012**, *3* (15), 2021–2024.

(44) Kubíčková, A.; Křížek, T.; Coufal, P.; Wernersson, E.; Heyda, J.; Jungwirth, P. Guanidinium Cations Pair with Positively Charged Arginine Side Chains in Water. *J. Phys. Chem. Lett.* **2011**, *2* (12), 1387–1389.

(45) Lv, X.-H.; Liao, W.-Q.; Wang, Z.-X.; Li, P.-F.; Mao, C.-Y.; Ye, H.-Y. Design and Prominent Dielectric Properties of a Layered Phase-Transition Crystal: (Cyclohexylmethylammonium)$_2$CdCl$_4$. *Cryst. Growth Des.* **2016**, *16* (7), 3912–3916.

(46) Sun, X.-F.; Wang, Z.; Li, P.-F.; Liao, W.-Q.; Ye, H.-Y.; Zhang, Y. Tunable Dielectric Responses Triggered by Dimensionality Modification in Organic–Inorganic Hybrid Phase Transition Compounds $(C_5H_6N)Cd_nCl_{2n+1}$ (n = 1 and 2). *Inorg. Chem.* **2017**, *56* (6), 3506–3511.

(47) Xu, C.; Zhang, W.; Gao, L.; Gan, X.; Sun, X.; Cui, Z.; Cai, H.-L.; Wu, X. S. A High-Temperature Organic–Inorganic Ferroelectric with Outstanding Switchable Dielectric Characteristics. *RSC Adv.* **2017**, *7* (76), 47933–47937.

(48) Gobbi, A.; Frenking, G. Y-Conjugated Compounds: The Equilibrium Geometries and Electronic Structures of Guanidine, Guanidinium Cation, Urea, and 1,1-Diaminoethylene. *J. Am. Chem. Soc.* **1993**, *115* (6), 2362–2372.

(49) Dougherty, D. A. Cation-π Interactions in Chemistry and Biology: A New View of Benzene, Phe, Tyr, and Trp. *Science (80-.).* **1996**, *271* (5246), 163 LP – 168.

(50) Ye, H.-Y.; Zhou, Q.; Niu, X.; Liao, W.-Q.; Fu, D.-W.; Zhang, Y.; You, Y.-M.; Wang, J.; Chen, Z.-N.; Xiong, R.-G. High-Temperature Ferroelectricity and Photoluminescence in a Hybrid Organic–Inorganic Compound: (3-Pyrrolinium)$MnCl_3$. *J. Am. Chem. Soc.* **2015**, *137* (40), 13148–13154.

(51) Orgel, L. E. Phosphorescence of Solids Containing the Manganous or Ferric Ions. *J. Chem. Phys.* **1955**, *23* (10), 1958.

(52) Orgel, L. E. Band Widths in the Spectra of Manganous and Other Transition-Metal Complexes. *J. Chem. Phys.* **1955**, *23* (10), 1824–1826.

(53) Lawson, K. E. Optical Studies of Electronic Transitions in Hexa- and Tetracoordinated Mn^{2+} Crystals. *J. Chem. Phys.* **1967**, *47* (9), 3627–3633.

(54) Pan, Y.; Su, Q.; Xu, H.; Chen, T.; Ge, W.; Yang, C.; Wu, M. Synthesis and Red Luminescence of Pr^{3+}-Doped $CaTiO_3$ Nanophosphor from Polymer Precursor. *J. Solid State Chem.* **2003**, *174* (1), 69–73.

Chapter 5

Crystal Structure and Magnetic Properties of Low-dimensional Spin-1/2 Antiferromagnetic Compound $(CH_6N_3)_2CuBr_4$

Summary

In this chapter, we present crystal structure and magnetic properties of a single crystalline low dimensional spin-1/2 antiferromagnetic hybrid, $(CH_6N_3)_2CuBr_{4.}$ At room temperature, the compound crystallizes in triclinic structure (space group $P\bar{1}$). The crystal structure is zero dimensional, consisting isolated $(CuBr_4)^{2-}$ tetrahedra separated by planar guanidinium cations. Extensive hydrogen bonding interactions are observed between guanidinium cations and $(CuBr_4)^{2-}$ tetrahedra. Also strong ion-pair interactions among guanidinium cations further stabilize the structure. Thus the structure retains the same space group symmetry down to 95 K where subtle changes in lattice parameters are observed. DC magnetization measurements on bulk sample reveal a broad anomaly centred at 10 K, indicating presence of low dimensional antiferromagnetism. Crystal structure analyses reveal Cu-Br$\cdots$Br-Cu two halide antiferromagnetic exchange pathway to be the mechanism. In crystallographic *ac*-plane and *bc*-plane, coupled and isolated spin ladder type interaction pathways are observed. respectively In *ab*-plane, a plaquette of nearest neighbour 2-D rectangular AFM layers can be portrayed. We have used the suspectibility expressions for spin-1/2 antiferromagnetic spin chain, ladder, square and rectangular lattice to fit the magnetic susceptibility as a function of temperature. The rectangular lattice model gives the best fitting parameter while spin ladder model fitting parameter are also qualitatively good.

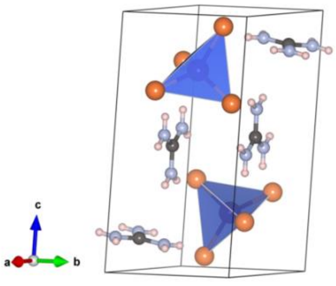

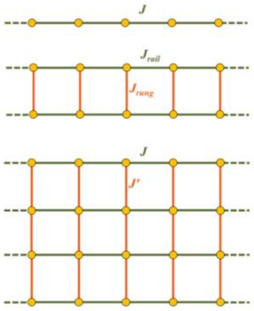

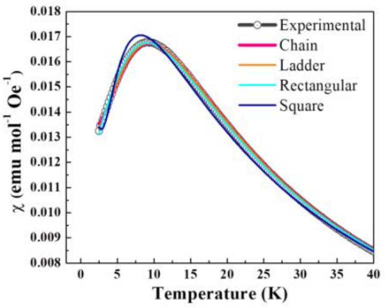

5.1 Introduction:

The contemporary research on low dimensional spin-1/2 magnetic materials have taken quantum leap since the advent of high temperature superconductivity in doped materials of parent cuprate La_2CuO_4.[1,2] Collectively, fundamental research on such materials had started much before, at around 70s, when notable research on structure and magnetic properties of layered hybrid halides with R_2CuX_4 formula (R: organic ammonium ion, X: halide ion) reported two dimensional ("in-layer") ferromagnetic interactions.[3–6] In similar period of time, a number of Spin-1/2 halides with one-dimensional ferromagnetic interactions, and also one/two dimensional antiferromagnetic materials were reported.[7–12] The commonality in all these materials is the magnetic exchange coupling mechanism which is the single halide Cu-X-Cu pathway. Later in 1980s, a unique antiferromagnetic exchange interaction was found to operate *via* two halide exchange pathways involving contacts between halide ions on neighboring copper centers.[13–18] Over the years, significant progress has been made in finding new low dimensional spin-1/2 magnetic halides featuring different types of antiferromagnetic interactions propagating in different dimensions (two and one dimensional magnetic sublattices).[17–22]

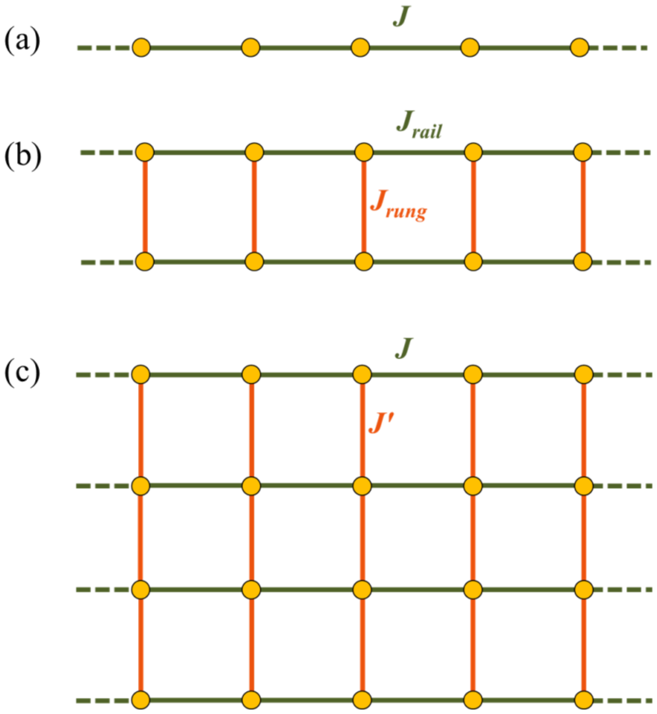

Scheme 5.1 Schematic illustrations of (a) Spin chain antiferromagnetic lattice, (b) antiferromagnetic spun ladder and (c) square lattice antiferromagnet.

The two halide exchange pathway has been found to be the mechanism behind the *1-D* and *2-D* antiferromagnetism in many spin-1/2 hybrid halides. In this pathway, the antiferromagnetic exchange propagates *via* non-bonding contacts between halide ions attached to different metal ions (**M-X···X-M** pathway see **Scheme 5.2**). Two halide exchange interaction mechanism and its strength was studied in detail by Drumheller and co-workers in a number alkanediammonium salts of copper (II) chloride.[13,16,23] They found that the exchange interaction strength is directly dependent on distance between the halide anions, not the metal ions and also the interaction is much stronger through Br···Br pathway than the chloride counterpart. Subsequent work by Block and Jensen also supported similar type of mechanism.[14,15] Overall, although such noteworthy research portrayed the interaction pathway to certain depth, it could not accurately delineate the parameters governing the mechanism. Later, substantial work by Willet and coworkers showed that almost all geometrical parameters associated with a M-X···X-M pathway have their effects on the exchange strength.[24] First of all, for hybrids featuring $(CuBr_4)^{2-}$in low dimensional magnetic sublattice, the tetrahedral geometry itself largely influence the electron delocalization from the metal to halogen ligand, as observed from EPR analyses.[25] The Jahn-Teller distortion in Cu^{2+} alters the tetrahedral geometry which often affects the linearity of the Cu-Br···Br-Cu bridge. This brings our attention to the second important aspect, the geometry of the pathway (see **Scheme 5.2**).

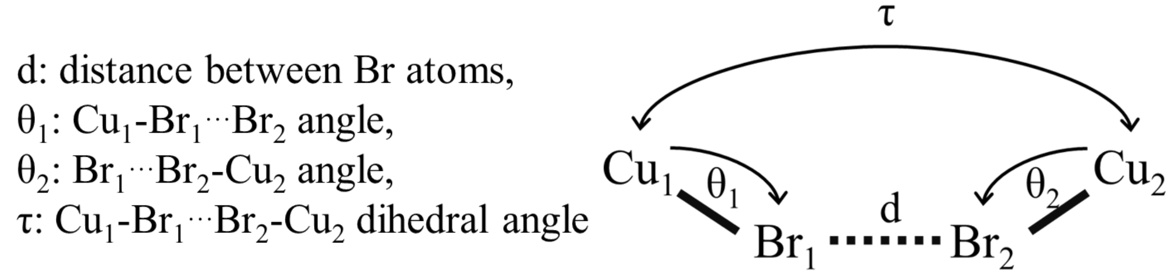

Scheme 5.2 Schematic illustration of Cu-Br···Br-Cu double halide antiferromagnetic exchange pathway (adapted after obtaining copyright permission from ©Elsevier.[22]

The third important factor influencing the interaction strength is the topology. The two halide exchange pathway can propagate through the corner, edge or face of two tetrahedra. Turnbull *et al.* have formulated a notation ***nij*** to describe the type of topology (where ***n*** is the number of interaction that a tetrahedron takes part in, ***i*** and ***j*** represent the topology).[22] They have qualitatively shown the dependence of exchange strength on the geometrical parameters. For interaction propagating through corners, the exchange strength was seen to rapidly decrease on increasing the Br···Br distance (d) and reaches almost zero when d > 5 Å. Also, the exchange strength was more when the sum of both Cu-Br···Br angles was higher which is probably due to better wave function overlap.

Fundamentally, in Cu-L_n complex (L = halide or oxide ligand), the orbital angular momentum of the unpaired electron at Cu (II) center is largely quenched by the ligand field (average *g*–factor ≈ 2.12 – 2.15) as a result of which, the corresponding moment of each ion has almost no preferred alignment.[26] This implies that in a one dimensional (*1-D*) spin-1/2 chain, the spin Hamiltonian will be isotropic. To mention, the magnetic lattice of a *1-D* antiferromagnetic chain is a lattice which consists of linearly arranged magnetically active ions featuring nearest neighbor antiferromagnetic exchange interaction, J (see **Scheme 5.1** (a)). Good examples of *1-D* spin-1/2 antiferromagnetic material are $Cupy_2Cl_2$ and $Cu(pz)(NO_3)_2$.[27–30] In the case of an antiferromagnetic spin ladder, two parallel chains of identical magnetically active ions can be considered, where two types of magnetic exchange interactions i.e. the intra-chain interaction (known as J_{rail}) and the inter-chain interaction (known as J_{rung}) are seen to compete against each other (see **Scheme 5.1** (b)). Depending on the strength of the magnetic interaction, a spin ladder is termed as "**strong rail**" (if $J_{rail} > J_{rung}$) or "**strong rung**" (if $J_{rung} > J_{rail}$) ladder. Ideal spin ladders have no inter ladder interaction resulting in evolution of gapped state in spin excitation spectrum. In such cases, the magnetic ground state is a singlet state while the triplet state constructs the excited state separated by an energy gap Δ. External magnetic field is applied to close the singlet-triplet gap and induce a moment in the ladder. With application of magnetic field, the gap closes at the lower critical field H_{C1} while at the second critical field, H_{C2}, all the moments get aligned with the field. These critical fields are directly dependent on the strength of magnetic exchange interaction and are very large for oxide based ladders and moderate for halide based ladders. Thus, molecule-based hybrid halides with ladder geometry have been studied in much detail as compared to oxide based ladders.[31–39] In recent years, research interest in spin ladders, Tomonaga-Luttinger spin liquids has been seen to have renewed.[39–41] Also, the AFM spin ladders have also exhibited superconducting phase in certain scenario.[32,42] There is another type of spin-1/2 antiferromagnets which need a mention as it is directly related to *1-D* chain and ladder in terms of lattice structure and magnetic behavior. It is the two dimensional (*2-D*) antiferromagnetic lattices which consist of a series of *1-D* chains and can be of two types; square lattice with equal nearest neighbor magnetic interactions (J) and rectangular lattice with two types of magnetic interactions (J and J') (**Scheme 5.1** (c)). The ***J′*** can be a fraction of ***J***, and can be represented as αJ ($0 < \alpha < 1$). In limiting case, when $\alpha = 0$, we can consider single chain (**Scheme 5.1** (a)). Most common example of this type of material is the layered cuprates $La_{2-x}Sr_xCuO_{4+y}$ in which the superconducting phase have been realized.[1,43,44] Among non-oxides, the compound $Cu(pz)_2(ClO_4)_2$ is well-known as it has one of the largest ***J*** value among copper pyrazine compounds.[45–47] Another example is the series of organic-inorganic halide hybrids of formula $(RH)_2CuX_4$ where R = 5-bromo-2-amino pyridine and 5-chloro-2-amino pyridine ion and X are halide ions.[11,12,48]

From crystallographic point of view, the low dimensional magnetism comes into play when the sublattice of magnetically active ions is forced to get separated from each other by a nonmagnetic sublattice (nonmagnetic atoms or molecules). This can be easily achieved in molecular systems where nonmagnetic molecules or ions can efficiently isolate the magnetic sublattice to lower dimension and confine the antiferromagnetic interaction within the same. In this context the copper (II) based organic-inorganic halides deserve strong limelight. In these materials, the ammonium cations are seen to occupy intermediate positions between copper-halide complexes, hindering the growth of the copper halide architecture in higher dimensions. As a result, the magnetic interactions or even ordering in these materials are seen to play in lower dimension, often featuring quantum antiferromagnetism in *1-D*, *2-D* or long range ferromagnetic order in *2-D*.[22,26,49,50] Among these, the *1-D* or *2-D* quantum antiferromagnetic exchange has mostly been observed to propagate via the two halide exchange pathway containing the nearest neighbor $(CuBr_4)^{2-}$ tetrahedra. To mention, Landee, Turnbull and coworkers have studied the structure and magnetism in a number of Cu-based hybrid halides and observed 1-D spin ladder and also 2-D rectangular lattice antiferromagnetism.[9,12,17,19,46,48,51]

In this chapter, we present our studies on a new organic-inorganic halide bis guanidinium copper bromide $(CN_3H_6)_2CuBr_4$ that exhibits low dimensional antiferromagnetic behavior. The compound (hereafter named as **3**), at room temperature, crystallizes into triclinic centrosymmetric structure ($P\bar{1}$) having isolated $(CuBr_4)^{2-}$ tetrahedral units separated from each other by planar guanidinium cations (GCs). A typical low dimensional antiferromagnetc behavior has been observed as dc magnetization measurements revealed a broad anomaly centred at 10 K. The isolated nature of $CuBr_4$ tetrahedra in crystal structure indicates Cu-Br···Br-Cu two halide exchange pathway to be the governing mechanism behind magnetism. The susceptibility as a function of temperature has been fitted using different suspectibility expressions for spin-1/2 antiferromagnetic spin dimer, chain, ladder, square and rectangular lattice. The rectangular lattice and one dimensional ladder model expressions have the best fitting parameters with the rectangular model fits slightly better.

5.2 Experimental Section:

5.2.1 Chemicals:

AR grade quality guanidine hydrobromide (CH_6N_3Br) and copper bromide ($CuBr_2$) were acquired from SDFCL and Sigma aldrich respectively. All chemicals were used without further purification.

5.2.2 Synthesis:

In a crystallization beaker, 0.6924 g (3.1 mmol) of $CuBr_2$ was dissolved thoroughly in 100 mL of deionized water under constant stirring. 0.8679 g (6.2 mmol) of CH_6N_3Br was then added into the solution and stirring was continued till complete dissolution. The whole solution was kept at room temperature for slow evaporation of solvent. Rod shaped opaque dark brown single crystals were obtained after about two weeks. As grown crystals were washed with hexane and taken for further studies. The formation process can be represented using simple addition reaction:

$$2\ CH_6N_3Br + CuBr_2 = (CH_6N_3)_2CuBr_4$$

5.2.3 Characterization:

The elemental analyses were carried out using Thermo Scientific Flash 2000 CHN analyzer. Suitable crystal piece was pre-dried under vacuum for 12 hours for this experiment.

For single crystal data collection, suitable crystal piece was mounted inside Lindemann capillary which was then mounted on top of the goniometer head. Variable temperature single crystal X-ray diffraction data were collected on an Oxford Xcalibur (Mova) diffractometer equipped with an EOS CCD detector and a microfocus sealed tube using Mo Kα radiation (λ = 0.71073 Å). Data collection at low temperature was performed using an Oxford Cobra open stream nonliquid nitrogen cooling device. Further, refinement of cell parameter, data integration and reduction were accomplished by using the program CrysalisPro.[52] The structure solution was obtained from SHELXS[53,54] and refined by using SHELXS 2018 included in the WinGX suite.[55]

DC magnetic susceptibility and magnetization measurements on crushed crystals were carried out using Quantum Design SQUID-based MPMSXL-3-type magnetometer. Zero field cooled (ZFC) and field cooled (FC) data were recorded in the temperature range of 1.8 K – 300 K with applied magnetic field of 0.01 T and 0.1 T. Isothermal magnetization has been measured at 1.8 K with field sweep range of ±7 T.

5.3 Results and Discussion:

5.3.1 Crystal Structure:

The phase purity of compound **3** was confirmed by CHNS elemental analysis method. The following table contains the elemental percentages obtained from CHNS analyses experiment.

Table 5.1 Elemental Purity Analysis:

Elements	Experimental Mass (%)	Calculated Mass (%)
H	2.37	2.40
C	4.91	4.77
N	16.53	16.69

The compound **3** at 295 K, crystallizes into centrosymmetric, triclinic structure (space group $P\bar{1}$) with a = 7.3419 (9) Å, b = 7.5395 (5) Å, c = 12.5534 (7) Å, α = 86.002 (6) °, β = 86.967 (4) °, γ = 78.091 (8) ° and Z=2 (refinement parameters and atomic coordinates are included in Table 5.2, Table 5.8, Table 5.9). At 295 K, the asymmetric unit contains one tetrahedral $(CuBr_4)^{2-}$ unit and two guanidinium cations with all the atoms occupying general crystallographic positions (Wyckoff: 2*i*) (Figure 5.1 (a)). Within single unit cell, the two $(CuBr_4)^{2-}$ units can be related using centre of symmetry and are separated from each other *via* two planar C2 guanidinium cations ($d_{Cu\text{-}Cu}$ = 8.9656 (17) Å) (Figure 5.1 (c)). Significantly, all the guanidinium cations are seen to be in thermally ordered state.On cooling the compound, the crystal structure symmetry does not change down to 95 K (space group $P\bar{1}$). At this temperature, weak changes in lattice parameters have been observed, a = 7.3419 (9) Å, b = 7.5395 (5) Å, c = 12.5534 (7) Å, α = 84.773 (10) °, β = 88.731 (10) °, γ = 78.966 (11) ° and Z = 2 (Table 5.2). In the asymmetric unit, the relative positions and orientations of all the components remain nearly same, all occupying general crystallographic positions (Wyckoff: 2*i*) (Figure 5.1 (b)).

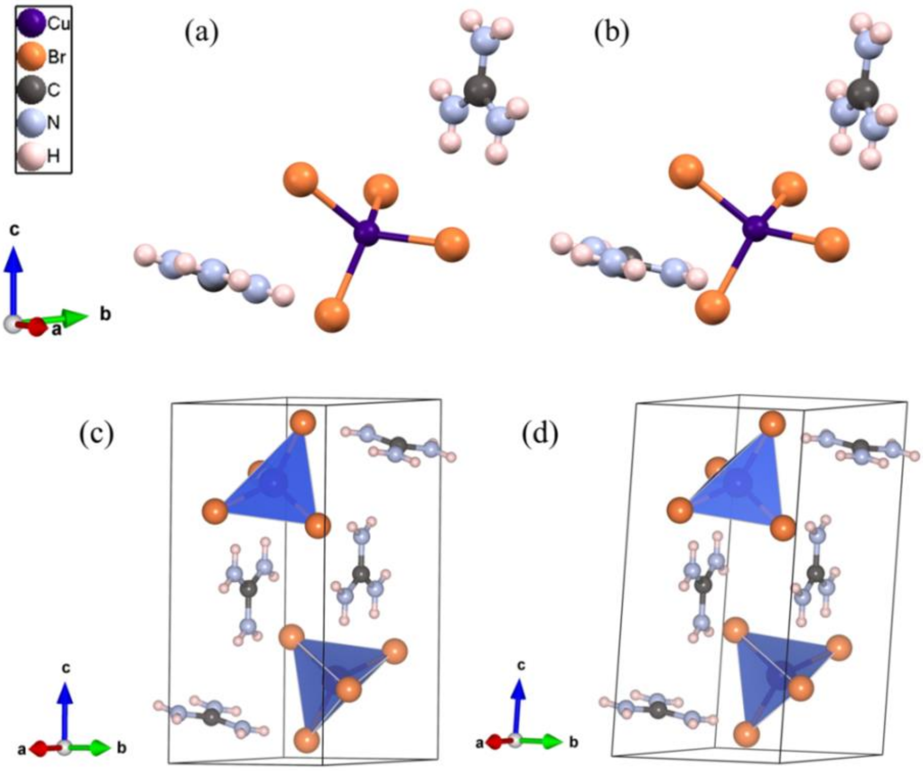

Figure 5.1 Molecular Structures of compound **3** at different temperatures: Asymmetric units (a) at 295 K and (b) at 95 K. Unit cell representations (c) at 295 K and at (d) 95 K.

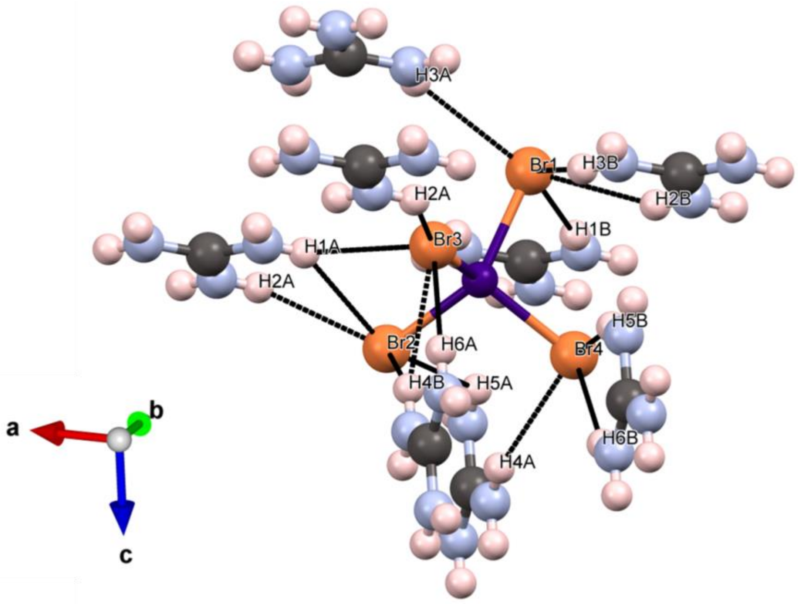

Figure 5.2 Extensive hydrogen bonding interactions among a $(CuBr_4)^{2-}$ tetrahedron and guanidinium cations in an asymmetric unit.

Table 5.2 Single crystal structure refinement details:

Parameters	RTP	LTP
Empirical formula	$C_2H_{12}Br_4CuN_6$	$C_2H_{12}Br_4CuN_6$
Formula weight (g/mol)	503.36	503.36
Temperature (K)	295	95
Wavelength (Å)	0.71073	0.71073
Crystal system	Triclinic	Triclinic
Space group	$P\bar{1}$	$P\bar{1}$
Unit cell dimensions (Å,°)	a = 7.3419 (9), α = 86.002 (6) b = 7.5395 (5), β = 86.967 (4) c = 12.5534 (7), γ = 78.091 (8)	a = 7.3419 (9), α = 84.773 (10) b = 7.5395 (4), β = 88.731 (10) c = 12.5534 (7), γ = 78.966 (11)
Volume ($Å^3$)	677.74 (11)	651.43 (14)
Z	2	2
Calculated density (g/cm^3)	2.467	2.566
Absorption coefficient (mm^{-1})	13.376	13.917
F(000)	470	470
Crystal dimension (mm^3)	0.12 x 0.09 x 0.15	0.12 x 0.09 x 0.15
Reflections collected	6084	4992
Independent reflections	3495 (R_{int} = 0.0578)	2650 (R_{int} = 0.0446)
Completeness to θ = 26°	99.8%	99.5%
Number of parameters	119	118
Goodness-of-fit	1.032	1.002
Final R indices [I > 2σ(I)]	R_{obs} = 0.0550, wR_{obs} = 0.1116	R_{obs} = 0.0361, wR_{obs} = 0.0680
R indices [all data]	R_{all} = 0.0965, wR_{all} = 0.1454	R_{all} = 0.0851, wR_{all} = 0.1618

Table 5.3 Cu-Br bond distances and Br-Cu-Br angles in a $CuBr_4$ tetrahedron:

295 K		95 K	
Label	**Bond distance (Å)**	**Label**	**Bond distance (Å)**
Cu1-Br1	2.3828 (11)	Cu1-Br1	2.3775 (9)
Cu1-Br2	2.3685 (10)	Cu1-Br2	2.3622 (9)
Cu1-Br3	2.3668 (11)	Cu1-Br3	2.3724 (8)
Cu1-Br4	2.3906 (11)	Cu1-Br4	2.3777 (9)
Label	**Bond angle (°)**	**Label**	**Bond angle (°)**
Br1-Cu1-Br2	131.76 (5)	Br1-Cu1-Br2	133.34 (4)
Br1-Cu1-Br3	100.16 (4)	Br1-Cu1-Br3	99.19 (3)
Br1-Cu1-Br4	99.83 (4)	Br1-Cu1-Br4	99.00 (3)
Br2-Cu1-Br3	100.99 (4)	Br2-Cu1-Br3	100.53 (3)
Br2-Cu1-Br4	99.11 (4)	Br2-Cu1-Br4	98.35 (3)
Br3-Cu1-Br4	129.56 (5)	Br3-Cu1-Br4	131.99 (4)

The Jahn-Teller distortion in Cu^{2+} ions is a well-known distortion which tends to flatten the $(CuBr_4)^{2-}$ and expand two of the six Br–Cu–Br angles. At 295 K, the $(CuBr_4)^{2-}$ unit is geometrically moderately distorted, featuring irregular Cu-Br distances (2.3668 (11) - 2.3828 (11) Å) and deviations in Br-Cu-Br bond angles (99.83 (4) - 131.76 (5)°) (see Table 5.3). At 95 K, the distortion increases very weakly in terms of variations in Cu-Br bond lengths (2.3622 (9) - 2.3777 (9) Å) and Br-Cu-Br bond angles (99.00 (3) – 133.34 (4)°) (**Table 5.3**). The effect of J-T distortion is evident from Br1-Cu1-Br2 and Br3-Cu1-Br4 angles at both temperatures.

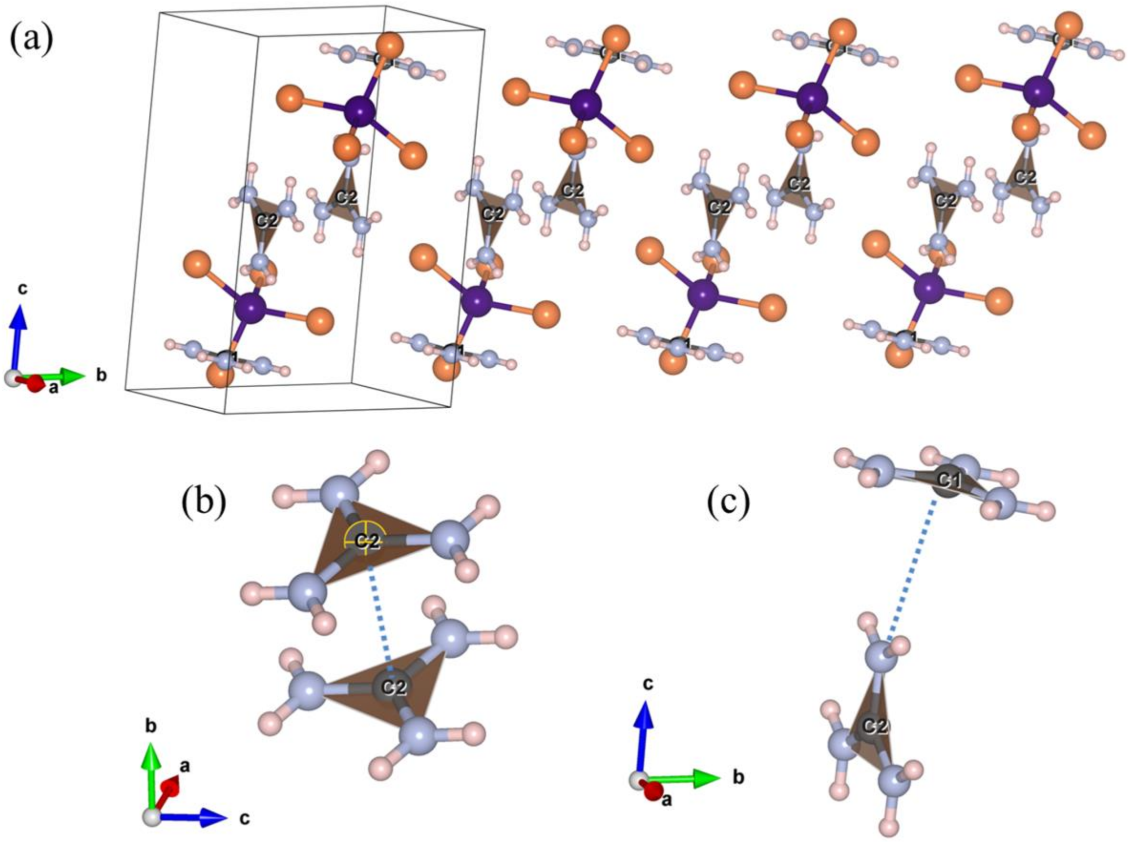

Figure 5.3 Views of ion-pair interactions observed among guanidinium cations in crystal at 95 K, (a) the arrangements of planar guanidinium cations (b) "eclipsed" ion-pair interaction among C2-C2 GCs (c) "head-on" ion-pair interaction among C1-C2 GCs.

Such crystalline phase stability across large temperature window of 200 K (295 K to 95 K) indicates that the components within crystal structure are stabilized via multiple supramolecular interactions. At 95 K, each tetrahedron is observed to take part in fifteen hydrogen bonding interactions with surrounding guanidinium cations (see **Figure 5.2**). The Br¨H bond distances (2.647-2.978 Å) indicate that the H-bonds are moderately strong. As we have discussed previously in chapter 4, the guanidinium cations with their nonzero quadrupole moment, cavitation effects and van der Waals interactions often take part in facile ion-pair interactions among themselves.[56–58]. At 95 K, two types of ion-pair interactions among planar GCs are observed. One is the“eclipsed” interaction between two parallel **C2** GCs while the other being the “head-on” interaction between **C1** and **C2** GCs ($d_{C1–C2}$ = 3.364 (8) Å and $d_{C1–C2}$ = 3.364 (8) Å) (**Figure 5.3** (b) and (c)). In crystallographic projection along *b*-axis (**Figure 5.3** (a)), we can see the above mentioned dimeric ion-pair interactions to propagate along *b*- and *c*-axis which induces more stability in the crystal structure.

5.3.2 Possible Two Halide Exchange Pathways:

Since the $(CuBr_4)^{2-}$ tetrahedra are isolated from each other, we expect the two halide exchange pathways to be the governing mechanism behind the antiferromagnetic interaction (if shown). In order to find all the possible pathways, we have considered following limiting factors:

- Only the nearest neighbor and next nearest neighbor Br···Br interactions among $(CuBr_4)^{2-}$ tetrahedra have been considered.
- As the dependence of interaction strength on Br···Br distance is qualitative, we have chosen a distance of 5.5 Å since this value has been observed in many materials to be the limiting distance above which the exchange strength becomes negligible.[22]
- More importance has been given on Br···Br distance as compared to the Cu-Br···Br and Br···Br-Cu bond angles and Cu-Br···Br-Cu dihedral angles during comparative discussion on the interaction strengths.

The comparative studies on Br···Br distances and the Cu-Br···Br, Br···Br-Cu bond angles and Cu-Br···Br-Cu dihedral angles along all possible directions were not straight forward due to the low symmetry of triclinic crystal structure of the compound **3**. We have observed that each $(CuBr_4)^{2-}$ tetrahedron takes part in different types of two halide interaction pathways with nearest neighbor tetrahedron along the three crystallographic axes (“**corner-corner**”, “**edge-edge**” and “**corner-edge**” interaction topologies).

5.3.2.1 *ac*-plane Projection:

When viewed along *b*-axis, each $(CuBr_4)^{2-}$ tetrahedron is seen to take part in eight possible two halide exchange pathways with nearest neighbor tetrahedra (see **Figure 5.4**, corresponding interaction parameters have been included in **Table 5.3**). The pathway with shortest Br$\cdots$Br distance is the Br1$\cdots$Br1 pathway which follows a "**corner$\cdots$edge**" interaction topology (***1ce***, $d_{\mathrm{Br1...Br1}}$ = 3.9329 (11) Å, blue dashed line). Although this interaction looks very promising due to very small distance, the $\theta_{\mathrm{Cu\text{-}Br1...Br1}}$ and $\theta_{\mathrm{Br1...Br1\text{-}Cu}}$ angles are very steep, making it difficult to comment on the interaction strength (**Table 5.3**).

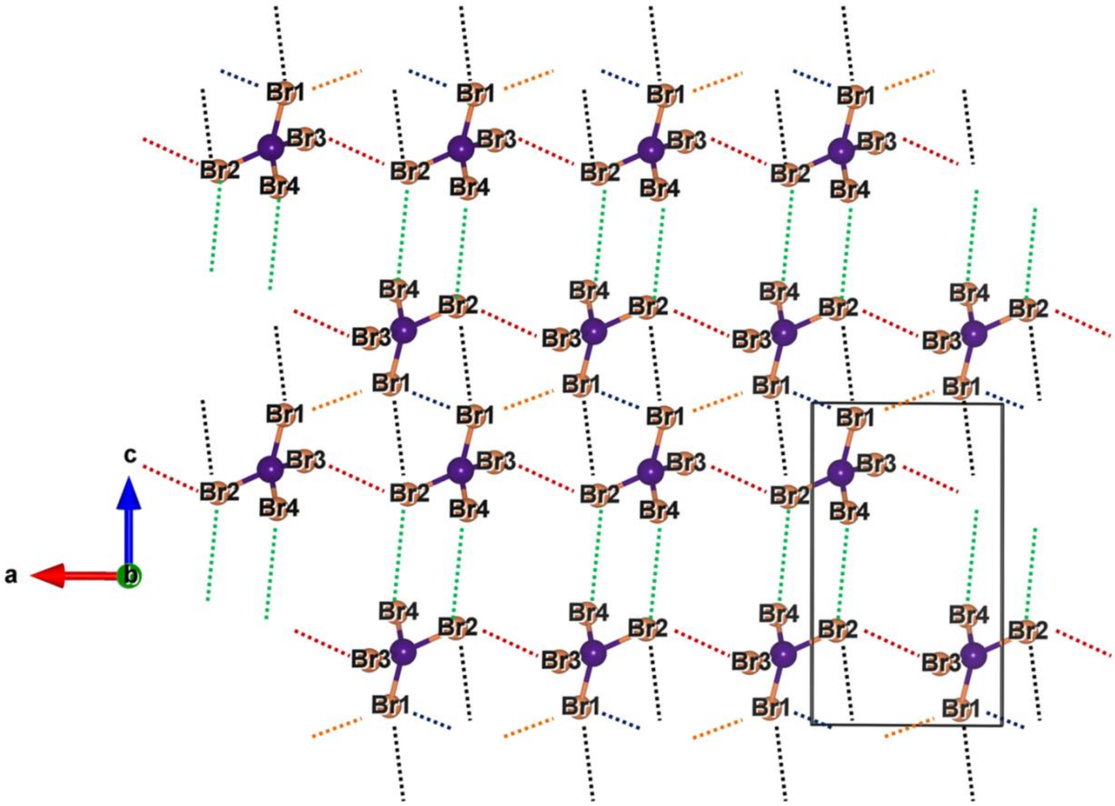

Figure 5.4 The possible two halide Cu-Br$\cdots$Br-Cu exchange pathways when in *ac*-plane. Corresponding structural parameters have been included in **Table 5.3**.

Table 5.3 Structural parameters for different Cu-Br-Cu-Br exchange pathways in *ac*-plane:

Topology	**$\theta_{\mathrm{Cu\text{-}Br1...Br1}}$ (°)**	**$d_{\mathrm{Br1...Br1}}$ (Å)**	**$\theta_{\mathrm{Br1...Br1\text{-}Cu}}$ (°)**	**$\tau_{\mathrm{Cu\text{-}Br1...Br1\text{-}Cu}}$ (°)**
1ce	81.71 (6)	3.9329 (11)	81.71 (6)	180.00 (3)
Topology	**$\theta_{\mathrm{Cu\text{-}Br1...Br1}}$ (°)**	**$d_{\mathrm{Br1...Br1}}$ (Å)**	**$\theta_{\mathrm{Br1...Br1\text{-}Cu}}$ (°)**	**$\tau_{\mathrm{Cu\text{-}Br1...Br1\text{-}Cu}}$ (°)**
1cc	92.60 (6)	5.4146 (13)	92.60 (6)	180.00 (3)
Topology	**$\theta_{\mathrm{Cu\text{-}Br1...Br2}}$ (°)**	**$d_{\mathrm{Br1...Br2}}$ (Å)**	**$\theta_{\mathrm{Br1...Br2\text{-}Cu}}$ (°)**	**$\tau_{\mathrm{Cu\text{-}Br1...Br2\text{-}Cu}}$ (°)**

2ee	144.67 (6)	4.2064 (9)	75.87 (5)	29.68 (3)
Topology	$\theta_{\text{Cu-Br2...Br3}}$ **(°)**	$d_{\text{Br2...Br3}}$ **(Å)**	$\theta_{\text{Br2...Br3-Cu}}$ **(°)**	$\tau_{\text{Cu-Br2...Br3-Cu}}$ **(°)**
2cc	130.01 (6)	4.1165 (10)	123.44 (6)	74.43 (3)
Topology	$\theta_{\text{Cu-Br2...Br4}}$ **(°)**	$d_{\text{Br2...Br4}}$ **(Å)**	$\theta_{\text{Br2...Br4-Cu}}$ **(°)**	$\tau_{\text{Cu-Br2...Br4-Cu}}$ **(°)**
2ee	124.54 (6)	4.7983 (10)	106.94 (5)	66.80 (3)

The Br1 atoms also exhibit another possible interaction pathway with each other which is associated with steep $\theta_{\text{Cu-Br1...Br1}}$ and $\theta_{\text{Br1...Br1-Cu}}$ angles ($d_{\text{Br1...Br1}}$ = 5.4146 (13) Å, orange dashed line in **Figure 5.4**). The other 6 interactions involve 3 sets of identical interaction pairs. One of these three pairs propagates along a chain involving the Br2 and Br3 atoms at the corners of nearest neighbor $(CuBr_4)^{2-}$ tetrahedra along *a*-axis (***2cc***, $d_{\text{Br2...Br3}}$ = 4.1165 (10) Å, red dashed line in **Figure 5.4**). Based on the magnitudes of the distance and the angles, this interaction is possibly a strong one. The other two interaction pairs are each dimeric in nature and follow edge-shared topology (***2ee***) involving the Br1···Br2 bridge ($d_{\text{Br1...Br2}}$ = 4.2064 (9) Å, black dashed lines in **Figure 5.4**) and Br2···Br4 bridge ($d_{\text{Br2...Br4}}$ = 4.7983 (10) Å, green dashed lines in **Figure 5.4**). The Cu-Br2···Br4-Cu interaction pathway has a large Br···Br distance and thus is expected to have weak interaction strength. In a nutshell, from this projection, we can propose that compound **3** in its *ac*-plane possibly has *1-D* antiferromagnetic ladder interactions where the chain interaction propagates through Cu-Br2···Br3-Cu pathway and the rung interaction propagates through Cu-Br2···Br4-Cu and Cu-Br1···Br1-Cu pathways. Also, the dimeric interaction pathway Cu-Br2···Br4-Cu indicates that the ladders can possibly have weak inter-ladder exchange interaction.

5.3.2.2 *bc*-plane Projection:

Now we focus on finding the possible interaction pathways in crystallographic *bc*-plane. Analyses on the *bc*-plane projection indicate that each $(CuBr_4)^{2-}$ tetrahedron takes part in seven possible exchange pathways (see **Figure 5.5**, **Table 5.4**). These consist of four different pathways in which three are identical pairs. From topological point of view, we can see that there is one "**corner···corner**" interaction (involving Br1···Br1, orange dashed line in **Figure 5.5**), one "**edge···edge**" interaction pair (Br1···Br3, green dashed line in **Figure 5.5**) and two different pairs of "**edge···corner**" interactions (Br2···Br4 and Br3···Br4, blue and red dashed lines in **Figure 5.5**). Considering the shortest Br···Br distance, the possible strongest interaction pathway seems to be the Cu-Br3···Br4-Cu pathway ($d_{Br3...Br4}$ = 4.2556 (11) Å), which is a *1-D* interaction pathway along *b*-axis. Second strongest interaction is possibly the one involving Cu-Br1···Br3-Cu pathway ($d_{Br1...Br3}$ = 4.3546 (10) Å). On the other hand, the dimeric Cu-Br1···Br1-Cu pathway with $d_{Br1...Br1}$ = 5.4146 (13) Å is possibly the weakest interaction pathway. In *bc*-plane, collectively, we observe *1-D* antiferromagnetic spin ladder interaction where the chain interaction propagates through Br3···Br4 and Br2···Br4 pathways and the rung interaction propagates through Br1···Br3 and Br1···Br3 pathways within a ladder (isolated ladders).

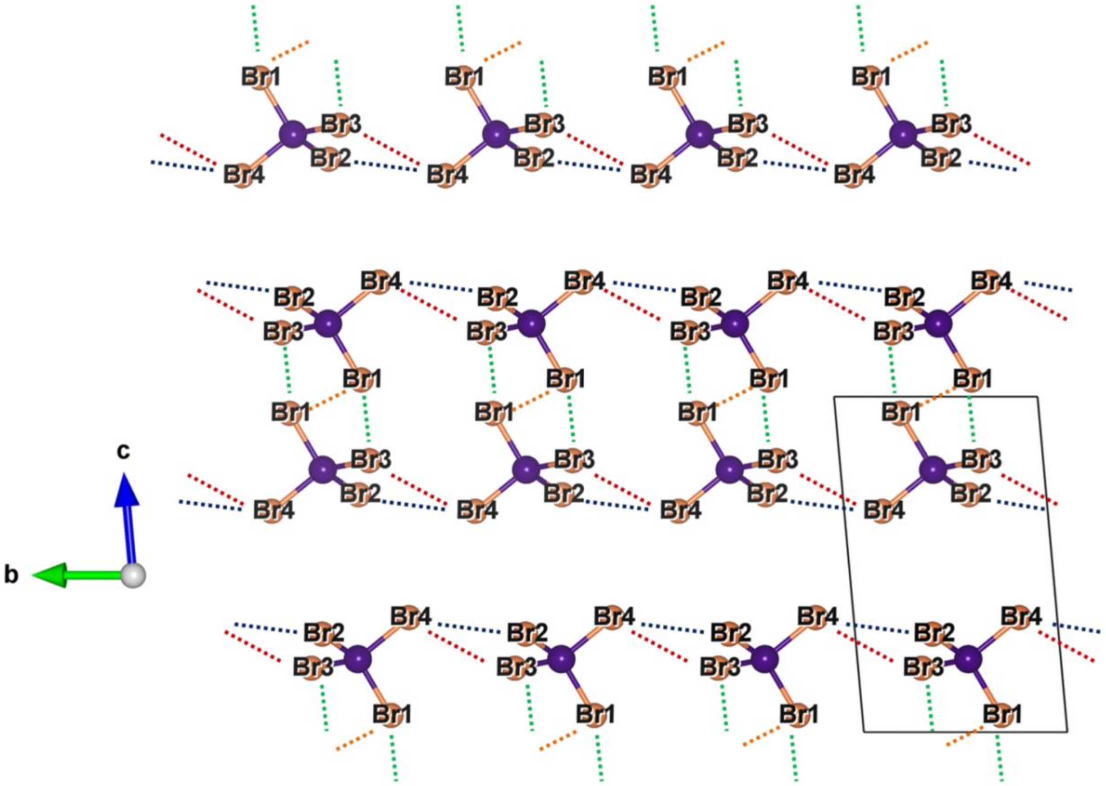

Figure 5.5 The possible two halide Cu-Br···Br-Cu exchange pathways when in *bc*-plane. Corresponding structural parameters have been included in Table **5.4**.

Table 5.4 Structural parameters for different Cu-Br-Cu-Br exchange pathways in *bc*-plane:

Topology	**$\theta_{Cu-Br1...Br1}$ (°)**	***d*$_{Br1...Br1}$ (Å)**	**$\theta_{Br1...Br1-Cu}$ (°)**	**$\tau_{Cu-Br1...Br1-Cu}$ (°)**
1cc	92.60 (6)	5.4146 (13)	92.60 (6)	180.00 (3)
Topology	**$\theta_{Cu-Br1...Br3}$ (°)**	***d*$_{Br1...Br3}$ (Å)**	**$\theta_{Br1...Br3-Cu}$ (°)**	**$\tau_{Cu-Br1...Br3-Cu}$ (°)**

2ee	133.59 (7)	4.3546 (10)	123.98 (5)	24.81 (3)
Topology	**$\theta_{Cu-Br2...Br4}$ (°)**	**$d_{Br2...Br4}$ (Å)**	**$\theta_{Br2...Br4-Cu}$ (°)**	**$\tau_{Cu-Br2...Br4-Cu}$ (°)**
2ec	92.68 (6)	5.2481 (12)	125.37 (6)	98.34 (3)
Topology	**$\theta_{Cu-Br3...Br4}$ (°)**	**$d_{Br3...Br4}$ (Å)**	**$\theta_{Br3...Br4-Cu}$ (°)**	**$\tau_{Cu-Br3...Br4-Cu}$ (°)**
2ec	121.48 (6)	4.2556 (11)	114.92 (5)	125.49 (2)

5.3.2.3 *ab*-plane Projection:

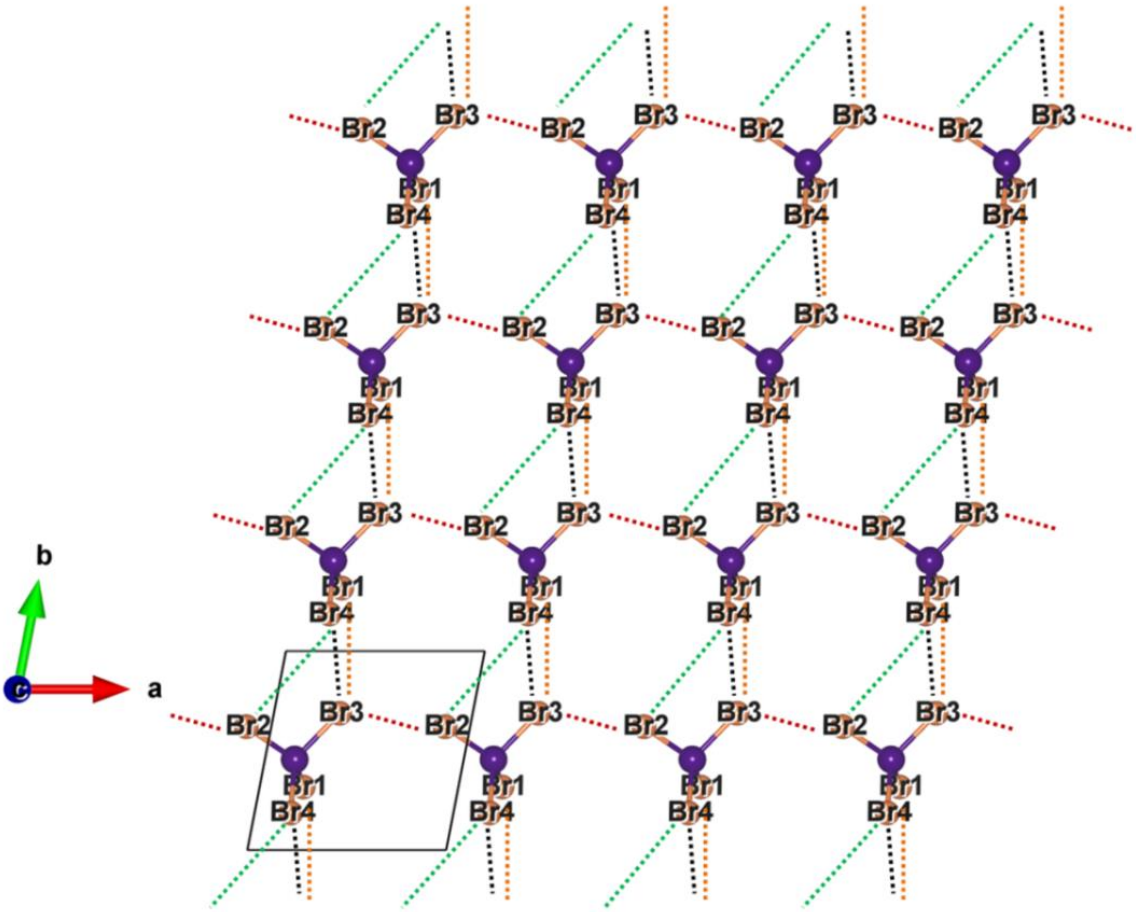

Figure 5.6 The possible two halide Cu-Br···Br-Cu exchange pathways when in *ab*-plane. Corresponding structural parameters have been included in Table **5.5**.

In order to identify possible exchange pathways in *ab*-plane, we have focused on a packing with keeping the *c*-axis length to half of *c* lattice parameter value for the sake of simplicity. In this projection, it can be observed that each $(CuBr_4)^{2-}$ tetrahderon is seen take part in eight possible interaction pathways (see **Figure 5.6** and **Table 5.5**). These interactions can be categorized into four distinct pathways with each of these being basically an identical pair of interactions. It is observed that in each tetrahedron, the Br3 atom takes part in three interaction pathways viz. two via "**corner**···**corner**" topology (***2cc***, red dashed line, Br2···Br3; black dashed line, Br3···Br4) as can be seen in **Figure 5.6**. Both of these interactions are associated with short Br···Br distances ($d_{Br2...Br3}$ = 4.1165 (10) Å, $d_{Br3...Br4}$ = 4.2556 (11) Å), **Table 5.5**) which is indicative of strong interaction strengths.

Table 5.5 Structural parameters for different Cu-Br-Cu-Br exchange pathways in *ab*-plane:

Topology	**$\theta_{Cu-Br1...Br3}$ (°)**	**$d_{Br1...Br3}$ (Å)**	**$\theta_{Br1...Br3-Cu}$ (°)**	**$\tau_{Cu-Br1...Br3-Cu}$ (°)**
2ee	99.40 (5)	4.7876 (11)	135.82 (7)	93.56 (3)
Topology	**$\theta_{Cu-Br2...Br3}$ (°)**	**$d_{Br2...Br3}$ (Å)**	**$\theta_{Br2...Br3-Cu}$ (°)**	**$\tau_{Cu-Br2...Br3-Cu}$ (°)**
2cc	130.01 (6)	4.1165 (10)	123.44 (6)	74.43 (3)
Topology	**$\theta_{Cu-Br2...Br4}$ (°)**	**$d_{Br2...Br4}$ (Å)**	**$\theta_{Br2...Br4-Cu}$ (°)**	**$\tau_{Cu-Br2...Br4-Cu}$ (°)**
2ee	92.68 (6)	5.2481 (12)	125.36 (6)	98.34 (3)
Topology	**$\theta_{Cu-Br3...Br4}$ (°)**	**$d_{Br3...Br4}$ (Å)**	**$\theta_{Br3...Br4-Cu}$ (°)**	**$\tau_{Cu-Br3...Br4-Cu}$ (°)**
2cc	128.48 (6)	4.2556 (11)	114.92 (5)	125.49 (2)

The other two interactions involve "**edge**···**edge**" topologies (***2ee***, orange dashed line, Br1···Br3; green dashed line, Br2···Br4, **Figure 5.6**). Among all possible pathways, the Cu-Br2···Br3-Cu pathway seems to be the strongest as it is associated with minimum Br···Br distance ($d_{Br2...Br3}$ = 4.1165 (10) Å). All the interaction pathways are seen to form different *1-D* chains, propagating along different directions. It is also observed that all the chains are linked to each other via orthogonal interaction pathways. Such interaction topology constructs a *2-D* rectangular lattice antiferromagnet model (in *ab*-plane). Additionally, if the *c*-axis length is increased, we can find "**edge**···**edge**" interactions through Br2···Br4 bridges within two planar sheets (***2ee***, green dashed lines in **Figure 5.4**). Thus, based on these interactions, a "plaquette" of a coupled *2-D* rectangular antiferromagnetic lattices can be portrayed.

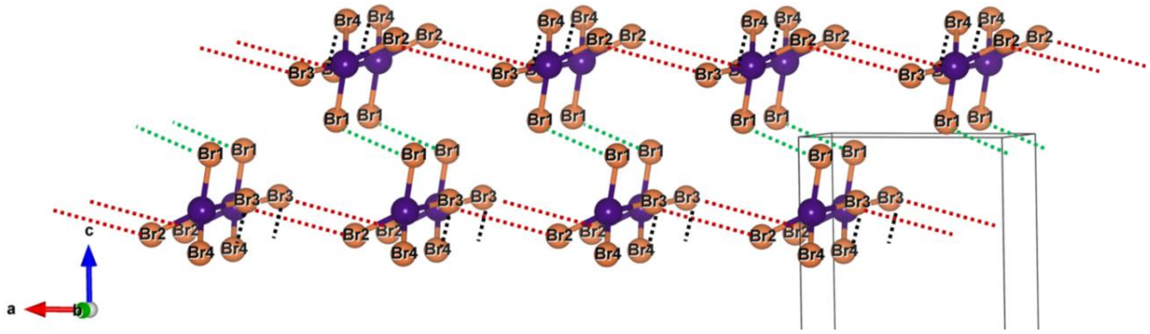

Figure 5.7 View of the coupled ladder geometry. J_{rail} is propagating through Br2···Br3 bridges between tetrahedra along *a*-axis, J_{rung} is propagating through dimeric Br1···Br1 bridges (strongest) between tetrahedra along *c*-axis and interladder interaction is propagating through Br3···Br4 bridge between tetrahedra along *b*-axis.

In a nutshell, we have observed that in compound **3**, each $(CuBr_4)^{2-}$ tetrahedron takes part in multiple number of two halide exchange pathways with nearest neighbor $(CuBr_4)^{2-}$ tetrahedra along all the crystallographic directions. The distances and angles of the interactions pathways indicate that the corresponding interaction strengths are comparable with each other. Coupled spin ladder interactions pathways are observed in *ac*-plane while in *bc*-plane the ladders seem to be isolated from each other. In *ab*-plane, we have observed the interaction pathways to construct a two dimensional rectangular lattice model while the rectangular lattices are seen to be coupled with each other ("plaquette" of Cu^{2+} ions). It has been observed in many reported materials that the interaction strength reduces significantly when the Br···Br distance difference becomes larger than 10% of the minimum Br···Br distance.[22] Among all the possible interaction pathways we have observed, the Cu-Br1···Br1-Cu pathway is the shortest pathway ($d_{Br1...Br1}$ = 3.9329 (11) Å, blue dashed line, **Figure 5.4**) which indicates that this pathway is possibly the strongest one. The second and third strongest pathways are the Cu-Br2···Br3-Cu pathway ($d_{Br2...Br3}$ = 4.1165 (10) Å, red dashed line in **Figure 5.4** and **Figure 5.6**) and Cu-Br3···Br4-Cu pathway ($d_{Br3...Br4}$ = 4.2556 (11) Å, red dashed line in **Figure 5.5**, black dashed line in **Figure 5.6**). Together, these three interactions constitute a coupled ladder arrangement (see in **Figure 5.7**) which has been termed as "plaquette" of rectangular lattice during discussion before.

5.3 Magnetic Properties:

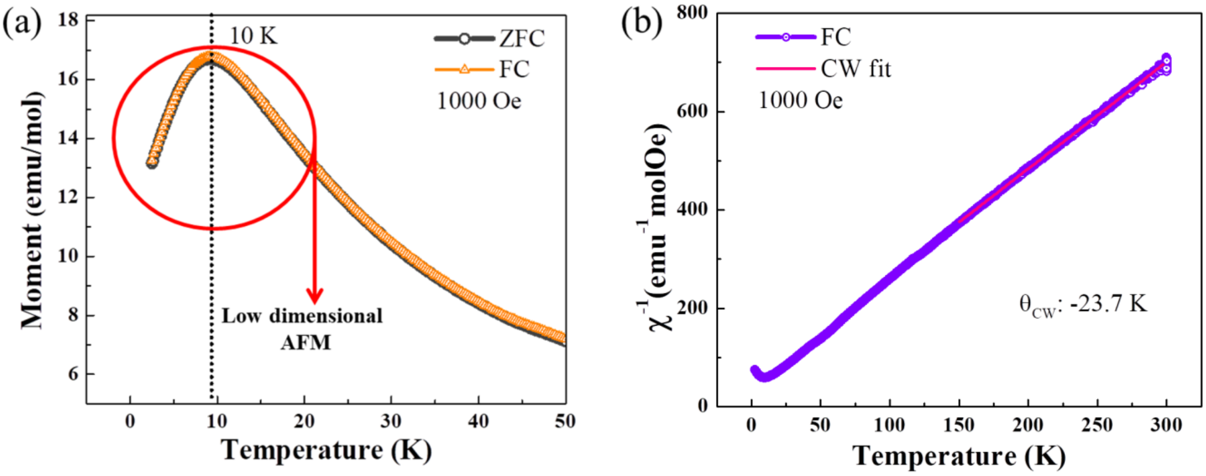

Figure 5.8 (a) Temperature dependent inverse magnetic moment of **3** under 1000 Oe dc field. (b) Inver dc magnetic susceptibility vs temperature data showing paramagnetic behavior. Curie-Weiss fitting has been carried out for the data within region 300-150 K.

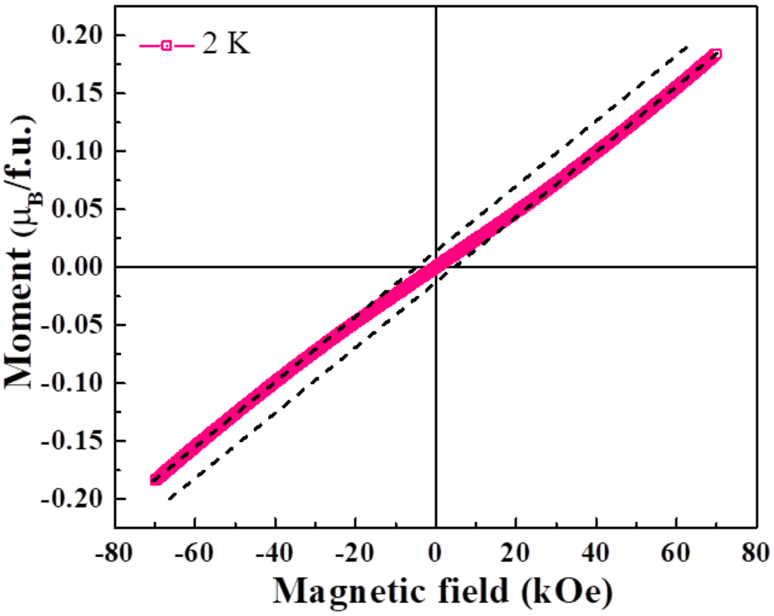

Figure 5.9 Isothermal magnetization against magnetic field data, as recorded at 2 K. Very weak field dependence can be observed, which indicates presence of strong competing magnetic frustration.

Table 5.6 Curie-Weiss fitting parameters:

Region (K)	***C* (emu mol^{-1} Oe^{-1})**	**θ_{CW} (K)**	**$\mu_{effective}$**	**R square**
300-150	0.461	-23.7	1.91 μ_B	0.99993

Temperature dependence of the dc magnetic susceptibility of compound **3** has been measured within the temperature range of 300 K-2 K under 1000 Oe applied field. In **Figure 5.8** (a), the susceptibility behavior is seen to be dominated by a rounded maximum at around 10 K followed by a rapid decrease till 2 K. The inverse magnetic susceptibility linearly decreases on reducing the temperature till nearly 15 K below which it starts increasing till 2 K (see **Figure 5.8** (b)). Curie-Weiss fitting has been carried out at high T region (300 K - 150 K) which gives negative Curie-Weiss constant value of -23.7 K indicating presence of antiferromagnetic interactions (see **Table 5.6**). Overall, such behavior is typical of a low dimensional spin-1/2 compound having Heisenberg antiferromagnetic interactions.

Isothermal magnetization dependence on applied field at 2 K shows spin flop nature where the magnetization features very weak magnetic field dependence. Maximum moment that could be attained is 0.18 μ_B/f.u. under 7 T magnetic field (see **Figure 5.9**). Also, due to the thermal energy influence on magnetic spins, the lower critical field H_{C1} could not be confirmed from this data. Here, it is important to mention that for low dimensional magnets with competing AFM interactions, almost no magnetization is expected as the ground state is spin-singlet (nonmagnetic). Gradual application of external magnetic field closes the gap between singlet and triplet state at certain field (first critical field H_{C1}) which further influences alignment of all spins in field direction (second critical field H_{C2}) towards complete saturation.

For analysing the magnetic susceptibility data, we have used the susceptibility expressions, for *1-D* spin ladder and for *2-D* square and rectangular lattice models. For both of these models, simplified expressions have been used to fit the susceptibility data.[26,59] **Figure 5.10** (a), (b), (c) and (d) shows the fitted susceptibility profiles for *1-D* spin chain, ladder, *2-D* square lattice and rectangular lattice models respectively. Corresponding fitting parameters have been included in **Table 5.7**.

For *1-D* models we have used simplified susceptibility expressions from equation[59]:

$$\chi_{mol}(1 - D\ QHAF) = \frac{C_{mol}}{T}\left[\frac{1 + \sum_{i=1}^{5} N_i \left(\frac{j}{k_B T}\right)^i}{1 + \sum_{i=1}^{6} D_i \left(\frac{j}{k_B T}\right)^i}\right]$$

For *2-D* models the simplified susceptibility expressions where derived from equation[59]:

$$\chi_{mol}(2-D\ QHAF) = \frac{C_{mol}}{T}\left[\frac{\sum_{i=1}^{5} N_i \left(\frac{j}{k_B T}\right)^i}{1+\sum_{i=1}^{5} D_i \left(\frac{j}{k_B T}\right)^i}\right]$$

Table 5.7 Fitting parameters for different models:

Model	C	*J* (K)	Difference in standard deviation $d_{s.d.} = d_{s.d.}^{experimental} - d_{s.d.}^{calculated}$
Spin Chain	0.461	-14.626	0.02904
Spin Ladder	0.461	J_{rail}: -14.454, J_{rung} : -0.254	0.02938
Square Lattice	0.461	-8.278	0.03171
Rectangular Lattice	0.861	*J*: -0.173, *J'* : -2.445	0.01833

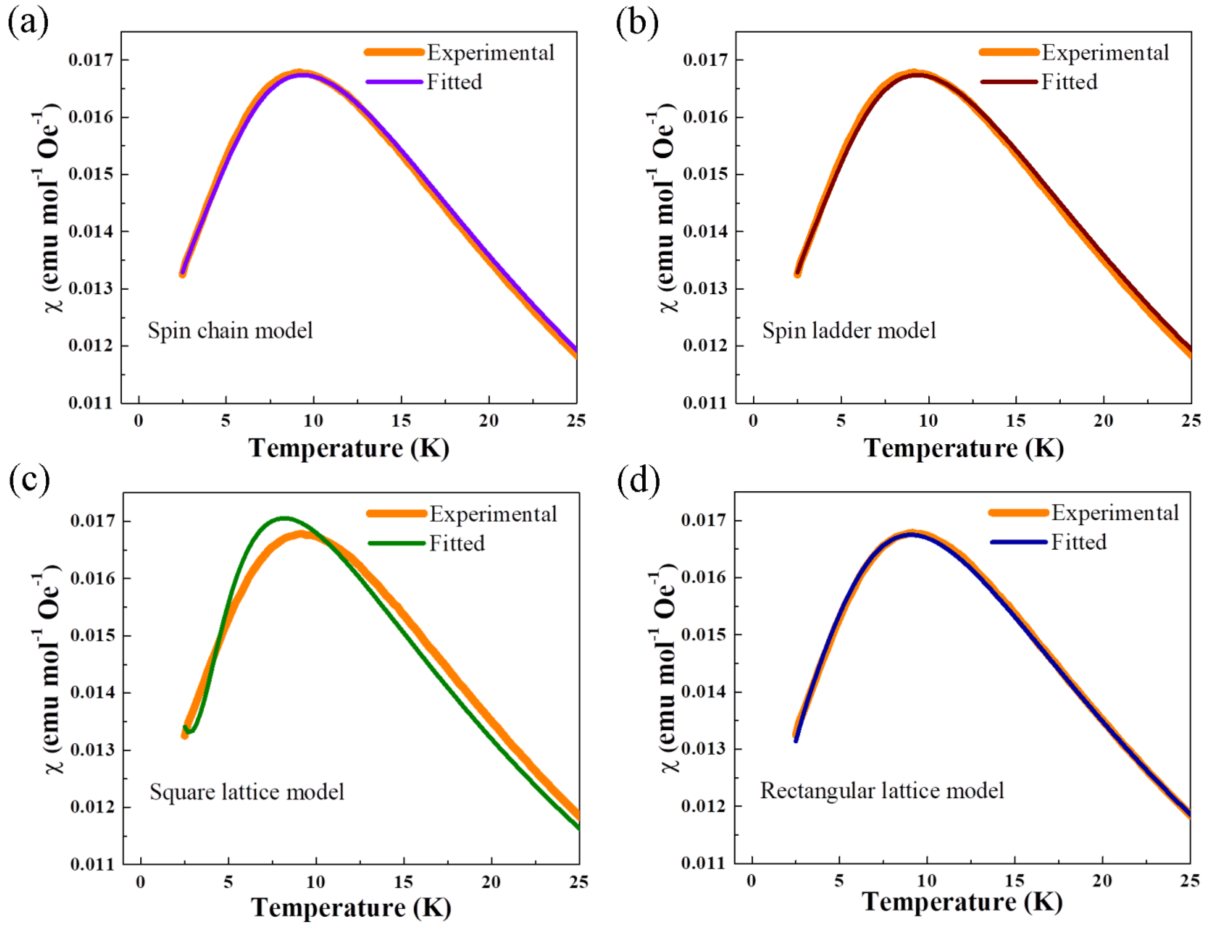

Figure 5.10 Magnetic susceptibility data of compound **3** fitted with susceptibility expressions for (a) spin chain, (b) spin ladder, (c) square lattice and (d) rectangular lattice models respectively.

It can be seen that the rectangular lattice model and the ladder model have qualitatively good fitting parameters. The square lattice model does not fit well, as can be seen from **Figure 5.10** (c) and **Table 5.7**. The spin chain and ladder models have comparable fitting parameters as the interaction strength along rung (***J_{rung}***), derived from ladder model fitting is miniscule. The ladder model fitting parameters indicate that the ladder geometry has strong interaction pathway propagating along the rail and weak pathway along rung of the ladder (***J_{rail}*** = -14.454 K, ***J_{rung}*** = -0.254 K, possible "**strong rail**" ladder). The plaquette geometry (derived from *ab*-plane analyses) could not be assessed via fitting as a suitable model could not be found. With such interaction strengths, where the material behaves as strong rail ladder, the magnetic behavior has compared with the strong rail copper bromide hybrids in the **Table 5.8**.[18,35]

Table 5.8 Literature comparison of magnetic interaction strengths:

Compound	Lattice model	*Exchange strength* J (K)	J_{rung}/J_{rail}	Reference
$(C_5H_{12}N)_2CuBr_4$	Ladder	J_{rail}: -11.6, J_{rung} : -5.5	0.45	35
$(2,3\text{-dmpyH})_2CuBr_4$	Ladder	J_{rail}: -17, J_{rung} : -9	0.53	18
$(CH_6N_3)_2CuBr_4$	Ladder	J_{rail}: -14.454, J_{rung} : -0.254	0.017	This work

5.4 Conclusion:

Thus, we present synthesis, single crystal structure analyses and studies on bulk magnetic properties of guanidinium ion containing Cu^{2+} based hybrid halide, $(CH_6N_3)_2CuBr_4$. At room temperature, the compound crystallizes into triclinic crystal structure featuring isolated $(CuBr_4)^{2-}$ tetrahedra separated by planar guanidinium cations. The guanidinium cations take part in H-bonding interactions with Br atoms of $(CuBr_4)^{2-}$ tetrahedra and also form strong ion-pair complex with each other (via "eclipsed" and "head-on" interactions), stabilizing the structure to large extent. Thus at 95 K, the structure remains nearly similar with only subtle changes that are observed in lattice parameters. DC magnetization measurements reveal a broad anomaly centred at 10 K, typical of a low dimensional antiferromagnetic compound. Crystal structure analyses reveal Cu-Br···Br-Cu two halide exchange pathway to be the mechanism. In crystallographic *ac*-plane and *bc*-plane, coupled and isolated spin ladder type interaction pathways are observed. In *ab*-plane, a plaquette of nearest neighbour 2-D rectangular AFM layers can be portrayed. We have used suspectibility expressions for spin-1/2 antiferromagnetic spin chain, ladder, square and rectangular lattice to analyse and fit susceptibility as a function of temperature behavior. The rectangular lattice model gives the best fitting parameters while spin ladder model fitting parameters are also qualitatively good. In future, we intend to study the susceptibility using a suitable expression for plaquette model. Also, we would like to determine the magnetic ground state of the material.

Atomic position lists:

Table 5.8 Atomic coordinates (x10^4) and equivalent isotropic displacement parameters (Å^{2}x10^3) for compound **3** at 95 K with estimated standard deviations in parentheses.

Label	x	Y	z	Occupancy	U_{eq}^*
Cu(1)	1498(1)	4552(1)	2178(1)	1	9(1)
Br(1)	2193(1)	3169(1)	498(1)	1	10(1)
Br(2)	-1257(1)	6202(1)	2923(1)	1	12(1)
Br(3)	3304(1)	6874(1)	1906(1)	1	12(1)
Br(4)	1818(1)	1864(1)	3414(1)	1	12(1)
C(1)	-2536(8)	1030(7)	1270(4)	1	10(2)
N(1)	-786(7)	177(6)	1339(4)	1	16(2)
H(1A)	-526	-984	1507	1	19
H(1B)	97	782	1216	1	19
N(2)	-3895(6)	108(6)	1458(4)	1	12(1)
H(2A)	-3639	-1054	1627	1	15
H(2B)	-5036	668	1413	1	15
N(3)	-2939(7)	2829(6)	1041(4)	1	18(2)
H(3A)	-2057	3440	938	1	22
H(3B)	-4082	3385	997	1	22
C(2)	3493(9)	7397(8)	5173(5)	1	14(2)
N(4)	1944(7)	7165(7)	4730(4)	1	17(2)
H(4A)	1004	7024	5142	1	21
H(4B)	1870	7154	4027	1	21
N(5)	3613(8)	7415(8)	6245(4)	1	24(2)
H(5A)	2675	7274	6660	1	28
H(5B)	4630	7567	6533	1	28
N(6)	4935(7)	7601(7)	4535(4)	1	18(2)
H(6A)	4858	7582	3833	1	21
H(6B)	5952	7754	4822	1	21

Table 5.9 Atomic coordinates (x10^4) and equivalent isotropic displacement parameters (Å^{2}x10^3) for compound **3** at 295 K with estimated standard deviations in parentheses.

Label	x	y	z	Occupancy	U_{eq}^*
N(4)	1903(10)	7262(10)	4750(6)	1	66(2)
H(4A)	1896	7205	4069	1	79
H(4B)	916	7192	5138	1	79

N(6)	4907(11)	7562(10)	4602(6)	1	74(2)
H(6A)	4899	7505	3921	1	89
H(6B)	5902	7690	4895	1	89
C(2)	3405(11)	7455(10)	5195(6)	1	48(2)
N(5)	3450(12)	7502(13)	6235(6)	1	104(4)
H(5A)	2479	7405	6631	1	125
H(5B)	4450	7630	6522	1	125
Br(1)	2270(2)	3180(1)	535(1)	1	46(1)
Br(2)	-1178(1)	6254(1)	2962(1)	1	53(1)
Br(3)	3470(2)	6775(2)	1983(1)	1	52(1)
Br(4)	1938(2)	1891(1)	3386(1)	1	51(1)
Cu(1)	1605(2)	4553(2)	2203(1)	1	39(1)
N(2)	-3758(9)	134(8)	1458(5)	1	55(2)
H(2A)	-3537	-992	1680	1	66
H(2B)	-4886	707	1372	1	66
C(1)	-2372(11)	977(9)	1250(5)	1	40(2)
N(1)	-654(9)	133(9)	1375(6)	1	60(2)
H(1A)	-414	-993	1596	1	72
H(1B)	241	702	1236	1	72
N(3)	-2751(10)	2716(9)	934(6)	1	70(2)
H(3A)	-1861	3296	810	1	84
H(3B)	-3887	3268	853	1	84

5.5 Bibliography:

(1) BEDNORZ, J. G.; MÜLLER, K. A.; TAKASHIGE, M. Superconductivity in Alkaline Earth-Substituted La_2CuO_{4-Y}; *Science (80-.).* **1987**, *236* (4797), 73 LP – 75.

(2) Tholence, J. L. Superconductivity of La_2CuO_4 and $YBa_2Cu_3O_7$. *Phys. B+C* **1987**, *148* (1), 353–356.

(3) de Jongh, L. J.; Miedema, A. R. Experiments on Simple Magnetic Model Systems. *Adv. Phys.* **1974**, *23* (1), 1–260.

(4) Steadman, J. P.; Willett, R. D. The Crystal Structure of $(C_2H_5NH_3)_2CuCl_4$. *Inorganica Chim. Acta* **1970**, *4*, 367–371.

(5) Barendregt, F.; Schenk, H. The Crystal Structure of $CuCl_4(NH_3C_3H_7)_2$. *Physica* **1970**, *49* (3), 465–468.

(6) Dupas, A.; Le Dang, K.; Renard, J. -P.; Veillet, P.; Daoud, A.; Perret, R. Magnetic Properties of the Nearly Two-dimensional Ferromagnets $[C_6H_5(CH_2)_NNH_3]_2CuCl_4$ with N=1,2,3. *J. Chem. Phys.* **1976**, *65* (10), 4099–4102.

(7) Willett, R. D.; Landee, C.; Swank, D. D. Magnetic Susceptibility of CuCl2·TMSO, a Ferromagnetic Spin 1/2 Linear Chain. *J. Appl. Phys.* **1978**, *49* (3), 1329–1330.

(8) Swank, D. D.; Landee, C. P.; Willett, R. D. Crystal Structure and Magnetic Susceptibility of Copper (II) Chloride Tetramethylsulfoxide $[CuCl_2(TMSO)]$ and Copper (II) Chloride Monodimethylsulfoxide $[CuCl_2(DMSO)]$: Ferromagnetic Spin-half Heisenberg Linear Chains. *Phys. Rev. B* **1979**, *20* (5), 2154–2162.

(9) Landee, C. P.; Willett, R. D. Tetramethylammonium Copper Chloride and Tris (Trimethylammonium) Copper Chloride: S=1/2 Heisenberg One-Dimensional Ferromagnets. *Phys. Rev. Lett.* **1979**, *43* (6), 463–466.

(10) Willett R.D., Gaura R.M., L. C. P. Ferromagnetism in Linear Chains. In: Miller J.S. (Eds) Extended Linear Chain Compounds. *Springer, Boston, MA* **1983**, 143–191.

(11) Woodward, F. M.; Albrecht, A. S.; Wynn, C. M.; Landee, C. P.; Turnbull, M. M. Two-Dimensional S=1/2 Heisenberg Antiferromagnets: Synthesis, Structure, and Magnetic Properties. *Phys. Rev. B* **2002**, *65* (14), 144412.

(12) Woodward, F. M.; Landee, C. P.; Giantsidis, J.; Turnbull, M. M.; Richardson, C. Structure and Magnetic Properties of $(5BAP)_2CuBr_4$: Magneto-Structural Correlations of Layered S=1/2 Heisenberg Antiferromagnets. *Inorganica Chim.*

Acta **2001**, *324* (1), 324–330.

(13) Snively, L. O.; Tuthill, G. F.; Drumheller, J. E. Measurement and Calculation of the Superexchange Interaction through the Two-Halide Bridge in the Eclipsed Layered Compounds $[NH_3(CH_2)_nNH_3]CuX$ for n=2−5 and X=Cl_4 and Cl_2Br_2. *Phys. Rev. B* **1981**, *24* (9), 5349–5355.

(14) Block, R.; Jansen, L. Theoretical Analysis of Double-Halide Superexchange in Layered Solids of the Compounds $[NH_3(CH_2)_nNH_3]CuX$ for n=2−5 and X=Cl_4 and Cl_2Br_2. *Phys. Rev. B* **1982**, *26* (1), 148–153.

(15) Straatman, P.; Block, R.; Jansen, L. Theoretical Analysis of Double-Halide Superexchange in Layered Solids of the Compounds $[NH_3(CH_2)_nNH_3]CuBr_4$ with n=3 and 4. *Phys. Rev. B* **1984**, *29* (3), 1415–1418.

(16) Rubenacker, G. V; Waplak, S.; Hutton, S. L.; Haines, D. N.; Drumheller, J. E. Magnetic Susceptibility and Magnetic Resonance in the Ordered State of Single-crystal $[NH_3(CH_2)_2HN_3]CuBr_4$. *J. Appl. Phys.* **1985**, *57* (8), 3341–3342.

(17) Willett, R. D.; Galeriu, C.; Landee, C. P.; Turnbull, M. M.; Twamley, B. Structure and Magnetism of a Spin Ladder System: $(C_5H_9NH_3)_2CuBr_4$. *Inorg. Chem.* **2004**, *43* (13), 3804–3811.

(18) Shapiro, A.; Landee, C. P.; Turnbull, M. M.; Jornet, J.; Deumal, M.; Novoa, J. J.; Robb, M. A.; Lewis, W. Synthesis, Structure, and Magnetic Properties of an Antiferromagnetic Spin-Ladder Complex: Bis(2,3-Dimethylpyridinium) Tetrabromocuprate. *J. Am. Chem. Soc.* **2007**, *129* (4), 952–959.

(19) Butcher, R. T.; Landee, C. P.; Turnbull, M. M.; Xiao, F. Rectangular Two-Dimensional Antiferromagnetic Systems: Analysis of Copper(II) Pyrazine Dibromide and Dichloride. *Inorganica Chim. Acta* **2008**, *361* (12), 3654–3658.

(20) Herringer, S. N.; Longendyke, A. J.; Turnbull, M. M.; Landee, C. P.; Wikaira, J. L.; Jameson, G. B.; Telfer, S. G. Synthesis, Structure, and Magnetic Properties of Bis(Monosubstituted-Pyrazine)Dihalocopper(II). *Dalt. Trans.* **2010**, *39* (11), 2785–2797.

(21) Butcher, R. T.; Novoa, J. J.; Ribas-Ariño, J.; Sandvik, A. W.; Turnbull, M. M.; Landee, C. P.; Wells, B. M.; Awwadi, F. F. Strong Through-Space Two-Halide Magnetic Exchange of −234 K in (2,5-Dimethylpyrazine)Copper(II) Bromide. *Chem. Commun.* **2009**, No. 11, 1359–1361.

(22) Turnbull, M. M.; Landee, C. P.; Wells, B. M. Magnetic Exchange Interactions in Tetrabromocuprate Compounds. *Coord. Chem. Rev.* **2005**, *249* (23), 2567–2576.

(23) Snively, L. O.; Haines, D. N.; Emerson, K.; Drumheller, J. E. Two-Halide Superexchange in $[NH_3(CH_2)_nNH_3]CuBr_4$ for n=3 and 4. *Phys. Rev. B* **1982**, *26* (9), 5245–5247.

(24) R.D. Willett, D. Gatteschi, O. K. (Eds. . Magneto-Structural Correlations in Exchange Coupled Systems. *Rei-del, Boston*, **1989**, 389.

(25) Chow, C.; Chang, K.; Willett, R. D. Electron Spin Resonance Spectra and Covalent Bonding in the Square-planar $CuCl_4^{2-}$ and $CuBr_4^{2-}$ Ions. *J. Chem. Phys.* **1973**, *59* (5), 2629–2640.

(26) Landee, C. P.; Turnbull, M. M. Review: A Gentle Introduction to Magnetism: Units, Fields, Theory, and Experiment. *J. Coord. Chem.* **2014**, *67* (3), 375–439.

(27) Morosin, B. Structure Refinements on Dichloro- and Dibromobis(Pyridine)Copper(II). *Acta Crystallogr. Sect. B* **1975**, *31* (2), 632–634.

(28) Duffy, W.; Venneman, J. E.; Strandburg, D. L.; Richards, P. M. Magnetic and Thermal Studies of Antiferromagnetic Linear Chains in Dichlorobis (Pyridine)Copper (II). *Phys. Rev. B* **1974**, *9* (5), 2220–2227.

(29) Santoro, A.; Mighell, A. D.; Reimann, C. W. The Crystal Structure of a 1:1 Cupric Nitrate{--}pyrazine Complex $Cu(NO_3)_2.(C_4N_2H_4)$. *Acta Crystallogr. Sect. B* **1970**, *26* (7), 979–984.

(30) Hammar, P. R.; Stone, M. B.; Reich, D. H.; Broholm, C.; Gibson, P. J.; Turnbull, M. M.; Landee, C. P.; Oshikawa, M. Characterization of a Quasi-One-Dimensional Spin-1/2 Magnet Which Is Gapless and Paramagnetic for $g\mu_BH < J$ and $k_BT << J$. *Phys. Rev. B* **1999**, *59* (2), 1008–1015.

(31) SCHMIDT, K. A. I. P.; UHRIG, G. S. SPECTRAL PROPERTIES OF MAGNETIC EXCITATIONS IN CUPRATE TWO-LEG LADDER SYSTEMS. *Mod. Phys. Lett. B* **2005**, *19* (24), 1179–1205.

(32) Nakanishi, T.; Motoyama, N.; Mitamura, H.; Takeshita, N.; Takahashi, H.; Eisaki, H.; Uchida, S.; Môri, N. Magnetic Field Effect on the Pressure-Induced Superconducting State in the Hole-Doped Two-Leg Ladder Compound $Sr_2Ca_{12}Cu_{24}O_{41}$. *Phys. Rev. B* **2005**, *72* (5), 54520.

(33) Vuletić, T.; Korin-Hamzić, B.; Ivek, T.; Tomić, S.; Gorshunov, B.; Dressel, M.; Akimitsu, J. The Spin-Ladder and Spin-Chain System $(La,Y,Sr,Ca)_{14}Cu_{24}O_{41}$: Electronic Phases, Charge and Spin Dynamics. *Phys. Rep.* **2006**, *428* (4), 169–258.

(34) Azuma, M.; Hiroi, Z.; Takano, M.; Ishida, K.; Kitaoka, Y. Observation of a Spin Gap in $SrCu_2O_3$ Comprising Spin-half Quasi-1D Two-Leg Ladders. *Phys. Rev.*

Lett. **1994**, *73* (25), 3463–3466.

(35) Willett, R. D.; Galeriu, C.; Landee, C. P.; Turnbull, M. M.; Twamley, B. Structure and Magnetism of a Spin Ladder System: $(C_5H_9NH_3)_2CuBr_4$. *Inorg. Chem.* **2004**, *43* (13), 3804–3811.

(36) Hong, T.; Zheludev, A.; Manaka, H.; Regnault, L.-P. Evidence of a Magnetic Bose Glass in $(CH_3)_2CHNH_3Cu(Cl_{0.95}Br_{0.05})_3$ from Neutron Diffraction. *Phys. Rev. B* **2010**, *81* (6), 60410.

(37) Schmidiger, D.; Mühlbauer, S.; Gvasaliya, S. N.; Yankova, T.; Zheludev, A. Long-Lived Magnons throughout the Brillouin Zone of the Strong-Leg Spin Ladder $(C_7H_{10}N)_2CuBr_4$. *Phys. Rev. B* **2011**, *84* (14), 144421.

(38) Jeong, M.; Mayaffre, H.; Berthier, C.; Schmidiger, D.; Zheludev, A.; Horvatić, M. Magnetic-Order Crossover in Coupled Spin Ladders. *Phys. Rev. Lett.* **2017**, *118* (16), 1–5.

(39) Perren, G. S.; Lorenz, W. E. A.; Ressouche, E.; Zheludev, A. Field-Induced Ordering in a Random-Bond Quantum Spin Ladder Compound with Weak Anisotropy. *Phys. Rev. B* **2018**, *97* (17), 174431.

(40) Hong, T.; Kim, Y. H.; Hotta, C.; Takano, Y.; Tremelling, G.; Turnbull, M. M.; Landee, C. P.; Kang, H.-J.; Christensen, N. B.; Lefmann, K.; et al. Field-Induced Tomonaga-Luttinger Liquid Phase of a Two-Leg Spin-1/2 Ladder with Strong Leg Interactions. *Phys. Rev. Lett.* **2010**, *105* (13), 137207.

(41) Bettler, S.; Simutis, G.; Perren, G.; Blosser, D.; Gvasaliya, S.; Zheludev, A. High-Pressure Raman Study of the Quantum Magnet $(C_4H_{12}N_2)Cu_2Cl_6$. *Phys. Rev. B* **2017**, *96* (17), 174431.

(42) Uehara, M.; Nagata, T.; Akimitsu, J.; Takahashi, H.; Môri, N.; Kinoshita, K. Superconductivity in the Ladder Material $Sr_{0.4}Ca_{13.6}Cu_{24}O_{41.84}$. *J. Phys. Soc. Japan* **1996**, *65* (9), 2764–2767.

(43) TARASCON, J. M.; GREENE, L. H.; MCKINNON, W. R.; HULL, G. W.; GEBALLE, T. H. Superconductivity at 40 K in the Oxygen-Defect Perovskites $La_{2-x}Sr_xCuO_{4-y}$; *Science (80-.).* **1987**, *235* (4794), 1373 LP – 1376.

(44) Ovchinnikov, S. G.; Sandalov, I. S. The Band Structure of Strong-Correlated Electrons in $La_{2-x}Sr_xCuO_4$ and $YBa_2Cu_3O_{7-y}$. *Phys. C Supercond.* **1989**, *161* (5), 607–617.

(45) Darriet, J.; Haddad, M. S.; Duesler, E. N.; Hendrickson, D. N. Crystal Structure and Magnetic Properties of Bis(Pyrazine)Copper(II) Perchlorate, $Cu(Pyz)_2(ClO_4)_2$,

a Two-Dimensional Heisenberg Antiferromagnet. *Inorg. Chem.* **1979**, *18* (10), 2679–2682.

(46) Woodward, F. M.; Gibson, P. J.; Jameson, G. B.; Landee, C. P.; Turnbull, M. M.; Willett, R. D. Two-Dimensional Heisenberg Antiferromagnets: Syntheses, X-Ray Structures, and Magnetic Behavior of $[Cu(Pz)_2](ClO_4)_2$, $[Cu(Pz)_2](BF_4)_2$, and $[Cu(Pz)_2(NO_3)](PF_6)$. *Inorg. Chem.* **2007**, *46* (10), 4256–4266.

(47) Xiao, F.; Woodward, F. M.; Landee, C. P.; Turnbull, M. M.; Mielke, C.; Harrison, N.; Lancaster, T.; Blundell, S. J.; Baker, P. J.; Babkevich, P.; et al. Two-Dimensional XY Behavior Observed in Quasi-Two-Dimensional Quantum Heisenberg Antiferromagnets. *Phys. Rev. B* **2009**, *79* (13), 134412.

(48) Butcher, R. T.; Turnbull, M. M.; Landee, C. P.; Shapiro, A.; Xiao, F.; Garrett, D.; Robinson, W. T.; Twamley, B. Crystal Structure and Magnetism of a Well Isolated 2D-Quantum Heisenberg Antiferromagnet, $(Quinolinium)_2CuBr_4{\cdot}2H_2O$, and Its Anhydrous Form. *Inorg. Chem.* **2010**, *49* (2), 427–434.

(49) Polyakov, A. O.; Arkenbout, A. H.; Baas, J.; Blake, G. R.; Meetsma, A.; Caretta, A.; van Loosdrecht, P. H. M.; Palstra, T. T. M. Coexisting Ferromagnetic and Ferroelectric Order in a $CuCl_4$-Based Organic–Inorganic Hybrid. *Chem. Mater.* **2012**, *24* (1), 133–139.

(50) Kundys, B.; Lappas, a.; Viret, M.; Kapustianyk, V.; Rudyk, V.; Semak, S.; Simon, C.; Bakaimi, I. Multiferroicity and Hydrogen-Bond Ordering in $(C_2H_5NH_3)_2CuCl_4$ Featuring Dominant Ferromagnetic Interactions. *Phys. Rev. B - Condens. Matter Mater. Phys.* **2010**, *81* (22), 1–6.

(51) Shapiro, A.; Landee, C. P.; Turnbull, M. M.; Jornet, J.; Deumal, M.; Novoa, J. J.; Robb, M. A.; Lewis, W. Synthesis, Structure, and Magnetic Properties of an Antiferromagnetic Spin-Ladder Complex: Bis(2,3-Dimethylpyridinium) Tetrabromocuprate. *J. Am. Chem. Soc.* **2007**, *129* (4), 952–959.

(52) G. M. Sheldrick, Go¨ttingen, G. SADABS,. **1997**.

(53) Sheldrick, G. M. No Title. *Acta Crystallogr., Sect. A Found. Adv.* **2015**, *71*, 3–8.

(54) Sheldrick, G. M. , SHELXTL, program for crystal structure refine-ment. , SHELXTL, Program for Crystal Structure Refine-Ment,. **1997**.

(55) Farrugia, L. WinGX. *J. Appl. Crystallogr.* **1999**, *32*, 837–838.

(56) Mason, P. E.; Neilson, G. W.; Enderby, J. E.; Saboungi, M.-L.; Dempsey, C. E.; MacKerell Alexander D.; Brady, J. W. The Structure of Aqueous Guanidinium Chloride Solutions. *J. Am. Chem. Soc.* **2004**, *126* (37), 11462–11470.

(57) Kubíčková, A.; Křížek, T.; Coufal, P.; Wernersson, E.; Heyda, J.; Jungwirth, P. Guanidinium Cations Pair with Positively Charged Arginine Side Chains in Water. *J. Phys. Chem. Lett.* **2011**, *2* (12), 1387–1389.

(58) Vazdar, M.; Uhlig, F.; Jungwirth, P. Like-Charge Ion Pairing in Water: An Ab Initio Molecular Dynamics Study of Aqueous Guanidinium Cations. *J. Phys. Chem. Lett.* **2012**, *3* (15), 2021–2024.

(59) Johnston, D. C.; Kremer, R. K.; Troyer, M.; Wang, X.; Klümper, A.; Bud'ko, S. L.; Panchula, A. F.; Canfield, P. C. Thermodynamics of Spin S=1/2 Antiferromagnetic Uniform and Alternating-Exchange Heisenberg Chains. *Phys. Rev. B* **2000**, *61* (14), 9558–9606.

Chapter 6

A Perovskite-like Hybrid $(C_6H_5CH_2NH_3)_2CuBr_4$ with Mirror-like Surface and Field Induced Metamagnetic Transitions

Summary

Hybrid halide $(C_6H_5CH_2NH_3)_2CuBr_4$ ($C_6H_5CH_2NH_3$ = Benzylammonium ion) has been reported previously to exhibit long range magnetic order and also visible spectrum absorption, although the crystal structure solution could not be obtained. In this chapter, we present our studies on single crystal growth, crystal structure, surface and magnetic properties of $(C_6H_5CH_2NH_3)_2CuBr_4$. The compound crystallizes as beautiful dark brown plate-shaped single crystals stacked on top of each other via solution growth technique. The crystals exhibit highly smooth, mirror-like surface having $RMS_{roughness}$ comparable with commercial sapphire, as studied using AFM technique. Room temperature single crystal structure (monoclinic, *C*2/*c*) features two dimensional layers consisting of corner shared inorganic $CuBr_4$ sheets with successive sheets interleaved by two layers of benzylammonium cations. The nearest neighbor Cu^{2+} ions within single sheet exhibit "in-plane" orthogonal Jahn-Teller distortions (*z*-axis elongation). Bulk magnetization studies reveal strong magnetocrystalline anisotropy with easy axis parallel to $CuBr_4$ layer (⊥ to *c*-axis). Remarkably, field induced metamagnetic phase transitions have been observed for applied field direction ⊥ to *c*-axis.

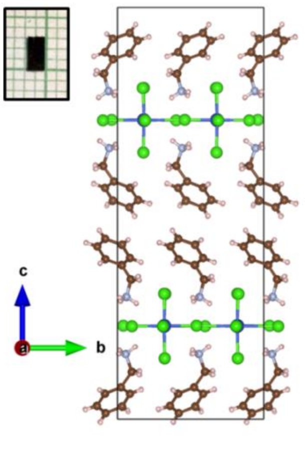

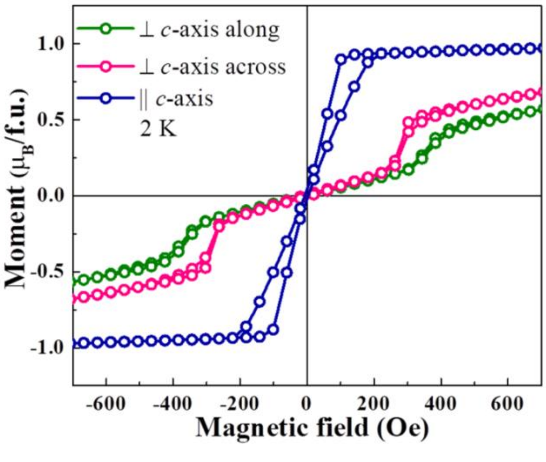

6.1 Introduction:

The Cu (II)-based organic-inorganic halide hybrids with R_2CuX_4 molecular formula and perovskite-like structure (R = organic ammonium cation, X = halide anion) are an exciting class of materials which exhibit facile integration of structural flexibility along with interesting optical properties, pressure dependent conductivity, battery applications, long-range magnetic and ferroelectric order.[1–6] Extensive research on this class of materials has been carried out for decades where at early stage, theoretical and experimental research by Drumheller *et al.*, de Jongh *et al.* and Willett *et al.* gave a comprehensive picture on the general crystal structure and magnetic properties of these compounds.[1,7–10] Later, the physical properties of these materials have been thoroughly studied as a function of temperature and pressure where ferroelectric, ferromagnetic, multiferroic, thermochromic and piezochromic phases have been realized in them.[2–4,10,11]

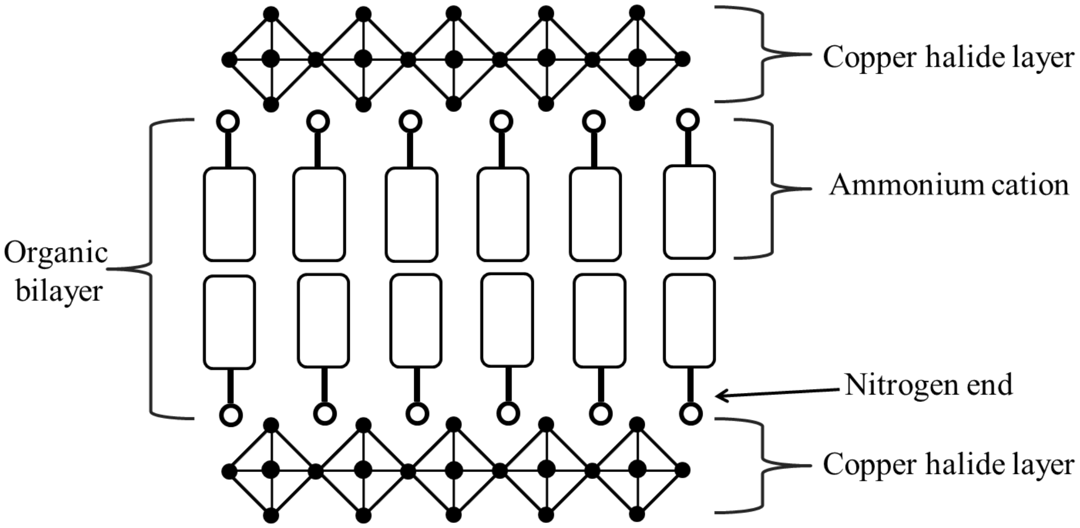

Scheme 6.1 Schematic illustration of crystal structure of layered R_2CuX_4 hybrid halides.

The crystal structures of the R_2CuX_4 materials feature two parts (see **Scheme 6.1**), one being the robust inorganic layers composed of "corner-shared" metal-halide octahedra which strongly influence the optoelectronic and magnetic properties. The other part contains the organic ammonium cations that occupy spaces in between consecutive inorganic layers with their nitrogen ends directed towards the metal-halide layers. The Cu^{2+} ($3d^9$) ions of "corner-shared" metal halide layer exhibit pronounced Jahn-Teller (J-T) distortion due to the unequal occupancy of electrons in degenerate orbitals under octahedral field. The J-T distortion is seen to influence copper-halide bond elongation (J-T elongation) within metal-halide plane where the distortions are seen to be orthogonal to each other amongst neighboring octahedra.[3,4] Such antiferrodistortive arrangement of the elongated bonds forces very poor interaction among the unpaired electron in the $d_{x^2-y^2}$ orbitals of neighboring Cu^{2+} ions, making these materials exhibit "in-layer" ferromagnetic interactions.[2,3,10,12,13] The magnetic interaction among adjacent layers is seen to be of antiferromagnetic nature with exchange strength being inversely proportional to the interlayer distance. The ammonium ions occupying the inter-layer spaces take part in hydrogen bond interactions with halide atoms which, along with a finite dipole moment of ammonium cations further impart a net polarization in the crystal structure. Thus, ferroelectric phase in these materials at certain temperature region often becomes a possibility, as have been realized in $(C_2H_5NH_3)_2CuCl_4$ and $(C_6H_5CH_2CH_2NH_3)_2CuCl_4$.[2,3] To mention, the compound $(C_2H_5NH_3)_2CuCl_4$ exhibits a very large electrical polarization of 37 μC cm^{-2} below curie temperature (237 K) due to the hydrogen bond ordering observed among ethylammonium cations.[2]

The layered hybrids with chemical formula $[C_6H_5(CH_2)_nNH_3]_2CuCl_4$ with $n = 1$, 2 and 3 were studied by Dupas *et al.* and Estes *et al.* where they predicted a layer crystal structure with possible lattice parameters (for $n = 1$; $a = 31.30$ Å, $b = 7.59$ Å and $c = 7.28$ Å) and observed ferromagnetic interaction within layers and weak antiferromagnetic inter-layer interaction.[14,15] The hybrid compound $(C_6H_5CH_2NH_3)_2CuBr_4$ ($C_6H_5CH_2NH_3$: benzylammonium cation) had been first reported as one of the series of layered materials with general formula $[C_6H_5(CH_2)_nNH_3]_2CuBr_4$ with $n = 1$, 2 and 3 by Drumheller and Willett.[1] They studied strong "in-layer" ferromagnetic interaction with strengths around 20-25 K and very weak interlayer exchange interaction (~1 K). They could not obtain a complete structure solution and predicted possible space group and lattice parameters (for $n = 1$; space group $A2/a$; $a = 10.558$ Å, $b = 10.486$ Å, $c = 63.473$ Å and $\beta = 98.08°$).[1] Recently, Li *et al.* have completely focused on the optoelectronic properties of $(C_6H_5CH_2NH_3)_2CuBr_4$ and reported it be a possible alternative of lead-based solar cells as it absorbs almost whole visible spectrum with an optical band gap of 1.81 eV.[6] Thus, although $(C_6H_5CH_2NH_3)_2CuBr_4$ is packed with brilliant features, the detailed knowledge on the exact crystal structure of $(C_6H_5CH_2NH_3)_2CuBr_4$ remain unclear. Moreover, recent studies on benzylammonium cation containing material $(C_6H_5CH_2NH_3)_2PbCl_4$ by R.G. Xiong *et al.* reports it to be a molecular ferroelectric semiconductor with an observed polarization value of 13 μC cm^{-2}.[16] This indicates that the polar benzylammonium cations with it's hydrogen bonding with halide radicals in layered hybrids can indeed influence the crystal structure to go into polar phase. Also in layered hybrids, the complete substitution of chloride radicals by bromide can have significant effect in orbital ordering and the resultant magnetic properties.

Based on this motivation, we prepared and studied the structure, surface and magnetic properties of single crystalline $(C_6H_5CH_2NH_3)_2CuBr_4$. The compound (hereafter named as **4**) crystallizes as beautiful plates stacked on top of each other via van der Waals force. The crystals are associated with highly smooth, mirror-like surface with a $RMS_{roughness}$ comparable with that of commercial sapphire substrate. The room temperature crystal structure (polar, monoclinic, *Cc*) exhibits two dimensional Cu-Br layers composed of corner shared $CuBr_6$ octahedra and two layers of benzylammonium cations lying in between successive layers. The “in-plane” Jahn-Teller distortions (*z*-axis elongation) in nearest neighbour Cu^{2+} ions within a single layer are seen to be orthogonal to each other, favouring “in-plane” ferromagnetism. Bulk magnetization studies reveal strong magnetocrystalline anisotropy with easy axis parallel to $CuBr_4$ layers ($\perp$ to *c*-axis). Remarkably, field induced metamagnetic phase transitions have been observed for applied field direction $\perp$ to *c*-axis.

6.2 Experimental Section:

6.2.1 Chemicals:

Analytical grade quality benzylammonium hydrobromide ($C_6H_5CH_2NH_3Br$) and copper bromide ($CuBr_2$) were acquired from Sigma Aldrich. All chemicals were used without further purification.

6.2.2 Synthesis:

In 80 ml of deionized water, 0.3104 g (1.389 mmol) of $CuBr_2$ was added and was dissolved thoroughly. Under constant stirring, 0.5226 g (2.779 mmol) of $C_6H_5CH_2NH_3Br$ was added into the same solution and stirring was continued till complete dissolution. The resultant solution was kept at room temperature inside crystallization beaker for slow evaporation of solvent. Dark brown colored single crystals in form of plate were seen to form stacked on top of each other after about two weeks. As grown crystals were washed with hexane and taken for further studies. The formation process can be represented using simple addition reaction:

$$2\ C_6H_5CH_2NH_3Br + CuBr_2 = (C_6H_5CH_2NH_3)_2CuBr_4$$

6.2.3 Characterization:

The C, H and N percentages were estimated using Thermo Scientific Flash 2000 CHN analyzer.

For single crystal data collection, the crystal stacking was broken in order to isolate a very thin crystal piece. Isolating thinnest possible crystal piece reduces the chance of having twinning feature in diffraction profile. The chosen crystal piece was further glued to a thin glass fibre which was then mounted on top of the goniometer head. Room temperature X-ray diffraction data were collected on an Oxford Xcalibur (Mova) diffractometer equipped with an EOS CCD detector and a microfocus sealed tube using Mo Kα radiation (λ = 0.71073 Å). Refinement of cell parameter, data integration and reduction were accomplished by using the program CrysalisPro.[17] The structure solution was obtained from SHELXS[18,19] included in the WinGX suite.[20]

DC magnetic susceptibility and magnetization measurements on single crystals were carried out using Quantum Design SQUID-based MPMSXL-3-type magnetometer along different crystallographic axes (described in magnetic properties section). Zero field cooled and field cooled data were recorded in the temperature range of 1.8 K – 350 K with applied magnetic field of 0.01 T and 0.1 T. Isothermal magnetization have been measured at 1.8 K and at 300 K with field sweep range of ±7 T. AC magnetization has been recorded in PPMS.

Temperature dependent heat capacity (C_P) was recorded in the temperature range of 2 K – 100 K using Quantum Design PPMS. To conduct the experiment, the heat capacity of addenda (Apeizon grease and sample platform), which defines the thermodynamic surrounding, was recorded at first. Then a suitable crystal piece was mounted on top of the same grease and the heat capacity of the whole setup (system + surrounding) was recorded. During both processes, the heat capacity was measured via relaxation technique. Further the C_P of addenda was auto subtracted to derive the C_P of the compound.

6.3 Results and Discussion:

6.3.1 Crystal Structure:

The phase purity of compound **4** was confirmed by elemental analysis which yielded the following mass percentage outputs tabulated in **Table 6.1**.

Table 6.1 Elemental Purity Analysis:

Elements	Experimental Mass (%)	Calculated Mass (%)
H	3.41	3.36
C	28.30	28.04
N	4.51	4.67

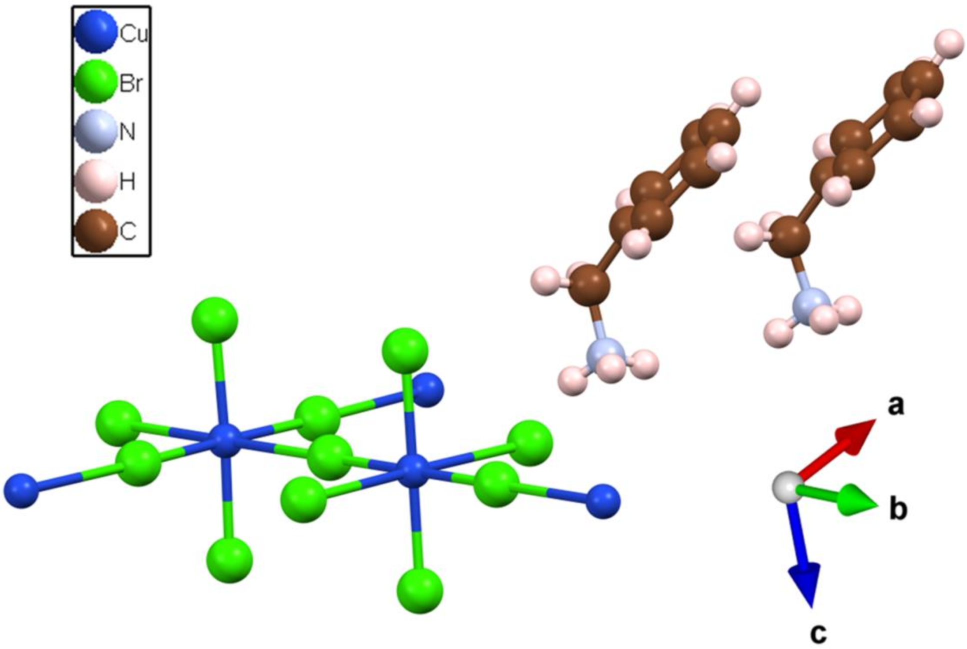

Figure 6.1 Molecular structure of compound **4** at room temperature.

As the crystals of compound **4** grew in form of two dimensional plates stacked on top of each other, isolating a very thin crystal devoid of twinning was a challenging task. Thus, we have chosen a number of thinnest possible crystals and recorded multiple X-Ray diffraction profiles in order to get the best data. Most of the diffraction profiles were seen to be plagued with twinning features where the specular reflection patterns indicated that a layered crystal structure could be a possibility. In this process, a qualitatively good single crystal diffraction profile was obtained where twinning feature was negligible. In the process of solving the structure, we found out that the benzylammonium cations are associated with large thermal parameters. As a result, determining the ammonium cation positions was challenging. We have addressed this issue by putting restraint on the ammonium ions and obtained two possible structure solutions in both of which the crystal structure is monoclinic. The solution with better R-factor (5.6%) is the noncentrosymmetric monoclinic space group *Cc*. The structure solution with centrosymmetric monoclinic space group *C*2/*c* was seen to be associated with a R-factor of 8.8% with some residual electron density. To confirm the space group symmetry, we have carried out polarization vs electric field measurements and piezoresponse force microscopic measurements (discussed in section 6.4 and 6.5) and found the material to be centrosymmetric at room temperature. Thus we considered C2/c as the structure solution which is also consistent with previous reports.[14,15] The structure with space group *C*2/*c* exhibits the following lattice parameters: a = 10.9553 (4) Å, b = 11.01493 (5) Å, c = 31.4615 (14) Å, β = 100.0240 (10)° and Z = 8 (see the refinement parameters and atomic postions in **Table 6.2**, **Table 6.5**). The molecular unit contains two benzylammonium cations and the Cu_5Br_{11} unit which is the basis of corner-shared architecture (see **Figure 6.1**).

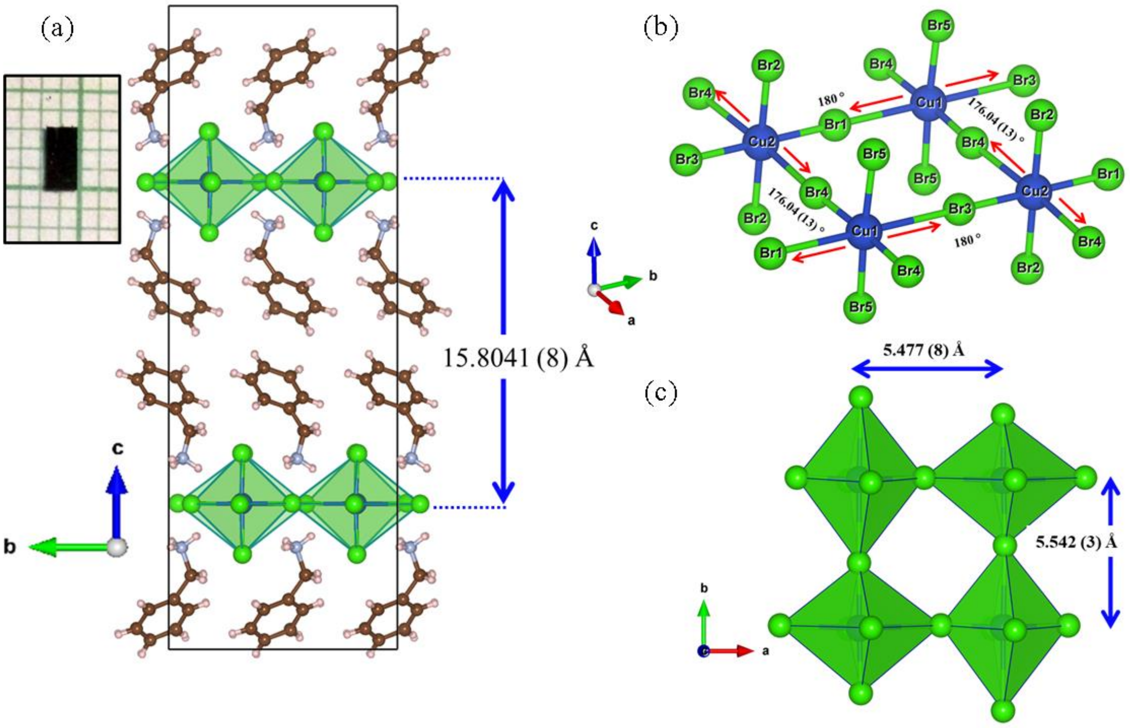

Figure 6.2 (a) Unit cell representation of compound **4**. A regular crystal piece has been included as inset picture. The interlayer separation is 15.8041 (8) Å, (b) View of the "In-layer" Jahn-Teller distortion in $CuBr_4$ sheets. The J-T distortions in neighboring Cu^{2+} ions are seen to be orthogonal to each other. (c) The z-elongation of $CuBr_6$ octahedra due to J-T elongation. Orthogonal J-T elongation in alternating octahedra is evident.

Table 6.2 Crystal Structures Refinement Details:

Parameters	***Cc***	***C2/c***
Empirical formula	$C_{14}H_{20}Br_4CuN_2$	$C_{14}H_{20}Br_4CuN_2$
Formula weight (g/mol)	599.50	599.50
Temperature (K)	295	295
Wavelength (Å)	0.71073	0.71073
Crystal system	Monoclinic	Monoclinic
Space group	*Cc*	*C*2/*c*
Unit cell dimensions (Å)	a = 10.9553 (4), α = 90.00° b = 11.0149 (5), β = 100.024 (10)° c = 31.4615 (14), γ = 90.00°	a = 10.9553 (4), α = 90.00° b = 11.0149 (5), β = 100.024 (10)° c = 31.4615 (14), γ = 90.00°
Volume ($Å^3$)	3738.6 (3)	3738.6 (3)
Z	8	8
Calculated density (g/cm^3)	2.130	2.130
Absorption coefficient (mm^{-1})	9.713	9.713
F(000)	2296	2296
Crystal dimension (mm^3)	0.35 x 0.42 x 0.13	0.35 x 0.42 x 0.13
Reflections collected	33087	33087
Independent reflections	7268 (R_{int} = 0.0816)	3845 (R_{int} = 0.1040)
Completeness	99.9% (θ = 26.44°)	99.9% (θ = 25.24°)
Number of parameters	112	108
Goodness-of-fit	1.016	1.067
Final R indices [$I > 2\sigma(I)$]	R_{obs} = 0.0563, wR_{obs} = 0.1412	R_{obs} = 0.0885, wR_{obs} = 0.2655
R indices (all data)	R_{all} = 0.1114, wR_{all} = 0.1692	R_{all} = 0.1322, wR_{all} = 0.2987

The unit cell diagram of compound **4** is represented **Figure 6.2** (a) which shows the layered arrangement of $CuBr_4$ units in *ab*-plane. The interlayer distance is 15.8041 (8) Å which is occupied by two layers of benzylammonium cations. The benzylammonium cations are arranged with their ammonium ends oriented towards the $CuBr_4$ layers and taking part in H-bonding interactions with Br ions. The π-electron rich phenyl rings in benzylammonium cations are seen to be distant from each other making it impossible for them to feature π-π interaction. Very importantly, each of the $CuBr_6$ octahedral unit is seen to have distorted octahedral geometry due to Jahn-Teller distortion in Cu^{2+} ion (*z*-axis elongation) as can be seen in **Figure 6.2** (b) and (c). In each $CuBr_6$ octahedron, the Cu-Br bond distances vary within range of 2.420 (5) - 3.103 (3) Å where two short and two long Cu-Br bonds are observed within $CuBr_4$ plane while two short Cu-Br bonds are observed to be oriented out of the plane (see **Table 6.3**). The Br-Cu-Br bond angles within one $CuBr_6$ octahedron vary in the range of 87.1 (2) – 91.9 (9)° (**Table 6.3**). The

Br-Cu-Br bridging angles between adjacent octahedra are seen to be within a range of 176.04 (13) - 180° (**Figure 6.2** (b), **Table 6.3**).

Table 6.3 The Cu-Br bond distances and bond angles at room temperature. J-T elongated bonds are in bold fonts:

295 K			
Label	**Bond distance (Å)**	**Label**	**Bond angle (°)**
Cu1-Br1	**3.057 (3)**	Br1-Cu1-Br3	180
Cu1-Br3	**3.103 (3)**	Br1-Cu1-Br4	88.1 (5)
Cu1-Br4	2.420 (5)	Br1-Cu1-Br5	91.9 (9)
Cu1-Br5	2.431 (3)	Br3-Cu1-Br4	91.8 (5)
Cu2-Br1	2.416 (3)	Br3-Cu1-Br5	88.0 (1)
Cu2-Br2	2.428 (1)	Br4-Cu1-Br5	90.0 (6)
Cu2-Br3	2.439 (2)	Br4-Cu1-Br5	87.1 (2)
Cu2-Br4	**3.060 (5)**	Br4-Cu1-Br4	176.0 (2)
		Br5-Cu1-Br5	176.0 (2)
		Br1-Cu2-Br2	89.7 (8)
		Br1-Cu2-Br3	180
		Br1-Cu2-Br4	92.1 (1)
		Br2-Cu2-Br2	179.5 (6)
		Br2-Cu2-Br3	90.2 (2)
		Br2-Cu2-Br4	90.0 (5)
		Br2-Cu2-Br4	89.9 (9)
		Br3-Cu2-Br4	87.9 (1)
		Br4-Cu2-Br4	175.7 (9)

6.3.2 Surface Properties:

We have also confirmed the crystallographic direction perpendicular to the surface of the plate-shaped single crystals. We identified the direction by carrying out profile fit on powder X-Ray diffraction data collected with keeping a single crystal piece in "in-plane" geometry where the incoming X-Ray falls on top surface and gets reflected (the profile fit graph is included in **Figure 6.3**). We have observed that peaks corresponding to the 00 *l* (*l* = 2*n*) planes are associated with large intensity which indicates that the top surface of compound **4** is perpendicular to the *c*-axis. As the crystals form as stacked layers attracting each other via van der Waals force, we believe that the top surface is composed of the metal halide layer which effectively covers the organic benzylammonium ions from atmosphere and thereby makes the material an atmospherically stable one.

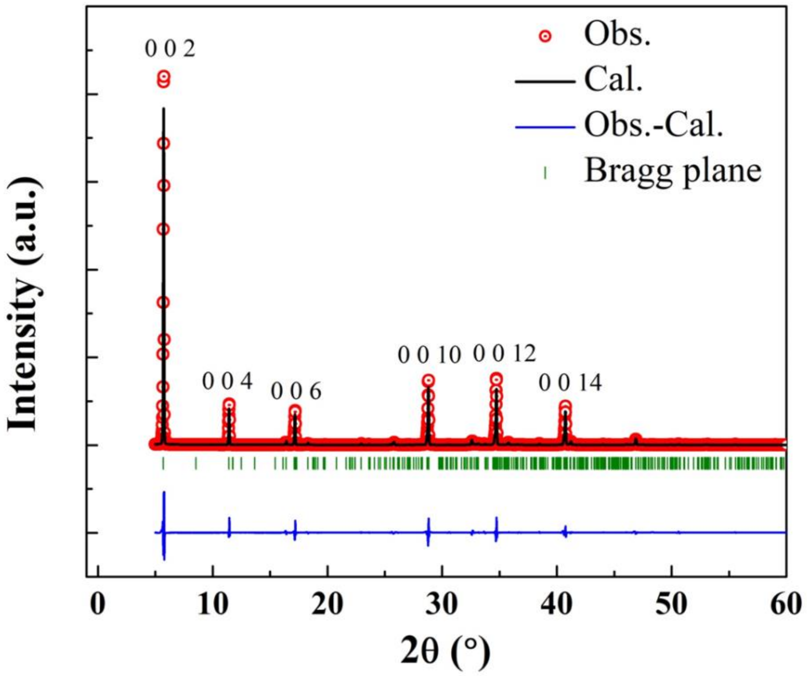

Figure 6.3 Profile fitting data of compound **4** carried out on powder X-Ray diffraction pattern collected in "in-plane" orientation of single crystal piece.

The as-grown opaque crystals were seen to feature highly reflective mirror-like surfaces. This prompted us to study the surface roughness using atomic force microscope (AFM). To compare, we have also calculated the surface roughness of commercial sapphire which is extensive used for epitaxial film growth and device fabrication.

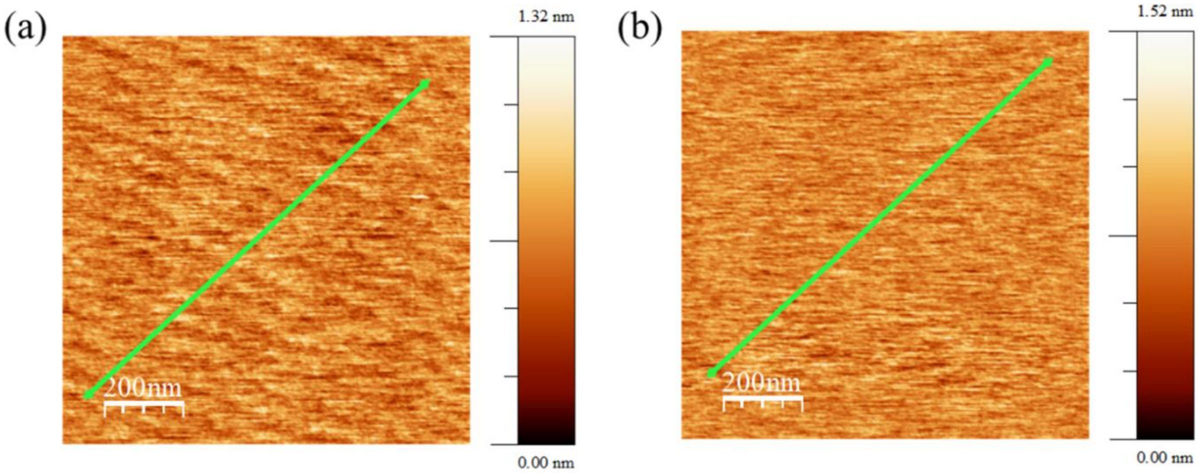

Figure 6.4 AFM height profile images of (a) commercial sapphire and (b) compound **4**.

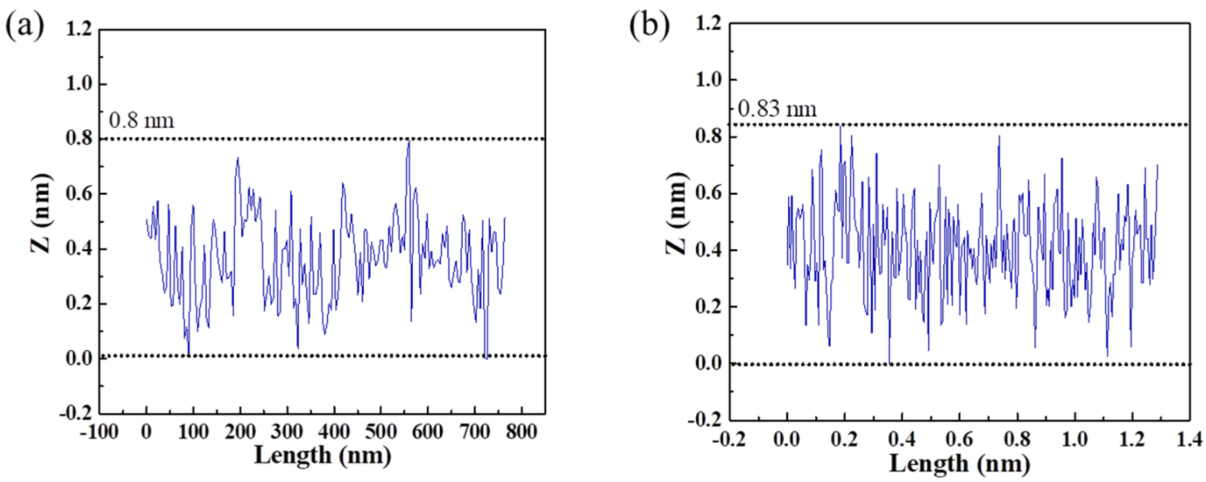

Figure 6.5 Corresponding line profile plots for (a) commercial sapphire and (b) compound **4**.

Table 6.4 Calculated surface roughness values of compound and sapphire:

Material	RMS roughness (nm)	RA roughness (nm)
Sapphire	0.1591	0.1269
$(C_6H_5CH_2NH_3)_2CuBr_4$	0.1606	0.1084

Remarkable surface roughness values have been observed for compound **4** which confirms that the crystal surfaces are indeed very smooth, comparable to that of commercial sapphire (**Figure 6.4**, **Figure 6.5**). The RMS roughness of compound **4** was found to be 0.1606 nm while that of commercial sapphire was 0.1591 nm (**Table 6.4**). This further supports our analogy that the layer by layer growth method from solution gives rise to plate-shaped crystals with metal halide layers as top surface. This ensures that the surface is smooth and shiny. Overall, the surface properties indicate that the crystals of compound **4** carries potential to be used as substrate in low temperature film growth and also for device fabrications.

6.3.3 Polarization vs Electric Field:

From structure solutions, it can be seen that among obtained monoclinic structures, the noncentrosymmetric space group *Cc* is associated with a lower R-factor value as compared to centrosymmetric space group *C*2/*c*. It is well-known that in X-Ray diffraction, both *Cc* and *C*2/*c* space groups feature exactly same reflection conditions which make it impossible to correctly detect the right structure solution. Thus, we have used the polarization vs electric field (P vs E loop) technique and the piezoelectric force microscopic technique at room temperature to confirm the space group symmetry by detecting the presence or absence of centre of symmetry. Thus, if the space group is Cc, the material will definitely be piezo-active (Since the Cc has corresponding point group *m* exhibits positive pyroelectric and piezoelectric response). For P vs E loop measurements we have applied electrical bias along [001] direction. Here, it is to be noted that for a noncentrosymmetric monoclinic crystal structure with space group *Cc* (Laue class *m*), the nonpolar direction is [010].[21] We have observed absence of any ferroelectric behaviour in the P vs E loop measurements, which indicates that the material is not ferroelectric in nature (see **Figure 6.6**).

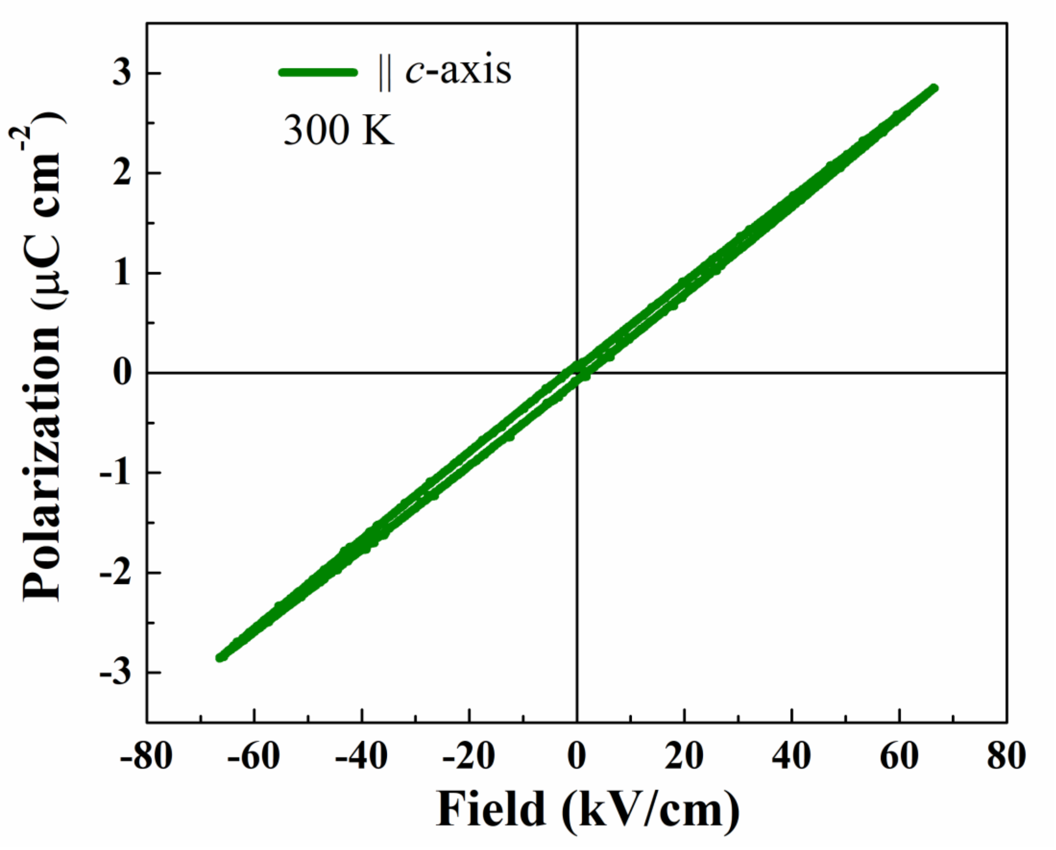

Figure 6.6 Polarization vs Electric field loop measured at 300 K. Electrical bias was applied along [001] direction (∥ *c*-axis).

6.3.4 Piezoelectric Force Microscopy:

Further, we have attempted to confirm the presence of polarity or piezoelectricity by carrying out piezoelectric force microscopic (PFM) measurements. For this, applied electrical bias direction was parallel to c-axis ([001]). The thin plates did not exhibit any signature of polarity or piezoelectricity detectable under PFM studies (see **Figure 6.7**).

This indicates that the structure of compound **4** is centrosymmetric monoclinic with space group C2/c.

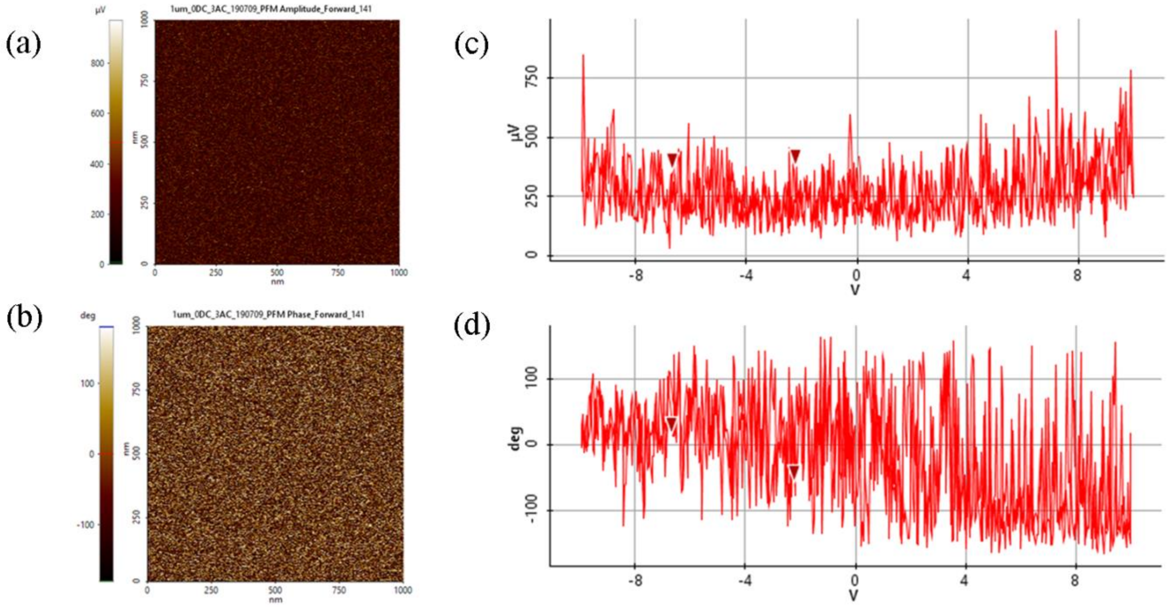

Figure 6.7 Piezoresponse force microscopy results: (a) amplitude and (c) phase micrographs under 3 V ac field applied parallel to *c*-axis, (b) amplitude vs voltage and (d) phase vs voltage indicating absence of polar or piezoelectric behavior.

6.3.5 Magnetic Properties:

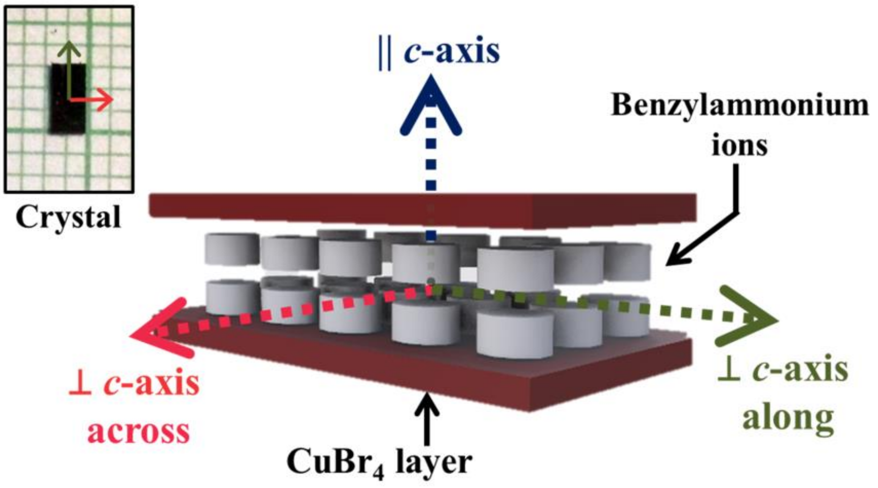

Scheme 6.2 Schematic illustration showing the applied dc field directions during the magnetic measurements of a single crystal of compound **4**.

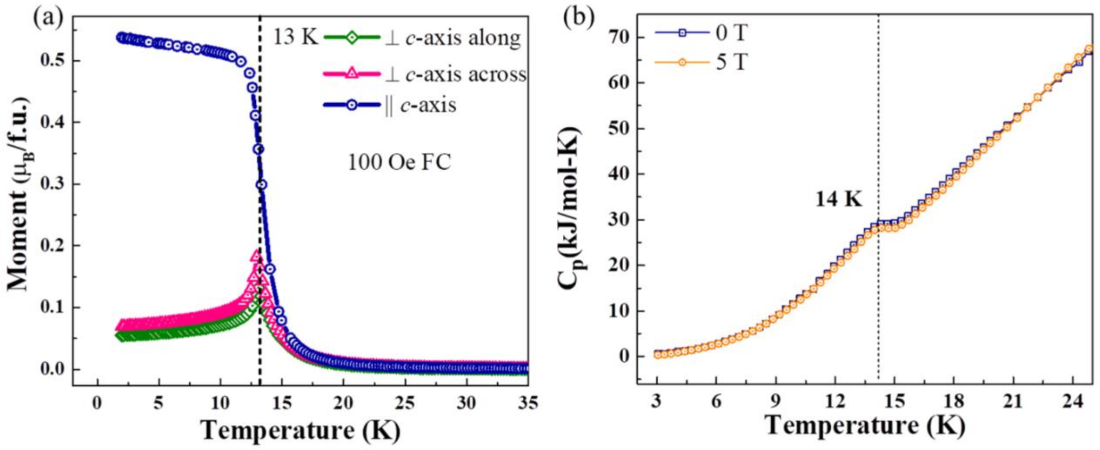

Figure 6.8 (a) Temperature dependent magnetic moment of **4** measured under 100 Oe dc field applied along different crystallographic directions. (b) Heat capacity in presence and absence of applied dc field showing magnetic transition feature.

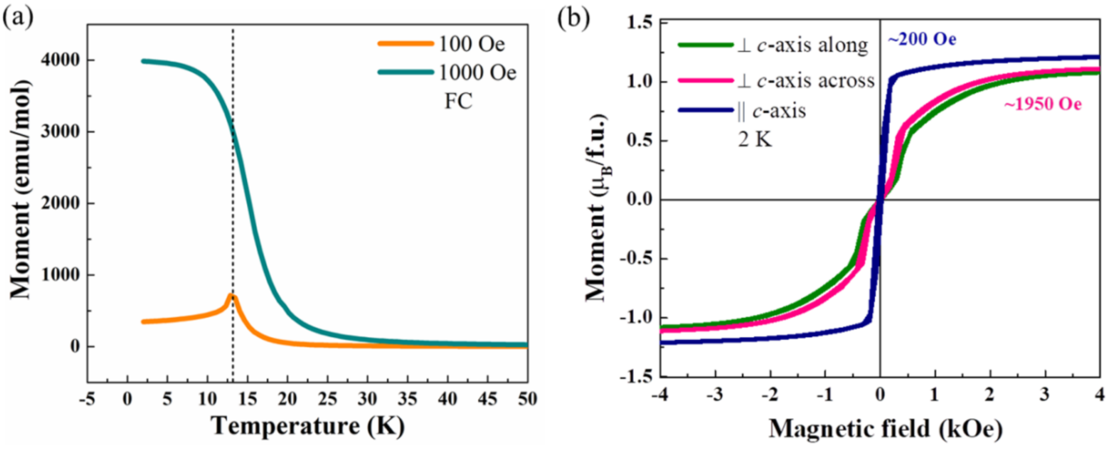

Figure 6.9 (a) Field cooled magnetization data under applied fields of 100 Oe and 1000 Oe with direction perpendicular to *c*-axis (along). (b) Isothermal magnetization data recorded at 2 K.

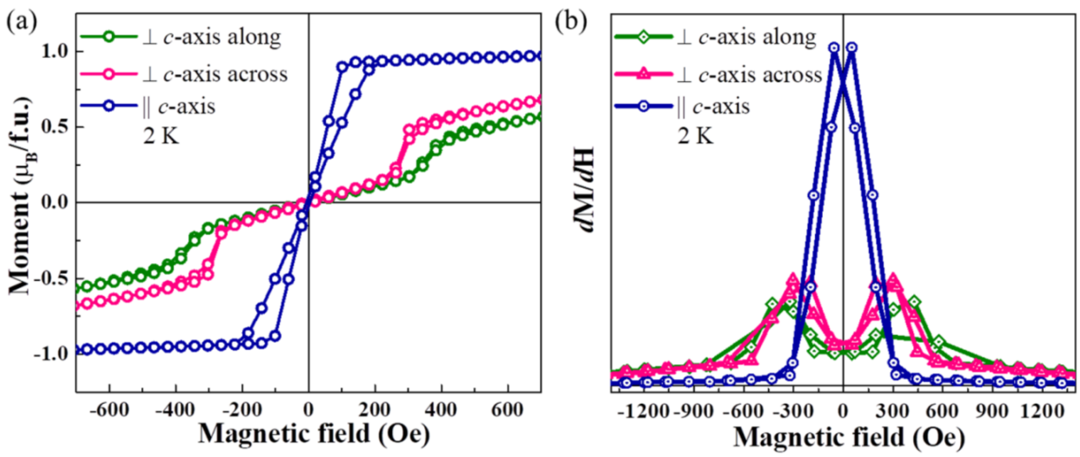

Figure 6.10 (a) Step-like isothermal magnetization plateau under applied field in direction perpendicular to *c*-axis. (b) dM/dH vs magnetic field showing quick saturation.

The bulk magnetic properties of powder samples of $(C_6H_5CH_2NH_3)_2CuBr_4$ have been studied by Drumheller and Willet *et al.* where they have observed ferromagnetic interactions propagating within metal-halide layer while adjacent layers are coupled via weak antiferromagnetic exchange interaction.[1] Magnetic properties of chloride counterpart of the compound, $(C_6H_5CH_2NH_3)_2CuCl_4$ have been studied by Dupas *et al.* who have also found two dimensional ferromagnetic interactions acting within meta-halide plane.[14] Pioneering work by de Jongh *et al.* on magnetic properties of compound $(C_2H_5NH_3)_2CuCl_4$ summarizes that the layered hybrids are basically two dimensional materials with in-layer ferromagnetic and inter-layer antiferromagnetic interactions where, the weaker antiferromagnetic interaction becomes prominent in the vicinity of magnetic phase transition temperature.[10] In this report, we present our studies on bulk dc magnetic properties of the plate shaped single crystals of compound **4**, as have been measured along different crystallographic directions (see **Scheme 6.2**).

Figure 6.8 (a) shows the temperature dependent magnetic moment under 100 Oe dc field as measured along different crystallographic directions of a single crystal piece. The compound **4** is seen to undergo a magnetic transition at 13 K where significant magnetocrystalline anisotropy has been observed. The magnetic transition has also been observed via heat capacity measurements as shown in **Figure 6.8** (b). From structural analyses, we can see that the antiferrodistortive arrangement of Cu^{2+} ions in $CuBr_4$ layer indicates that a ferromagnetic interaction should propagate within the $CuBr_4$ layer (parallel to *ab*-plane, perpendicular to *c*-axis). Interestingly, it was seen the susceptibility vs temperature data for field along *c*-axis exhibits higher magnetization value below transition (**Figure 6.8** (a)). In contrast, the magnetization behavior with field perpendicular to *c*-axis seems antiferromagnetic-like transition. We believe that in the vicinity of transition temperature, the antiferromagnetic inter-layer exchange interaction, which is typically weaker than in-layer ferromagnetic interaction, becomes very prominent and governs the overall magnetization. Thus the material in the vicinity of transition temperature behaves as a three-dimensional magnet. Further, field cooled measurements under different dc fields applied perpendicular to *c*-axis indicated that the transition nature changes from antiferromagnetic like to ferromagnetic like when the applied field is increased (see **Figure 6.9** (a)).

The isothermal magnetization measurements (Moment vs Field measurements) below the transition temperature indicate that the magnetization quickly saturates under small applied field (1 μ_B / Cu^{2+} ion) (**Figure 6.9** (b)). When applied field direction is parallel to *c*-axis, only 200 Oe field is required to reach saturation value while for field direction perpendicular to *c*-axis, about 2000 Oe field is required to saturate the moments (**Figure 6.9** (b), **Figure 6.10** (a) (b)). Most interestingly, field induced step-like magnetization switching have been observed in isothermal magnetization when applied field directions were perpendicular to *c*-axis (pink and grey lines in **Figure 6.9** (b) and **Figure 6.10** (a)). Such step-like metamagnetic transition plateaus are unprecedented and have never been observed in any Cu-based layered halides before. Higher density data collection in low field region shows that the steps separate into multiple smaller sized steps (**Figure 6.11**). We believe that the detailed understanding of magnetic spin structure will help in shedding light into the interesting properties.

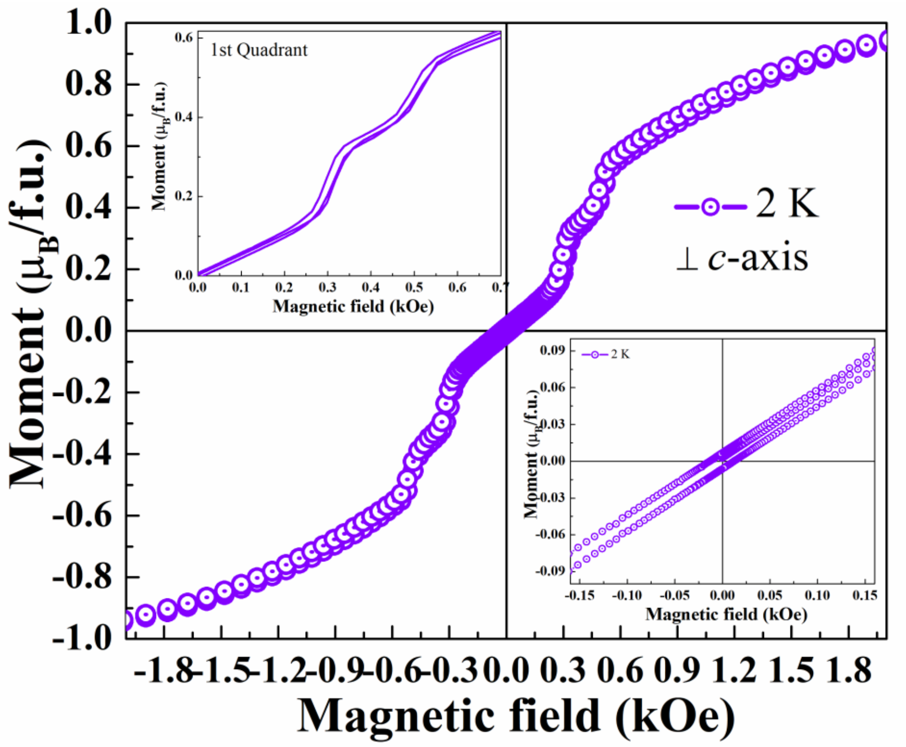

Figure 6.11 Field induced magnetization plateau observed under applied magnetic field direction perpendicular to *c*-axis.

6.4 Conclusion:

In conclusion, we have prepared single crystals of hybrid halide $(C_6H_5CH_2NH_3)_2CuBr_4$ ($C_6H_5CH_2NH_3^+$: Benzylammonium cation) and studied it's crystal structure, crystal surface properties, Polarization vs Electric field behavior, piezoelectric response and magnetic properties. The single crystals of the compound are dark brown, plate-shaped which form as stacked on top of each other via solution growth technique. AFM studies reveal that the opaque crystals are associated iwth highly smooth, mirror-like surface which has $\mathrm{RMS}_{\mathrm{roughness}}$ comparable with commercial sapphire. Thorough single crystal X-Ray diffraction analyses lead to a structure solution (centrosymmetric monoclinic, $C2/c$) which was further confirmed via P vs E loop and PFM measurements. The structure features two dimensional layers consisting of corner shared inorganic $\mathrm{CuBr_4}$ sheets with successive sheets interleaved by benzylammonium cations. The nearest neighbor $\mathrm{Cu^{2+}}$ ions within single sheet exhibit “in-plane” orthogonal Jahn-Teller distortion (z-axis elongation). Bulk magnetization studies reveal strong magnetocrystalline anisotropy with easy axis parallel to $\mathrm{CuBr_4}$ layer (perpendicular to c-axis). Remarkably, field induced metamagnetic transition plateaus have been observed for applied field direction perpendicular to c-axis. Clear understanding on the spin structure below the transition temperature is needed to explain the magnetic properties thoroughly.

Atomic position list:

Table 6.5 Atomic coordinates (x10^4) and equivalent isotropic displacement parameters (Å^{2}x10^3) for compound **4** at 295 K with estimated standard deviations in parentheses.

Label	**x**	**y**	**z**	**Occupancy**	**U_{eq}^***
N(1)	2124(19)	9427(18)	1813(6)	1	94(3)
H(1A)	1903.35	8831.87	1975.17	1	140
H(1B)	2915.09	9617.48	1904.62	1	140
H1C()	1651.81	10075.72	1832.2	1	140
N(2)	7205(19)	9432(19)	1821(6)	1	98(3)
H(2A)	6939.33	8884.1	1992.01	1	147
H(2B)	8024.02	9509.54	1893.09	1	147
H2C()	6846.23	10143.9	1852.79	1	147
C(10)	6670(20)	10840(20)	859(8)	1	98(3)
H(10)	5971.86	11169.72	945.98	1	117
C(3)	1670(20)	10860(20)	861(8)	1	94(3)
H(3)	1001.01	11203.37	962.12	1	112
C(1)	1960(20)	9030(20)	1366(6)	1	94(3)
H(1D)	1100.47	8781.52	1291.87	1	112
H(1E)	2447.7	8292.82	1369.09	1	112
C(8)	6890(20)	9040(20)	1373(6)	1	98(3)
H(8A)	5997.4	8919.06	1318.04	1	117
H(8B)	7255.63	8241.39	1361.09	1	117
C(9)	7190(20)	9730(20)	993(8)	1	98(3)
C(2)	2220(20)	9740(20)	985(7)	1	94(3)
C(6)	3920(20)	9690(20)	545(7)	1	94(3)
H(6)	4631.64	9384.04	462.15	1	112
C(7)	3230(20)	9170(20)	851(8)	1	94(3)
H(7)	3460.71	8404.81	963.76	1	112
C(13)	8180(20)	9150(20)	843(8)	1	98(3)
H(13)	8365.81	8357.9	932.99	1	117
C(12)	8300(20)	10780(20)	413(8)	1	98(3)
H(12)	8555.41	11150.91	177.8	1	117
C(5)	3290(20)	10770(20)	397(8)	1	94(3)
H(5)	3549.84	11138.99	162.74	1	112
C(4)	2330(20)	11360(20)	552(8)	1	94(3)
H(4)	2102.46	12128.76	445.74	1	112

C(11)	7350(20)	11380(20)	572(8)	1	98(3)
H(11)	7156.26	12173.79	483.69	1	117
C(14)	8920(20)	9700(20)	560(8)	1	98(3)
H(14)	9652.36	9405.72	489.61	1	117
Br(1)	0	4600(2)	2500	1	50(1)
Cu(1)	0	1825(2)	2500	1	28(1)
Br(4)	2208(2)	1896(2)	2500(1)	1	49(1)
Br(3)	0	9008(2)	2500	1	45(1)
Cu(2)	0	6794(2)	2500	1	27(1)
Br(2)	391(2)	6786(2)	3284(1)	1	53(1)
Br(5)	391(2)	1748(2)	3284(1)	1	54(1)

6.5 Bibliography:

(1) Zhou, P.; Drumheller, J. E.; Patyal, B.; Willett, R. D. Magnetic Properties and Critical Behavior of Quasi-Two-Dimensional Systems $[C_6H_5(CH_2)_nNH_3]_2CuBr_4$ with n = 1, 2, and 3. *Phys. Rev. B* **1992**, *45* (21), 12365–12376.

(2) Kundys, B.; Lappas, a.; Viret, M.; Kapustianyk, V.; Rudyk, V.; Semak, S.; Simon, C.; Bakaimi, I. Multiferroicity and Hydrogen-Bond Ordering in $(C_2H_5NH_3)_2CuCl_4$ Featuring Dominant Ferromagnetic Interactions. *Phys. Rev. B - Condens. Matter Mater. Phys.* **2010**, *81* (22), 1–6.

(3) Polyakov, A. O.; Arkenbout, A. H.; Baas, J.; Blake, G. R.; Meetsma, A.; Caretta, A.; van Loosdrecht, P. H. M.; Palstra, T. T. M. Coexisting Ferromagnetic and Ferroelectric Order in a $CuCl_4$-Based Organic–Inorganic Hybrid. *Chem. Mater.* **2012**, *24* (1), 133–139.

(4) Jaffe, A.; Lin, Y.; Mao, W. L.; Karunadasa, H. I. Pressure-Induced Conductivity and Yellow-to-Black Piezochromism in a Layered Cu–Cl Hybrid Perovskite. *J. Am. Chem. Soc.* **2015**, *137* (4), 1673–1678.

(5) Shi, P.-P.; Tang, Y.-Y.; Li, P.-F.; Liao, W.-Q.; Wang, Z.-X.; Ye, Q.; Xiong, R.-G. Symmetry Breaking in Molecular Ferroelectrics. *Chem. Soc. Rev.* **2016**, *45* (14), 3811–3827.

(6) Li, X.; Li, B.; Chang, J.; Ding, B.; Zheng, S.; Wu, Y.; Yang, J.; Yang, G.; Zhong, X.; Wang, J. $(C_6H_5CH_2NH_3)_2CuBr_4$: A Lead-Free, Highly Stable Two-Dimensional Perovskite for Solar Cell Applications. *ACS Appl. Energy Mater.* **2018**, *1* (6), 2709–2716.

(7) Steadman, J. P.; Willett, R. D. The Crystal Structure of $(C_2H_5NH_3)_2CuCl_4$. *Inorganica Chim. Acta* **1970**, *4*, 367–371.

(8) de Jongh, L. J.; Miedema, A. R. Experiments on Simple Magnetic Model Systems. *Adv. Phys.* **1974**, *23* (1), 1–260.

(9) de Jongh, L. J.; Botterman, A. C.; de Boer, F. R.; Miedema, A. R. Transition Temperature of the Two-Dimensional Heisenberg Ferromagnet with S=½. *J. Appl. Phys.* **1969**, *40* (3), 1363–1365.

(10) De Jongh, L. J.; Van Amstel, W. D.; Miedema, A. R. Magnetic Measurements on $(C_2H_5NH_3)_2CuCl_4$: Ferromagnetic Layers Coupled by a Very Weak Antiferromagnetic Interaction. *Physica* **1972**, *58* (2), 277–304.

(11) Šenjug, P.; Dragović, J.; Kalanj, M.; Torić, F.; Rubčić, M.; Pajić, D. Magnetic Behaviour of $(C_2H_5NH_3)_2CuCl_4$ Type Multiferroic. *J. Magn. Magn. Mater.* **2019**, *479*, 144–148.

(12) Nugroho, A. A.; Hu, Z.; Kuo, C. Y.; Haverkort, M. W.; Pi, T. W.; Onggo, D.; Valldor, M.; Tjeng, L. H. Cross-Type Orbital Ordering in the Layered Hybrid Organic-Inorganic Compound $(C_6H_5CH_2CH_2NH_3)_2CuCl_4$. *Phys. Rev. B* **2016**, *94* (18), 184404.

(13) Asghar, M. A.; Zhang, S.; Khan, T.; Sun, Z.; Zeb, A.; Ji, C.; Li, L.; Zhao, S.; Luo, J. Reversible Phase Transition Driven by Order-Disorder Transformations of Metal-Halide Moieties in $[(C_6H_{14})NH_2]_2CuBr_4$. *J. Mater. Chem. C* **2016**, *4* (32), 7537–7540.

(14) Dupas, A.; Le Dang, K.; Renard, J. -P.; Veillet, P.; Daoud, A.; Perret, R. Magnetic Properties of the Nearly Two-dimensional Ferromagnets $[C_6H_5(CH_2)NNH_3]_2CuCl_4$ with N=1,2,3. *J. Chem. Phys.* **1976**, *65* (10), 4099–4102.

(15) Estes, W. E.; Losee, D. B.; Hatfield, W. E. The Magnetic Properties of Several Quasi Two-dimensional Heisenberg Layer Compounds: A New Class of Ferromagnetic Insulators Involving Halocuprates. *J. Chem. Phys.* **1980**, *72* (1), 630–638.

(16) Liao, W.-Q.; Zhang, Y.; Hu, C.-L.; Mao, J.-G.; Ye, H.-Y.; Li, P.-F.; Huang, S. D.; Xiong, R.-G. A Lead-Halide Perovskite Molecular Ferroelectric Semiconductor. *Nat. Commun.* **2015**, *6*, 7338.

(17) G. M. Sheldrick, Go¨ttingen, G. SADABS,. **1997**.

(18) Sheldrick, G. M. No Title. *Acta Crystallogr., Sect. A Found. Adv.* **2015**, *71*, 3–8.

(19) Sheldrick, G. M. , SHELXTL, program for crystal structure refine-ment. , SHELXTL, Program for Crystal Structure Refine-Ment,. **1997**.

(20) Farrugia, L. No Title. *J. Appl. Crystallogr.* **1999**, *32*, 837–838.

(21) *International Tables for Crystallography Volume A: Space-Group Symmetry*, 5th ed.; HAHN, T., Ed.; SPRINGER 2005, 2005.

Summary of the thesis

The broad structural diversity along with the interesting structure-property relationships exhibited by the organic-inorganic hybrid halides are truly fascinating and thus have drawn huge focus among materials research community. In this thesis, we have aimed to explore the structural diversity and the associated physical properties of a few transition metal ion containing organic-inorganic hybrid halides with general molecular formula A_2BX_4. We have studied the effect of different ammonium ions and transition metal cations on the crystal structure and the associated physical properties. At first, we have prepared and studied the physical properties and band structure of a hybrid compound, $(C_2H_5NH_3)_2CoCl_4$. Detailed studies show that the compound features noncentrosymmetric yet nonpolar space group $P2_12_12_1$ (possible piezoelectric phase) below 235 K. Also the material exhibits paramagnetism down to 2 K with featuring sizable magnetocaloric effect. Further, we have prepared two guanidinium caion containing hybrid halides, $(CN_3H_6)_2MnCl_4$ and $(CN_3H_6)_2CuBr_4$ and studied their physical properties thoroughly. Both of these materials exhibit zero-dimensional crystal structures where extensive ion-pair interactions among guanidinium cations and also hydrogen bonding have been observed. The $(CN_3H_6)_2MnCl_4$ compound is structurally unique, featuring face-shared trimeric $(Mn_3Cl_{12})^{6-}$ units. This compound is highly luminescent with sizeable quantum yield and lifetime features. It also exhibits large hysteresis across structural phase transition coupled with dielectric and weak magnetic switching. We have shown that the large hysteresis across phase transition is governed by the extensive nature of the supramolecular interactions present among the components. We have shown that the large hysteresis across phase transition is governed by the extensive nature of the supramolecular interactions present among the components.The compound $(CN_3H_6)_2CuBr_4$, on the other hand was seen to behave as a low dimensional coupled spin ladder antiferromagnet where the magnetic interaction propagates in two halide magnetic exchange pathways. In the last chapter, we have prepared layered compound $(C_6H_5CH_2NH_6)_2CuBr_4$ which contains benzylammonium cations and we have studied the crystal structure, surface, electrical and magnetic properties. Thorough experimental studies reveal that the crystals form as stacked layers with ultra-smooth mirror-like surfaces in centrosymmetric monoclinic structure ($C2/c$). Strong magnetocrystalline anisotropy was observed in magnetic measurements where we have observed unprecedented field-induced metamagnetic transitions with applied field perpendicular to *c*-axis.